

The Electrode-Electrolyte Interface
from the Perspective of
Density Functional Theory
Decay Lengths, Differential Capacitance, Machine Learning

Peter Cats

About the cover:

Odin, the chief of the Aesir (Norse gods), has many names and is often portrayed as an old man, dressed in grey, with a wide-brimmed hat, and one eye. Odin is constantly in pursuit of gaining knowledge and wisdom, often in exchange of a sacrifice; he gave his eye to drink from the well of Mimir, which contains much wisdom, and even hung himself at Yggdrasil (the world tree) pierced by his own spear Gungnir for nine days and nights in order to understand the runes, which also contained wisdom and knowledge. He does not seek knowledge and wisdom only for himself, but he wants to learn anything that might prevent catastrophe at Ragnarok. Moreover in the poem Hávamál (part of the Edda), meaning "words of the high one" (a reference to Odin), he gives wisdom and advice on how to live a good life, e.g. never stop learning, and do not drink too much alcohol.

Front cover: "Odhin" (1901), by Johannes Gehrts

Copyright ©2022 Peter Cats. All right reserved.

*The Electrode-Electrolyte Interface
from the Perspective of
Density Functional Theory:
Decay Lengths, Differential Capacitance, Machine Learning*

*Het Elektrode-Elektrolyt Interface
vanuit het Perspectief van
Dichtheidsfunctionaaltheorie:
Correlatielengte, Differentiële Capaciteit, Machinaal Leren
(met een samenvatting in het Nederlands)*

Proefschrift

ter verkrijging van de graad van doctor aan de Universiteit Utrecht op gezag van de rector magnificus, prof.dr. H.R.B.M. Kummeling, ingevolge het besluit van het college voor promoties in het openbaar te verdedigen op woensdag 23 februari 2022 des middags te 2.15 uur

door

Peter Cats

geboren op 1 November 1991 te Oosterhout (NB)

Promotor: Prof. dr. R. van Roij

Dit proefschrift werd mede mogelijk gemaakt met financiële steun van de Nederlandse Organisatie voor Wetenschappelijk Onderzoek (NWO).

CONTENTS

1	INTRODUCTION	1
1.1	Thermodynamics of the Confined Electrolyte between Electrodes	4
1.2	A Microscopic Model for the Electrode-Electrolyte Interface	8
1.2.1	The Primitive Model for the Electrolyte	8
1.2.2	The Model for the Electrode	11
1.3	From Microscopic Model to Macroscopic Thermodynamics	13
1.4	Theories	15
1.4.1	Density Functional Theory	15
1.4.2	DFT for the Electrode-Electrolyte Interface	20
1.4.3	Poisson-Boltzmann Theory	23
1.5	Capacitance of the Electrode-Electrolyte Interface	24
	Appendices	27
1.A	Fundamental Measure Theory	27
2	PRIMITIVE MODEL ELECTROLYTES IN THE NEAR AND FAR FIELD: DECAY LENGTHS FROM DFT AND SIMULATIONS	33
2.1	DFT for the Primitive Model	34
2.1.1	Homogeneous Electrolytes	35
2.1.2	Inhomogeneous Electrolytes	39
2.2	DFT Calculations and MD Simulations for the RPM at a Planar Electrode	43
2.3	Results For Density Profiles and Decay Lengths	45
2.3.1	Near Field	45
2.3.2	Far Field	45
2.4	Summary and discussion	58
2.5	Conclusion	61
	Appendices	63
2.A	Mean Spherical Approximation	63
2.B	Adding Electrostatic Energy terms to the functional and the inconsistency of the MSAu	64
2.C	Decay of the Density Profile versus that of the Bulk Correlation Function	67
2.D	Analysing the Euler Lagrange Equations in the Far Field	69
2.E	Thermodynamics of three functionals	71
2.F	Asymptotic Decay Lengths	74
2.F.1	FMT Decay Length	75
2.F.2	MSAc Decay Length	76

3	CAPACITANCE AND STRUCTURE OF ELECTRIC DOUBLE LAYERS: COMPARING BROWNIAN DYNAMICS AND CLASSICAL DENSITY FUNCTIONAL THEORY . . .	77
3.1	Model	79
3.2	Method	81
3.2.1	Brownian Dynamics	81
3.2.2	Density Functional Theory	82
3.3	Thermodynamics	82
3.4	Results	86
3.4.1	Reference system	86
3.4.2	Varying ion concentrations	88
3.4.3	Differently-sized ions	88
3.4.4	Changing the Surface Potential	89
3.4.5	Different Valencies	89
3.4.6	Slit width	90
3.4.7	Capacitance	90
3.5	Discussions, Conclusions and Outlook	92
	Appendices	95
3.A	Thermodynamics Derivation	95
3.B	Calculation of the Capacitance	96
3.C	Adsorption Inconsistency	97
3.D	Constant potential versus fixed charge	97
4	THE DIFFERENTIAL CAPACITANCE AS A PROBE FOR THE ELECTRIC DOUBLE LAYER STRUCTURE AND THE ELECTROLYTE BULK COMPOSITION	99
4.1	Differential Capacitance	100
4.1.1	The System	100
4.1.2	Thermodynamics in the Pore	102
4.1.3	Differential Capacitance Revisited	103
4.1.4	Density Functional Theory	105
4.1.5	Simulations	106
4.2	Capacitance Curves	107
4.2.1	First Glance: Symmetric Electrolyte	107
4.2.2	Second Glance: Asymmetric Electrolytes	111
4.2.3	Impurities	116
4.3	Conclusion	118
	Appendices	121
4.A	Capacitive Energy	121
4.B	Density Profiles: Impurities	121
5	MACHINE-LEARNING FREE-ENERGY FUNCTIONALS USING DENSITY PROFILES FROM SIMULATIONS	123
5.1	classical density functional theory	125

5.1.1	Formalism	125
5.1.2	Planar geometry	128
5.2	System	129
5.3	Methods	130
5.3.1	Simulations	130
5.3.2	Machine Learning Methods	132
5.3.3	The Training Process	133
5.4	Results for the Lennard-Jones System	134
5.4.1	The Kernels	134
5.4.2	The Density Profiles	135
5.4.3	Mechanical equation of state of the bulk	135
5.4.4	The structure of the bulk fluid	138
5.5	Summary, discussion, and outlook	142
6	SUMMARY, CONCLUSION AND OUTLOOK	145
7	SAMENVATTING	153
	References	157
	About the Author	169
	Acknowledgments	171

This Thesis is based upon the following publications:

- [1] P. Cats, R. Evans, A. Härtel, and R. van Roij, "Primitive model electrolytes in the near and far field: Decay lengths from DFT and simulations", *J. Chem. Phys.* **154**, 124504 (2021)
- [2] P. Cats, R. S. Sitlapersad, W. K. den Otter, A. R. Thornton, and R. van Roij, "Capacitance and Structure of Electric Double Layers: Comparing Brownian Dynamics and Classical Density Functional Theory", *J. Solution Chem.* (2021)
- [3] P. Cats and R. van Roij, "The differential capacitance as a probe for the electric double layer structure and the electrolyte bulk composition", *J. Chem. Phys.* **155**, 104702 (2021)
- [4] P. Cats, S. Kuipers, S. de Wind, R. van Damme, G. M. Coli, M. Dijkstra, and R. van Roij, "Machine-learning free-energy functionals using density profiles from simulations", *APL Materials* **9**, 031109 (2021)

Other publications by the author:

- P. Cats, A. Quelle, O. Viyuela, M. A. Martin-Delgado, and C. Morais Smith, "Staircase to higher-order topological phase transitions", *Phys. Rev. B* **97**, 121106(R) (2018)

INTRODUCTION

This thesis will be a journey to the world of ions near charged surfaces, with the aim to understand how ions behave in that environment and how that knowledge can be used to save the world. The term ion was coined in 1834 by Michael Faraday to describe the chemical species that travel from one electrode to another in an aqueous (water-like) solution, and derives from the Greek word *ion* or *ienai*, meaning "to go" (they go towards oppositely charged electrodes) [5]. He also introduced the terms cathode (negatively charged electrode) and anode (positively charged electrode) that attract the cations (positively charged ions that go towards the cathode) and anions (negatively charged ions that go towards the anode), respectively. Those two terms derive from the Greek words *kata-* "down" and *ana-* "up", respectively, and the word *hodos* "a way, path, road"; it describes the supposed route that electrons ought to make. Here, let us just stick to the definition that ions are molecules or atoms that have a net charge due to an excess or deficit of electrons in their outer shells. Ions are everywhere and play an important role in biology, chemistry and physics. A few examples of common ions are Sodium Na^+ , Chloride Cl^- , Calcium Ca^{2+} , and Carbonate CO_3^{2-} , the former two make up table salt, NaCl , and the latter two are causing limescale, CaCO_3 , that forms at faucets (as illustrated in Fig. 1.1).

The amount of charge on ions is specified by the valency (superscript, e.g. $+$, $-$, $2+$, and $2-$) that indicates the excess (negative) or deficit (positive) number of electrons present in the ion. Due to the universe being charge neutral, ions make up uncharged crystals (e.g. NaCl and CaCO_3). In air at room temperature, individual ions are almost non-existent because of the strong attraction between the cations and anions. That is why one can buy



Figure 1.1: Common examples of Sodium Chloride (left: made by Alexander Barnavelli) and Calcium Carbonate (right)

table salt in crystalline form, and why limescale is formed at faucets after the water has evaporated, leaving behind an ionic crystal. In order to study the behavior of ions, one needs another medium/solvent in which the interaction between the ions is much weaker. One such a solvent that we all know and love is water H_2O . The reason that the interaction between the ions is much weaker in water, is because water molecules have a dipole that can “screen” the charge on the ions, as depicted in Fig. 1.2. Hence, most salts dissolve in water, at least below the saturation concentrations. The solution of the solvent with the dissolved ions is referred to as an electrolyte.

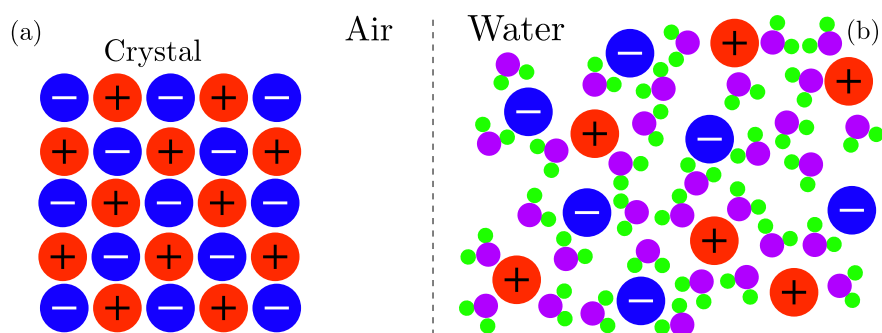


Figure 1.2: Schematic illustration of ions in air (a) and water (b), and how the water molecules (purple(O)-green(H) particles) screen the charge on the ions, causing the salt molecules to dissolve.

One of the applications for which the electrolyte-electrode interface is relevant concerns energy storage, one of the major technological challenges nowadays. There are many “green” methods nowadays to transform one energy form into another [6], with electricity as the favoured end product, but the options to store it efficiently on a large scale are limited. With solar and wind energy on the rise, there is a need for an increasing flexibility of the power system [7, 8], due to the sunshine and wind being intermittent (i.e. the amount of harvested energy is not constant and can fluctuate quite drastically over time and geographic position). Therefore, efficient ways of storing energy is very much sought after, especially given the glooming energy shortage. Technologies for energy storage vary immensely and several classifications can be considered, for instance the actual technology used (e.g. chemical, electrochemical, electrical, mechanical and thermal) or the scale of storage (e.g. small scale, short term, large scale, long term); each of these subcategories has its own strengths, weaknesses and range of applicability [9, 10]. Electric-energy storage is mostly relevant for smaller-scale applications like mobile electric devices (smartphones, notebooks, etc), and electric vehicles (cars, busses, trains, etc). Currently, the most common batteries for this type of energy storage rely on the Lithium ion, whose mining is known to be rather environmental unfriendly [11, 12, 13, 14, 15, 16, 17]. For instance, it requires 2 million litres of water to mine one ton of Lithium, harming the surrounding soil, ruining farm lands, causing air contamination and the death of many animals. Hence, the search for alternatives to store energy is ongoing, and necessary for the energy transition to be successful and to fulfil its goal. One of the technologies to store electric energy employs the Electric Double Layer (EDL), in which the spatial distribution of ions in electrolytes

in contact with electrodes allows for storage of electric energy. Basically, such a device is comprised of a charged conductor (an electrode) immersed in an electrolyte, where the electron charge on the electrode is screened by the ions in the electrolyte. Such a system behaves in some sense similar to a conventional capacitor of two electric conductors, however with a much smaller distance between the oppositely charged entities, which in this case consists of an immobile electrode with, say, a positive electronic charge in close contact with a layer of mobile ions in the electrolyte with a net negative charge. Generally, the electrodes of EDL capacitors have a porous structure with a gigantic surface-to-volume ratio (up to $2000 \text{ m}^2 \text{ g}^{-1}$, see e.g. Refs. [18, 19]), and no chemical reactions take place at the surface. The large area, combined with the short distance between the charge on the electrode and in the electrolyte, leads to a large capacitance and therefore to a large amount of energy stored compared to conventional capacitors and the absence of reactions leads to long lifetimes compared to conventional batteries, which makes them “greener” as well. One of the disadvantages of EDL capacitors is the rather small energy density compared to common Lithium-ion batteries (by roughly a factor of 20) [20]. But, how ideal would it be if one could make energy-storage devices using merely seawater as an electrolyte? In Chapters 3 and 4 we dive into the differential capacitance, the quantity of interest for energy storage. Alternative electrolytes that are applied for energy-storage devices are ionic liquids [21, 22, 23], which are electrolytes without a solvent such that each constituent is charged. Basically, the ions in ionic liquids are sufficiently asymmetric and large that forming crystals is energetically unfavorable, causing a very low freezing temperature (down to room temperature or even below), especially compared to conventional salts that have freezing temperature around 800 degrees Celsius. Hence, understanding fully the structure of EDLs at high ionic concentrations is therefore important for fundamental reasons. Moreover, understanding EDLs in all their glory is also directly relevant for other practical devices that hinge on mobile ions in a liquid. For instance, heat-to-current conversion [24], and porous carbon electrodes immersed in aqueous electrolytes can be used for harvesting blue energy [25, 26] or desalinating water [27]. These engineering applications are in addition to the important role of water-dissolved ions in, for instance, biology (the action potential, homeostasis, etc.) and geology (mineral stability, dissolution rates, etc.).

Models describing the EDL have progressed from a simplistic double layer capacitor model, proposed by Helmholtz [28] from which the name EDL originates, to the first Primitive Model (PM) description by Gouy [29], Chapman [30], and Debye and Hückel [31] (DH), where the electrolyte is modeled explicitly in terms of discrete ions embedded in a uniform dielectric medium, to current all-atom models [32, 33], where both the solvent molecules and the ions are treated explicitly. In recent years, classical Density Functional Theory (DFT) and Integral Equation Theories (IET) have been employed, alongside Molecular Dynamics (MD), Brownian Dynamics (BD) and Monte Carlo (MC) simulations, to study the EDL. Given the rich collection of theories and simulation methods used to investigate various models, one might have expected a comprehensive description of the EDL to have emerged. However, recent experiments suggest otherwise. Over the last few years, several experimental groups have measured anomalously large decay lengths of the force between

two charged cylindrical surfaces immersed in concentrated electrolytes (e.g. concentrations larger than about 1 M of NaCl dissolved in water) or in ionic liquids [34, 35, 36, 37]; see also the summary article Ref. [38]. We refer to these experiments as Surface Force Apparatus (SFA) studies. Although these measurements relate to *confined* liquids, it is well-known that the asymptotic solvation force, as is assumingly measured by the SFA, is determined by the asymptotic decay of the one-body density profiles at an individual surface. It turns out that this decay length is actually a bulk property of the electrolyte, and will be the main topic of interest in Chapter 2.

In this introduction, we will give an overview of the thermodynamics behind the electrode-electrolyte interface, the models to describe them, and the theories to tackle the model. Each subsequent chapter will go into more detail regarding their own specific theoretical setting. At the end we also introduce the notion of differential capacitance, which is the main topic of interest in Chapters 3 and 4.

1.1 THERMODYNAMICS OF THE CONFINED ELECTROLYTE BETWEEN ELECTRODES

In order to model the system (the confined electrolyte between electrodes), we need a clear picture on what we actually want to describe. Although different chapters in this thesis address different aspects, the underlying thermodynamics has many common features. Here, we present a general thermodynamic macroscopic description of the system considered.

We wish to model a system of an electrolyte confined between two parallel planar surfaces as depicted in Fig. 1.3 (the part inside the dashed lines). The electrolyte in the system has a fixed temperature T , fixed volume V , and is in chemical (diffusive, osmotic) equilibrium with an ionic reservoir with which it can exchange ions. For simplicity, we consider an electrolyte with only one type of cation (+) and anion (-), while ignoring the solvent by assuming it to be an inert continuum (more on this in section 1.2.1). Hence, the number of cations and anions in the system fluctuates around their mean values $\langle N_+ \rangle$ and $\langle N_- \rangle$, respectively, while the total number of cations and anions in the system plus the ionic reservoir is fixed at \mathcal{N}_+ and \mathcal{N}_- . The two planar surfaces of the electrodes with surface area A are positioned at, say, the planes with Cartesian coordinates $x = 0$ and $x = H$. They are electronically connected to charge reservoirs, and by applying electric potentials Φ_0 and Φ_H on the two charge reservoir (and hence the electrodes) w.r.t. the grounded ionic reservoir, an electronic charge Q_0 and Q_H is transferred from the charge reservoir to the electrode by the exchange of work $\Phi_0 Q_0$ and $\Phi_H Q_H$. The charge on the surface, therefore, fluctuates around its mean value $\langle Q_0 \rangle$ and $\langle Q_H \rangle$, while the total electronic charge on the surface in the system plus that in the reservoir is fixed at \mathcal{Q}_0 and \mathcal{Q}_H . Global charge neutrality requires that $\mathcal{Q}_0 + \mathcal{Q}_H + z_+ \mathcal{N}_+ + z_- \mathcal{N}_- = 0$, where z_{\pm} denotes the valency of the cations/anions.

Because we fix the temperature T , volume of the system V , surface area A , and surface separation H , we will omit their dependence in the discussion below to simplify the nota-

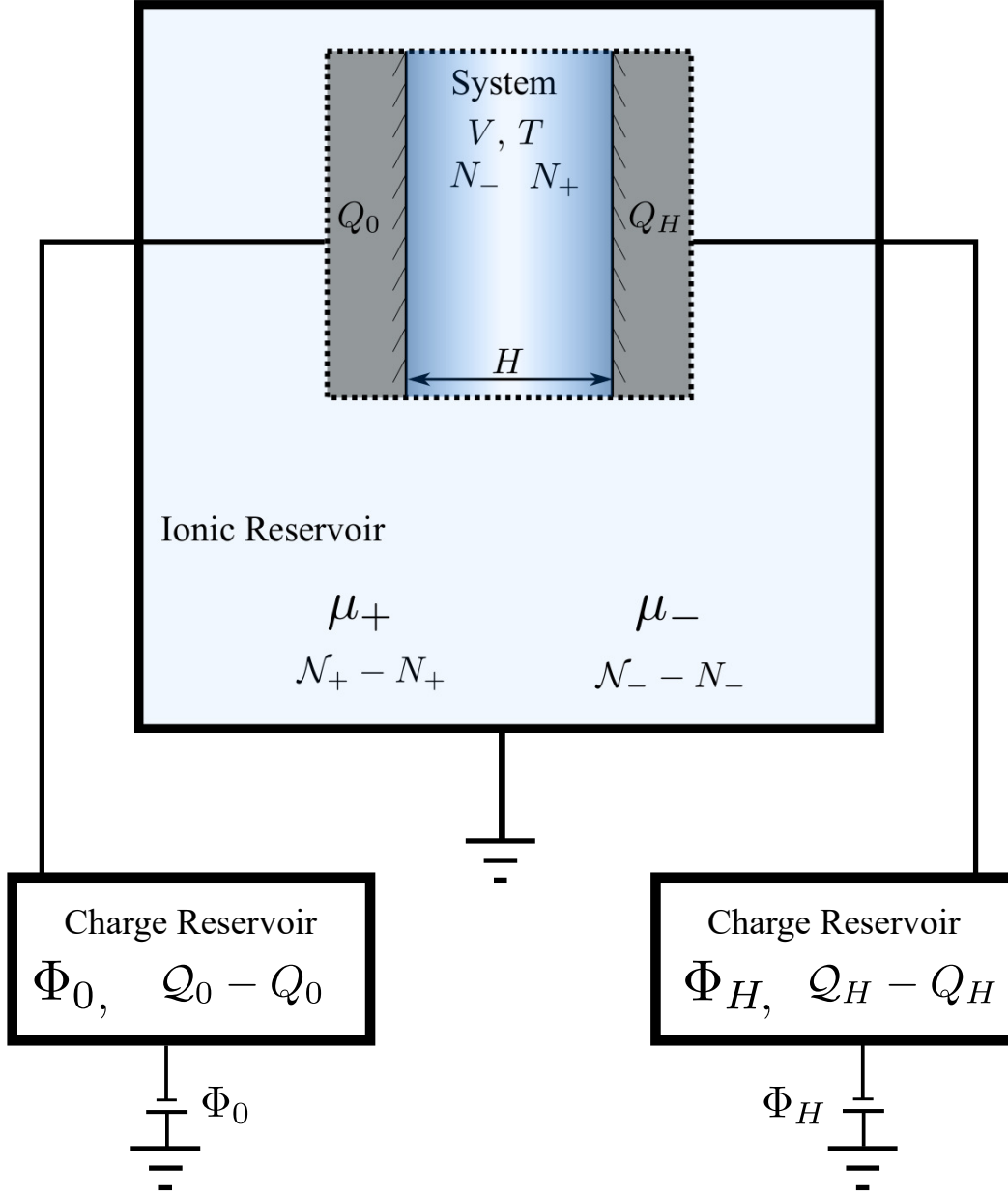


Figure 1.3: Schematic depiction of the thermodynamic description of the system of interest. The electrolyte is confined between two parallel planar charged surfaces and is in chemical (diffusive, osmotic) equilibrium with an ionic reservoir with which it can exchange ions. The two conductive surfaces of the electrodes are separated by a distance H and are held at a surface potential Φ_0 and Φ_H w.r.t. the grounded ionic reservoir, and are in electric equilibrium with their charge reservoirs with which they can exchange electronic charge.

tion. The total system, i.e. the system plus the reservoirs, is described canonically within the $(\mathcal{N}_+, \mathcal{N}_-, Q_0, Q_H)$ ensemble, corresponding to the Helmholtz free energy

$$\begin{aligned}
 F_{tot}(\mathcal{N}_\pm, N_\pm, Q_{0/H}, Q_{0/H}) = & F_{Nres}(\mathcal{N}_+ - N_+, \mathcal{N}_- - N_-) + \\
 & F_{Qres}(Q_0 - Q_0, Q_H - Q_H) + \\
 & F_{sys}(N_\pm, Q_{0/H}),
 \end{aligned} \tag{1.1}$$

where F_{Nres} is the free energy of the ionic reservoir with which the system can exchange ions, F_{Qres} the free energy of both the charge reservoirs with which the electrodes can exchange charge, and F_{sys} the free energy of the system of interest. Since the reservoirs are considered to be much larger than the system of interest, such that $N_{\pm} \ll \mathcal{N}_{\pm}$ and $Q_{0/H} \ll \mathcal{Q}_{0/H}$, we can expand around the reservoir particle numbers \mathcal{N}_{\pm} and charges $\mathcal{Q}_{0/H}$, obtaining to linear order

$$\begin{aligned}
F_{tot}(\mathcal{N}_{\pm}, N_{\pm}, \mathcal{Q}_{0/H}, Q_{0/H}) = & F_{Nres}(\mathcal{N}_{+}, \mathcal{N}_{-}) + F_{Qres}(\mathcal{Q}_0, \mathcal{Q}_H) + \\
& - \frac{\partial F_{Nres}(\mathcal{N}_{+}, \mathcal{N}_{-})}{\partial \mathcal{N}_{+}} N_{+} - \frac{\partial F_{Nres}(\mathcal{N}_{+}, \mathcal{N}_{-})}{\partial \mathcal{N}_{-}} N_{-} + \\
& - \frac{\partial F_{Qres}(\mathcal{Q}_0, \mathcal{Q}_H)}{\partial \mathcal{Q}_0} Q_0 - \frac{\partial F_{Qres}(\mathcal{Q}_0, \mathcal{Q}_H)}{\partial \mathcal{Q}_H} Q_H + \\
& F_{sys}(N_{\pm}, Q_{0/H}) + \mathcal{O}(N_{\pm}^2, Q_{0/H}^2),
\end{aligned} \tag{1.2}$$

where we note that the derivatives are taken by fixing the other variables. Recognizing that $\frac{\partial F_{Nres}}{\partial \mathcal{N}_{\pm}} = \mu_{\pm}$ and $\frac{\partial F_{Qres}}{\partial \mathcal{Q}_{0/H}} = \Phi_{0/H}$, allows us to write

$$\begin{aligned}
F_{tot}(\mathcal{N}_{\pm}, N_{\pm}, \mathcal{Q}_{0/H}, Q_{0/H}) = & F_{Nres}(\mathcal{N}_{+}, \mathcal{N}_{-}) + F_{Qres}(\mathcal{Q}_0, \mathcal{Q}_H) + \\
& - \mu_{+} N_{+} - \mu_{-} N_{-} + \\
& - \Phi_0 Q_0 - \Phi_H Q_H + F_{sys}(N_{\pm}, Q_{0/H}).
\end{aligned} \tag{1.3}$$

The total free energy F_{tot} strives to a minimum w.r.t. N_{\pm} and $Q_{0/H}$ at a fixed μ_{\pm} and $\Phi_{0/H}$. By noting that the first two terms on the right-hand side of Eq. (1.3) do not depend on the system parameters N_{\pm} and $Q_{0/H}$, one finds the condition

$$\Omega_{sys}(\mu_{\pm}, \Phi_{0/H}) = \min_{N_{\pm}, Q_{0/H}} [F_{sys}(N_{\pm}, Q_{0/H}) - \mu_{+} N_{+} - \mu_{-} N_{-} - \Phi_0 Q_0 - \Phi_H Q_H], \tag{1.4}$$

where Ω_{sys} is the grand potential (at fixed electrode and chemical potential) of the system. Minimizing the part within the brackets in Eq. (1.4) w.r.t. N_{\pm} and $Q_{0/H}$ gives the conditions

$$\left. \frac{\partial F_{sys}(N_{\pm}, Q_{0/H})}{\partial N_{\pm}} \right|_{N_{\pm}^*} = \mu_{\pm}, \tag{1.5}$$

$$\left. \frac{\partial F_{sys}(N_{\pm}, Q_{0/H})}{\partial Q_{0/H}} \right|_{Q_{0/H}^*} = \Phi_{0/H}, \tag{1.6}$$

where N_{\pm}^* and $Q_{0/H}^*$ denote the values satisfying the minimization condition, and which are the mean values in the thermodynamic limit of the system, i.e. $N_{\pm}^* = \langle N_{\pm} \rangle$ and $Q_{0/H}^* = \langle Q_{0/H} \rangle$. Therefore, the ionic reservoir and the system share the same chemical potentials and the charge reservoir and its respective electrode share the same electric potential. One can argue similarly that the global charge neutrality condition $Q_0 + Q_H + z_{+} \mathcal{N}_{+} + z_{-} \mathcal{N}_{-} = 0$ implies that the system itself is charge neutral on average,

i.e. $\langle Q_0 \rangle + \langle Q_H \rangle + z_+ \langle N_+ \rangle + z_- \langle N_- \rangle = 0$. Combining Eqs.(1.4), (1.5) and (1.6) allows us to write the grand potential Ω_{sys} as

$$\Omega_{sys}(\mu_{\pm}, \Phi_{0/H}) = F_{sys}(N_{\pm}^*, Q_{0/H}^*) - \mu_+ N_+^* - \mu_- N_-^* - \Phi_0 Q_0^* - \Phi_H Q_H^*, \quad (1.7)$$

which is the proper Legendre transform from the Helmholtz free energy, which is a function of $(N_{\pm}, V, T, Q_{0/H}, A, H)$ (the canonical ensemble), to the grand potential, which is a function of $(\mu_{\pm}, V, T, \Phi_{0/H}, A, H)$ (the constant-potential grand-canonical ensemble). Taking the differential, one consequently finds

$$d\Omega(\mu_{\pm}, V, T, \Phi_{0/H}, A, H) = -SdT - pdV - \sum_{j=\pm} N_j d\mu_j - \sum_{s \in \{0, H\}} Q_s d\Phi_s + \gamma dA - f dH, \quad (1.8)$$

where S denotes the entropy, p the pressure, $\gamma = \sum_s \gamma_s$ the surface tension (or surface free energy) of the combined surfaces s , and f the solvation force between the plates directing outwards. By extensivity arguments, one can argue that $\Omega = -pV + \gamma A$, which by taking its differential and comparing it to Eq. (1.8) leads to the Lippmann equation

$$d\gamma = - \sum_j \Gamma_j d\mu_j - \sum_s \sigma_s d\Phi_s - \frac{f}{A} dH, \quad (1.9)$$

where $\sigma_s = Q_s/A$ denotes the average surface charge density on the electrode surface at $x = s$, and Γ_j the adsorption of ion species j , which quantity can also be expressed as

$$\Gamma_j = \int_0^H dx (\rho_j(x) - \rho_{b,j}), \quad (1.10)$$

with $\rho_j(x)$ denoting the local density of particles of species j (see section 1.4.1), and $\rho_{b,j}$ the bulk density in the reservoir. Using the Lippmann Eq. (1.9), one can obtain the following relations

$$\left(\frac{\partial \gamma}{\partial \mu_j} \right)_{\Phi_s, H} = -\Gamma_j, \quad \left(\frac{\partial \gamma}{\partial \Phi_s} \right)_{\mu_j, H} = -\sigma_s, \quad \left(\frac{\partial \gamma}{\partial H} \right)_{\mu_j, \Phi_s} = -\frac{f}{A} \quad (1.11)$$

and consequently the Maxwell relation

$$\left(\frac{\partial \Gamma_j}{\partial \Phi_s} \right)_{\mu_j, H} = \left(\frac{\partial \sigma_s}{\partial \mu_j} \right)_{\Phi_s, H}, \quad (1.12)$$

which will play an important role in Chapter 3.

The discussion thus far assumes electrodes on which the electric potential is fixed, which is relevant for experimental systems or practical devices that are connected to an external power source, of which EDL capacitors are a good example (see Chapter 4). In experiments, controlling the potential on the electrodes can be done with an external power source, but controlling the surface charge is often rather difficult, because it requires knowledge of the actual surface groups and the chemical reactions that take place at the surface. However,

one can circumvent this hassle and assign a fixed charge distribution to the electrode, which is often done in MD, BD, or MC simulations wherein the canonical ensemble comes natural; fixing the surface potential in simulations requires generally more effort [23, 39, 40, 41]. As a final note, let us emphasize that constant-charge boundary conditions belong to a different ensemble than constant-potential boundary conditions, and therefore they have a different free energy that is to be minimized; the same holds for constant particle number versus constant chemical potential, a situation described in more detail in Chapter 3.

1.2 A MICROSCOPIC MODEL FOR THE ELECTRODE-ELECTROLYTE INTERFACE

In this section we continue the analysis of the electrode-electrolyte interface by focusing on the microscopic model that will be used throughout this thesis: the Primitive Model (PM) confined between two smooth parallel planar surfaces. We show the simplification steps and assumptions made to arrive at this model.

The system in Fig. 1.3 consists of an electrolyte containing N_+ cations (of the same species), N_- anions (of the same species), and N_s solvent particles positioned at $\mathbf{r}_{\pm}^{N_{\pm}} = (\mathbf{r}_{\pm,1}, \mathbf{r}_{\pm,2}, \dots, \mathbf{r}_{\pm,N_{\pm}})$ and $\mathbf{r}_s^{N_s} = (\mathbf{r}_{s,1}, \mathbf{r}_{s,2}, \dots, \mathbf{r}_{s,N_s})$, respectively, confined between two solid electrodes containing atoms/molecules, whose fixed positions determine the external potential $\mathcal{V}_{ext}(\mathbf{r}_s^{N_s}, \mathbf{r}_+^{N_+}, \mathbf{r}_-^{N_-})$ with the electrolyte. The electronic charge distribution inside the electrodes at, say, $x = 0$ and $x = H$, is given by $q_0(\mathbf{r})$ and $q_H(\mathbf{r})$, and is induced by the applied (constant) electric potential Φ_0 and Φ_H , respectively. Fixing the positions of the electrode particles is already a simplification, since it allows us to ignore the interparticle interactions within the solid electrode. Those interactions can generally not be described classically, and therefore are beyond the scope of this thesis. We thus assume the electrode to be inert in all respects, except for its charge. The resulting Hamiltonian for this system reads

$$\begin{aligned} \mathcal{H}(\mathbf{p}_+^{N_+}, \mathbf{p}_-^{N_-}, \mathbf{p}_s^{N_s}, \mathbf{r}_+^{N_+}, \mathbf{r}_-^{N_-}, \mathbf{r}_s^{N_s}, [q_0], [q_H]) = & \sum_{j=\{+,-,s\}} \sum_{k=1}^{N_j} \frac{\mathbf{p}_{j,k}^2}{2m_j} + U_{int}(\mathbf{r}_s^{N_s}, \mathbf{r}_+^{N_+}, \mathbf{r}_-^{N_-}) + \\ & U_{el}(\mathbf{r}_s^{N_s}, \mathbf{r}_+^{N_+}, \mathbf{r}_-^{N_-}, [q_0], [q_H]) + U_{self}([q_0], [q_H]) + \mathcal{V}_{ext}(\mathbf{r}_s^{N_s}, \mathbf{r}_+^{N_+}, \mathbf{r}_-^{N_-}), \end{aligned} \quad (1.13)$$

where $\mathbf{p}_{j,k}$ denotes the momentum of the k -th particle of species j , $U_{int}(\mathbf{r}_s^{N_s}, \mathbf{r}_+^{N_+}, \mathbf{r}_-^{N_-})$ the multibody interaction potential of the mobile particles, $U_{el}(\mathbf{r}_s^{N_s}, \mathbf{r}_+^{N_+}, \mathbf{r}_-^{N_-}, [q_0], [q_H])$ the interaction potential between the charged electrodes and the mobile particles in the electrolyte, $U_{self}([q_0], [q_H])$ the electrostatic self energy of the electrodes and $\mathcal{V}_{ext}(\mathbf{r}_s^{N_s}, \mathbf{r}_+^{N_+}, \mathbf{r}_-^{N_-}) = \sum_{j=\{+,-,s\}} \sum_{k=1}^{N_j} V_{ext}^j(\mathbf{r}_{j,k})$ the (non-electrostatic) external potential. The brackets [...] indicate functional dependence.

1.2.1 The Primitive Model for the Electrolyte

First, let us focus on the multibody interaction potential of the mobile particles. Strictly

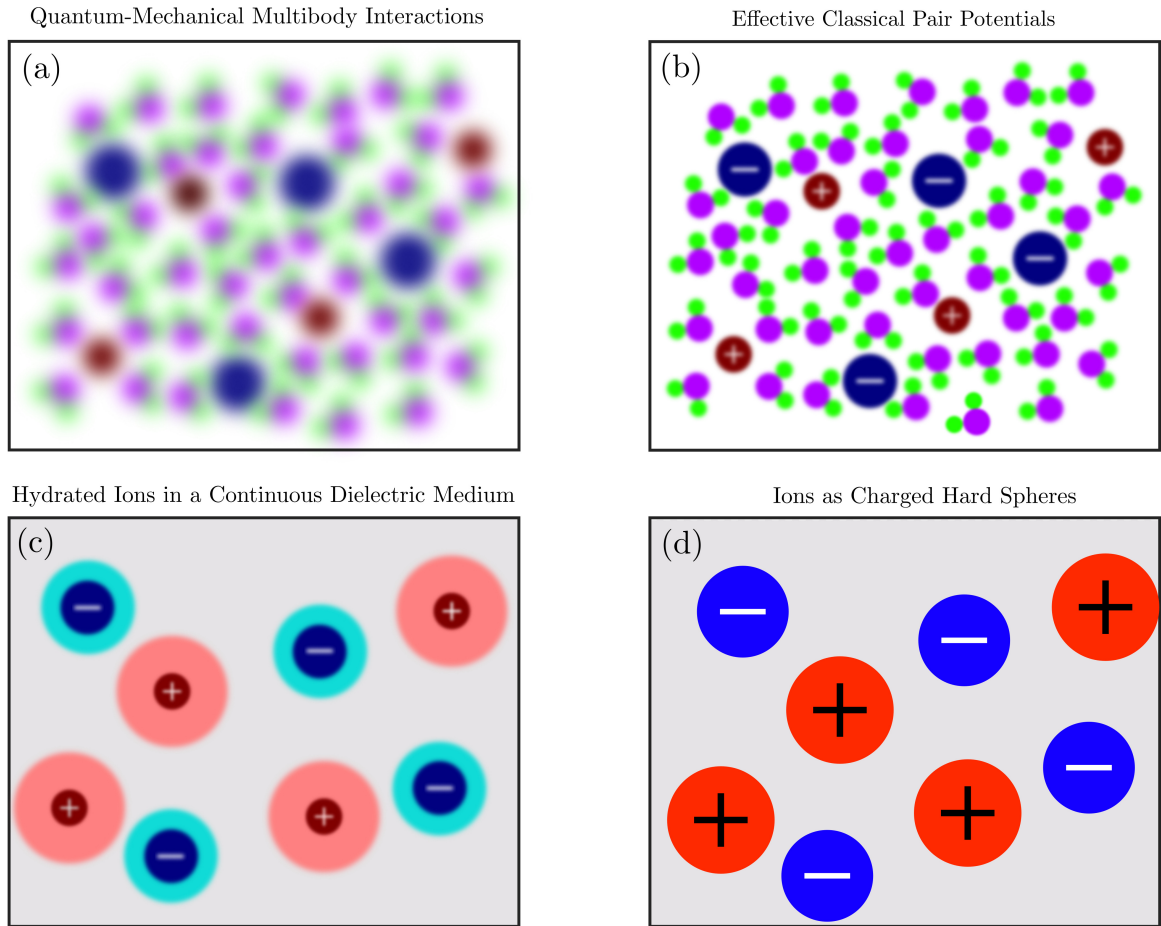


Figure 1.4: Illustration to depict the simplification steps underlying the PM. In (a), the quantum-mechanical multibody interaction potential gives a blurry view, due to the electron cloud around each particle. First from (a) to (b), the interaction potential gets simplified by assuming that this can be described via only (effective classical) pair potentials, giving rise to a clearer picture for the particles. Then from (b) to (c) the solvent is integrated out, leaving behind a continuous dielectric medium (grey) and furthermore influences the effective radius/diameter of the ions due to the hydration shell around each ion (the aura around the ions). Finally from (c) to (d), the only pairwise interaction between the ions is the combined Coulombic and hard-sphere interaction, removing the fuzziness.

speaking, the ions and solvent all interact with each other via the multibody interaction potential

$$U_{int}(\mathbf{r}_s^{N_s}, \mathbf{r}_+^{N_+}, \mathbf{r}_-^{N_-}) = U^{nonES}(\mathbf{r}_s^{N_s}, \mathbf{r}_+^{N_+}, \mathbf{r}_-^{N_-}) + U^{ES}(\mathbf{r}_s^{N_s}, \mathbf{r}_+^{N_+}, \mathbf{r}_-^{N_-}), \quad (1.14)$$

where we separated the non-electrostatic steric and dispersion interactions between the particles U^{nonES} from the electrostatic interactions between the particles U^{ES} . Note that these interactions do not need to be pairwise additive. However, in most practical cases the superposition principle can be applied to the electrostatics part and the dispersion

interaction are generally written as a pairwise interaction as well (see Fig. 1.4(a) to (b)). This reduces Eq. (1.14) to

$$U_{int}(\mathbf{r}_s^{N_s}, \mathbf{r}_+^{N_+}, \mathbf{r}_-^{N_-}) = \frac{1}{2} \sum_{i,j=\{s,+, -\}} \sum_{k \neq k'} \left[u^{nonES}(\mathbf{r}_{i,k}, \mathbf{r}_{j,k'}) + u^{ES}(\mathbf{r}_{i,k}, \mathbf{r}_{j,k'}) \right], \quad (1.15)$$

where the factor $1/2$ is to correct for overcounting and the lower case letter u is reserved to denote pair potentials. The solvent can be integrated out from the partition function (introduced below in section 1.3), leaving behind a dielectric continuous medium, and furthermore affects the effective size of the ions due to hydration (see Fig. 1.4(b) to (c)). For the case that this medium polarizes linearly with the electric field and the medium is homogeneous,¹ the effective pair potential u between two ions of species i and j with charge ez_i and ez_j , respectively, separated by a distance r , is given by the Coulomb (C) pair potential

$$u_{ij}^C(r) = \frac{1}{4\pi\epsilon_r\epsilon_0} \frac{ez_i ez_j}{r}, \quad (1.16)$$

where ϵ_0 is the dielectric permittivity of free space, ϵ_r the relative dielectric permittivity (or dielectric constant) as a result of integrating out the solvent, z_j the valency of ions of species j , and e the elementary charge. Typically, the non-electrostatic interaction between particles have a typical repulsive part, due to the Pauli exclusion principle, and an attractive part, due to induced dipole-dipole interactions, described by the Lennard-Jones (LJ) pair potential (see Chapter 5), for instance. Using this pair potential, one ends up with an expression that is much more tractable, although still impossible to use for analytical purposes

$$U_{int}(\mathbf{r}_+^{N_+}, \mathbf{r}_-^{N_-}) = \frac{1}{2} \sum_{i,j=\{+, -\}} \sum_{k \neq k'} \left[u^{LJ}(\mathbf{r}_{i,k}, \mathbf{r}_{j,k'}) + u^C(\mathbf{r}_{i,k}, \mathbf{r}_{j,k'}) \right]. \quad (1.17)$$

Because the attractive part of the dispersion interaction is often less relevant than the repulsive part [42], one often neglects the attractions and treat the repulsive interactions via hard-core or hard-sphere (HS) interactions. This last simplification (see Fig. 1.4(c)-(d)) results in the interaction potential of the Primitive Model (PM)

$$\begin{aligned} U^{PM}(\mathbf{r}_+^{N_+}, \mathbf{r}_-^{N_-}) &= \frac{1}{2} \sum_{i,j=\{+, -\}} \sum_{k \neq k'} \left[u^{HS}(|\mathbf{r}_{i,k} - \mathbf{r}_{j,k'}|) + u^C(|\mathbf{r}_{i,k} - \mathbf{r}_{j,k'}|) \right] \\ &\equiv \frac{1}{2} \sum_{i,j=\{+, -\}} \sum_{k \neq k'} u_{i,j}^{CHS}(|\mathbf{r}_{i,k} - \mathbf{r}_{j,k'}|), \end{aligned} \quad (1.18)$$

¹ In general, one can expand the polarization $\mathbf{P}(\mathbf{r})$ at position \mathbf{r} in terms of the electric field $\mathbf{E}(\mathbf{r})$ according to $\mathbf{P}(\mathbf{r}) = \epsilon_0 \chi_e(\mathbf{r}) \mathbf{E}(\mathbf{r}) + \mathcal{O}(\mathbf{E}^2)$, where $\chi_e(\mathbf{r})$ is the local electric susceptibility. Within linear response, one can ignore the higher orders in \mathbf{E} , given that \mathbf{E} is not too large. Interestingly, a polarizable medium in an external electric field $\mathbf{E}(\mathbf{r})$ gives rise to bound charge $q_b(\mathbf{r})$, via $q_b(\mathbf{r}) = -\nabla \cdot \mathbf{P}(\mathbf{r})$. Hence, Gauss' law $\nabla \cdot \mathbf{E}(\mathbf{r}) = -(q_{tot}(\mathbf{r}) + q_b(\mathbf{r}))/\epsilon_0$ (or the Poisson Eq. (1.56) introduced below) can be rewritten as $\nabla \cdot (\epsilon_r(\mathbf{r}) \mathbf{E}(\mathbf{r})) = -q_{tot}(\mathbf{r})/\epsilon_0$, where $\epsilon_r(\mathbf{r}) = 1 + \chi_e(\mathbf{r})$ is the relative dielectric permittivity (or dielectric constant) and $q_{tot}(\mathbf{r})$ denotes the combined charge of the ions and on the electrodes. For a homogeneous medium, where ϵ_r is independent of position, one obtains the more recognizable Gauss' law in the form $\nabla \cdot \mathbf{E} = -q_{tot}/\epsilon_r \epsilon_0$, from which one can derive the Coulomb pair potential in Eq. (1.16).

where the charged-hard-sphere (CHS) pair potential reads

$$\beta u_{i,j}^{CHS}(r) = \begin{cases} \infty & \text{for } r < d_{ij}; \\ z_i z_j \frac{\lambda_B}{r} & \text{for } r \geq d_{ij}. \end{cases} \quad (1.19)$$

The parameter $\lambda_B = \beta e^2 / 4\pi\epsilon_r\epsilon_0$ is the so-called Bjerrum length, indicating the distance between two charged particles with elementary charge $\pm e$ at which the thermal energy $\beta^{-1} = k_B T$ equals the Coulomb energy, where k_B denotes the Boltzmann constant and T the temperature. In air, where the solvent is absent, the dielectric constant is unity, while in water at room temperature the dielectric constant is around 78. This translates into $\lambda_B \approx 0.73$ nm in water and $\lambda_B \approx 57$ nm in air. Hence, the electrostatic energy in water is 78 times smaller than that in air, meaning that ions can dissolve much easier in water than in air. Equivalently, taking two oppositely charged ions in water, thermal fluctuations only need to kick the two ions apart by about their diameter (typically ranging from 0.2 nm to 0.8 nm) in order to separate them and let them enjoy their entropy by living an independent life, while in air thermal fluctuations need to kick them about 100 ion diameters apart in order to separate them, which is extremely unlikely and causes the ions to form crystals in air.

The interaction potential in Eq. (1.18) describes the primitive model (PM), namely an electrolyte in which the solvent is treated as a continuous medium with dielectric constant ϵ_r and whose ions are charged hard spheres.

1.2.2 The Model for the Electrode

Let us now focus on the model for the electrode. The study of the (atomic) details regarding charged surfaces of electrodes deserves its own thesis, due to its immense complexity (see, e.g. [43, 44]); the electrode is made up of atoms with their respective nontrivial electron clouds, which might chemically react with the ions or solvent molecules in the electrolyte, and which might be released from the surface or causing ions to adsorb, etc. One can get rid of this complexity by simplifying the electrode as a rigid chemically-inert coarse-grained crystalline electrode build from spherical particles (that may or may not interact non-electrostatically with the particles in the electrolyte). This is often a convenient approach, and was already hinted at by stating that the electrode particles positions are fixed and determine $\mathcal{V}_{ext}(\mathbf{r}_+^{N+}, \mathbf{r}_-^{N-})$, but are otherwise unspecified. This approach will, for instance, be used in the BD simulations in Chapter 3. In that chapter, we also show, by comparing BD simulations with DFT calculation, that the atomic details of the surface of the electrode do actually not have a significant effect on the density profiles of the ions [2]. Besides, even the coarse-grained electrodes made up of spherical particles is challenging to study within DFT, because it requires a three-dimensional description of the system. Therefore, we consider the simplest approach for the surface of the electrode, namely a perfectly smooth surface, which would correspond to smearing out the particles in the electrode, i.e. a continuous-solid electrode at which no chemical reactions takes place and

that blocks any ion from penetrating the electrode. In a later section 1.4.2 we will show that this allows us to describe the system effectively one dimensional.

By employing perfectly-flat continuous electrode surfaces, one can drop the notion of particles in the electrodes, and consider, for convenience, infinitely large planar parallel electrodes positioned at $x = 0$ and $x = H$. The external potential $\mathcal{V}_{ext}(\mathbf{r}_+^{N+}, \mathbf{r}_-^{N-}) = \sum_{j=\pm} \sum_{k=1}^{N_j} V_{ext}^j(\mathbf{r}_{j,k})$ then determines the location of the electrodes. For convenience, we consider the external hard-wall potential $V_{ext}^j(\mathbf{r}_{j,k})$ acting on the ions in the electrolyte, which reads

$$\beta V_{ext}^j(\mathbf{r}_{j,k}) = \begin{cases} \infty & \text{for } (x < d_j/2, y, z)_{j,k} \text{ or } (x > H - d_j/2, y, z)_{j,k}; \\ 0 & \text{for } (x \geq d_j/2, y, z)_{j,k} \text{ or } (x \leq H - d_j/2, y, z)_{j,k}, \end{cases} \quad (1.20)$$

i.e. the ions can approach the surfaces at $x = 0$ and $x = H$ up to their radius $d_j/2$, due to having a hard core. This approach ignores all the non-electrostatic interactions between the electrode and the ions in the electrolyte, which is a strong simplification of the real situation. However, from a theoretical perspective, it simplifies the equation for the pressure on the surface, for instance, which in turn leads to valuable insight in the underlying physics, as we show in Chapter 4.

For perfect conductors, all charge in the electrode will reside on the surface, resulting in an electrode charge density $q_s(\mathbf{r}) = \delta(x - s)\sigma_s(y, z)$, where $s \in \{0, H\}$. That is, the electrode charge now fully resides on the surfaces at $x = 0$ and $x = H$ instead of penetrating into the electrode bulk, avoiding complicated electrode charge distributions². Note that the surface charge density $\sigma_{0/H}(y, z)$ does not need to be homogeneous, which explains the y, z dependence, and actually fluctuates as a result of exchanging charge with the charge reservoirs (see again Fig. 1.3). For now, we retain the notation $q_s(\mathbf{r})$ for the electronic charge distribution in the electrodes for future reference, instead of already substituting for surface charge density $\sigma_s(y, z)$. As in the PM, we assume that the interaction potential between the charge on the surface with the ions in the electrolyte is given by the Coulomb potential

$$U_{el}(\mathbf{r}_+^{N+}, \mathbf{r}_-^{N-}, [q_0], [q_H]) = \sum_{s=\{0,H\}} \sum_{j=\pm} \sum_{k=1}^{N_j} \int d\mathbf{r} q_s(\mathbf{r}) \frac{ez_j}{4\pi\epsilon_r\epsilon_0|\mathbf{r} - \mathbf{r}_{j,k}|}, \quad (1.21)$$

where \mathbf{r} denotes the vector pointing towards the charge $d\mathbf{r}q_s(\mathbf{r})$ in the electrode. Similarly, we can write the self energy of the electrodes as³

$$U_{self}([q_0], [q_H]) = \frac{1}{2} \sum_{ss'} \int d\mathbf{r} d\mathbf{r}' \frac{q_s(\mathbf{r})q_{s'}(\mathbf{r}')}{4\pi\epsilon_r\epsilon_0|\mathbf{r} - \mathbf{r}'|}. \quad (1.22)$$

² We do like to mention that the electrode structure and the non-electrostatic interaction with the ions for a specific electrode material, specified by \mathcal{V}_{ext} , the electron charge density in the electrode $q_s(\mathbf{r})$, the electrostatic interaction with the ions U_{el} , and its self energy U_{self} , can be taken into account explicitly using quantum (or electronic) DFT (e.g. see Ref. [44]), but that lies beyond the scope of this thesis.

³ Here, it is implicitly understood that ϵ_r is spatially constant.

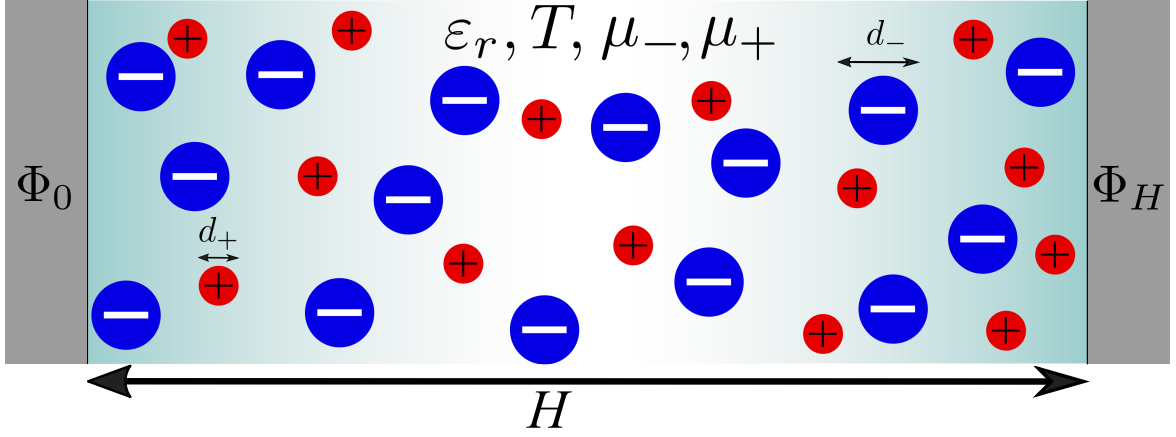


Figure 1.5: An illustration of the confined PM electrolyte between two electrode surfaces that are separated by a distance H and have a fixed surface potential Φ_0 and Φ_H . The cations and anions are modeled as charged hard spheres with diameter d_+ and d_- , respectively, and reside within a continuous dielectric medium with dielectric constant ϵ_r and temperature T , and are in chemical equilibrium with an ion reservoir at chemical potential μ_+ and μ_- .

Hereby, we have specified all the terms in the Hamiltonian of Eq. (1.13). The model corresponding to this Hamiltonian, is depicted in Fig. 1.5.

1.3 FROM MICROSCOPIC MODEL TO MACROSCOPIC THERMODYNAMICS

Within the configurational picture (ions at specific position $\mathbf{r}_\pm^{N_\pm}$ and a specific charge distribution $q_{0/H}(\mathbf{r})$), it is convenient to consider the probability distribution to find the system in a certain state. The probability distribution contains the Boltzmann factor of the Hamiltonian

$$\mathcal{H}(\mathbf{p}_+^{N_+}, \mathbf{p}_-^{N_-}, \mathbf{r}_+^{N_+}, \mathbf{r}_-^{N_-}, [q_0], [q_H]) = \sum_{j=\pm} \sum_{k=1}^{N_j} \frac{\mathbf{p}_{j,k}^2}{2m_j} + U^{PM}(\mathbf{r}_+^{N_+}, \mathbf{r}_-^{N_-}) + U_{el}(\mathbf{r}_+^{N_+}, \mathbf{r}_-^{N_-}, [q_0], [q_H]) + U_{self}([q_0], [q_H]) + \mathcal{V}_{ext}(\mathbf{r}_+^{N_+}, \mathbf{r}_-^{N_-}) \quad (1.23)$$

minus the work that is exchanged with the reservoirs. The work that is needed to fill the system with N_\pm cations/anions from the reservoir that has chemical potential μ_\pm is $\sum_{j=\pm} \mu_j N_j$, and the work that is needed to put the total charge $Q_{0/H} = \int d\mathbf{r} q_{0/H}(\mathbf{r}) = \int dy \int dz \sigma_{0/H}(y, z)$ on the surfaces from the charge reservoir by applying the electric potential $\Phi_{0/H}$ is $\sum_{s=\{0,H\}} Q_s \Phi_s$. Hence, the probability of finding N_\pm ions in the system at positions $\mathbf{r}_\pm^{N_\pm}$, given that the surfaces have a fixed potential $\Phi_{0/H}$ and that the system is in chemical equilibrium with an ion reservoir at μ_\pm , reads

$$P(\mathbf{r}_\pm^{N_\pm} | \Phi_{0/H}, \mu_\pm) = \frac{1}{\Xi(\mu_\pm, \Phi_{0/H})} \frac{1}{N_+! N_-! h^{3(N_+ + N_-)}} \int \mathcal{D}q_0 \int \mathcal{D}q_H \int d\mathbf{p}_+^{N_+} \int d\mathbf{p}_-^{N_-} \exp \left[-\beta \mathcal{H}(\mathbf{p}_+^{N_+}, \mathbf{p}_-^{N_-}, \mathbf{r}_+^{N_+}, \mathbf{r}_-^{N_-}, [q_0], [q_H]) + \beta \sum_{j=\pm} \mu_j N_j + \beta \sum_{s=0,H} Q_s \Phi_s \right], \quad (1.24)$$

where the factorial $N_{\pm}!$ is to correct for overcounting due to the ions being indistinguishable, h is Planck's constant, the normalization factor $\Xi(\mu_{\pm}, \Phi_{0/H})$ is the partition function discussed below (we again omitted the V, T, A, H dependence for brevity), and $\mathcal{D}q_{0/H}$ denotes the path integral over $q_{0/H}$. The momentum integrals are trivial and can be carried out straightforwardly, obtaining

$$\begin{aligned}
P(\mathbf{r}_{\pm}^{N_{\pm}} | \Phi_{0/H}, \mu_{\pm}) &= \frac{1}{\Xi(\mu_{\pm}, \Phi_{0/H})} \frac{1}{N_+! N_-! \Lambda_+^{3N_+} \Lambda_-^{3N_-}} \int \mathcal{D}q_0 \int \mathcal{D}q_H \\
&\exp \left[-\beta U^{PM}(\mathbf{r}_+^{N_+}, \mathbf{r}_-^{N_-}) - \beta U_{el}(\mathbf{r}_+^{N_+}, \mathbf{r}_-^{N_-}, [q_0], [q_H]) + \right. \\
&\quad - \beta U_{self}([q_0], [q_H]) - \beta \sum_{j=\pm} \sum_{k=1}^{N_j} V_{ext}^j(\mathbf{r}_{j,k}) + \\
&\quad \left. \beta \sum_{j=\pm} \mu_j N_j + \beta \sum_{s=0,H} Q_s \Phi_s \right], \tag{1.25}
\end{aligned}$$

where Λ_{\pm} is the thermal wavelength of the cations/anions (obtained from integrating out the kinetic energy), which at room temperature is at least typically 10 times smaller than the ion sizes considered and therefore a classical approach is justified. The electrode charge distribution $q_{0/H}^*$ that maximizes the integrand is the one that minimizes the term in the exponential [23] (see also Eqs. (1.5) and (1.6)). The condition satisfying this constraint reads

$$\left. \frac{\delta \left(U_{el}(\mathbf{r}_+^{N_+}, \mathbf{r}_-^{N_-}, [q_0], [q_H]) + U_{self}([q_0], [q_H]) - \sum_{s=0,H} Q_s \Phi_s \right)}{\delta q_s(\mathbf{r})} \right|_{q_s=q_s^*} = 0, \tag{1.26}$$

or equivalently

$$\left. \frac{\delta \left(U_{el}(\mathbf{r}_+^{N_+}, \mathbf{r}_-^{N_-}, [q_0], [q_H]) + U_{self}([q_0], [q_H]) \right)}{\delta q_s(\mathbf{r})} \right|_{q_s=q_s^*} = \Phi_s. \tag{1.27}$$

By substituting Eqs. (1.21) and (1.22) in the expression above, and by recalling that $q_s(\mathbf{r}) = \sigma_s(y, z)\delta(x-s)$, one finds the Coulombic expression for the electrostatic potential at $x=s$, namely

$$\Phi_s = \sum_{j=\pm} \sum_{k=1}^{N_j} \frac{ez_j}{4\pi\epsilon_r\epsilon_0|\mathbf{r}_s - \mathbf{r}_{j,k}|} + \sum_{s'} \int d\mathbf{r}' \frac{\sigma_s(y', z')\delta(x'-s)}{4\pi\epsilon_r\epsilon_0|\mathbf{r}_s - \mathbf{r}'|}, \tag{1.28}$$

where we note that Φ_s is homogeneous (independent on y, z) by construction, $\mathbf{r}_s = (x=s, y, z)$ denotes the vector locating a position on the surface, and $d\mathbf{r} = dx dy dz$. Because we impose Φ_s , Eq. (1.28) can be considered a constraint on the electrode charge distribution for a given ion configuration. In section 1.4.2 we will cast this expression in a more recognizable form.

Let us finish this discourse by writing down the partition function

$$\begin{aligned} \Xi(\mu_{\pm}, V, T, \Phi_{0/H}, A, H) &= \sum_{N_+} \sum_{N_-} \frac{1}{N_+! N_-! \Lambda_+^{3N_+} \Lambda_-^{3N_-}} \int d\mathbf{r}_+^{N_+} \int d\mathbf{r}_-^{N_-} \int \mathcal{D}q_0 \mathcal{D}q_H \\ &\exp \left[-\beta U^{PM}(\mathbf{r}_+^{N_+}, \mathbf{r}_-^{N_-}) - \beta U_{el}(\mathbf{r}_+^{N_+}, \mathbf{r}_-^{N_-}, [q_0], [q_H]) + \right. \\ &\quad \left. - \beta U_{self}([q_0], [q_H]) - \beta \sum_{j=\pm} \sum_{k=1}^{N_j} V_{ext}^j(\mathbf{r}_{j,k}) + \right. \\ &\quad \left. \beta \sum_{j=\pm} \mu_j N_j + \beta \sum_{s=0,H} Q_s \Phi_s \right] \quad (1.29) \\ &\equiv e^{-\beta \Omega_{sys}(\mu_{\pm}, V, T, \Phi_{0/H}, A, H)}, \quad (1.30) \end{aligned}$$

where the last equality connects the grand potential from Eq. (1.7) to the partition function Eq. (1.29). Hence, we established the beautiful connection between the *microscopic* description of the system, starting with the Hamiltonian, and the *macroscopic* thermodynamic description from section 1.1. In the following sections we go from a specific configuration of the electrolyte to thermally averaged quantities.

1.4 THEORIES

One can imagine that solving the multidimensional integral to obtain the partition function in Eq. (1.29) is simply impossible. Therefore, one can either come up with good approximations to be able to calculate the partition function, which is very difficult for these types of integrals, or one should take another route. Here we choose another route by employing classical Density Functional Theory (DFT).

1.4.1 Density Functional Theory

The first word ‘density’ already reveals the main subject within DFT, namely the density profile of the particles of interest. The density profile $\rho_j(\mathbf{r})$ of ions of species j is the ensemble (or time) average of the density operator $\hat{\rho}_j(\mathbf{r})$, i.e.

$$\rho_j(\mathbf{r}) = \langle \hat{\rho}_j(\mathbf{r}) \rangle = \left\langle \sum_{k=1}^{N_j} \delta(\mathbf{r} - \mathbf{r}_{j,k}) \right\rangle. \quad (1.31)$$

The ensemble average of an operator \mathcal{O} within the grand-canonical $(\mu_{\pm}, V, T, \Phi_{0/H}, A, H)$ ensemble reads

$$\langle \mathcal{O} \rangle = \sum_{N_+} \sum_{N_-} \int d\mathbf{r}_+^{N_+} d\mathbf{r}_-^{N_-} \mathcal{O} P(\mathbf{r}_{\pm}^{N_{\pm}}, V, T, A, H | \Phi_{0,H}, \mu_{\pm}), \quad (1.32)$$

with P taken from Eq. (1.25). Using this notion, one can prove (not presented here) that there exists a grand potential functional $\Omega[\{\rho\}]$ of the density profiles $\{\rho\}$ that is minim-

ized by the equilibrium density profiles $\{\rho_0\}$, where the brackets indicate the set of density profiles of all species (e.g. $\{\rho\} = \{\rho_+, \rho_-\}$), and the minimum is the actual thermodynamic grand potential Ω_{sys} of the system [42, 45, 46]. That is,

$$\left. \frac{\delta\Omega[\{\rho\}]}{\delta\rho_j(\mathbf{r})} \right|_{\{\rho\}=\{\rho_0\}} = 0, \quad (1.33)$$

and

$$\Omega[\{\rho_0\}] = \Omega_{sys}(\{\mu\}, V, T, \Phi_{0/H}, A, H), \quad (1.34)$$

respectively. Moreover, the grand potential can actually be written as

$$\Omega[\{\rho\}] = \mathcal{F}[\{\rho\}] - \sum_j \int d\mathbf{r} \rho_j(\mathbf{r}) \left[\mu_j - V_{ext}^j(\mathbf{r}) \right] - \sum_s Q_s \Phi_s, \quad (1.35)$$

where $\mathcal{F}[\{\rho\}]$ is the Helmholtz free energy functional and is intrinsic by definition. That means it contains only the intrinsic degrees of freedom and depends on the temperature and the interparticle interactions, but not on $\mu_j - V_{ext}^j(\mathbf{r})$, a feature that will be exploited in Chapter 5. However, we note that, although $\mathcal{F}[\{\rho\}]$ is intrinsic, its value at $\{\rho_0\}$ changes upon changing $\mu_j - V_{ext}^j(\mathbf{r})$ caused by the fact that the equilibrium density profiles are affected by it. Note that the appearance of the factor $\sum_s Q_s \Phi_s$ in Eq. (1.35) has the same origin as is Eq. (1.7), and is the factor related to the Legendre transform from fixed surface charge to fixed surface potential. Hence, when fixing the surface charge, instead of the surface potential, one should omit this contribution. The density profiles that follow from minimizing the grand potential functional are actually not affected by $\sum_s Q_s \Phi_s$, but it is important when analyzing the grand potential of the system.

An exact expression exists for the Helmholtz free energy functional [45, 46], but that one is basically just as useless and difficult to calculate exactly as Eq. (1.29). However, approximating the Helmholtz free energy functional is infinitely easier to do than to approximate the partition function, the main reason being that the latter regards a $6N$ dimensional integral over phase space, while the former only regards an integration over the volume. Moreover, one can use the formalism of thermodynamics to come up with approximations for $\mathcal{F}[\{\rho\}]$.

There are two cases for which $\mathcal{F}[\{\rho\}]$ is known exactly. The first and most obvious is the "ideal" case in which there are no interparticle interactions, i.e. $U(\{\mathbf{r}^N\}) = 0$, for which $\mathcal{F}[\{\rho\}]$ reads (see e.g. Refs. [42, 46])

$$\beta\mathcal{F}_{id}[\{\rho\}] = \int d\mathbf{r} \sum_j \rho_j(\mathbf{r}) \left[\log \Lambda_j^3 \rho_j(\mathbf{r}) - 1 \right]. \quad (1.36)$$

When turning on interparticle interactions, one prefers to write the Helmholtz free energy functional as $\mathcal{F}[\{\rho\}] = \mathcal{F}_{id}[\{\rho\}] + \mathcal{F}_{ex}[\{\rho\}]$, where $\mathcal{F}_{ex}[\{\rho\}]$ is called the over-ideal or excess Helmholtz free energy functional. By doing so, one can conveniently separate $\mathcal{F}[\{\rho\}]$ into a part that describes only the contribution due to the interparticle interactions $\mathcal{F}_{ex}[\{\rho\}]$

and a term $\mathcal{F}_{id}[\{\rho\}]$ that is always there and is independent of the presence and type of interparticle interactions.

The second case for which $\mathcal{F}[\{\rho\}]$ is known exactly is the one-dimensional hard-rod system, upon which the approximate but accurate functional for the hard-sphere system in three dimensions is based. This hard-sphere functional goes by the name fundamental measure theory (FMT), due to the use of “fundamental” measures of the spheres, like volume, surface area, radius. A lot has been written on this well-established functional and we refer the reader for details regarding this functional to Refs.[47, 48, 49, 50, 51] and also to Appendix 1.A.

1.4.1.1 Approximating the Helmholtz Free Energy Functional

There are different tools to approximate $\mathcal{F}_{ex}[\{\rho\}]$. First, let us introduce the pair distribution function

$$\rho_{ij}^{(2)}(\mathbf{r}, \mathbf{r}') = \left\langle \sum_{k=1}^{N_i} \sum_{\substack{l=1 \\ \mathbf{r}_{i,k} \neq \mathbf{r}_{j,l}}}^{N_j} \delta(\mathbf{r} - \mathbf{r}_{i,k}) \delta(\mathbf{r}' - \mathbf{r}_{j,l}) \right\rangle, \quad (1.37)$$

which is a measure for the probability to find a particle of species j at \mathbf{r}' given a particle of species i at \mathbf{r} . For a homogeneous isotropic bulk system, one can write the pair distribution function in terms of the bulk densities $\rho_{b,i}$ and $\rho_{b,j}$ of species i and j , respectively, and the radial distribution function $g_{ij}(r)$, according to

$$\rho_{ij}^{(2)}(\mathbf{r}, \mathbf{r}') = \rho_{b,i} \rho_{b,j} g_{ij}(|\mathbf{r} - \mathbf{r}'|). \quad (1.38)$$

From the pair distribution function one has access to the pressure p via the virial route

$$\beta p = \sum_j \rho_{b,j} - \frac{\beta}{6V} \int d\mathbf{r} \int d\mathbf{r}' \sum_{ij} r u'_{ij}(|\mathbf{r} - \mathbf{r}'|) \rho_{ij}^{(2)}(\mathbf{r}, \mathbf{r}'), \quad (1.39)$$

but most importantly (for this thesis) to the excess internal energy E_{ex} via the caloric/energy route

$$E_{ex} = \frac{1}{2} \int d\mathbf{r} \int d\mathbf{r}' \sum_{i \neq j} u_{ij}(|\mathbf{r} - \mathbf{r}'|) \rho_{ij}^{(2)}(\mathbf{r}, \mathbf{r}'), \quad (1.40)$$

where $u_{ij}(r)$ denotes the pair potential between two particles of species i and j separated by a distance r . The last route in Eq. (1.40) relates to the excess Helmholtz free energy via the relation $E_{ex} = \partial \beta \mathcal{F}_{ex} / \partial \beta$. This route is used for the so-called MSAu functional described in Chapter 2.

Interestingly, $\mathcal{F}[\{\rho\}]$ is also related to the pair distribution function by [46]

$$\rho_{ij}^{(2)}(\mathbf{r}, \mathbf{r}') = 2 \frac{\delta \mathcal{F}_{ex}[\{\rho\}]}{\delta u_{ij}(\mathbf{r}, \mathbf{r}')}, \quad (1.41)$$

which can be functionally integrated to obtain, for example, [42, 52, 53]

$$\mathcal{F}_{ex}[\{\rho\}] = \frac{1}{2} \sum_{ij} \int_0^1 d\alpha \int d\mathbf{r} \int d\mathbf{r}' \rho_{ij}^{(2)}(\alpha u; \mathbf{r}, \mathbf{r}') u_{ij}(\mathbf{r}, \mathbf{r}'), \quad (1.42)$$

where α is a switching parameter with which the interaction pair potential is turned on. By writing $\rho_{ij}^{(2)} = \rho_i(\mathbf{r}) g_{ij}(|\mathbf{r} - \mathbf{r}'|) \rho_j(\mathbf{r}')$, Eq. (1.42) casts the form

$$\mathcal{F}_{ex}[\{\rho\}] = \frac{1}{2} \sum_{ij} \int_0^1 d\alpha \int d\mathbf{r} \int d\mathbf{r}' \rho_i(\mathbf{r}) u_{ij}(|\mathbf{r} - \mathbf{r}'|) g_{ij}(\alpha; |\mathbf{r} - \mathbf{r}'|) \rho_j(\mathbf{r}'). \quad (1.43)$$

Within the mean-field approximation $g_{ij}(r) = 1$ one is allowed to write the simpler form

$$\mathcal{F}_{ex}^{MF}[\{\rho\}] = \frac{1}{2} \sum_{ij} \int d\mathbf{r} \int d\mathbf{r}' \rho_i(\mathbf{r}) u_{ij}(|\mathbf{r} - \mathbf{r}'|) \rho_j(\mathbf{r}'), \quad (1.44)$$

which is often a good approach to start with [54] (see Chapter 5), especially for soft pair potentials and low bulk concentrations. However, it falls short for strong external potentials, strong pair-potentials, and high bulk concentrations, i.e. when the density profiles are expected to have strong correlations. In that case, one needs to work harder to obtain better approximations.

Another important approximation scheme can be found from realizing that $\mathcal{F}_{ex}[\{\rho\}]$ is the generator for the so-called direct correlation functions, i.e.

$$c_{i_1, i_2, \dots, i_n}^{(n)}(\mathbf{r}, \mathbf{r}', \dots, \mathbf{r}^{(n)}; [\{\rho\}]) = -\beta \frac{\delta^n \mathcal{F}_{ex}[\rho]}{\delta \rho_{i_1}(\mathbf{r}) \delta \rho_{i_2}(\mathbf{r}') \dots \delta \rho_{i_n}(\mathbf{r}^{(n)})}, \quad (1.45)$$

of which the first $c^{(1)}$ and second direct correlation $c^{(2)}$ function are the most important ones (within this thesis)

$$c_i^{(1)}(\mathbf{r}; [\{\rho\}]) = -\beta \frac{\delta \mathcal{F}_{ex}[\rho]}{\delta \rho_i(\mathbf{r})}, \quad (1.46)$$

$$c_{ij}^{(2)}(\mathbf{r}, \mathbf{r}'; [\{\rho\}]) = -\beta \frac{\delta^2 \mathcal{F}_{ex}[\rho]}{\delta \rho_i(\mathbf{r}) \delta \rho_j(\mathbf{r}')}. \quad (1.47)$$

Throughout this thesis we use the standard notation $c_{ij}(r)$ for the second direct correlation function in the bulk, i.e. for the homogeneous isotropic system $c_{ij}(r) = c_{ij}^{(2)}(r; \{\rho_b\})$. By Taylor expanding $\mathcal{F}[\{\rho\}]$ around the bulk concentrations $\{\rho_b\}$ one finds another commonly-used approximation for the excess Helmholtz free energy functional

$$\begin{aligned} \beta \mathcal{F}_{ex}[\{\rho\}] = & \mathcal{F}_{ex}[\{\rho_b\}] + \sum_j \int d\mathbf{r} \beta \mu_j^{ex}(\{\rho_b\}) (\rho_j(\mathbf{r}) - \rho_{b,j}) - \\ & \frac{1}{2} \sum_{ij} \int d\mathbf{r} \int d\mathbf{r}' (\rho_i(\mathbf{r}) - \rho_{b,i}) c_{ij}^{(2)}(|\mathbf{r} - \mathbf{r}'|; \{\rho_b\}) (\rho_j(\mathbf{r}') - \rho_{b,j}) + \dots, \end{aligned} \quad (1.48)$$

where we identified $c_{b,j}^{(1)} = -\beta \mu_j^{ex}$ as the excess chemical potential of species j in the bulk. This approach was used to establish the so-called MSAC functional introduced in Chapter 2.

Important to note at this point is that $c_{ij}^{(2)}(r; \{\rho_b\})$ is a *function* the bulk densities $\{\rho_b\}$ and hence of $\{\mu\}$, which brings along inconsistencies, because it strictly should only be a *functional* of the density profiles. Examples, where such inconsistency are seeping through, and need to be accounted for, are shown in Chapter 3. Interestingly $c_{ij}^{(2)}(r)$ was first introduced by Ornstein and Zernike to determine the total correlation function $h_{ij}(r) = g_{ij}(r) - 1$ via the Ornstein-Zernike (OZ) equation [46, 55]

$$h_{ij}(\mathbf{r}, \mathbf{r}') = c_{ij}(\mathbf{r}, \mathbf{r}') + \sum_k \int d\mathbf{r}'' c_{ik}(\mathbf{r}, \mathbf{r}'') \rho_k(\mathbf{r}'') h_{kj}(\mathbf{r}'', \mathbf{r}'), \quad (1.49)$$

which forms a starting point for an Integral Equation Theory (IET). One should read this equation as: the total correlation $h_{ij}(\mathbf{r}, \mathbf{r}')$ between two particles of species i and j located at \mathbf{r} and \mathbf{r}' , respectively, is given by their direct correlation c_{ij} as though there are no other particles interfering, plus the correlations due to the interference of all the other particles $\sum_k c_{ik} \rho_k h_{kj}$. In Chapter 2 we go into details regarding the properties and connection between $\mathcal{F}[\{\rho\}]$ and $c_{ij}^{(2)}(r)$ for the PM, showing both the mean-field results as well as the results using the Mean-Spherical Approximation (MSA), which is a closure relation to solve the OZ equation in bulk.

1.4.1.2 Minimizing the Grand Potential Functional

The aim with DFT is to find the equilibrium density profiles $\rho_{0,j}(\mathbf{r})$ from which one has access to all the thermodynamic quantities. In practice, one needs to solve the Euler-Lagrange Eq. (1.8), which can be rewritten as

$$\rho_j(\mathbf{r}) = \rho_{b,j} \exp \left[-\beta V_{ext}^j(\mathbf{r}) + c_j^{(1)}(\mathbf{r}; [\{\rho\}]) - c_{b,j}^{(1)}(\{\rho_b\}) \right], \quad (1.50)$$

where $\rho_{b,j}$ denotes the bulk concentration defined by

$$\rho_{b,j} = \frac{e^{\beta \mu_j + c_{b,j}^{(1)}(\{\rho_b\})}}{\Lambda_j^3}, \quad (1.51)$$

and $c_{b,j}^{(1)}(\{\rho_b\})$ is the value of $c_j^{(1)}(\mathbf{r}; [\{\rho\}])$ in the bulk. Solving self-consistently for the density profiles from Eq. (1.50) is a tedious process, and requires an iterative scheme. The most common iterative scheme, that was also used for the work presented in this thesis, makes use of Picard iterations shown below.

Solving the Euler-Lagrange equation Eq. (1.50) with Picard iteration

Choose bulk densities $\rho_{b,j}$ and the external potentials $V_{ext}^j(\mathbf{r})$

Choose all other system parameters

Calculate the bulk values $c_{b,j}^{(1)}(\{\rho_b\})$

Choose starting density profiles $\tilde{\rho}_j^{(0)}(\mathbf{r})$

$\rho_j^{(1)}(\mathbf{r}) = \tilde{\rho}_j^{(0)}(\mathbf{r})$

iteration parameter $k = 0$

Choose mixing parameter $\alpha(1)$

Set Tolerance tol

Set error $error = 2tol$

while $error > tol$

$k = k + 1$

Mix the new and old solutions: $\tilde{\rho}_j^{(k)} = \alpha(k)\rho_j^{(k)}(\mathbf{r}) + (1 - \alpha(k))\tilde{\rho}_j^{(k-1)}(\mathbf{r})$

Calculate $c_j^{(1)}(\mathbf{r}; [\{\tilde{\rho}^{(k-1)}\}])$ from Eq. (1.47)

Calculate $\rho_j^{(k)}(\mathbf{r})$ from Eq. (1.50)

Calculate the error: $error = \log [\max_{j,\mathbf{r}} (|\rho_j^{(k)}(\mathbf{r}) - \tilde{\rho}_j^{(k-1)}(\mathbf{r})| / \rho_{b,j})]$

Choose a proper mixing parameter $\alpha(k)$

end

Equilibrium density profiles (within the tolerance): $\rho_j^{(k)}(\mathbf{r})$.

Letting the mixing parameter $\alpha(k)$ be dependent on the iteration number k allows for a faster convergence of the density profiles. The self-composed code that was used throughout this thesis, and which is made accessible for others to use at [56], was able to calculate the equilibrium density profiles in the order of seconds to minutes, depending on the system parameters and tolerance, on a desktop computer.

1.4.2 DFT for the Electrode-Electrolyte Interface

The system that is considered throughout this thesis has been introduced in the previous sections 1.2.1 and 1.2.2, and will be investigated in detail in Chapter 2. However, let us consider one more step towards simplification and consider the planar geometry. This implies integrating over the in-plane coordinates y , and z . By doing so, one loses all the information in the y, z plane, but gains in computational speed by reducing the problem to an effective one-dimensional problem; the only coordinate of relevance is the normal

coordinate x . One can enforce this symmetry by applying an external potential that is only dependent on x , like the hard-wall external potential in Eq. (1.20) that reduces to

$$V_{ext}^j(x) = \begin{cases} \infty & \text{for } x < d_j/2; \\ 0 & \text{for } x \geq d_j/2. \end{cases} \quad (1.52)$$

Let us recall that fixing the electric potential on the surface $\Phi_{0/H}$ of the electrodes gives rise to the inhomogeneous charge distributions $\sigma_{0/H}(y, z)$. However, by integrating over the inner-plane coordinates, one loses valuable information on the charge fluctuations on the surface, which is the price we pay for speed and simplicity. Consequently, we only have access the average surface charge density that we simply denote by $\sigma_{0/H} = \frac{1}{A} \int dy \int dz \sigma_{0/H}(y, z)$. Recalling the electric potential at the surface in Eq. (1.28), we can cast this equation in a simpler form using the definition for the density operator $\hat{\rho}_j(\mathbf{r}) = \sum_k \delta(\mathbf{r} - \mathbf{r}_k)$, to find

$$\Phi_s = \int d\mathbf{r}' \frac{\hat{q}_{tot}(\mathbf{r}')}{4\pi\epsilon_r\epsilon_0|\mathbf{r}_s - \mathbf{r}'|}, \quad (1.53)$$

with $\hat{q}_{tot}(\mathbf{r}) = e \sum_j z_j \hat{\rho}_j(\mathbf{r}) + \sum_s \sigma_s(y, z) \delta(x - s)$ denoting the total charge density operator. This can be straightforwardly generalized to the electric potential profile $\hat{\Phi}(\mathbf{r})$ for a specific configuration of ions $\mathbf{r}_{\pm}^{N_{\pm}}$ and surface charge density distribution $\sigma_{0/H}(y, z)$,

$$\hat{\Phi}(\mathbf{r}) = \int d\mathbf{r}' \frac{\hat{q}_{tot}(\mathbf{r}')}{4\pi\epsilon_r\epsilon_0|\mathbf{r} - \mathbf{r}'|}, \quad (1.54)$$

which, after taking the ensemble average, gives the expression for the average electric potential

$$\Phi(\mathbf{r}) = \int d\mathbf{r}' \frac{q_{tot}(\mathbf{r}')}{4\pi\epsilon_r\epsilon_0|\mathbf{r} - \mathbf{r}'|}, \quad (1.55)$$

where $q_{tot}(\mathbf{r}) = e \sum_j \rho_j(\mathbf{r}) + \sum_s \sigma_s \delta(x - s)$ denotes the average total charge density, with $e \sum_j \rho_j(\mathbf{r})$ the charge density profile of the mobile ions and $\sigma_{0/H}$ the average surface charge density on the electrodes. Taking the Laplacian of $\Phi(\mathbf{r})$ results in the well-known Poisson equation for the mean electric potential

$$\nabla^2 \Phi(\mathbf{r}) = -\frac{q_{tot}(\mathbf{r})}{\epsilon_r\epsilon_0} = -\frac{1}{\epsilon_r\epsilon_0} \left[e \sum_j z_j \rho_j(\mathbf{r}) + \sum_s \sigma_s \delta(x - s) \right]. \quad (1.56)$$

Now, let us consider the total electrostatic energy U^{ES} in the system, which is the combined Coulombic interaction between the ions $\sum_{i \neq j} u_{ij}^C$, the Coulombic electrode-ion interactions U_{el} , and the Coulombic self energy of the electrodes U_{self} , which combined can be cast in the form

$$U^{ES} = \frac{1}{2} \int d\mathbf{r} \int d\mathbf{r}' \frac{\hat{q}_{tot}(\mathbf{r}) \hat{q}_{tot}(\mathbf{r}')}{4\pi\epsilon_r\epsilon_0|\mathbf{r} - \mathbf{r}'|}. \quad (1.57)$$

Again, we are not interested in any specific configuration of the system, but rather focus on the average quantities. Taking the average of this expression will contain the quantity $\langle \hat{q}_{tot}(\mathbf{r})\hat{q}_{tot}(\mathbf{r}') \rangle$ one needs to deal with. The simplest approach would be a mean-field approximation for which $\langle \hat{q}_{tot}(\mathbf{r})\hat{q}_{tot}(\mathbf{r}') \rangle = q_{tot}(\mathbf{r})q_{tot}(\mathbf{r}')$. However, a more general notion would be to introduce a pair charge distribution function $q^{(2)}(\mathbf{r}, \mathbf{r}') = q_{tot}(\mathbf{r})q_{tot}(\mathbf{r}')g_q(\mathbf{r}, \mathbf{r}')$, similar to the pair distribution function $\rho_{ij}^{(2)}(\mathbf{r}, \mathbf{r}')$, where $g_q(\mathbf{r}, \mathbf{r}')$ takes the role of the radial distribution function. Then, taking the ensemble average of Eq. (1.57) returns

$$\langle U^{ES} \rangle = \frac{1}{2} \int d\mathbf{r} \int d\mathbf{r}' \frac{q_{tot}(\mathbf{r})q_{tot}(\mathbf{r}')g_q(\mathbf{r}, \mathbf{r}')}{4\pi\epsilon_r\epsilon_0|\mathbf{r} - \mathbf{r}'|}, \quad (1.58)$$

where it is understood that taking $g_q(\mathbf{r}, \mathbf{r}') = 1$ reduces Eq. (1.58) to the mean-field expression

$$\langle U^{ES} \rangle = \mathcal{F}_{ex}^{MFC}[\{\rho\}] = \frac{1}{2} \int d\mathbf{r} q_{tot}(\mathbf{r})\Phi(\mathbf{r}). \quad (1.59)$$

Hence, we presented an explicit example for the construction of a mean-field (MF) approximation for the Helmholtz free energy that deals with the Coulombic (C) interactions, while in Chapter 2 we will also present beyond-mean-field approximations. One notion to emphasize is that, throughout this thesis, we separate the non-electrostatic external potential $V_{ext}^j(\mathbf{r})$ from electrostatic external contributions, like the ion-electrode interaction potential due to the surface charge that results from applying an electric potential. The reason for doing so, is that this allows us to consider the total mean electric potential $\Phi(\mathbf{r})$, which can be readily obtained from the Poisson equation (1.56), instead of having to split it into a surface contribution and an ion contribution.

To summarize, we consider two planar hard walls at $x = 0$ and $x = H$, described by the external potential $V_{ext}^j(x)$ in Eq. (1.20), at which an electric potential $\Phi_{0/H}$ is applied that gives rise to an average surface charge density $\sigma_{0/H}$. Hence, the only spatial dimension of interest is the normal coordinate x , reducing the system to an effective one-dimensional problem. This simplifies DFT description of the system, because all the spatial-dependent quantities now only depend on x . The integration over the in-plane coordinates (see also appendix 2.A), reduces the grand potential functional to

$$\Omega[\{\rho\}] = \mathcal{F}_{id}[\{\rho\}] + \mathcal{F}_{ex}[\{\rho\}] - A \sum_j \int dx \rho_j(x) [\mu_j - V_{ext}^j(x)] - A \sum_s \sigma_s \Phi_s, \quad (1.60)$$

where

$$\beta \mathcal{F}_{id}[\{\rho\}] = A \sum_j \int dx \rho_j(x) [\log \Lambda_j^3 \rho(x) - 1]. \quad (1.61)$$

Now that we established the theoretical framework for DFT for our model/system, let us first consider one of the simplest approaches to deal with the electrode-electrolyte interface, namely the Poisson-Boltzmann theory.

1.4.3 Poisson-Boltzmann Theory

The most common and easiest theory to tackle electrolytes is the Poisson-Boltzmann (PB) theory, which makes one more simplification on the PM, namely to treat the ions as point-like particles. By doing so, one only has to deal with the Coulomb pair potential between the particles, for which the Helmholtz free energy functional $\mathcal{F}^{MFC}[\{\rho\}]$ from Eq. (1.59) suffices. Hence, Eq. (1.50) for the density profiles, reduces to the Boltzmann distribution of the electrostatic potential

$$\rho_j(\mathbf{r}) = \rho_{b,j} e^{-z_j e \beta \Phi(\mathbf{r})}, \quad (1.62)$$

with $\rho_{b,j}$ the bulk density, where the electrostatic potential $\Phi(\mathbf{r})$ vanishes. The latter is determined by the Poisson equation (1.56). Considering the simple case of a planar geometry containing a single charged hard wall at $x = 0$ with surface charge density σ , and introducing the dimensionless electrostatic potential $\phi(x) = e\beta\Phi(x)$, reduces the PB equations to

$$\rho_j(x) = \rho_{b,j} e^{-z_j \phi(x)}, \quad (1.63)$$

$$\partial_x^2 \phi(x) = -4\pi\lambda_B \left[\sum_j z_j \rho_j(x) + \frac{\sigma}{e} \delta(x) \right]. \quad (1.64)$$

When the electrostatic potential is small for all x , one can linearize the PB equations to obtain one second-order ordinary differential equation with the two boundary conditions

$$\partial_x^2 \phi(x) = \kappa_D^2 \phi(x) \quad (1.65)$$

$$\phi(\infty) = 0 \quad (1.66)$$

$$\phi'(0) = -4\pi\lambda_B \sigma / e \quad (1.67)$$

where $\kappa_D = \sqrt{4\pi\lambda_B \sum_j z_j^2 \rho_{b,j}} = 1/\lambda_D$ denotes the famous inverse Debye length, and $\phi'(0)$ the spatial derivative of the electrostatic potential evaluated at $x = 0$. We will, depending on the context, interchangeably use either κ_D or λ_D throughout this thesis. Solving this differential equation results in an exponential monotonic decaying potential profile (and density profiles) with decay length λ_D . Gouy and Chapman also solved, independently, the full non-linear PB equations within the planar geometry [29, 30], finding qualitatively similar monotonic decaying profiles with the same decay length λ_D . Hence, the typical thickness of the electrode-electrolyte interface (EDL) within PB theory is given by the Debye length λ_D , which, in water at room temperature, takes typical values ranging from 10 nm for bulk concentrations of $\rho_b = 1$ mM to 0.3 nm for bulk concentrations of $\rho_b = 1$ M. The latter case makes it explicit that PB theory has a limited applicability, due to the absence of any steric interactions (finite-sized ions with radii that can be larger than the Debye length at high concentrations), which can result in unphysically large densities near charged surfaces. One noteworthy approach is the modified PB theory [57], a lattice-gas approach, in which finite-size effects are taken into account on a rudimentary but elegant

manner. However, this approach has its limitations due to being a lattice-gas approximation, which can be improved significantly by incorporating FMT in DFT, which describe hard-sphere interactions fairly well.

1.5 CAPACITANCE OF THE ELECTRODE-ELECTROLYTE INTERFACE

One of the important thermodynamic quantities that we study here using DFT, is the differential capacitance. In our early science and engineering classes the concept of the capacitor was introduced as a relative simple device with two parallel charged plates (electrodes) with surface area A separated by a distance H with an inert (dielectric) medium in between. This will lead to a constant electric field \mathbf{E} with energy density $u = \frac{\varepsilon_r \varepsilon_0}{2} \mathbf{E}^2$ inside the capacitor, where ε_0 is the dielectric permittivity in vacuum and ε_r the relative permittivity of the medium (dielectric constant). The electric field perpendicular to the electrodes arises due to the surface charge σ on the electrodes. Since the medium in between the electrodes is inert, Gauss' law reduces to $\partial_x E_x = \sigma(\delta(x) - \delta(H))/\varepsilon_r \varepsilon_0$, where we assume that the electrodes are located at $x = 0$ and $x = H$ have the same but opposite surface charge σ . Solving this equation returns $E_x = \sigma/\varepsilon_r \varepsilon_0$, and hence the energy density in between the electrodes is $u = \frac{\sigma^2}{2\varepsilon_r \varepsilon_0}$, leading to a total energy $E_{\text{cap}} = AHu = \frac{\sigma^2 AH}{2\varepsilon_r \varepsilon_0}$, which scales with the area. A convenient measure to describe a capacitor is the differential capacitance per unit area

$$C = \frac{1}{A} \frac{dQ}{d\Psi}, \quad (1.68)$$

where Ψ denotes the potential *difference*⁴ between the electrodes. The capacitance C is a measure for the ability of a capacitor to store energy. For our simple case, the potential drop is linear between the electrodes, leading to $C = Q/\Psi A = \varepsilon_r \varepsilon_0/H$. Hence, the larger the surface area and the smaller the separation between the electrodes, the larger the total capacitance AC . One can also work out that the energy stored inside the capacitor is $E_{\text{cap}} = \frac{1}{2} AC\Psi^2$. The main message following this discussion is that the larger the capacitance, the larger the energy stored inside of it at a given Ψ .

This situation gets more complicated when the medium in between the electrodes is not a linearly polarisable dielectric medium such as air, but an electrolyte with dissolved ions in water, for instance. The presence of the mobile ions will introduce a complexity that changes the whole story. In the previous case, the medium in between the electrodes did not really interact with the electrodes, except for polarization that accounts for the dielectric constant ε_r . With the introduction of ions, this is no longer the case, and the interaction between the mobile ions and the electrode will cause the previously-mentioned EDL. What happens is that the ions interact with the electric field induced by the surface charge on the electrodes. That is, the ions feel the force $\mathbf{F} = ez\mathbf{E}$, where z denotes their valency, which, because of their mobility, pushes cations (anions) towards the negatively (positively) charged electrode, repelling the anions (cations), precisely as Faraday observed.

⁴ We reserve Ψ for the potential *difference* between the two electrode surfaces, while $\Phi_{0/H}$ denotes the potential at the electrode surface at $x = 0/H$ w.r.t. the grounded ionic reservoir.

The accumulation of oppositely charged ions near the electrodes will counter the electric field caused by the surface charge on the electrodes; this is referred to as screening. The repulsion between the like-charged ions near the electrode together with entropy, which prefers a homogeneous system, results in an extended charge density near the electrode that decays to zero towards the bulk on a length scale that reduces to the Debye length λ_D in the dilute limit. This decaying charge density due to the (electronically) charged surface is referred to as the EDL, and is captured by PB theory of Eqs (1.67)-(1.67).

One can imagine that the total energy inside such a system is very different from a simple two-plate capacitor from the previous paragraph. First of all, the electric field is not spatially constant anymore in between the electrodes. Where the electric field was first determined only by the fixed charge on the surfaces $f(\mathbf{r})$, now one also has to deal with the mobile ions in the electrolyte and therefore a non-vanishing charge density $q(\mathbf{r})$ in between the electrodes:

$$\nabla \cdot \varepsilon_r \varepsilon_0 \mathbf{E}(\mathbf{r}) = q(\mathbf{r}) + f(\mathbf{r}). \quad (1.69)$$

Again considering two parallel electrodes, Gauss' law effectively reduces to a one-dimensional problem $\partial_x \varepsilon_r \varepsilon_0 \mathbf{E}(x) = q(x) + \sigma_0 \delta(x) + \sigma_H \delta(x - H)$, with σ_0 and σ_H the surface charge density on the electrodes at $x = 0$ and $x = H$, respectively. The internal energy density $u(x)$ is therefore also spatially dependent on x and the total electric energy inside the capacitor should now be calculated via the integral

$$E_{\text{cap}} = A \int_0^H dx u(x) = A \int_0^H dx \frac{\varepsilon_r \varepsilon_0}{2} E_x^2(x). \quad (1.70)$$

Using the Poisson equation from Eq. (1.56), Eq. (1.70) can also be expressed as

$$\begin{aligned} E_{\text{cap}} &= A \int_0^H dx \frac{\varepsilon_r \varepsilon_0}{2} (\partial_x \Phi(x))^2 \\ &= A \frac{\varepsilon_r \varepsilon_0}{2} \Phi(x) \partial_x \Phi(x) \Big|_0^H - A \int_0^H dx \frac{\varepsilon_r \varepsilon_0}{2} \Phi(x) \partial_x^2 \Phi(x) \\ &= \frac{A}{2} (\sigma_0 \Phi_0 + \sigma_H \Phi_H) + \frac{A}{2} \int_0^H dx \Phi(x) q(x), \end{aligned} \quad (1.71)$$

where we used Gauss' law to find

$$\lim_{\varepsilon \downarrow 0} \partial_x \Phi(\varepsilon) - \lim_{\varepsilon \uparrow 0} \partial_x \Phi(\varepsilon) = -\frac{\sigma}{\varepsilon_r \varepsilon_0} \quad (1.72)$$

with the assumption that the electric field inside the electrodes vanishes (as is the case for conductive electrodes). In the absence of mobile ions and by applying a potential difference Ψ between the electrodes one straightforwardly solves the Poisson equation, finding $\Phi(x) = (\frac{1}{2} - \frac{x}{H})\Psi$. Indeed, this leads to $E_{\text{cap}} = \frac{1}{2} AC \Psi^2$ as stated before. Including the mobile ions creates the two unknowns $\Phi(x)$ and $q(x)$ that one has to account for, which is a complicated problem. Of course, there are approximations, varying in complexity, but especially at high ion concentrations where electrostatics is not the only player, it becomes increasingly difficult to tackle realistic models. One noteworthy result to mention is the

differential capacitance that follows from the exact solution for the density and potential profiles within the mean-field Poisson-Boltzmann theory with point-like ions, found independently by Gouy [29] and Chapman [30] (GC). They derived the equation

$$C_{\mu}^{GC} = \frac{\varepsilon\varepsilon_0}{\lambda_D} \cosh\left(\frac{\beta e\Phi_0}{2}\right), \quad (1.73)$$

which is dependent on Φ_0 , and moreover it is unbounded. The latter is problematic and is typical for the mean-field theory for point ions. Introducing finite-sized particles will solve this problem as explained in Chapter 4. In Chapters 3 and 4 we delve into the differential capacitance in more detail, showing its rich behavior using Density Functional Theory (DFT), and presenting its deep connection with thermodynamics.

Chapter 2 will further discuss the PM and its implementation in DFT. Special attention is given on several treatments for the electrostatic interactions, and we show how results from the DFT calculations compare with those from simulations and other works in literature. In particular, we investigate one of the open problems, which is that of the asymptotic decay in high-concentrated electrolytes. In Chapter 3 we further test the functional that appears most accurate from Chapter 2, and consider many different electrolytes. Moreover, we investigate the differential capacitance and show the excellent agreement between DFT and Brownian Dynamics simulations. The next Chapter 4 further analyses the differential capacitance, where a new equation is derived that gives a lot of insight into the behavior of the differential capacitance. Specifically, we show that impurities in the electrolyte can lead to large changes in the differential capacitance. The final chapter 5 is dedicated to improving a DFT for a Lennard-Jones system using machine-learning techniques, with the aim to implement and improve upon the PM by including dispersion relations. Interestingly, the functional that was obtained from this machine-learning algorithm, in which a planar geometry was considered, also performs well in a spherical geometry. Hence, the learned functional has embedded information of the bulk system, and not only of the specific geometry for which it was learned. Of course, there is a summary, conclusion and outlook at the end of the thesis.

APPENDIX

1.A FUNDAMENTAL MEASURE THEORY

Fundamental Measure Theory (FMT) is nowadays the state of the art when dealing with DFT of hard-core particles. Originally developed for spheres, it can be applied to other shapes as well, due to its generic features. Its name has its origin from the way that this theory describes systems of hard-core particles (from now on we will be interested in hard-spheres), namely by using quantities that are related to the volume, surface area, radius and topology, i.e. the fundamental properties or measures of the particle.

One of the starting points for the development of FMT was the weighted density approximation, where the grand potential functional is described in terms of a weighted density $\bar{\rho}(\mathbf{r})$, rather than in terms of the local density $\rho(\mathbf{r})$. These weighted densities are used to incorporate non-locality in the theory, which is necessary to allow oscillatory local density profiles due to packing effects. That is, since crystals exhibit delta-function-like density profiles, we know that one should not bound the density profile ρ itself (as is done in modified PB), but a weighted density $\bar{\rho}$. In this way, ρ can still be very large locally, but needs to drop off fast enough to not exceed the bound that is set on $\bar{\rho}$. The procedure of using this averaged, or weighted, density in a DFT is called the weighted-density approximation.

One other important theory for the development of FMT was scaled particle theory (SPT), which makes use of the fact that hard-sphere systems are scale-invariant. That is, it does not matter whether you describe thermal mixtures of nanoparticles or thermal mixtures of planet-sized particles, their macroscopic equilibrium properties all are characterized by only one parameter, the packing fraction

$$\eta = \frac{\pi}{6} \sum_j d_j^3 \rho_{b,j}, \quad (1.74)$$

where d_j is the diameter of particles of species j and $\rho_{b,j}$ the bulk density of species j . The chemical potential μ , which coincides with the work required to make a cavity of the size of a certain particle with radius R , can therefore be written as the expansion

$$\beta\mu = pV + \gamma S + \kappa R + \mathcal{O}(1) \underset{\lim_{R \rightarrow \infty}}{=} pV, \quad (1.75)$$

where the first term pV is the work against the pressure p to make a cavity of volume V of the particle, the second term is the work against the surface tension γ by creating a surface area S of the size of the particle and the last term is also related to the surface tension since it depends on the curvature R of the particle. Due to scale invariance, taking the limit of infinite-sized particles justifies the last equality.

On the other hand, one of the most important insights was that the Mayer function $f_{ij}(r)$, which arises in the expansion of the excess free energy in the low-density limit as

$$\begin{aligned} \beta\mathcal{F}_{ex}[\{\rho_i\}] = & -\frac{1}{2} \sum_{i,j} \int d\mathbf{r}_1 \int d\mathbf{r}_2 \rho_i(\mathbf{r}_1) f_{ij}(r_{12}) \rho_j(\mathbf{r}_2) \\ & -\frac{1}{6} \sum_{i,j,k} \int d\mathbf{r}_1 \int d\mathbf{r}_2 \int d\mathbf{r}_3 \rho_i(\mathbf{r}_1) f_{ij}(r_{12}) \rho_j(\mathbf{r}_2) f_{jk}(r_{23}) \rho_k(\mathbf{r}_3) f_{ki}(r_{31}), \end{aligned} \quad (1.76)$$

where $r_{ij} = |\mathbf{r}_i - \mathbf{r}_j|$, can be written as a convolution of weight functions ω_α^i (in the case of a hard-core potential). For a hard-sphere mixture this relation is given by

$$-f_{ij}(r) = \omega_3^i \otimes \omega_0^j + \omega_0^i \otimes \omega_3^j + \omega_2^i \otimes \omega_1^j + \omega_1^i \otimes \omega_2^j - \omega_2^i \otimes \omega_1^j - \omega_1^i \otimes \omega_2^j, \quad (1.77)$$

where the symbol \otimes denotes a convolution in three-dimensional space and the weight functions read

$$\omega_3^i(r) = \Theta(R_i - r), \quad (1.78)$$

$$\omega_2^i(r) = \delta(R_i - r), \quad (1.79)$$

$$\omega_1^i(r) = \frac{\omega_2^i(r)}{4\pi R_i}, \quad (1.80)$$

$$\omega_0^i(r) = \frac{\omega_2^i(r)}{4\pi R_i^2}, \quad (1.81)$$

$$\omega_2^i(\mathbf{r}) = \frac{\mathbf{r}}{r} \delta(R_i - r), \quad (1.82)$$

$$\omega_1^i(\mathbf{r}) = \frac{\omega_2^i(\mathbf{r})}{4\pi R_i}. \quad (1.83)$$

In the low-density limit, the first line in the excess free energy functional Eq. (1.76) can be written as

$$\lim_{\rho_i \rightarrow 0} \beta\mathcal{F}_{ex}[\{\rho_i\}] = \int d\mathbf{r}' [n_0(\mathbf{r})n_3(\mathbf{r}) + n_1(\mathbf{r})n_2(\mathbf{r}) - \mathbf{n}_1(\mathbf{r})\mathbf{n}_2(\mathbf{r})], \quad (1.84)$$

where

$$n_\alpha(\mathbf{r}) = \sum_{i=1}^{\nu} \int d\mathbf{r}' \rho_i(\mathbf{r}') \omega_\alpha^i(\mathbf{r} - \mathbf{r}') \quad (1.85)$$

are the weighted densities, which are convolutions between the densities ρ_i and the weight functions ω_α^i . The label α stands for all the possible weight functions. The dimension of the weighted densities obeys the relation $[n_\alpha] = L^{\alpha-3}$, where L stands for length.

In bulk, the weighted densities reduce to the so-called SPT variables

$$n_3 \rightarrow \xi_3 = \sum_{i=1}^{\nu} \rho_b^i \frac{4\pi}{3} R_i^3 \quad (1.86)$$

$$n_2 \rightarrow \xi_2 = \sum_{i=1}^{\nu} \rho_b^i 4\pi R_i^2 \quad (1.87)$$

$$n_1 \rightarrow \xi_1 = \sum_{i=1}^{\nu} \rho_b^i R_i \quad (1.88)$$

$$n_0 \rightarrow \xi_0 = \sum_{i=1}^{\nu} \rho_b^i, \quad (1.89)$$

where ξ_3 is the total packing fraction, bounded by one. Note that \mathbf{n}_1 and \mathbf{n}_2 vanish in the bulk, due to $\omega_{1/2}$ being anti-symmetric. Now, Eq. (1.84) only holds in the low-density limit and to go to higher densities, one must extrapolate this to the high-density limit.

1.A.0.1 The Functional

To extrapolate this idea to higher densities, one makes the basic assumption that the excess free energy functional for the hard spheres \mathcal{F}_{ex}^{HS} is a functional of the weighted densities $n_\alpha(\mathbf{r})$ of the form

$$\beta \mathcal{F}_{ex}^{HS}[\{n_\alpha\}] = \int d\mathbf{r} \Phi(\{n_\alpha\}), \quad (1.90)$$

where $\Phi(\{n_\alpha\})$ is the reduced free energy density, which is a *function* of the weighted densities n_α . In the low-density limit, this functional should reduce to Eq. (1.76) and (1.84). This suggests that, based on dimensional analysis, Φ casts the form

$$\Phi(\{n_\alpha\}) = f_1(n_3)n_0 + f_2(n_3)n_1n_2 + f_3(n_3)\mathbf{n}_1 \cdot \mathbf{n}_2 + f_4(n_3)n_2^3 + f_5(n_3)n_2\mathbf{n}_2 \cdot \mathbf{n}_2. \quad (1.91)$$

There are several ways to find the functions f_j . The first approach by Rosenfeld was to use the SPT result

$$\lim_{R_i \rightarrow \infty} \frac{\beta \mu_{ex}^i}{V_i} = \lim_{R_i \rightarrow \infty} \frac{\partial \Phi}{\partial \rho_i} = \lim_{R_i \rightarrow \infty} \sum_{\alpha} \frac{\partial \Phi}{\partial n_\alpha} \frac{\partial n_\alpha}{\partial \rho_i} = \frac{\partial \Phi}{\partial n_3} = \beta p, \quad (1.92)$$

where the last equality follows from Eq. (1.75). However, one also has the relation $\Omega_b = -pV$, which translates to

$$\beta p = -\frac{\beta \Omega_b}{V} = -\Phi + \beta f_{id} - \sum_i \rho_b^i \beta \mu_i = -\Phi + \sum_{\alpha} \frac{\partial \Phi}{\partial n_\alpha} n_\alpha + n_0. \quad (1.93)$$

Hence, one finds the differential equation

$$\frac{\partial \Phi}{\partial n_3} = -\Phi + \sum_{\alpha} \frac{\partial \Phi}{\partial n_\alpha} n_\alpha + n_0 \quad (1.94)$$

that one can solve by collecting all the terms proportional to each n_α . This way, Rosenfeld [58] obtained the free energy density

$$\Phi^{RF} = -n_0 \ln(1 - n_3) + \frac{n_1 n_2 - \mathbf{n}_1 \cdot \mathbf{n}_2}{1 - n_3} + \frac{n_2^3 - 3n_2 \mathbf{n}_2 \cdot \mathbf{n}_2}{24\pi(1 - n_3)^2}. \quad (1.95)$$

Though this version of FMT predicted density profiles rather well and even generates the Percus-Yevick (PY) compressibility equation of state and the PY direct correlation functions, it did not predict correctly the freezing transition. Hence, the general idea of Rosenfeld's FMT and was taken to a higher level, for instance the White-Bear II (WBII) version of FMT [48]. Instead of using the SPT equation of state Eq. (1.75), one can use another equation of state p_{input} that is known to describe (mixtures of) hard-sphere fluids accurately and then put this into Eq. (1.94), i.e.

$$\beta p_{\text{input}} = -\Phi + \sum_{\alpha} \frac{\partial \Phi}{\partial n_{\alpha}} n_{\alpha} + n_0. \quad (1.96)$$

One suitable choice for this p_{input} would be the well-known Carnahan-Starling (CS) equation of state that describes hard-spheres very accurately. However, this only describes single-component systems, while we are mostly interesting in multi-component mixtures. Therefore, one can use the generalized CS equation of state [48]

$$\beta p_{CSIII} = \frac{n_0}{1 - n_3} + \frac{n_1 n_2 (1 + \frac{1}{3} n_3^2)}{(1 - n_3)^2} + \frac{n_2^3 (1 - \frac{2}{3} n_3 + \frac{1}{3} n_3^2)}{12\pi(1 - n_3)^3}. \quad (1.97)$$

Putting this equation of state in Eq. (1.96) and solving the differential equation results in

$$\Phi_{WBII} = -n_0 \ln(1 - n_3) + \left(1 + \frac{1}{9} n_3^2 \phi_2(n_3)\right) \frac{n_1 n_2 - \mathbf{n}_1 \cdot \mathbf{n}_2}{1 - n_3} + \quad (1.98)$$

$$\left(1 - \frac{4}{9} n_3 \phi_3(n_3)\right) \frac{n_2^3 - 3n_2 \mathbf{n}_2 \cdot \mathbf{n}_2}{24\pi(1 - n_3)^2} \quad (1.99)$$

with

$$\phi_2(n_3) = \frac{6n_3 - 3n_3^2 + 6(1 - n_3) \ln(1 - n_3)}{n_3^3} \quad (1.100)$$

$$\phi_3(n_3) = \frac{6n_3 - 9n_3^2 + 6n_3^3 + 6(1 - n_3)^2 \ln(1 - n_3)}{4n_3^3}. \quad (1.101)$$

For a one-component fluid, one can see immediately the improvement w.r.t. the Rosenfeld version, because it obeys

$$\frac{\partial \Phi_{WBII}}{\partial n_3} = \beta p_{CS} \quad (1.102)$$

with p_{CS} the accurate CS equation of state.

Actually, this is not yet the end of the story, because the WBII version of FMT still does not predict the correct hard-sphere freezing transition. To correct for this, one can include

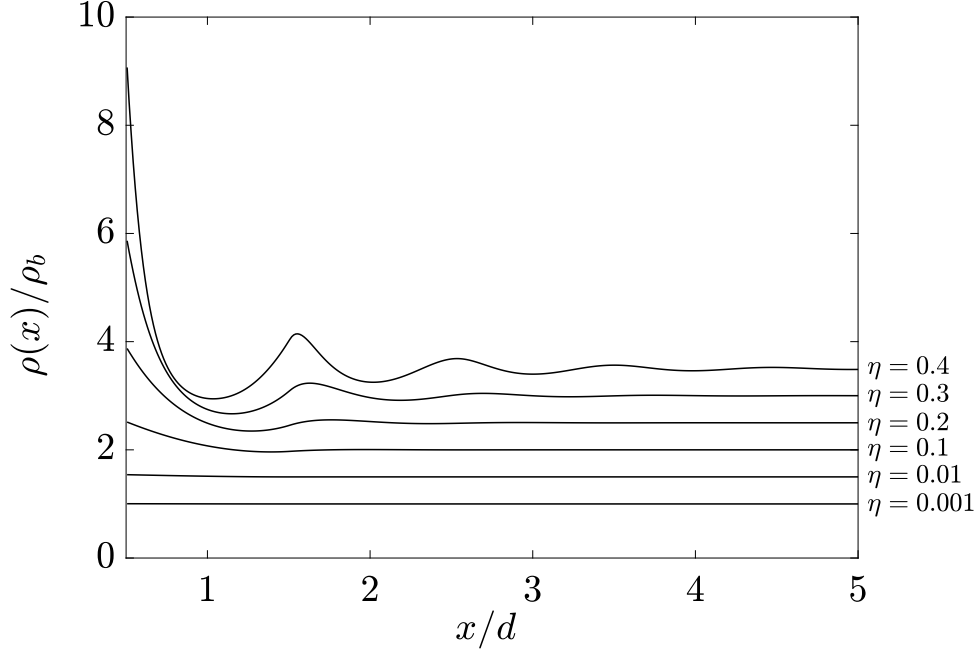


Figure 1.A.1: Density profiles $\rho(x)/\rho_b$ for hard spheres at packing fractions ranging from $\eta = 0.001$ to $\eta = 0.4$. The bulk values of the density profiles are shifted for visibility.

weight functions of higher order, like second or even higher order tensors. However, the most common correction is to include the weight function

$$\bar{\omega}_m(\mathbf{r}) = \left(\frac{\mathbf{r} \cdot \mathbf{r}^T}{r^2} - \frac{1}{3} \mathbb{1} \right) \delta(R_i - r), \quad (1.103)$$

where T stands for transpose and $\mathbb{1}$ is the unit matrix. The resulting energy density then reads

$$\Phi_{WBII_t} = \Phi_{WBII} + \frac{9(\mathbf{n}_2 n_m \mathbf{n}_2 - \frac{1}{2} \text{Tr}(n_m^3))}{24\pi(1 - n_3)^2}. \quad (1.104)$$

However, within the planar geometry, there is hardly any difference between Φ_{WBII} and Φ_{WBII_t} , which let us to use the non-tensor version Φ_{WBII} , instead.

Density profiles $\rho(x)/\rho_b$ with for the WBII FMT functional for packing fractions ranging from $\eta = 0.001$ to $\eta = 0.4$ are plotting in Fig. 1.A.1. The bulk density for the packing fractions $\eta = 0.01$ to $\eta = 0.4$ are shifted for better visibility. The density profiles for $\eta = 0.001$ and $\eta = 0.01$ barely show any feature. The first packing fraction for which the density profile is plotted at which structure is seen is at $\eta = 0.1$, where a clear first peak is observed at $x = 0.5d$, and a barely visible second peak is forming around $x = 2d$. Increasing the packing fraction causes the second peak to shift to $x = 1.5d$, and makes the subsequent peaks more visible.

PRIMITIVE MODEL ELECTROLYTES IN THE NEAR AND FAR FIELD: DECAY LENGTHS FROM DFT AND SIMULATIONS

Inspired by recent experimental observations of anomalously large decay lengths in concentrated electrolytes, we revisit the Restricted Primitive Model (RPM) for an aqueous electrolyte. We investigate the asymptotic decay lengths of the one-body ionic density profiles for the RPM in contact with a planar electrode using classical Density Functional Theory (DFT) and compare these with the decay lengths of the corresponding two-body correlation functions in bulk systems, obtained in previous Integral Equation Theory (IET) studies. Extensive Molecular Dynamics (MD) simulations are employed to complement the DFT and IET predictions. Our DFT calculations incorporate electrostatic interactions between the ions using three different (existing) approaches: one is based on the simplest mean-field treatment of Coulomb interactions (MFC), while the other two employ the Mean Spherical Approximation (MSA). The MSAC invokes only the MSA bulk direct correlation function, whereas the MSAu also incorporates the MSA bulk internal energy. Although MSAu yields profiles that are in excellent agreement with MD simulations in the near field, in the far field, we observe that the decay lengths are consistent between IET, MSAC, and MD simulations, whereas those from MFC and MSAu deviate significantly. Using DFT, we calculated the solvation force, which relates directly to surface force experiments. We find that its decay length is neither qualitatively nor quantitatively close to the large decay lengths measured in experiments and conclude that the latter cannot be accounted for by the primitive model. The anomalously large decay lengths found in surface force measurements require an explanation that lies beyond primitive models.

In this chapter we investigate the structure of EDLs, focusing on the decay lengths of the one-body density profiles and how these are determined by the decay of two-body correlation functions in the bulk liquid. The former aspect is investigated using DFT and MD simulation while the latter is examined using IET and MD simulation. We specialize to the Restricted Primitive Model (RPM) where the ionic species have equal size and equal but opposite charge. This choice simplifies theoretical treatments: number and charge density profiles, and the corresponding two-body correlation functions, (essentially) decouple, allowing us to treat both pieces independently. Implementing DFT, we consider three different treatments of the electrostatic interactions, while employing the same Fundamental Measure Theory (FMT) to describe the hard-sphere (HS) interactions that mimic the steric forces.

This chapter is arranged as follows: Section 2.1 sets out the basic theory for homogeneous as well as for inhomogeneous electrolytes. In Section 2.1.2, the three functionals for the electrostatic interactions are introduced: a mean-field Coulomb functional, and two functionals based on the Mean Spherical Approximation (MSA). Section 2.2 lays out the details of the model, its parameters and how we translate between DFT and simulation. Section 2.3 describes the results of our DFT calculations and MD simulations and how these connect with results from previous IET studies [59, 60, 61] that examined the decay of bulk pair correlation functions. Our MD simulations were designed to check predictions of DFT for the one-body density profiles in the near field, Sec. 2.3.1, and to examine the asymptotic decay of both the one- and two-body profiles in Sec. 2.3.2. Our DFT results for the decay length of the solvation force, obtained from the grand potential of the RPM confined between two planar electrodes, are presented in Sec. 2.3.2.3 where they are compared with the decay lengths measured in IET and DFT studies of the structure of the RPM and with decay lengths measured in SFA experiments. Section 2.4 describes a summary and discussion of our results whilst Section 2.5 provides concluding remarks.

2.1 DFT FOR THE PRIMITIVE MODEL

We investigate the Primitive Model (PM) of an aqueous electrolyte in three spatial dimensions, either in a homogeneous bulk state or in contact with a single planar electrode at surface potential Φ_0 , as depicted in Fig. 2.1.1. The ions are modeled as hard spheres with diameter d_j and charge ez_j , where j refers to the species and e is the elementary charge. We consider mainly the Restricted Primitive Model (RPM), in which the electrolyte consists of two species (cat- and anions) that are characterized by $z_{\pm} = \pm 1$ and $d_{\pm} \equiv d$. The pair potential of the RPM therefore reads

$$\beta u_{ij}^{RPM}(r) = \begin{cases} \infty, & \text{for } r < d; \\ z_i z_j \frac{\lambda_B}{r}, & \text{for } r \geq d. \end{cases} \quad (2.1)$$

One way of tackling the thermodynamics and the structure of the inhomogeneous PM is by applying DFT. As mentioned in the introduction, the starting point of classical DFT is the grand potential functional Ω of the density profiles $\rho_j(\mathbf{r})$, which reads [42, 45, 46]

$$\Omega[\{\rho\}] = \mathcal{F}[\{\rho\}] - \sum_j \int d\mathbf{r} \rho_j(\mathbf{r}) \left[\mu_j - V_{ext}^j(\mathbf{r}) \right] - Q_0 \Phi_0. \quad (2.2)$$

where \mathcal{F} is an intrinsic property of the system which depends on the temperature and the interparticle interactions, but not on $\mu_j - V_{ext}^j$, and Q_0 is the charge on the surface due to applying the surface potential Φ_0 . Moreover, \mathcal{F} is in general not known exactly, so DFT hinges on approximations for \mathcal{F} . It is convenient to separate \mathcal{F} into an ideal gas free-energy functional \mathcal{F}_{id} from Eq. (1.36), and the excess (over ideal) functional \mathcal{F}_{ex} that accounts for the interactions, i.e.

$$\mathcal{F}[\{\rho\}] = \mathcal{F}_{id}[\{\rho\}] + \mathcal{F}_{ex}[\{\rho\}]. \quad (2.3)$$

Importantly, one can show [46] that \mathcal{F}_{ex} is also the generator for the direct correlation functions, in particular

$$c_{ij}^{(2)}(\mathbf{r}, \mathbf{r}') = -\beta \left. \frac{\delta^2 \mathcal{F}_{ex}[\{\rho\}]}{\delta \rho_i(\mathbf{r}) \delta \rho_j(\mathbf{r}')} \right|_{\{\rho_0\}} \quad (2.4)$$

is the pair (two-body) direct correlation function which is related to the total (pair) correlation function via the Ornstein-Zernike (OZ) equation. For a uniform liquid with constant (bulk) densities $\{\rho_b\}$, the OZ equation [55] reads:

$$h_{ij}(r) = c_{ij}(r) + \sum_k \rho_{b,k} \int d\mathbf{r}' c_{ik}(|\mathbf{r} - \mathbf{r}'|) h_{kj}(r'), \quad (2.5)$$

where the sum is over all species k . Eqs. (2.4) and (2.5) reveal an elegant relation between the total correlation functions h_{ij} and the direct correlation functions c_{ij} obtained from free-energy functionals.

Constructing approximate DFTs that generate accurate one-body (density) profiles for fluids at substrates and for two-body correlation functions in bulk is a challenge across liquid-state physics [62]. When electrostatics is involved, it is especially demanding due to the long range character of the Coulomb potential. Tackling Coulombic interactions within DFT is non-trivial, as explained in detail in a recent review [63].

In subsequent sections we present theories for both homogeneous and inhomogeneous systems, i.e. without and with electrodes, respectively. We consider to what extent state of the art density functional theories incorporate correlation effects.

2.1.1 Homogeneous Electrolytes

Here, we review briefly the properties of bulk (homogeneous) fluid systems, considering results of both the mean-field Debye-Hückel (DH) theory and the Mean Spherical Approx-

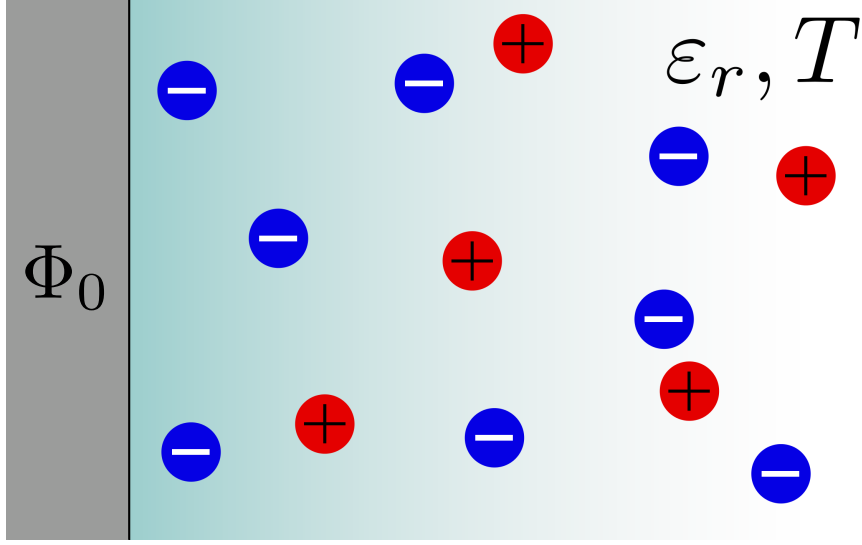


Figure 2.1.1: An illustration of the system considered throughout this study. The cations and anions (in red and blue, respectively) have equal size and valency ± 1 and reside in a dielectric continuum at temperature T and relative dielectric permittivity ϵ_r . The electrolyte is in contact with a planar electrode at surface potential Φ_0 w.r.t. a grounded bulk electrolyte, which causes a nonzero charge density profile near the electrode as depicted by the background shading.

imation (MSA) which is used as a closure to solve the (bulk) OZ equation. Subsequent subsections build upon these results.

2.1.1.1 Debye Hückel Theory

Electrolyte solutions were already investigated in some detail by Debye and Hückel [31] (DH) using the (linearized) Poisson-Boltzmann equations. The Poisson equation for a point charge ze in the origin of an electrolyte reads

$$\nabla^2 \Phi(\mathbf{r}) = -\frac{1}{\epsilon_r \epsilon_0} \left[\sum_j e z_j \rho_j(\mathbf{r}) + e z \delta(\mathbf{r}) \right], \quad (2.6)$$

and the Boltzmann distribution for the ionic density profiles is given by

$$\rho_j(\mathbf{r}) = \rho_{b,j} e^{-z_j \beta e \Phi(\mathbf{r})}, \quad (2.7)$$

which is valid in the limit where the total electrostatic potential Φ and the ionic bulk concentrations $\rho_{b,j}$ are small. In particular, DH studied the RPM and considered one finite-sized ion with valency $z \in \{\pm 1\}$ and diameter d at the origin in bath of point ions. For

convenience, we introduce the dimensionless potential $\phi = e\beta\Phi$ so that the linearized Poisson-Boltzmann equation reduces to

$$\nabla^2\phi(\mathbf{r}) = \begin{cases} -4\pi\lambda_B z\delta(\mathbf{r}) & \text{for } r < d/2, \\ \kappa_D^2\phi(\mathbf{r}) & \text{for } r \geq d/2, \end{cases} \quad (2.8)$$

with $\kappa_D = \sqrt{8\pi\lambda_B\rho_b}$, the inverse Debye length for the two-component RPM for which $\rho_{b,+} = \rho_{b,-} \equiv \rho_b$. The DH solution for ϕ in the RPM reads

$$\phi(r) = \begin{cases} z\frac{\lambda_B}{r} - z\frac{\lambda_B\kappa_D}{1+d\kappa_D/2} & \text{for } r < d/2, \\ z\frac{\lambda_B}{r}\frac{e^{-\kappa_D(r-d/2)}}{1+d\kappa_D/2} & \text{for } r \geq d/2. \end{cases} \quad (2.9)$$

From this expression one can conclude that each ion is screened by a cloud of ions of opposite charge over a typical distance κ_D^{-1} , i.e. the potential around that ion decays exponentially with the decay length κ_D^{-1} for $r > d/2$. The electrostatic self energy U_{ion}^{ES} of a monovalent ion due to its surrounding is thus given by

$$\beta U_{ion}^{ES} = z \lim_{r \rightarrow 0} \left(\phi(r) - z\frac{\lambda_B}{r} \right) = -\frac{\lambda_B\kappa_D}{1+d\kappa_D/2}. \quad (2.10)$$

Interestingly, this is the energy of a spherical capacitor of radius $d/2 + \kappa_D^{-1}$, with charge ez at the origin and $-ez$ homogeneously distributed at the outer shell. The total electrostatic energy density follows as

$$\frac{\beta U^{ES}}{V} = \frac{1}{2V} \sum_{j=1}^{2N} \beta U_{ion}^j = -\frac{1}{2}\lambda_B \frac{2\rho_b\kappa_D}{1+d\kappa_D/2}, \quad (2.11)$$

where N denotes the number of ion pairs, V the total volume and $2\rho_b$ the total ion density. Note that the energy of each ion is negative and scales, in the dilute limit $d\kappa_D \ll 1$, with the square root of the density. Hence, it is energetically favorable for an ion to be surrounded by many other oppositely charged ions. Another route that gives the same expression (2.11) for the energy density can be obtained by following the energy route [42]. Using the radial distribution functions $g_{ij}(r)$ for the RPM from the linearized PB approximation: $g_{\pm\pm}(r > d/2) = 1 \mp e\phi(r)$ and $g_{\pm\pm}(r < d/2) = 0$, in the exact energy equation:

$$\beta \frac{U^{ES}}{V} = 4\pi\lambda_B\rho_b^2 \int_0^\infty dr r h_Z(r), \quad (2.12)$$

where $h_Z = h_{++} - h_{+-}$, we recover Eq. (2.11). The internal energy opens the gateway to the other thermodynamic potentials, e.g. the electrostatic Helmholtz free energy is obtained by inverting $U^{ES} = \partial\beta F^{ES}/\partial\beta$, which results in [31]:

$$\frac{\beta F^{ES}}{V} = -\frac{1}{\pi d^3} \left[(d\kappa_D/2)^2 - d\kappa_D + 2\log(d\kappa_D/2 + 1) \right], \quad (2.13)$$

where V is the total volume. In the limit $d\kappa_D \rightarrow 0$ this reduces to the famous limiting law, exact in the dilute limit,

$$\frac{\beta F^{ES}}{V} = -\frac{\kappa_D^3}{12\pi}. \quad (2.14)$$

which predicts that the electrostatic free energy density is negative (so has a cohesive character) and vanishes with bulk concentration as $\rho_b^{3/2}$; note that in the RPM both species have the same bulk concentration ρ_b .

Although DH wrote down a generalized free energy expression, appropriate to models that encompass more species with different radii and valencies, the DH theory provides an accurate description for dilute systems only. In order to progress one requires more sophisticated extensions to DH theory that can tackle concentrated electrolytes. An important extension is the mean spherical approximation (MSA), a closure to the OZ equation in which the hard core repulsion between ions is enforced from the outset by requiring the radial distribution functions $g_{ij}(r) = h_{ij}(r) + 1$ vanish inside the hard core.

2.1.1.2 Mean-Spherical Approximation

The MSA is frequently employed to solve the OZ Eq. (2.5). For the PM the MSA imposes the conditions:

$$g_{ij}(r) = 0, \quad r < d_{ij}, \quad (2.15)$$

$$c_{ij}^{(2)}(r) = -z_i z_j \frac{\lambda_B}{r}, \quad r \geq d_{ij}, \quad (2.16)$$

where $d_{ij} = (d_i + d_j)/2$ denotes the average hard sphere diameter of species i and j . The first is an exact condition whereas the second constitutes the approximation. The full solution for the direct and total correlation functions, as well as the energy within the MSA, was found by Blum and others in the 70's [64, 65, 66, 67] (see also Appendix 2.A) building upon the pioneering work of Waisman and Lebowitz [68, 69, 70]. The solution for the direct correlation functions can be written as

$$c_{ij}^{MSA}(r) = c_{ij}^{HS}(r) + \Delta c_{ij}^{MSA}(r), \quad (2.17)$$

where the first term is the well-known Percus-Yevick direct correlation function for hard spheres (HS), see for instance Ref. [42], and the second term arises from the electrostatic interactions. For the RPM, $\Delta c_{ij}^{MSA}(r)$ takes the simple form:

$$\Delta c_{ij}^{MSA}(r) = \begin{cases} -z_i z_j \frac{\lambda_B}{r} \frac{2Dr - r^2}{D^2}, & r < d; \\ -z_i z_j \frac{\lambda_B}{r}, & r \geq d, \end{cases} \quad (2.18)$$

where $D = d + 1/Y$, with $2Y$ a parameter depending on ρ_b and discussed below. The results for the electrostatic internal and free energy of the RPM are given by:

$$\beta \frac{U^{ES}}{V} = -\lambda_B \frac{2\rho_b Y(\rho_b) + dq\eta(\rho_b)}{1 + dY(\rho_b)}, \quad (2.19)$$

$$\beta \frac{F^{ES}}{V} = -\lambda_B \frac{2\rho_b Y(\rho_b) + dq\eta(\rho_b)}{1 + dY(\rho_b)} + \frac{Y^3(\rho_b)}{3\pi}, \quad (2.20)$$

where $q = \rho_+ z_+ + \rho_- z_-$ is the charge density. Of course, this vanishes in the bulk; for convenience, we retain q for future reference. For every state point $\{\rho_b d^3, d/\lambda_B\}$, the parameters $Y(\rho_b)$ and $\eta(\rho_b)$ must be determined self-consistently using the relations:

$$Y^2 = \pi \lambda_B \frac{2\rho_b - 2d^2 q \eta + 2\rho_b d^4 \eta^2}{(1 + dY)^2}, \quad (2.21)$$

$$\eta = \frac{1}{H(Y)} \frac{dq}{1 + dY}, \quad (2.22)$$

where it is understood H and Y are functions of ρ_b , and $H(\rho_b)$ is given by

$$H = \frac{d^3 2\rho_b}{1 + dY} + \frac{2}{\pi} \left(1 - \frac{\pi}{6} d^3 2\rho_b \right). \quad (2.23)$$

The parameter $2Y$ reduces to the inverse Debye length κ_D in the limit $d\kappa_D \rightarrow 0$. However, whereas κ_D^{-1} plays the role of a screening length in the dilute limit as we will see, $1/2Y$ is merely an intermediate parameter of the theory and should not be regarded as a physical screening length. The parameter η characterizes the symmetry of the electrolyte; it vanishes for the RPM and also for symmetric $z : z$ electrolytes with ion valencies z provided the ionic radii are equal. In general, however, η is non-zero for asymmetric electrolytes, see for instance Ref. [71]. Hence, note the striking similarity between the expressions for internal energy density $\beta U^{ES}/V$ from DH Eq. (2.11) and MSA Eq. (2.19). Also, taking $\lim_{d \rightarrow 0}$ in Eq. (2.20) reduces to the limiting law in Eq. (2.14).

We now turn our attention to inhomogeneous systems, for which DFT provides a powerful theoretical framework.

2.1.2 Inhomogeneous Electrolytes

DFT is designed to treat both the thermodynamic and structural equilibrium properties of inhomogeneous many-body systems. The key ingredient is the excess Helmholtz free energy functional \mathcal{F}_{ex} defined by Eq. (2.3), which for our case should contain both the hard-core interactions and the Coulomb interactions of the ions as described by the pair potential Eq. (2.1). Those two types of interactions (hard-core and Coulombic) will be treated separately, and we split \mathcal{F}_{ex} accordingly as

$$\mathcal{F}_{ex}[\{\rho\}] = \mathcal{F}_{ex}^{HS}[\{\rho\}] + \mathcal{F}_{ex}^{ES}[\{\rho\}]. \quad (2.24)$$

The first term on the right-hand side is the Helmholtz excess functional that accounts for the hard-core repulsion; this is well described by White-Bear II (WBII) version of Fundamental Measure Theory (FMT) for hard spheres (HS), see e.g. Ref. [47]. The second term accounts for the electrostatic interactions, which are inherently difficult to treat [63]. In the next paragraphs we describe three functionals that treat the electrostatic (Coulombic) interactions: a functional based on a mean-field approximation, one that uses the MSA direct correlation function Eq. (2.18) and one that uses both the MSA direct correlation function and the MSA expression for the Helmholtz free energy Eq. (2.20). For simplicity, we focus on the RPM, but our treatment can be extended to more general cases.

2.1.2.1 Mean-Field Coulomb Functional

The easiest way to include electrostatics is within a mean-field (MF) approximation for the Coulomb (C) pair potential (that we call MFC), i.e. we set

$$\beta\mathcal{F}_{ex}^{ES}[\{\rho\}] = \beta\mathcal{F}_{ex}^{MFC}[\{\rho\}] \equiv \frac{1}{2} \int d\mathbf{r} Q(\mathbf{r})\phi(\mathbf{r}), \quad (2.25)$$

where $\phi(\mathbf{r})$ denotes the dimensionless electrostatic potential, and $eQ(\mathbf{r})$ the total charge density $Q(\mathbf{r}) = Q_{ion}(\mathbf{r}) + Q_{ext}(\mathbf{r})$, with $Q_{ion}(\mathbf{r}) = \sum_j z_j \rho_j(\mathbf{r})$ denoting the charge density of the ions and $eQ_{ext}(\mathbf{r})$ the charge density of fixed charges, such as those on the electrode. The potential and charge density are related by the Poisson equation

$$\nabla^2 \phi(\mathbf{r}) = -4\pi\lambda_B Q(\mathbf{r}). \quad (2.26)$$

Eq. (2.25) corresponds to treating Coulombic contributions on a mean-field level; correlation effects are omitted. Note that the free energy vanishes for a homogeneous bulk system, where $Q(\mathbf{r}) = 0$ and $\phi(\mathbf{r}) = 0$. We have chosen to include the fixed charges in \mathcal{F}_{ex}^{MFC} , whereas formally these should be included in the external potential. However, writing \mathcal{F}_{ex}^{MFC} this way is convenient since it allows us to treat the full electrostatic potential that includes contributions from the external charges and the response of the ionic charges. With this choice, it is understood implicitly that $V_{ext}^j(\mathbf{r})$ contains only the non-electrostatic part of the external potential.

It is well known that mean-field approaches remain reliable if the density fluctuations are small at all positions. This implies that the accuracy of this MFC functional is restricted to low values of the bulk ionic densities and of the fixed-charge densities. In order to describe systems with stronger electrostatic coupling, we must extend the theory. This can be achieved using results from MSA. In the following subsections we borrow from the presentation of Ref. [63].

2.1.2.2 Mean Spherical Approximation: Correlation Function

Given the relation in Eq. (2.4) between the pair direct correlation function and the excess Helmholtz free energy functional, a natural way to implement the explicit MSA result Eq. (2.18) is

$$\beta\mathcal{F}_{ex}^{ES}[\{\rho\}] = -\frac{1}{2} \sum_{ij} \int d\mathbf{r} \int d\mathbf{r}' \rho_i(\mathbf{r}) \Delta c_{ij}^{MSA}(|\mathbf{r} - \mathbf{r}'|; \rho_b) \rho_j(\mathbf{r}'). \quad (2.27)$$

This approximation, which has origins in Ref. [72], inputs the MSA direct correlation functions evaluated at the *bulk* densities $\rho_{b,\pm} = \rho_b$. Thus the functional is built around a certain *bulk* reference system. It is convenient to split this functional into a mean-field contribution MFC, as in Eq. (2.25), plus corrections, i.e.

$$\Delta c_{ij}^{MSA}(r) = -z_i z_j \frac{\lambda_B}{r} + \Delta c_{ij}^{MSAc}(r), \quad (2.28)$$

where the first term is the MFC contribution and from Eq. (2.18) one finds for the RPM that

$$\Delta c_{ij}^{MSAc}(r) = \begin{cases} z_i z_j \frac{\lambda_B}{r} \frac{(r-D)^2}{D^2} & r < d; \\ 0 & r \geq d. \end{cases} \quad (2.29)$$

The quantity D was introduced previously just below Eq. (2.18). It follows that, $\mathcal{F}_{ex}^{ES} = \mathcal{F}_{ex}^{MFC} + \mathcal{F}_{ex}^{MSAc}$, where the first term is given by Eq. (2.25), and

$$\beta\mathcal{F}_{ex}^{MSAc}[\{\rho\}] = -\frac{1}{2} \sum_{ij} \int d\mathbf{r} \int_{|\mathbf{r}-\mathbf{r}'|<d} d\mathbf{r}' \rho_i(\mathbf{r}) \Delta c_{ij}^{MSAc}(|\mathbf{r} - \mathbf{r}'|; \rho_b) \rho_j(\mathbf{r}'). \quad (2.30)$$

Within the RPM, Eq. (2.30) reduces to

$$\beta\mathcal{F}_{ex}^{MSAc}[\{\rho\}] = -\frac{1}{2} \int d\mathbf{r} \int d\mathbf{r}' Q_{ion}(\mathbf{r}) \Delta c^{MSAc}(|\mathbf{r} - \mathbf{r}'|; \rho_b) Q_{ion}(\mathbf{r}'), \quad (2.31)$$

where the $z_i z_j$ term (the only ij dependence) in Δc_{ij}^{MSAc} is used in defining the charge densities Q_{ion} . Hence, we have shown explicitly that this functional depends only on the charge density profiles $Q_{ion}(\mathbf{r})$ and not on the total number density profile $\rho_+(\mathbf{r}) + \rho_-(\mathbf{r})$. The dependence on the total *bulk* density is manifest via the spatially-constant parameter $D = d + 1/Y(\rho_b)$ that enters the direct correlation functions of the bulk reference system. We emphasize that the part of the MSA direct correlation function incorporating the short-range steric repulsions, i.e. c_{ij}^{HS} in Eq. (2.17), is treated by an accurate HS (FMT) functional; see Refs. [63, 73]. The review by Roth [47] provides an excellent account of the FMT for HS.

2.1.2.3 Mean Spherical Approximation: Free Energy

In the previous sub-section structural information from the MSA, i.e. the bulk direct correlation function, was used in constructing the approximate electrostatic DFT. However, we saw earlier that the MSA also provides the internal and free energy of the homogeneous bulk system. A natural way to incorporate the bulk free energy density from MSA into a functional is by replacing the bulk densities with local or weighted densities. Specifically, we replace the charge density q and the total density $2\rho_b$, respectively, with the weighted densities [71, 74]

$$\tilde{n}_Z(\mathbf{r}) = \int d\mathbf{r}' (\rho_+(\mathbf{r}') - \rho_-(\mathbf{r}')) \omega(|\mathbf{r} - \mathbf{r}'|), \quad (2.32)$$

$$\tilde{n}_N(\mathbf{r}) = \int d\mathbf{r}' (\rho_+(\mathbf{r}') + \rho_-(\mathbf{r}')) \omega(|\mathbf{r} - \mathbf{r}'|), \quad (2.33)$$

where the weight function $\omega(r) = \delta(r - D/2)/\pi D^2$ is chosen. That is, ions are smeared out over a shell with diameter D , which is supposed to represent the range over which the charge is screened in bulk. However, as pointed out in Sec. 2.1.1.2, the parameter Y should not be regarded as an inverse screening length. Notwithstanding, we follow the methodology of Refs. [71, 74]. Replacing directly the densities results in the reduced free energy density (in units of $k_B T$), see Eq. (2.20), used in Ref. [71]

$$\Phi^{MSA}(\{\tilde{n}(\mathbf{r})\}) = -\lambda_B \frac{\tilde{n}_N(\mathbf{r})Y(\{\tilde{n}(\mathbf{r})\}) + d\tilde{n}_Z(\mathbf{r})\eta(\{\tilde{n}(\mathbf{r})\})}{1 + dY(\{\tilde{n}(\mathbf{r})\})} + \frac{Y(\{\tilde{n}(\mathbf{r})\})^3}{3\pi}. \quad (2.34)$$

where $\{\tilde{n}(\mathbf{r})\} = \{\tilde{n}_N(\mathbf{r}), \tilde{n}_Z(\mathbf{r})\}$. Here, Y and η are point-wise versions of Eqs. (2.21)-(2.23), i.e. they are determined in exactly the same way as for the bulk values but using $\tilde{n}_N(\mathbf{r})$ and $\tilde{n}_Z(\mathbf{r})$ at points \mathbf{r} instead of $2\rho_b$ and q . Note that, although η vanishes in the RPM in the bulk, the quantity $\eta(\mathbf{r})$ can be non-zero in the RPM when there is a non-zero fixed charge density, i.e. near charged surfaces. The additional functional that arises from this treatment reads

$$\beta\mathcal{F}_{ex}^{MSAu}[\{\rho\}] = \int d\mathbf{r} \Phi^{MSA}(\{\tilde{n}(\mathbf{r})\}), \quad (2.35)$$

and the approximation becomes $\beta\mathcal{F}_{ex}^{ES} = \beta\mathcal{F}_{ex}^{MFC} + \beta\mathcal{F}_{ex}^{MSAc} + \beta\mathcal{F}_{ex}^{MSAu}$; see Eq. (30) of Ref. [71]. We use the superscript u to indicate the energy route.

This final addition to the electrostatic functional brings both advantages and disadvantages. By including this additional contribution one obtains rather accurate results for density profiles for a wide range of parameters, compared to simulations [71, 73]. The contribution is also significant for the energetics, especially at lower concentrations where the electrostatic free energy scales with $\rho_b^{3/2}$. Moreover, when entering the realm of asymmetric electrolytes the η term in Eq. (2.20) becomes important and can give a substantial contribution to the bulk free energy. On the downside, it turns out that this functional breaches various requirements of consistency (see Appendix 2.B). We shall show that these considerations are important in determining the asymptotic decay of bulk pair correlation functions and one-body density profiles.

Three electrostatic functionals are employed in this chapter. The simplest functional \mathcal{F}_{ex}^{MFC} , which uses only the Coulomb potential, is referred to as the mean-field Coulomb functional. The second functional, $\mathcal{F}_{ex}^{MFC} + \mathcal{F}_{ex}^{MSAc}$, which uses the bulk direct correlation function from the MSA, is referred to as the MSAc functional. And the third functional, $\mathcal{F}_{ex}^{MFC} + \mathcal{F}_{ex}^{MSAc} + \mathcal{F}_{ex}^{MSAu}$, which uses both the bulk direct correlation function and the free energy from the MSA, is referred to as the MSAu functional. In Ref. [71] the authors use the acronym FMT/fMSA for the third functional.

2.2 DFT CALCULATIONS AND MD SIMULATIONS FOR THE RPM AT A PLANAR ELECTRODE

We apply the density functionals of Sec. 2.1.2 to 1:1 ionic solutions in an aqueous medium (the solvent is not treated explicitly) with a constant dielectric relative permittivity $\epsilon_r = 78$ and temperature $T = 293.41$ K, corresponding to a Bjerrum length of $\lambda_B = 0.73$ nm. The electrolyte consists of equal-sized cat- and anions, with hard-core diameters $d_+ = d_- = d = 0.5$ nm, in contact with a planar electrode located at $x = 0$ and at a fixed surface potential Φ_0 . Given the planar symmetry, and in the absence of any symmetry-breaking transition, the ionic density profiles $\rho_+(x)$ and $\rho_-(x)$ are a function of the distance x from the wall. For the RPM we define the dimensionless charge and *excess* number densities as

$$\rho_Z(x) = \frac{\rho_+(x) - \rho_-(x)}{\rho_b}, \quad (2.36)$$

$$\rho_N(x) = \frac{\rho_+(x) + \rho_-(x)}{\rho_b} - 2, \quad (2.37)$$

where the bulk densities $\rho_{b,+} = \rho_{b,-} \equiv \rho_b$. As a measure for the concentrations we use the dimensionless quantity $d\kappa_D$, which scales as $\sqrt{\rho_b}$. In the electrolyte literature it is customary to introduce a reduced temperature $T^* = d/\lambda_B$. For the model we consider $T^* \approx 0.685$, which is far above the critical temperature $T_c^* \approx 0.05$ of the 1 : 1 RPM [75]. Thus, we avoid complications associated with liquid-gas phase separation. In practice we consider a planar slit geometry with two identical charged walls at $x = 0$ and $x = H$ separated by a distance H , sufficiently large that the density profiles for $x = H/2$ are very close to their bulk values at the specified chemical potential and temperature. In order to test the predictions of the various DFT approximations, our collaborators carried out extensive Molecular Dynamics (MD) simulations of the density profiles for the same range of parameters using the ESPResSo package [76].

Whereas our DFT calculations are performed in a grand canonical ensemble with fixed chemical potentials μ_{\pm} and fixed surface potential Φ_0 , the MD simulations are naturally performed in the canonical ensemble with fixed numbers of ions N_{\pm} and fixed homogeneous surface charge densities $\pm eQ_W$ at the walls. We employ two oppositely charged electrodes and fix $N = N_+ = N_-$. Direct comparison between DFT and MD results is possible because we matched the bulk concentrations in DFT such that the concentration in the center of the slit at $x = H/2$ coincided with the MD simulation.

The hard-core interactions in the MD between ions are modeled by the Weeks-Chandler-Anderson potential [77, 78]

$$u^{\text{WCA}}(r) = \begin{cases} 4\epsilon \left(\left(\frac{\sigma_{\text{LJ}}}{r} \right)^{12} - \left(\frac{\sigma_{\text{LJ}}}{r} \right)^6 + \frac{1}{4} \right) & r < d \\ 0 & r \geq d, \end{cases} \quad (2.38)$$

with $\epsilon = 0.5 \cdot 10^4 k_B T$ and $\sigma_{\text{LJ}} = d/2^{1/6}$ such that the potential is purely (and strongly) repulsive and its derivative is continuous at the diameter d . In order to model the effect of the hard walls we set the wall-ion interaction potential to $u^{\text{WCA}}(-\frac{d}{2} + x)$ for the wall at $x = 0$ and $u^{\text{WCA}}(H + \frac{d}{2} - x)$ for the wall at $x = H$.

For making comparisons, the starting MD values are obtained by preliminary DFT calculations in order to achieve approximately the same $d\kappa_D$ and the potential Φ_0 of interest. Then, $d\kappa_D$ and the surface potential Φ_0 were deduced from the MD simulations, which are subsequently used as input for the DFT calculations. The input values for the MD simulations (Q_W , N and L_x) and DFT calculations ($d\kappa_D$ and Φ_0) for the following three sets were

Set 1 $Q_W = 0.00427 e \text{ nm}^{-2}$, $N = 1977$, $L_x = 50 \text{ nm}$ $d\kappa_D = 0.619$, $\Phi_0 = 1 \text{ mV}$,

Set 2 $Q_W = 0.913 e \text{ nm}^{-2}$, $N = 1983$, $L_x = 22.5 \text{ nm}$ $d\kappa_D = 1.286$, $\Phi_0 = 105 \text{ mV}$,

Set 3 $Q_W = 1.334 e \text{ nm}^{-2}$, $N = 1968$, $L_x = 13.5 \text{ nm}$ $d\kappa_D = 2.243$, $\Phi_0 = 72.19 \text{ mV}$.

Profiles are shown in Fig. 2.3.1 where comparison is made with the corresponding DFT results, as explained in the the next section.

The reader can skip to the next section and come back to this alinea for details regarding the the extraction of the decay lengths from simulatiosn. In order to calculate the decay lengths ξ_N and ξ_Z of, respectively, the total number and charge bulk pair correlations $h_N(r)$ and $h_Z(r)$ we first choose to fit with functions of the form of Eq. (2.41) (see below), that assumes simple poles determine the asymptotic decay, over a range where our simulation data is sufficiently accurate. Typically we fit over a short range, approximately between $r = 0.9 \dots 1.1 \text{ nm}$, limited by numerical noise and short decay lengths. Nevertheless, depending on the system parameters, this range could span down to d and up to several nanometers. Furthermore, at these relatively short distances, often more than one pair (A_n, α_n) of amplitudes and poles (exponentials with different decay lengths) is required to fit the pair correlation functions obtained from simulations. Performing individual fits for each state point, we find two pairs are sufficient to fit the data. However, for number correlations at low concentrations we were guided by earlier literature [60, 79] on asymptotic decay in bulk electrolytes where it was established that a branch point singularity dominates the decay except at extremely large r . The predicted decay for $h_N(r)$ is given in Eq. (2.44) (see below). For the narrow range of r we have data available, a function of this form with $B = 0$ provides an adequate fit. Although more advanced methods are available to extract the asymptotic decay lengths [79, 80], the relatively simple scheme we implement proved to be sufficient.

2.3 RESULTS FOR DENSITY PROFILES AND DECAY LENGTHS

DFT proves to be a valuable microscope in the near field, close to the electrode, where comparison with simulation is rather straightforward. It is also crucially important as a telescope in the far field, where the simulation results are limited by system size and noise.

2.3.1 Near Field

In Fig. 2.3.1 we plot the charge density profiles $\rho_Z(x)$ (left column) and excess number density profiles $\rho_N(x)$ (right column) obtained from the functionals MFC (red), MSAC (black) and MSAu (blue) and from MD simulations (green) for the sets of parameters given in the previous section.

In the near field, there is excellent agreement between the density profiles obtained from the MSAC and MSAu functionals and those from simulations, with the exception of $\rho_N(x)$ in Fig. 2.3.1(b). For this low concentration and low surface potential one observes depletion in the excess number density $\rho_N(x)$ near an electrode. This is caused by the negative electrostatic free energy (accounted for only by the MSAu functional) which dominates over the hard-sphere free energy; whereas the latter scales as ρ_b^2 , the former scales as $\rho_b^{3/2}$, and thus dominates at low enough ρ_b . Apart from these special cases, the difference between the MSAC and MSAu profiles in the near field is negligible. Hence, we deduce that adding the energy term to the functional is only important for the RPM at small concentrations and surface potentials.

Note that the density profiles from the MFC functional are quite different from those of the MSA functionals. Clearly the details of near-field structure depend on the terms in the functional carrying the direct pair correlation function (see Eq. (2.30)), that are absent in the MFC.

Although in the near field the distinction in the density profiles between the MSAC and MSAu functionals is fairly small, one can easily distinguish those in the far field (see insets in Fig. 2.3.1). We focus on this important observation in the next subsection and in Appendix 2.B.

2.3.2 Far Field

We turn now to the interpretation of the far-field density profiles, i.e. results pertinent to large x in Fig. 2.3.1. The insets show that oscillations develop in the asymptotic decay of both the charge and number density profiles as the concentration in $d\kappa_D$ is increased. This is especially clear in the sequence for the MSAC number density profiles.

2.3.2.1 Asymptotic Decay of Bulk Pair Correlations

In the far field, we focus on the asymptotic decay of the one-body charge $\rho_Z(x)$ and excess number $\rho_N(x)$ densities far from the electrode(wall). The leading asymptotics for

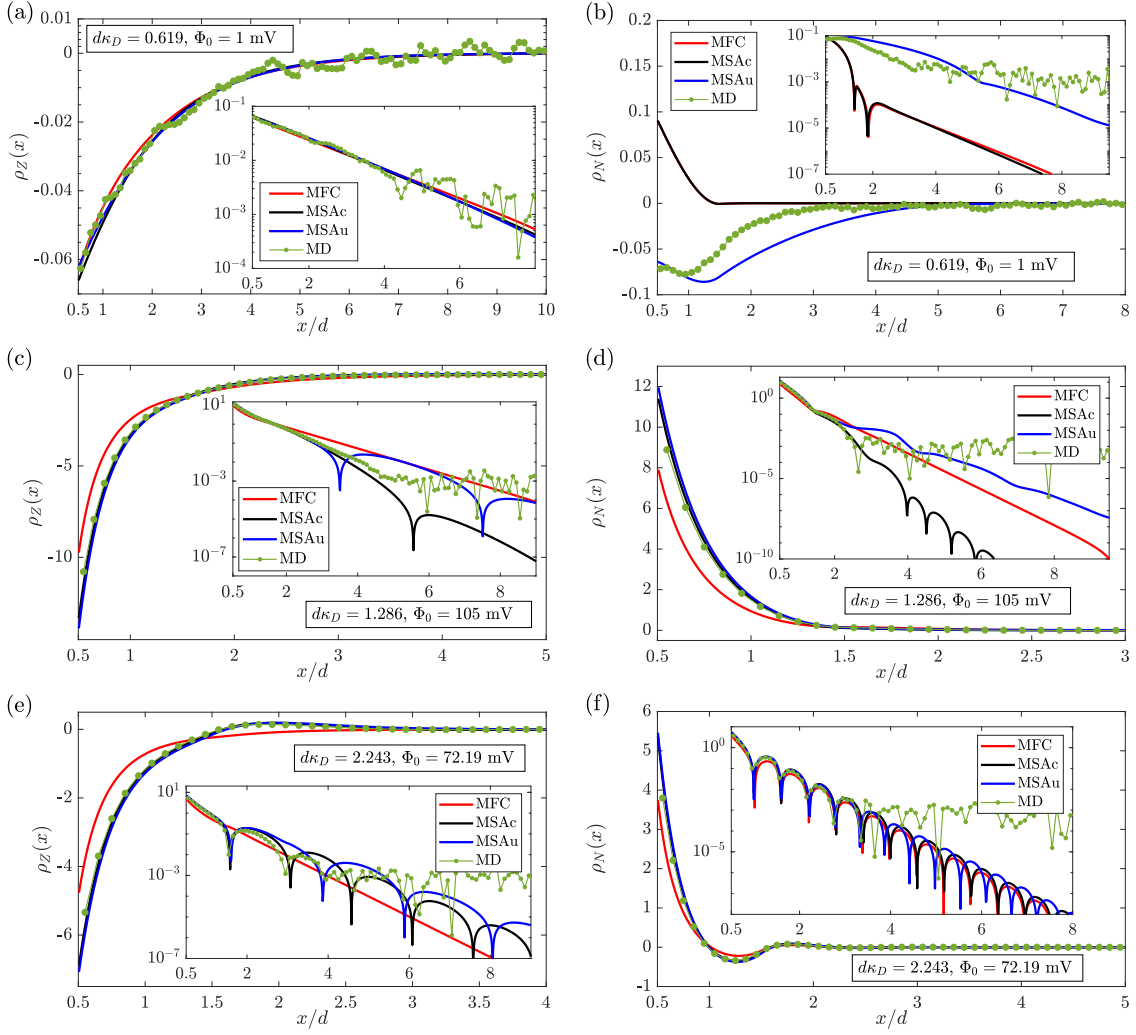


Figure 2.3.1: In (a), (c), and (e) the dimensionless charge density profile $\rho_Z(x)$ and in (b), (d), and (f) the dimensionless excess number density profile $\rho_N(x)$ for the RPM, modelling an aqueous 1:1 electrolyte, with ionic diameter $d = 0.5$ nm in contact with a charged planar electrode located at $z = 0$. The surface potential Φ_0 and the ionic concentration, expressed as $d\kappa_D$, are given in each panel, while the number of ions and surface charge density for the simulations are given in Sec. 2.2. Results obtained from MD simulation (green dots) and the three different DFT approximations (solid lines) are shown. The insets show the modulus of the density profiles plotted on a logarithmic scale. These plots, together with many others not shown here, are used to determine asymptotic decay lengths in the DFT studies.

these densities are determined by the asymptotic decay of pair correlation functions in the corresponding uniform (bulk) fluid [81, 82, 83, 84, 85]. Appendix 2.C provides a simple argument for this statement. In the bulk, the asymptotic, large r , behavior of pair correlation functions can be obtained from the singularities that appear in the Fourier-transformed OZ equation (Eq. (2.5)). For a single-component (neutral) system this takes the form

$$\hat{h}(k) = \frac{\hat{c}^{(2)}(k)}{1 - \rho_b \hat{c}^{(2)}(k)}. \quad (2.39)$$

For models with short-ranged pair potentials (exponentially or faster decaying or of finite range) we expect the dominant singularities in Eq.(2.39) to be simple poles, at least for intermediate to high bulk concentrations. In this case the leading decay in three dimensions is given by

$$rh(r) \approx \sum_n \text{Re} \left(A_n e^{i\alpha_n r} \right), \quad (2.40)$$

where Re denotes taking the real part, A_n is an amplitude, and $\{\alpha\}$ denotes the set of poles α_n with positive imaginary part in the complex k -plane, that satisfy the condition $1 - \rho_b \hat{c}^{(2)}(\alpha_n) = 0$. When the poles are complex the asymptotic behavior is determined by the pole $\alpha = 2\pi/\lambda + i\kappa$ ($\lambda, \kappa \in \mathbb{R}$), and its conjugate, having the smallest imaginary part κ . The leading oscillatory decay of the total correlation function is then given in 3 dimensions by

$$rh(r) \underset{r \rightarrow \infty}{\approx} A \cos(2\pi r/\lambda + \varphi) e^{-\kappa r}, \quad (2.41)$$

where the amplitude A and phase φ can be obtained from the residues [81, 84]. Generally, there are also pure imaginary poles $\alpha_n = i\kappa$ giving rise to purely exponential decay of $rh(r)$. Whether the ultimate decay of $rh(r)$ is damped oscillatory or monotonic at a particular state point depends on whether the lowest lying pole, i.e. that with the smallest value of κ , is complex or pure imaginary. For model fluids exhibiting repulsive and attractive portions in the pair potential there is a crossover line in the phase diagram where the asymptotic decay of $rh(r)$ changes from monotonic to damped oscillatory, termed the Fisher-Widom (FW) line [61, 81, 84, 86, 87]. The procedure we employ for obtaining the asymptotic decay length, $\xi = 1/\kappa$, in the bulk fluid is termed the IET route, since we usually invoke an integral equation closure or another explicit approximation, gleaned say from DFT, for the bulk pair direct correlation function.

For a system with two species, in our case cations (+) and anions (-), we must consider the total correlation matrix

$$H(r) = \begin{bmatrix} h_{++}(r) & h_{+-}(r) \\ h_{-+}(r) & h_{--}(r) \end{bmatrix} \quad (2.42)$$

for which the Fourier-transformed OZ equation reads

$$\hat{H}(k) = \left(\mathbb{1} - \hat{C}(k)\rho \right)^{-1} \hat{C}(k), \quad (2.43)$$

where \hat{C} has the same structure as in Eq. (2.42) and ρ is a diagonal matrix whose elements are the bulk densities of each species. Singularities on the r.h.s. of Eq. (2.43) determine the asymptotic decay of the total correlation functions. Within the RPM, $h_{++} = h_{--}$ and $h_{+-} = h_{-+}$ and it is convenient to work with the combinations $h_N = h_{++} + h_{+-}$ and $h_Z = h_{++} - h_{+-}$, corresponding to the number-number N and charge-charge Z total correlation function, respectively. The combinations h_N and h_Z also follow naturally for the RPM from diagonalizing the matrix H . The special symmetry of the RPM suggests that

these are decoupled and therefore the inverse decay lengths κ_N and κ_Z are independent. Indeed within IET's that admit only simple poles this is the case [61]. Fig. 2.3.2 summarises the pole structure of h_N and h_Z obtained from an approximate IET study (See Ref. [61]). The inverse decay length κ is plotted on the vertical axis and the inverse wavelength $2\pi/\lambda$ on the horizontal axis; crosses indicate a pole. The N pole structure indicates that for small concentrations the pole with the smallest imaginary part is pure imaginary, and therefore the pair correlation function h_N must decay monotonically. At larger concentrations, the conjugate pair of poles with the smallest imaginary part has a non-zero real part; h_N will then exhibit oscillatory asymptotic decay. Hence, there should be crossover from monotonic to oscillatory asymptotic N decay, c.f. the FW crossover described above, as the concentration $d\kappa_D$ is increased. The Z pole structure is different, as shown in the bottom panel of Fig. 2.3.2. Although one finds monotonic asymptotic decay of $rh_Z(r)$ at low concentrations and oscillatory decay at large concentrations, the crossover mechanism is that due to Kirkwood Ref. [88]. The key difference between the two types of crossover is: at a FW point the real part of the pole with the smallest imaginary part jumps discontinuously from zero to some non-zero value, whereas at a Kirkwood point the pole with the smallest imaginary part moves continuously away from the imaginary axis. Hence, the wavelength of oscillations diverges for the Z decay at a Kirkwood point, but not for the N decay at a FW point. (See Ref. [61]).

Ionic systems bring additional subtleties. In particular, singularities other than simple poles are expected, reflecting 'residual' coupling between number and charge correlations. This was recognized long ago by Kjellander and coworkers, e.g. Refs. [60, 79, 85, 89]. A careful asymptotic analysis for the bulk RPM reveals both a pole and a branch point singularity for number-number correlations implying

$$h_N(r) \approx B \frac{e^{-\kappa_N r}}{r} + A \frac{e^{-\beta_N r}}{r^2} \quad (2.44)$$

should provide an adequate description of the asymptotic decay. At moderately large values of r and for low-intermediate ionic concentrations the second (branch point) term is expected to dominate. The same asymptotic analysis shows that the branch point term gives the exponential decay length $\beta_N^{-1} = \kappa_Z^{-1}/2$, i.e. half that of the charge correlation length κ_Z^{-1} . At low ionic concentrations $B \rightarrow 0$ and we choose to fit $h_N(r)$ from simulations according to Eq. (2.44) with $B = 0$, as indicated earlier. This procedure is, of course, empirical. In reality $B \neq 0$ and the pole contribution takes over as the concentration increases; see e.g. Eq. (44) in Ennis et al. and Fig. 1 in Ulander and Kjellander [79]. The decay length ξ_N reported later, will be the larger of either $1/\kappa_N$ (pole) and $1/\beta_N$ (branch point). In Appendix 2.D we discuss the origin of the term in the one-body number density profile at a planar wall that is analogous to the term corresponding to the branch point in Eq. (2.44).

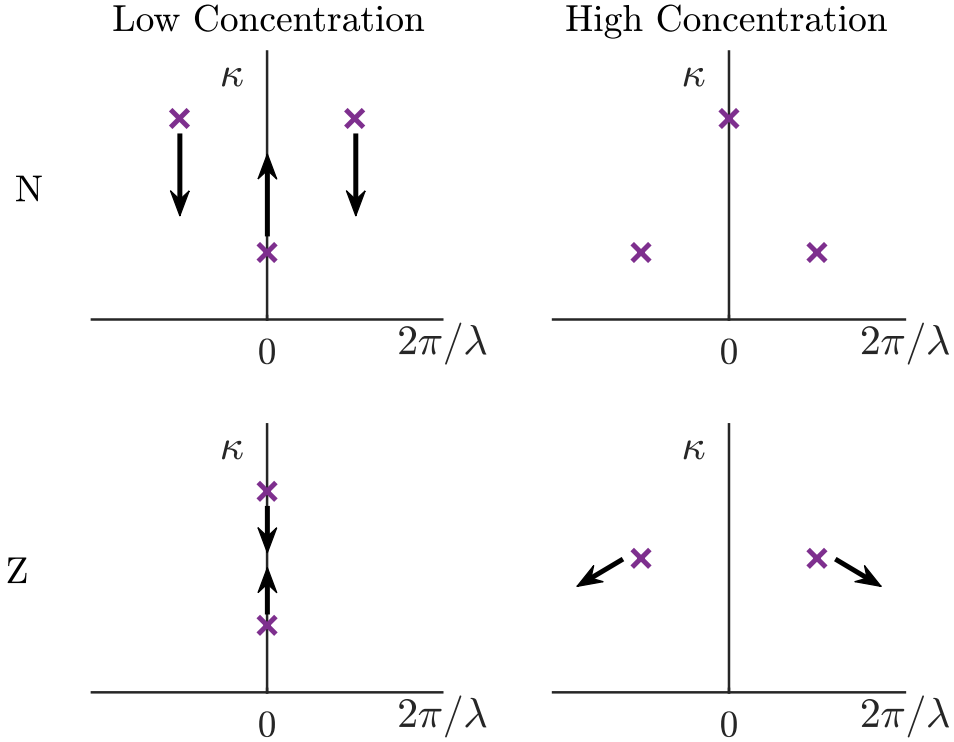


Figure 2.3.2: The pole structure of the number-number (N) (top) and charge-charge (Z) (bottom) pair correlation function when increasing from low (dimensionless) concentrations $d\kappa_D$ (left) to high concentrations (right), as determined by IET. The top describes Fisher-Widom crossover and the bottom Kirkwood crossover. The scenario presented here makes no reference to other possible singularities, e.g. branch points; see text.

2.3.2.2 Asymptotic Decay of One-Body Density Profiles at a Planar Electrode

As mentioned above, there is a large body of work demonstrating that the asymptotic decay of the one-body density profiles of fluids adsorbed at planar walls is governed by the same physics that determines the decay of bulk pair correlation functions. Specifically, if we know the leading singularities from a calculation of the bulk pair direct correlation functions, in principle we know the decay lengths and the wavelength of any oscillations pertinent to the asymptotic decay of the density profiles at a planar electrode, see Appendix 2.C. This key observation motivates our subsequent analysis. For example, as $x \rightarrow \infty$, the charge and total density profiles in the RPM should take the form:

$$\rho_i(x) \propto \cos(2\pi x/\lambda_i) e^{-x/\xi_i}, \quad i \in \{Z, N\}, \quad (2.45)$$

when an oscillatory contribution dominates. Then the asymptotic decay lengths ξ_Z and ξ_N are identical to the corresponding decay length of the bulk fluid. In an oscillatory regime, the wavelengths λ_Z and λ_N are identical to the corresponding bulk values. Moreover, any crossover that occurs in bulk must be reflected in the decay of the one-body profiles. Note that we have not indicated any amplitudes or phases in this equation. There is no simple way of determining these. Contrast this with the decay of bulk pair correlation functions where the amplitudes and phases are determined from the residues in the OZ analysis.

Guided by these observations, we can attempt to analyze the far-field results in Fig. 2.3.1. Extracting the asymptotic decay lengths from the one-body profiles calculated within DFT and simulations is non-trivial, since we must deal with numerical limitations. Within DFT the asymptotic decay lengths ξ_Z and ξ_N and wavelengths λ_Z and λ_N are extracted from fits to the density profiles in Fig. 2.3.1. For MD our collaborators performed bulk simulations to achieve better statistics; see Sec. 2.2. We confirmed that the results for the various decay lengths in DFT were independent of the surface potential Φ_0 . In Fig. 2.3.3, we present the decay lengths, multiplied by the inverse Debye length κ_D (solid lines), and wavelengths divided by the HS diameter (dotted lines) obtained by fitting the DFT results together with results from the IET route (purple). For the latter we use the ZZ pair direct correlation function from the MSA to determine the decay. This MSA result is well-known and the resulting poles are reported, e.g. in Refs. [61, 90]. The HS pair direct correlation function from FMT (WBII) is used for the N decay. This treatment of number-number correlations captures only the contributions from HS (steric) interactions. The results from the MFC functional are plotted in red and those of the MSAc(u) functional in black(blue) while the results from MD simulations are plotted in green.

As predicted, ξ_Z in Fig. 2.3.3(a) extracted from the MFC functional (red line) is given by the Debye length for all concentrations. At very low concentrations, $d\kappa_D \ll 1$, the true decay length must converge to the Debye length for all theories, as dictated by the limiting law. Precisely how $\xi_Z\kappa_D$ approaches unity at $d\kappa_D = 0$ is important and we return to this later. At intermediate concentrations ($d\kappa_D > 0.5$), the limiting law is no longer valid and ξ_Z is found to be smaller than the Debye length. The decay length obtained from the MSA IET is universal as a function of $d\kappa_D$ [61] and is given by the purple line. From its construction, the MSAc functional should yield identical results and within our numerical accuracy it does; see black line. The MSAu functional (blue line), on the other hand, behaves quite differently. We argue this is due to the inconsistency inherent within this functional (Appendix 2.B), which results in incorrect asymptotic behaviour. The kinks that are observed for the DFT results indicate that the Kirkwood transition occurs at (using the notation $\mathcal{X} = d\kappa_D$) $\mathcal{X}_K^{MSAc} \approx 1.24$ and $\mathcal{X}_K^{MSAu} \approx 0.7004$ while the MSA IET value is $\mathcal{X}_K^{IET} \approx 1.229$. As expected, the MSAc and IET Kirkwood points agree closely, i.e. to within 1 percent which is within the error of the fitting procedure used to calculate ξ_Z^{MSAc} . Strikingly, the MSAu Kirkwood point is smaller by almost a factor of two. The genesis of the kinks becomes clear when, within MSA IET, one plots the second smallest imaginary pole (purple-dashed line in Fig. 2.3.3(a)). This plot indicates that the two smallest poles lie on the imaginary axis and move towards each other with increasing $d\kappa_D$, merging at the Kirkwood point. For larger concentrations the poles move away from the imaginary axis, one to positive real values and the other to equal but negative real values (as depicted in Fig. 2.3.2). The density profiles develop oscillatory decay for $d\kappa_D > \mathcal{X}_K$ (see dotted lines), beginning with infinite wavelength at $d\kappa_D = \mathcal{X}_K$. We find that the wavelengths from the MSAc and IET results are almost identical while the wavelength from the MSAu functional is very different. The MD results (in green) agree rather well with those from MSAc, and therefore with MSA IET. There is an indication within MD of

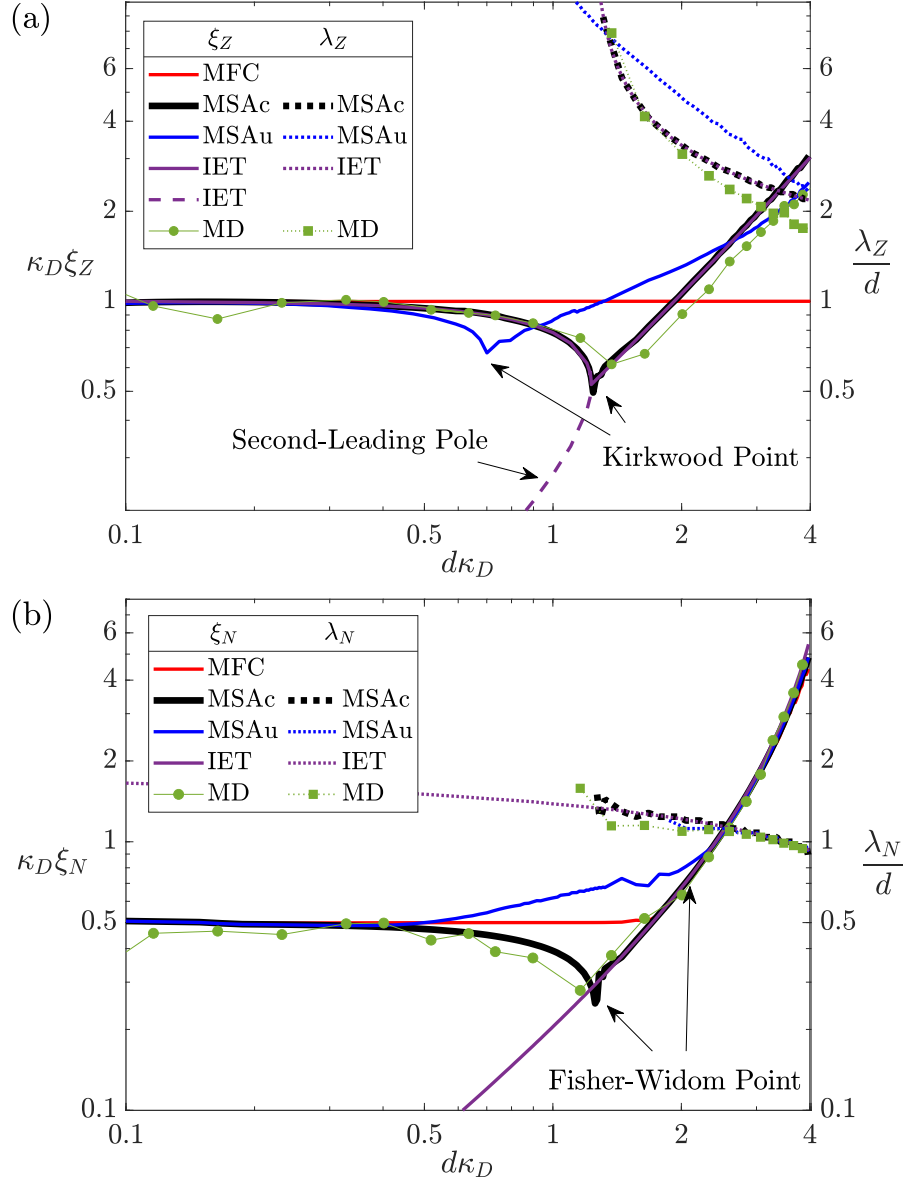


Figure 2.3.3: (a) The charge decay length ξ_Z (solid) and wavelength λ_Z (dotted) plotted as a function of $d\kappa_D$. The DFT results are for the one body density profiles obtained from the MFC (red), MSAc (black) or MSAu (blue) functional for the electrostatics. The results from IET (purple) correspond to the bulk IET MSA closure. These and the MD simulation results (green) are for the decay of bulk pair correlation functions. The dashed-purple line in (a) represents the pole with the second-smallest imaginary part, i.e. the second-leading pole. Arrows point to the cusps where (Kirkwood) crossover from monotonic to oscillatory decay occurs. (b) The number decay length ξ_N and wavelength λ_N uses the same color coding as in (a). The IET route uses the FMT (HS) direct correlation function. The MD data for the decay length ξ_N below the Fisher-Widom point were fitted using the functional form of Eq. (2.44) with $B = 0$. Our numerical results imply ξ_N is close to the theoretical prediction $\xi_N = 1/2\kappa_Z$. Results for ξ_N calculated from the DFTs are plotted for the surface potential $\Phi_0 = 100$ mV; see text. Arrows point to a (Fisher-Widom) crossover from monotonic to oscillatory decay.

a Kirkwood point at around $d\kappa_D \approx 1.37$ and for larger values of $d\kappa_D$ the MD results for $\xi_{Z\kappa_D}$ increase linearly with $d\kappa_D$ as found in MSA IET. Moreover, the wavelengths are close.

In Fig. 2.3.3 (b) we present the corresponding results for ξ_N and λ_N ; the color coding is the same as in (a). For the MFC functional ξ_N is exactly one half the Debye length until pure HS correlations dominate at high concentrations. For the other two functionals, $\xi_{N\kappa_D}$ is close to 1/2 at small concentrations, $d\kappa_D < 0.5$. This is expected and will be explained below. At high concentrations, $d\kappa_D > 2$, the N decay lengths collapse onto a single curve and follow the result from IET, where, for all concentrations, ξ_N is obtained from the HS pair direct correlation function given by FMT. This collapse indicates that for sufficiently high concentrations the asymptotic N decay is determined by hard-sphere repulsion: electrostatic interactions hardly play a role. This is also reflected in the wavelengths (dotted lines). For the IET route λ_N corresponds to the wavelength of the bulk (asymptotic) oscillations for the HS fluid and the MD simulation results (plotted in green) agree closely. At intermediate concentrations, $0.5 < d\kappa_D < 2$, the three DFT functionals show very different results. The decay lengths extracted from the MD simulations agree well with those from MSAC, for both the N and Z decay lengths. There are small differences in the Z decay length for concentrations beyond the Kirkwood point. However, as we will see in Fig. 2.3.5, the differences are smaller when compared with the more accurate HNC IET results from Ref. [59]. From the number density profiles calculated in DFT we were able to determine the wavelength of oscillations for concentrations beyond the crossover from monotonic to oscillatory decay that we choose to term the FW point, i.e. for $d\kappa_D > \mathcal{X}_{FW}$, where $\mathcal{X}_{FW}^{MSAc} \approx 1.26$ and $\mathcal{X}_{FW}^{MSAu} \approx 1.77$ for the MSAC and MSAu functionals, respectively. These values bracket the result $\mathcal{X}_{FW} = 1.41$ found in the Generalized MSA (GMSA) IET study [61] of the bulk electrolyte; see below. Close to the FW point, ascertaining the concentration at which the oscillatory branch has the slower decay is not straightforward and, at first glance, appears to depend on the surface potential. This is illustrated in Fig. 2.3.4, where we plot $\rho_N(x)$ obtained from minimising the MSAC functional for surface potentials ranging from $\Phi_0 = 0.01$ mV (blue line) to $\Phi_0 = 100$ mV (purple line) at a fixed value of $d\kappa_D$, somewhat below the FW value. Although the true asymptotic decay must be monotonic, for the smallest surface potential we observe only oscillatory decay in the range of x that we can access. For larger surface potentials we observe the correct monotonic decay at sufficiently large x . Such behaviour can be explained if we assume the decay of the number density profile has two competing portions:

$$\rho_N(x) = A_1 e^{-\alpha_1 x} + A_2 e^{-\alpha_2 x} \cos(\omega x), \quad (2.46)$$

For $d\kappa_D < \mathcal{X}_{FW}$ we know $\alpha_1 < \alpha_2$. However, if $A_1 < A_2$, then for a certain $x < x^*$, the second term dominates and we observe oscillatory decay. Only for $x > x^*$ will the first term dominate and then we observe the true asymptotic monotonic decay.

Understanding how the number and charge decay lengths obtained from the three functionals vary with concentration and how their behaviour differs from MSA IET is non-trivial. It is necessary to consider the Euler-Lagrange equation obtained by minimizing

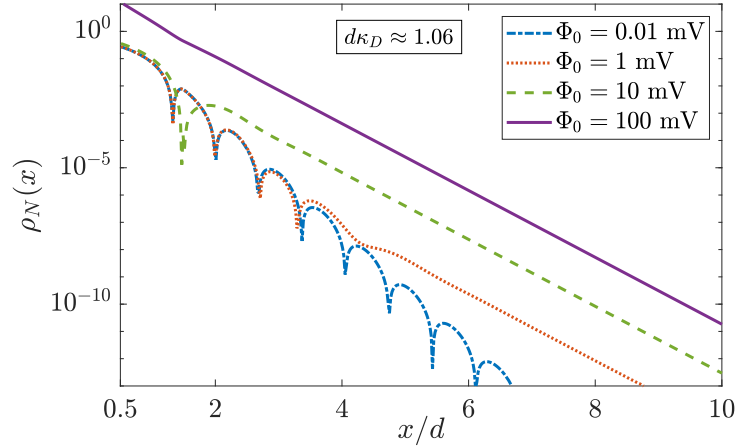


Figure 2.3.4: The decay of the excess number density $\rho_N(x)$ obtained using the MSAC functional for several surface potentials Φ_0 at fixed concentration $d\kappa_D = 1.0589$ that is slightly below the Fisher-Widom point (see Fig. 2.3.3). For $\Phi_0 = 0.01$ mV we appear to observe only oscillatory asymptotic decay whereas for larger Φ_0 we observe the true monotonic decay; see text.

the grand potential functional. In the far field, the number and charge densities can be expressed (see Eqs. (2.94) and (2.95) in Appendix 2.D) as

$$\rho_Z(x) \approx 2\Delta c_1(x; [\rho_Z, \rho_N]), \quad (2.47)$$

$$\begin{aligned} \rho_N(x) &\approx 2\Delta c_2(x, [\rho_N, \rho_Z]) + \Delta c_1(x; [\rho_Z, \rho_N])^2, \\ &= 2\Delta c_2(x, [\rho_N, \rho_Z]) + \frac{1}{4}\rho_Z(x)^2, \end{aligned} \quad (2.48)$$

where $\Delta c_1(x) = c_1(x) - c_{1,b}$ denotes the deviation from bulk of the part of the one-body direct correlation function that is proportional to the valency of the species and $\Delta c_2(x) = c_2(x) - c_{2,b}$ is the part that is the same for the cations and anions; see Eqs. (2.90) and (2.91). For the simplest case, the MFC functional, these reduce to:

$$\rho_Z(x) \approx 2\Delta c^{(1),MFC}(x; [\rho_Z]) = A \exp(-x/\xi_{MFC}), \quad (2.49)$$

$$\begin{aligned} \rho_N(x) &\approx 2\Delta c^{(1),HS}(x; [\rho_N]) + \frac{1}{4}\rho_Z^2(x) \\ &= B \cos(2\pi x/\lambda_{N,FMT}) \exp(-x/\xi_{FMT}) + C \exp(-2x/\xi_{MFC}). \end{aligned} \quad (2.50)$$

where we identified $\Delta c_1(x) = c^{(1),MFC}(x; [\rho_Z])$, $\Delta c_2 = \Delta c^{(1),HS}(x; [\rho_N])$ and A, B, C are non-universal coefficients. Whilst the asymptotic decay of $\rho_Z(x)$ in the MFC is always given by the Debye length, i.e. $\xi_{MFC} = \kappa_D^{-1}$, for the number density $\rho_N(x)$ one finds a competition between terms decaying with the FMT (HS) decay length ξ_{FMT} , dominating at high concentration, and those with half the Debye length, dominating at low concentration.

The competition results in the monotonic to oscillatory crossover (FW) point observed in Fig. 2.3.3. For the MSAC functional we find a similar result,

$$\begin{aligned}\rho_Z(x) &\approx 2c^{(1),MFC}([\rho_Z]; x) + 2c^{(1),MSAc}([\rho_Z]; x) \\ &= A \exp(-x/\xi_{MSAc}),\end{aligned}\quad (2.51)$$

$$\begin{aligned}\rho_N(x) &\approx 2\Delta c^{(1),HS}(x; [\rho_N]) + \frac{1}{4}\rho_Z^2(x) \\ &= B \cos(2\pi x/\lambda_{N, FMT}) \exp(-x/\xi_{FMT}) + C \exp(-2x/\xi_{MSAc}),\end{aligned}\quad (2.52)$$

where we identified $\Delta c_1(x) = c^{(1),MFC}(x; [\rho_Z]) + c^{(1),MSAc}(x; [\rho_Z])$ and $\Delta c_2(x)$ is the same as for the MFC. Hence, the decay has the same form as for the MFC functional except that $\xi_{MFC} = \kappa_D^{-1}$ is replaced with ξ_{MSAc} (which is not $1/2Y$), i.e. the value of the leading pole from the IET route. Note the presence of the Kirkwood point within MSAC leads to oscillatory decay of $\rho_Z(x)$ for $d\kappa_D > \mathcal{X}_K^{MSAc}$. From the results in Fig. 2.3.3 it is clear that the MSAu functional exhibits very different behaviour from the other two functionals, regarding predictions for asymptotic decay of correlations. In Appendix 2.B we argue that MSAu has severe inconsistencies that lead to erroneous predictions. The felon leading this inconsistency is the term $\eta(\{\tilde{n}(\mathbf{r})\})$ in Eq. (2.34), which of course, vanishes in the bulk RPM. Indeed one might argue that, given the symmetry of the RPM, the term should be omitted from the outset. If one adopts this strategy MSAu returns the same asymptotic Z decay as found with the MSAC, while the number decay remains virtually unchanged. This is explained further in Appendices 2.C and 2.D.

How do our far field results fare in the light of previous studies of asymptotic decay in the RPM? Fig. 2.3.5 attempts to address this question. We display the decay lengths calculated using different bulk IET, namely the GMSA [61] and the hypernetted chain approximation (HNC) [59, 60] and we present these in ranges for which we believe we can extract reliable numerical results from figures in the published papers. The Z decay length obtained from our simulations follows the theoretical predictions quite well at small values of $d\kappa_D$. Note that the HNC results from Ennis et al. focused on this regime where this closure is expected to yield very accurate (bulk) decay lengths. Comparing Kirkwood points, it is important to note that the crossover value is universal within the MSA for the RPM: $\mathcal{X}_K^{IET} \approx 1.229$. This is not the case within HNC where there is a very weak dependence on d . In the HNC results that we display in Fig. 2.3.5, Attard [59] used the same diameter as we used, $d = 0.5$ nm, while Ennis et al. [60] report results for $d = 0.46$ nm. The numerical values determined from HNC for Kirkwood crossover are very close to each other, i.e. Attard [59] found $\mathcal{X}_K \approx 1.3$ and Ennis et al. [60] found $\mathcal{X}_K \approx 1.293$, which should be compared to the MSA/GMSA value $\mathcal{X}_K^{MSA} \approx 1.229$, and our simulation result $d\kappa_D \approx 1.37$. Note that the original Kirkwood theory gives a value $\mathcal{X}_K = 1.03$ while the Modified Poisson Boltzmann theory [91] yields $\mathcal{X}_K = 1.241$.

Locating the crossover for N decay is arguably more delicate as this depends on incorporating properly hard-core correlations alongside any residual effects arising from the (net) electrostatics. GMSA and HNC theories attempt this. It is straightforward to show that the location of the FW point, as a function of $d\kappa_D$, is not universal. Using the MSAC

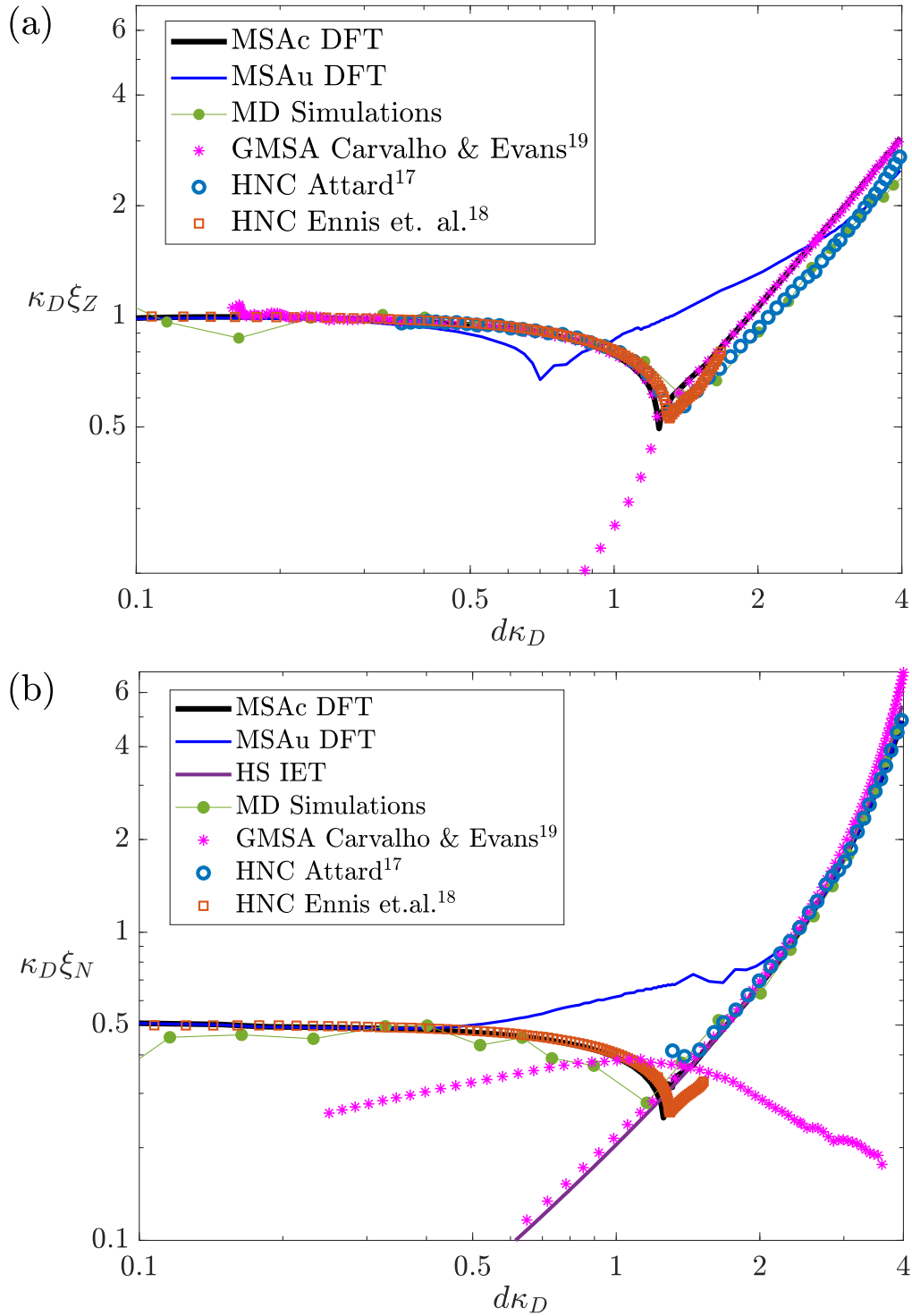


Figure 2.3.5: The decay lengths obtained from different theories are compared with simulation results for the bulk decay lengths (green dots). In (a) the Z decay length obtained from our DFT calculations of one-body profiles (solid lines) are shown along with the bulk decay lengths obtained using the GMSA from Carvalho & Evans Ref. [61] (purple asterisks), the HNC from Attard [59] (blue circles) and the HNC from Ennis et al. [60] (orange squares). In (b) the N decay length from the same sources, but also including the result from the HS IET (solid purple line).

functional, we found crossover at $\chi_{FW}^{MSAc} \approx 1.26$; see Fig. 2.3.5(b). Using the (bulk) HNC, Ennis et al. [60] (their Fig. 6) found crossover to oscillatory decay at $\chi_{FW}^{Ennis} \approx 1.52$. From Fig. 5(a) of Attard [59] we can deduce a value of $\chi_{FW}^{Attard} \approx 1.46$. In their pole analysis of the GMSA Carvalho and Evans found $\chi_{FW}^{GMSA} \approx 1.41$. Note, however, the GMSA predicts values of $\xi_{N\kappa_D} \ll 1/2$ for small values of $d\kappa_D$. This defect of the GMSA is elaborated upon in Appendix 2.C. Our MD simulation results shown in Figs. 2.3.3 and 2.3.5 indicate crossover at a value of $d\kappa_D$ similar to that obtained from MSAC.

We remark that Attard, using HNC, and Carvalho and Evans, using GMSA, locate the point at which the N decay length becomes larger than the Z decay length; this occurs near $d\kappa_D \approx 3.0$ in both theories. The significance of this crossover will become clear in the next subsection.

2.3.2.3 Asymptotic Decay of the Solvation Force

In light of the recent experimental surface force measurements [34, 35, 36, 37] that report long decay lengths, it is important to enquire what our DFT results predict for the decay length of the solvation force for a RPM electrolyte confined between two planar electrodes, separated by a distance H . The solvation force, see for instance Ref. [92], is defined formally by

$$f_s(H) = - \left. \frac{\partial \gamma(H)}{\partial H} \right|_{T, \mu, \Phi_0}, \quad (2.53)$$

evaluated at fixed temperature T , chemical potential μ and surface potential Φ_0 . Here $\gamma = (\Omega + pV)/A$ is the surface tension, defined as the excess over bulk grand potential per unit area of the confined liquid. Here, A denotes the area of the electrodes, $V = AH$ is the accessible volume and p is the bulk pressure, fixed by the reservoir chemical potential and temperature. The excess pressure due to confinement $f_s(H)$, is related directly to the force measured in SFA experiments. It is not immediately obvious that the asymptotic, large H , decay of this thermodynamic quantity should be given by the same singularities that determine the asymptotic decay of the bulk pair correlation functions and of the one body density profiles. That this is the case, has been discussed by several authors, e.g. see Refs. [81, 82, 83, 84, 85]. The basic argument is that the potential of mean force between two big (spherical) solute particles immersed at infinite dilution in a reservoir of small 'solvent' particles must, for large centre to centre separations H , decay with the same (exponential) decay length and period of oscillations (when the ultimate decay is oscillatory) as determined by the decay of the bulk pair correlation function in the small 'solvent'. For the RPM the ions constitute the small 'solvent' in this analysis. Allowing the radius of the big solute particle to become infinite we recover the case of two planar walls and then the potential of mean force yields the solvation force, or excess pressure. Since we have calculated the (bulk) charge and number decay lengths as a function of concentration, and examined the competition between these, we know the ultimate decay of the (thermodynamic) solvation force for each concentration. We denote the corresponding length scale as ξ , which repres-

ents the true correlation length in the liquid. The upshot is that the solvation force should decay as

$$f_s(H) \propto \cos(2\pi H/\lambda + \varphi)e^{-H/\xi}, \quad H \rightarrow \infty, \quad (2.54)$$

where ξ is the longest decay length in the system. In an oscillatory asymptotic regime, λ is the wavelength of the slowest decaying (pole) contribution and φ a non-universal phase shift.

The decay length ξ extracted from changing the planar distance H from 2.5 to 40 nm at various (dimensionless) concentrations $d\kappa_D$ is presented in Fig. 2.3.6, where we used the MSAC functional to calculate the grand potential. For low concentrations $d\kappa_D < 3.2$, ξ is determined by the charge density decay ξ_Z , while for higher concentrations, $d\kappa_D > 3.2$, ξ_N is longer. It is important to compare with results for bulk correlation lengths. From the HNC [59] and from the GMSA [61] calculations one finds this crossover occurs at $d\kappa_D \approx 3.0$, which is quite close to our DFT value. The decay length, ξ_{exp} , that can be measured in an SFA experiment, at large plate separations H , should be the largest decay length in the confined liquid (the physical system), i.e. $\xi_{\text{exp}}(d\kappa_D) = \max_a \xi_a(d\kappa_D)$ where in our case $a \in \{Z, N\}$.

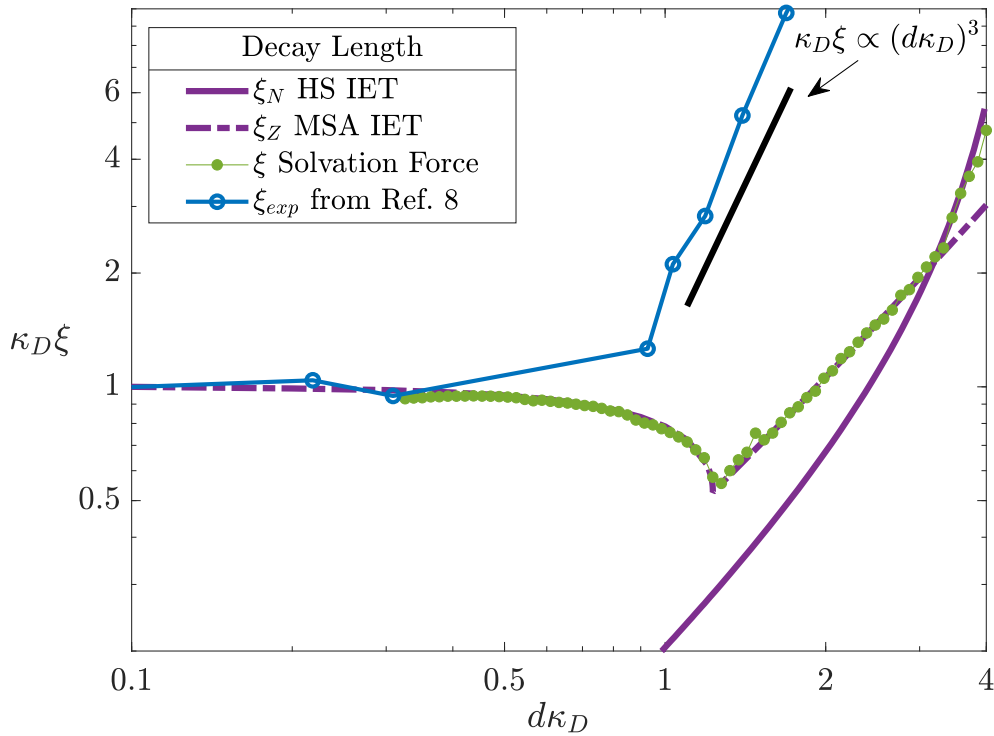


Figure 2.3.6: The decay length ξ (green circles) of the solvation force obtained by measuring the grand potential of the electrolyte, calculated from the MSAC functional, see Eqs. (2.53) and (2.54), as a function of the distance H between two identical planar electrodes, for various bulk concentrations $d\kappa_D$. ξ is the larger of the charge (dashed-dot purple) and the total number (solid purple) decay lengths from IET. The latter predict a cross-over, near $d\kappa_D \approx 3.1$, from longest-ranged decay governed by ξ_Z to that governed by ξ_N . The experimental data (blue dots connected by a blue line) is for an aqueous NaCl electrolyte extracted from Ref. [37], and the black line indicates the often-cited power law $\xi \kappa_D \propto (d\kappa_D)^3$.

In Fig. 2.3.6 we also plotted in blue symbols the experimental results from Ref. [38] for NaCl dissolved in water. Clearly, the decay lengths extracted from the SFA experiments are very different from those calculated for the RPM, except at very low concentrations. Interestingly, the decay length ξ_{exp} measured for $d\kappa_D > 1$ follows the power law $\kappa_D \xi \propto (d\kappa_D)^3$ as reported and emphasized in Refs. [37, 38, 93, 94, 95, 96, 97]. This behavior is depicted by the black line in the figure and is argued to be ‘universal’, i.e. it describes a broad range of electrolytes and ionic liquids. This ‘universal’ power law is not found within the RPM.

2.4 SUMMARY AND DISCUSSION

In this chapter we investigate the one- and two-body correlation functions of the RPM, a model electrolyte composed of equal-sized charged spheres of equal but opposite valency dissolved in a dielectric continuum with a Bjerrum length that is 1.46 times larger than the ionic diameter –these parameters are chosen to mimic an aqueous electrolyte with monovalent ions, e.g. KCl, at room temperature. Using integral equation theory (IET), density functional theory (DFT), and molecular dynamics (MD) simulations, we focus on the asymptotic (far-field) decay of the correlation functions for a large range of ionic concentrations that extends from the very dilute regime where the Debye-Hückel limiting law applies up to the regime where ionic hard-sphere packing dominates. The one-body density profiles are calculated for the RPM in contact with a planar electrode at a fixed potential difference between the electrode and the bulk electrolyte, whereas the two-body correlations pertain to a homogeneous bulk system. Our DFT calculations make predictions for the asymptotic decay of the solvation force between two charged planar surfaces immersed in the RPM. The solvation force is the quantity that relates directly to the experimental SFA measurements, where anomalously large decay lengths were observed at high salt concentrations, and which stimulated this study

We distinguish between number-number and charge-charge correlations, which are decoupled in the bulk RPM, where number-charge correlations are identically zero. The IET results for the decay of bulk pair correlations are based on two well-known direct correlation functions: the number-number combination uses the one obtained from fundamental measure theory (FMT) [47] and the charge-charge correlation function uses the one that stems from the mean-spherical approximation (MSA) [68, 69, 70]. In our DFT treatment we describe short-range repulsion in the RPM in terms of the FMT hard-sphere free-energy functional. We explore three different approximations to account for the electrostatic contributions to the free-energy functional, (i) the Poisson-Boltzmann-like mean-field expression (MFC) for the internal electrostatic energy, (ii) a correction to MFC that accounts for the finite-ion diameter by incorporating the MSA direct correlation function (MSAc) into the functional, and (iii) a further correction to MSAc that accounts for the correlation-induced MSA internal energy, termed MSAu. In the near-field, at distances of the order of the ion diameter, results from IET and all three versions of DFT agree reasonably well with those from MD although only the MSAu can account for the ionic depletion observed in the

number density profile calculated in simulations at low external electrode potentials; see Fig. 2.3.1. In contrast, in the far-field regime, i.e. for distances and separations much larger than the ion diameter, our IET and DFT results are mutually consistent apart from the MSAu implementation of DFT. It follows that employing a functional that yields optimal near-field performance does not guarantee the correct asymptotic behavior, crucial for interpreting SFA measurements. In Appendix 2.E, we also briefly compare the thermodynamic quantities, namely the adsorption and differential capacitance, showing the small differences between the MSA functionals and the large deviations with the MFC functional.

Two key results of our study are shown in Figs. 2.3.3 and 2.3.5. These concern the concentration dependence of the correlation lengths ξ_Z and ξ_N that dictate the asymptotic charge-charge and number-number decay lengths, respectively, and where we characterise the concentration in terms of the dimensionless quantity $d\kappa_D$. At low concentrations, $d\kappa_D < 0.5$, all the approaches we consider agree that ξ_Z is close to κ_D^{-1} and ξ_N is close to $\frac{1}{2}\kappa_D^{-1}$, except for the GMSA results for ξ_N . At very high concentrations, $d\kappa_D > 2$, we find good agreement between results from all the approaches apart from ξ_Z in MFC which, of course, takes its dilute-limit value κ_D^{-1} for all $d\kappa_D$. In this high concentration regime the structure of the RPM is dominated by steric repulsions rather than by Coulombic interactions. It follows that a DFT must incorporate properly hard-sphere correlations; this is not the case in MFC. In the intermediate concentration regime, $0.5 < d\kappa_D < 2$, we find some substantial differences between several of our approaches, especially for ξ_N . This increases (MSAu), or decreases and then increases (MSAc), or stays constant (MFC) as the concentration increases. For ξ_N the MSAc functional performs best, when compared to our MD simulations but also when compared to IET results from earlier studies [59, 60, 61]. For ξ_Z , the MSAc results agree quite well with those of the MD simulations, although at concentrations above the Kirkwood point it slightly overestimates the charge decay length. Overall, the MSAc results agree very well with those of HNC calculations in the range $0.5 < d\kappa_D < 1.5$ where we could extract reliable numbers from Ref. [60]. A very recent paper [98] introduced some new modifications/extensions of DH theory which make predictions for decay lengths. As far as we can tell, these are not significantly different from the results we present here.

Although our focus was on the RPM throughout, we also performed PM calculations (not reported here) with various ionic valency and diameter asymmetries. The resulting asymptotic decay properties are very similar to those of the RPM reported here. We find no long decay lengths, in line with what was reported in Ref. [95].

The third key result, that connects with the SFA experiments, is presented in Fig. 2.3.6. This shows the (true) decay length ξ that characterises the decay of the solvation force as obtained from Eqs. (2.53) and (2.54) using the excess grand potential determined from the MSAc functional. We find that for each concentration $\xi = \max(\xi_Z, \xi_N)$. There is excellent agreement between ξ and ξ_Z from MSA-based IET up to concentrations $d\kappa_D \approx 3$, and between ξ and ξ_N from IET for hard spheres (FMT) at higher concentrations. Given the good agreement between MD simulations and DFT/IET for ξ_Z at low concentrations and

ξ_N at high concentrations, we are confident that our MSAc findings for ξ in the RPM are reliable, at least for our parameter choice $T^* = d/\lambda_B = 0.685$. Recall this choice describes a typical 1:1 aqueous electrolyte at room temperature. However, turning to the experimental data, the decay length in aqueous NaCl as presented in Fig. 2.3.6 is vastly different from our theoretical predictions. The huge difference between the experimental results and those for the RPM is illustrated by comparing at 4.93 M NaCl concentration, where $d_{exp}\kappa_D^{exp} \approx 2.2$ (using $d_{exp} = 0.294$ nm and $\epsilon_r = 78$ instead of the concentration dependent ϵ_r used in Ref. [37]). One finds $\kappa_D^{exp}\xi_{exp} \approx 24$ in the experiment [37] whereas our RPM results predict $\kappa_D\xi \approx 2.3$. The difference is about a factor 10, and is larger at higher concentrations. This cannot be explained easily by some degree of arbitrariness in the exact definition of the ionic diameter, the slightly different size of sodium and chloride ions, or the small change of the dielectric constant at concentrations beyond say 2M NaCl from that of pure water; such considerations might allow at most a factor of 2 or so. Moreover aqueous NaCl is not special. A great variety of ionic systems has been investigated experimentally in recent years using SFA or closely related techniques [37, 38, 93, 94]. These include aqueous LiCl, KCl, CsCl, but also several ionic liquid solutions in a particular solvent, as well as pure (room temperature) ionic liquids. As mentioned in Sec. IV B.3, the experimental correlation lengths (scaled as we scale Fig.2.3.6) appear to fall on top of the result for NaCl. The empirical ‘universal’ scaling relation $\kappa_D\xi \propto (d\kappa_D)^3$ for $d\kappa_D > 1$ actually extends way beyond the scale of Fig.2.3.6, up to data points for ionic liquids at $d\kappa_D \approx 7$ where $\kappa_D\xi \approx 120$. From the SFA measurements one might conclude that the measured correlation length in concentrated electrolytes and ionic liquids is at least an order of magnitude larger than our RPM predictions. It is important to recognize that the large correlation lengths were measured at separations of several nanometers in the SFA experiments [37]. At shorter separations, an additional *structural* decay length was measured [99], which is much shorter. Although our DFT calculations find no indication of a long decay length, and we measure across 8 decades, we cannot rule out the possibility of a large decay length, buried in the noise that sets in beyond about three decades in our MD results.

The full story is more subtle. There is good reason to reconsider earlier work on molten alkali halides, conventionally regarded as archetypal ionic liquids. Of course, these salts have high melting temperatures, making experiments difficult. Nevertheless, it is well known that the RPM accounts well for the main features of the partial structure factors of molten salts such as KCl or NaCl where cations and anions have similar size [42]. Careful neutron (isotopic substitution) diffraction experiments [100] for molten NaCl at 1093 K extracted the three partial structure factors from which the total pair correlation functions $h_{ij}(r)$ can be obtained by Fourier Transforming. Fitting the resulting data to formulae equivalent to the mixture generalization of Eq. (2.41), decay lengths for the partial (and thus the total number and charge correlation functions) were determined, along with accompanying wavelengths. At this temperature, not far above the melting point, the longest decay length observed is about 0.46 nm, i.e. < 2 ionic diameters. There is no indication of a long decay length. Also pertinent are MD simulations for NaCl from Keblinski et al. [101]

These employ a symmetrized version of the standard Born-Mayer-Huggins potentials for alkali halides, i.e. the anion-anion and the cation-cation potentials are identical, mimicking the symmetry of the RPM. Data were analyzed using a mean diameter of $d = 0.276$ nm. Key observations from this far-reaching study are: i) for fixed, very high temperature well above the critical temperature, which is slightly below 3000 K in their model, the authors find (Kirkwood) crossover between monotonic and oscillatory decay of charge correlations at $d\kappa_D \approx 1.4$, a value that does not depend much on their choice of (high) temperature. This scenario is predicted within the MSA for the RPM, where the Kirkwood line is universal, and is almost vertical in the $\rho^* - T^*$ plane; see Fig. 1 of Ref. [61]. ii) Keblinsky et al. find crossover between monotonic and oscillatory decay of the total number correlations at fixed $T = 3000$ K. Although they do not locate the crossover density precisely, the broad range identified brackets the FW crossover density predicted by the GMSA; see Fig. 1 of Ref. [61]. iii) Most importantly, at all state points away from the critical point, the decay lengths reported in [101] are short, i.e. $< 2d$.

2.5 CONCLUSION

Our main conclusion, which, of course, also relies upon significant previous literature on bulk decay lengths, is that the (R)PM in equilibrium cannot explain the experimental (SFA) measurements reporting an anomalously large decay length of the solvation force in concentrated electrolytes and certain ionic liquids. This is in line with findings reported in less idealized models, e.g. Refs. [32, 33, 95, 96]. Perhaps this inability to explain the experimental observation is not too surprising when addressing room temperature ionic liquids with non-spherical ions that contain organic rings and tails etc. It is more disconcerting in the case of aqueous alkali halide solutions. We distinguish here between the model (the RPM in thermodynamic equilibrium) and the method used to analyse it (DFT, IET, MD). Given that the various theories and simulation methods mutually agree on their predictions for the longest correlation length ξ , the source of the discrepancy must lie in the model. The RPM seems to lack a crucial ingredient to explain the experimental findings. Assuming the experiments pertain to equilibrium, the key question is ‘Which piece of physics is missing?’ Before addressing this question, we emphasize once again that careful experimental (neutron diffraction) [100] and simulation studies [101] of the bulk pair correlation functions in molten NaCl, an archetypal ionic liquid, find no evidence for a long decay length. More specifically, we find that the MD results of Keblinsky et al. for a Born-Mayer-Huggins model of molten NaCl at $T = 10000$ K and $T = 50000$ K agree qualitatively with our RPM results for all concentrations and quantitatively (within 15%) for concentrations exceeding the Kirkwood point. For example, for $T = 10000$ K these authors report at $d\kappa_D = 3.1$ (using their $d = 0.276$ nm) a decay length $\xi\kappa_D \approx 1.7$, see their Fig. 8, whereas we report $\xi\kappa_D \approx 2$.

Noting that we have already pointed out that asymmetries of the ionic valencies and diameters yield decay lengths very similar to those of the RPM, the first possible candidate to explain the discrepancy between predictions from the (R)PM and the SFA meas-

urements is the description of the solvent as a (uniform) dielectric continuum. However, recent computer simulations and theories for several electrolyte models that include the solvent explicitly also find decay lengths, measured at high ionic concentrations, of the order of the particle diameter. A broad range of models is considered: the solvent is either modeled as a hard-sphere fluid [95, 96], or as the SPC/E model for water [32, 33] in the case of aqueous alkali halides. For the ionic liquids, models of organic solvents such as dimethoxyethane-dioxolane [33] or racemic propylene-carbonate [32] are considered. Although these explicit-solvent models show an increase of the longest correlation length at high concentrations, the observed increase is very similar to the one we find here for the RPM. We conclude that current treatments of solvent effects changes little the primitive model predictions of decay/correlation lengths that are about an order of magnitude smaller than measured in SFA experiments.

Another obvious candidate is the omission of polarizability; this is absent completely in the RPM and is, at best, included approximately in some of the explicit-solvent models. An interesting approach was put forward by Kjellander [98, 102, 103], who shows that electrostatic screening and the static dielectric function $\varepsilon(k)$, with wave-number k , are intimately coupled, such that the long-wavelength limit $\varepsilon(0)$ equals the static dielectric constant only in the absence of ions, e.g in dipolar fluids or non-electrolytes, but not in their presence. The upshot is that in an electrolyte, the screening and the dielectric response cannot be disentangled [102]. To best of our knowledge, there are no specific predictions for decay lengths that might be tested quantitatively against experimental results. Polarizability also leads to fluid-fluid and fluid-wall dispersion forces, giving rise to a power-law decay of the solvation force [104]. Although dispersion forces are long-ranged, we expect these to be relatively weak such that they become manifest in the solvation force only beyond separations of many particle diameters, for instance beyond $15d$ for the (reasonable) parameters of Ref. [104].

Of course, there are other factors that could account for the disagreement between results of theory and simulation on the one hand and SFA experiments on the other. Strictly speaking, there is a possibility that the measured long decay length could just be buried in the noise of all our calculations and all simulation studies [32, 33], although for instance the simulations of Ref. [32] show statistics that allow observation of decay over as many as five decades before the signal disappears in the noise, and over eight decades in our DFT calculations. Significantly, the variety and number of experimental systems studied, along with the apparent success of the empirical power law scaling mentioned earlier, suggest there should be a *general*, rather than a materials specific, explanation of the difference. Our present contribution, which establishes the consistency of results from DFT, IET and MD for the RPM, makes very clear why it is important to understand the origin of the difference. We conclude by re-emphasizing: the large decay length measured in SFA experiments, for a variety of concentrated electrolytes and several room temperature ionic liquids, cannot be accounted for by primitive electrolyte models. New physical ingredients and/or new interpretations of the experiments are required in order to understand the recent SFA results.

APPENDIX

2.A MEAN SPHERICAL APPROXIMATION

In the bulk, the direct correlation function of a primitive model electrolyte with ionic diameters d_j and valency z_j , $\Delta c^{MSAc}(r)$, is given by [67]

$$\Delta c_{ij}^{MSAc}(r, \{\rho_b\}) = \begin{cases} c_{ij}^{MSAsh}(r, \{\rho_b\}) + z_i z_j \frac{\lambda_B}{r}, & 0 \leq r \leq \Delta d_{ij}; \\ c_{ij}^{MSAl}(r, \{\rho_b\}) + z_i z_j \frac{\lambda_B}{r}, & \Delta d_{ij} < r \leq d_{ij}; \\ 0, & r > d_{ij}; \end{cases} \quad (2.55)$$

where $\Delta d_{ij} = |d_i - d_j|/2$ and $d_{ij} = (d_i + d_j)/2$. For $d_i < d_j$ the first term for short (sh) separations reads

$$c_{ij}^{MSAsh}(r; \{\rho_b\}) = 2\lambda_B \left[z_i N_j + d_i \zeta \left(X_i + \frac{1}{3} d_i^2 \zeta \right) \right], \quad (2.56)$$

with

$$X_j = \frac{z_j - d_j^2 \zeta}{1 + Y d_j}; \quad (2.57)$$

$$N_j = \frac{X_j - z_j}{d_j}; \quad (2.58)$$

$$Y = \pi \lambda_B \sum_j \rho_{b,j} X_j^2; \quad (2.59)$$

$$\zeta = \frac{1}{H} \sum_j \frac{\rho_{b,j} d_j z_j}{1 + Y d_j}; \quad (2.60)$$

$$H = \sum_j \frac{\rho_{b,j} d_j^3}{1 + Y d_j} + \frac{2}{\pi} (1 - \eta_b). \quad (2.61)$$

The second term in Eq. (2.55) for the longer-ranged part (l) for $\Delta d_{ij} < r \leq d_{ij}$ is given by

$$c_{ij}^{MSAl}(r; \{\rho_b\}) = \frac{\lambda_B}{r} \left[A_{ij} + B_{ij} r + C_{ij} r^2 + F_{ij} r^4 \right]; \quad (2.62)$$

with

$$A_{ij} = -\Delta d_{ij}^2 \left[\zeta(X_i + X_j) + \zeta^2 d_{ij}^2 - N_i N_j \right], \quad (2.63)$$

$$B_{ij} = -(X_i - X_j)(N_i - N_j) - (X_i^2 + X_j^2)Y - 2d_{ij}N_i N_j + \frac{1}{3}\zeta^2(d_i^3 + d_j^3), \quad (2.64)$$

$$C_{ij} = -\zeta(X_i + X_j) + N_i N_j - \frac{1}{2}\zeta^2(d_i^2 + d_j^2), \quad (2.65)$$

$$F_{ij} = \frac{1}{3}\zeta^2. \quad (2.66)$$

These rather involved expressions become more tractable for the monovalent RPM, where $c_{ij}^{MSAsh}(r; \rho_b) = 0$, $\zeta = 0$ and $\Delta d_{ij} = 0$, such that

$$c_{ij}^{MSAl}(r; \rho_b) = \frac{\lambda_B}{r} \left[\left(-(X_i - X_j)(N_i - N_j) - 2X^2Y - 2dN_i N_j \right) r + N_i N_j r^2 \right], \quad (2.67)$$

which can be simplified by introducing $D = d + 1/Y$, so that with

$$X_j = \frac{z_j}{YD}, \quad (2.68)$$

$$N_j = -\frac{z_j}{D}, \quad (2.69)$$

one finds

$$c_{ij}^{MSAl}(r; \rho_b) = z_i z_j \frac{\lambda_B}{r} \frac{-2Dr + r^2}{D^2}. \quad (2.70)$$

For a planar geometry, one integrates out the planar coordinates, for which one needs the following relation for any positive a and b , and $k \neq -2$

$$\begin{aligned} & \int_{-\infty}^{\infty} dy \int_{-\infty}^{\infty} dz r^k \Theta(r-a) \Theta(b-r) \\ &= 2\pi \int_0^{\infty} du u (u^2 + x^2)^{k/2} \Theta(u^2 + x^2 - a^2) \Theta(b^2 - u^2 - x^2) \\ &= 2\pi \int_{|x|}^b dv v^{k+1} \Theta(|x| - a) \Theta(b - |x|) + 2\pi \int_a^b dv v^{k+1} \Theta(a - |x|) \Theta(b - |x|) \\ &= \frac{2\pi}{k+2} \left[\left(d^{k+2} - |x|^{k+2} \right) \Theta(|x| - a) + \left(b^{k+2} - a^{k+2} \right) \Theta(a - |x|) \right] \Theta(b - |x|), \end{aligned} \quad (2.71)$$

and apply it to each term in Eqs. (2.55), (2.56), and (2.62). In the first step, we used polar coordinates with $u^2 = y^2 + z^2$ and in the second step we made the substitution $v^2 = u^2 + x^2$.

2.B ADDING ELECTROSTATIC ENERGY TERMS TO THE FUNCTIONAL AND THE INCONSISTENCY OF THE MSAU

In this section we focus on the electrostatics part of the functional, especially on (the lack of) consistency between several routes one can take from a free-energy functional to thermodynamic and structural properties of the electrolyte. The pair direct correlation

functions obtained from the crudest MF/Poisson-Boltzmann treatment and from the MSA closure for the bulk RPM are such that the ionic valencies can be factored out so that $c_{ij}^{(2),ES}(r) = z_i z_j c^{ES}(r)$. Here $c^{ES}(r)$ depends on the closure but vanishes for $r \rightarrow \infty$. This structural form of the direct correlations can be reconstructed by considering second functional derivatives of an (electrostatic) excess free-energy functional of the form

$$\beta \mathcal{F}_{ex}^{ES,c}[\{\rho\}] = -\frac{1}{2} \int d\mathbf{r} \int d\mathbf{r}' \rho_Z(\mathbf{r}) c^{ES}(|\mathbf{r} - \mathbf{r}'|; \{\rho_b\}) \rho_Z(\mathbf{r}'), \quad (2.72)$$

where $\rho_Z = \sum_j z_j \rho_j = \rho_+ - \rho_-$. (Note that ρ_Z introduced in the main text was normalized w.r.t. the bulk density ρ_b). In a bulk system, where the profiles are constant and charge neutrality holds such that $\rho_Z = 0$, a functional of the form of Eq. (2.72) gives a vanishing electrostatic free energy. However, if we calculate the bulk pair direct correlation function $c_Z(r) = c_{++}^{(2),ES}(r) - c_{+-}^{(2),ES}(r) = 2c^{ES}(r)$ from Eq. (2.72), and use the OZ equation to find $h_Z(r)$, the electrostatic internal energy U^{ES} follows via the energy route as

$$\beta \frac{U^{ES}}{V} = 4\pi \lambda_B \rho_b^2 \int_0^\infty dr r h_Z(r). \quad (2.73)$$

The internal energy can then be used to obtain the Helmholtz free energy F^{ES} via the standard temperature or charging integration

$$\beta F^{ES}(\beta) = \int_0^\beta d\beta' U^{ES}(\beta'). \quad (2.74)$$

In the dilute limit the resulting reduced free energy density $\Phi^{ES} = \beta F^{ES}/V$ should reduce to the exactly known limiting law

$$\lim_{\{\rho_b\} \rightarrow 0} \Phi^{ES}(\{\rho_b\}) = -\frac{\kappa_D^3(\{\rho_b\})}{12\pi}, \quad (2.75)$$

which is manifestly non-zero. Hence, using the same $c^{ES}(r)$ in Eq. (2.72) we find, depending on the chosen route, either a vanishing or the correct (physical) non-zero bulk electrostatic free energy. Revisiting the original DH paper[31], or considering the exact expression given by Eq. (2.73), shows that one can interpret the internal energy U^{ES} as the sum of Coulomb energies of each ion with its surrounding screening cloud of ions of opposite sign. This is overall a negative energy contribution arising from the cohesive energy due to the Coulombic attraction between (relatively) nearby opposite charges that dominates over positive energy contributions from the repulsion between like charges at (relatively) large distances. In order to remedy the inconsistency between these two routes, one might consider including an additional term in the free-energy functional that takes the cohesive Coulomb energy into account explicitly, e.g.

$$\beta \mathcal{F}^{ESu}[\{\rho\}] = \int d\mathbf{r} \Phi^{ES}(\{\tilde{\rho}(\mathbf{r})\}), \quad (2.76)$$

where $\tilde{\rho}$ denotes a weighted density with an arbitrary weight function ω that does *not* depend on the bulk density. However, in order to retain consistency between the two

routes discussed above, such an additional term as written in Eq. (2.76) must be chosen such that it does not affect the bulk direct correlation function c_Z that enters the calculation of the charge correlation function h_Z from which the internal energy of Eq. (2.73) follows. This implies that the contribution to $c_Z(r)$ due to Eq. (2.76) must vanish, i.e.

$$-\beta \frac{\delta^2 \mathcal{F}_{ex}^{ESu}[\{\rho\}]}{\delta \rho_Z(\mathbf{r}) \delta \rho_Z(\mathbf{r}')} = 0, \quad (2.77)$$

Hence, $\Phi^{ES}(\{\tilde{\rho}\})$ may be at most linear in ρ_Z . If this is the case, then the sum of Eq. (2.72) and the additional Helmholtz free-energy contribution of Eq. (2.76) is consistent, when comparing the free energy that results from evaluating the resulting functional in bulk, with the one from the energy route leading to Eqs. (2.74) and (2.75). Moreover, if c_Z does not change by adding Eq. (2.76) to the free-energy functional, then the asymptotic decay of the charge-charge correlations also remains unchanged.

If we consider Eq. (2.75), and recognize that κ_D depends only on the total density $\rho_N = \rho_+ + \rho_-$ in the RPM, it is clear that including a contribution to the free-energy functional such as

$$\beta \mathcal{F}_{ex}^{ES,F}[\{\rho\}] = - \int d\mathbf{r} \frac{\kappa_D^3(\{\tilde{\rho}(\mathbf{r})\})}{12\pi} \quad (2.78)$$

does not breach electrostatic consistency. We found that minimizing the resulting functional actually accounts for the depletion observed in the number density profile in Fig. 2.3.1(a). Importantly, however, the MSAu functional that we used in the main text has a different structure as it depends not only on the number density but *also* on the square of the charge density. This can be ascertained by examining the MSAu contribution to the functional and write Eq. (2.34) as

$$\Phi_{RPM}^{MSA}(\tilde{n}_Z(\mathbf{r}), \tilde{n}_N(\mathbf{r})) = \vartheta_1(\tilde{n}_N(\mathbf{r})) + \vartheta_2(\tilde{n}_N(\mathbf{r}))\tilde{n}_Z^2(\mathbf{r}), \quad (2.79)$$

where $\vartheta_1(\tilde{n}_N)$ and $\vartheta_2(\tilde{n}_N)$ are functions of \tilde{n}_N and not of \tilde{n}_Z . The final term in this equation originates in the term proportional to η in Eq. (2.34). It follows that Φ^{ES} is quadratic in ρ_Z and will therefore breach consistency. This suggests that the MSAu functional, as implemented by Roth and Gillespie Ref. [71], appears to perform well for density profiles close to charged surfaces[73], but suffers from inconsistencies that dictate its (poor) performance in the far-field regime. In order to investigate further, we examined the MSAu functional for the case where $\eta(\{\tilde{n}(\mathbf{r})\}) = 0$ for all positions. Then ϑ_2 vanishes and we retrieve precisely the same asymptotic Z decay as from MSAC and IET. We note, however, any infinitesimal asymmetry in the ion sizes will cause the η term to reappear, creating the same issues. For these reasons we choose to work with a non-vanishing η , in line with Ref. [71], and our figures display results for this choice.

2.C DECAY OF THE DENSITY PROFILE VERSUS THAT OF THE BULK CORRELATION FUNCTION

We show that the asymptotic decay of the one-body density profile is determined by the asymptotic decay of the bulk pair correlation function. The Euler-Lagrange equation for a single species system is:

$$\rho(\mathbf{r}) = \rho_b \exp\left(-\beta V_{ext}(\mathbf{r}) + c^{(1)}(\mathbf{r}; [\rho]) - c_b^{(1)}\right), \quad (2.80)$$

with the one-body direct correlation function $c_b^{(1)} = c^{(1)}(\rho_b)$. We choose the external potential $V_{ext}(\mathbf{r})$ to correspond to a planar wall or to a big (spherical) solute, such that $V_{ext}(\mathbf{r}) \rightarrow 0$ as $\mathbf{r} \rightarrow \infty$, and $\rho(\mathbf{r}) \rightarrow \rho_b$, the bulk reservoir value. Asymptotically ($\mathbf{r} \rightarrow \infty$) the term in the exponential is small, which allows us to write

$$\rho(\mathbf{r}) = \rho_b \left(1 - \beta V_{ext}(\mathbf{r}) + c^{(1)}(\mathbf{r}; [\rho]) - c_b^{(1)}\right). \quad (2.81)$$

Noting that $c^{(1)}(\mathbf{r}; [\rho])$ is both a functional of ρ and a function of \mathbf{r} , we can expand this term around the bulk density to lowest order:

$$c^{(1)}(\mathbf{r}; [\rho]) = c_b^{(1)} + \int d\mathbf{r}' \left. \frac{\delta c^{(1)}(\mathbf{r}; [\rho])}{\delta \rho(\mathbf{r}')} \right|_{\rho=\rho_b} (\rho(\mathbf{r}') - \rho_b) \quad (2.82)$$

and write,

$$c^{(1)}(\mathbf{r}; [\rho]) - c_b^{(1)} = \int d\mathbf{r}' c^{(2)}(|\mathbf{r} - \mathbf{r}'|; \rho_b) \Delta\rho(\mathbf{r}'), \quad (2.83)$$

with density deviation $\Delta\rho(\mathbf{r}) = \rho(\mathbf{r}) - \rho_b$. The density deviation can then be expressed, in lowest order, as

$$\frac{\Delta\rho(\mathbf{r})}{\rho_b} = -\beta V_{ext}(\mathbf{r}) + \int d\mathbf{r}' c^{(2)}(|\mathbf{r} - \mathbf{r}'|; \rho_b) \Delta\rho(\mathbf{r}'). \quad (2.84)$$

We now suppose that $V_{ext}(\mathbf{r})$ is sufficiently smooth that its Fourier transform exists. Then

$$\frac{\Delta\hat{\rho}(k)}{\rho_b} = -\beta \hat{V}_{ext}(k) + \hat{c}^{(2)}(k; \rho_b) \Delta\hat{\rho}(k). \quad (2.85)$$

and the Fourier transform of the density deviation takes the simple form:

$$\Delta\hat{\rho}(k) = \frac{-\beta \hat{V}_{ext}(k) \rho_b}{1 - \rho_b \hat{c}^{(2)}(k; \rho_b)}. \quad (2.86)$$

Note that the Fourier transform, denoted by $\hat{\cdot}$, is three-dimensional. For the spherical solute, the structure of Eq. (2.86) is equivalent to that of the bulk OZ Eq. (2.39). In that case poles of the total pair correlation function $\hat{h}(k)$ are determined by the zeroes of $1 - \hat{c}^{(2)}(k; \rho_b) \rho_b$. Similarly the poles of the density deviation $\Delta\hat{\rho}(k)$ for a (large) solute are determined by the same zeroes. In practice, this means that we should consider model

fluids where the pair potential $u(r)$ is short-ranged, i.e. it should decay faster than power law and the potential $V_{ext}(r)$ should decay faster than power-law and, if this is exponentially decaying, should have a decay length that is shorter than the bulk correlation length of the liquid. This simple argument focuses on the poles. We do not address explicitly the case of branch point singularities.

An important limiting case is when the solute is made identical to a solvent particle. Then the one-body density profile $\rho(r) = \rho_b g(r) = \rho_b(1 + h(r))$, which is the famous Percus test particle result[105]. It follows that employing the test particle route within the framework of DFT must yield the same poles, where these dictate the decay, and therefore the same asymptotic decay length and wavelength, where pertinent, as those determined from the bulk OZ equation (2.39), with $\hat{c}^{(2)}(k; \rho_b)$ obtained from Eq. (2.4) in the homogeneous limit, see Refs. [106, 107].

Taking the limit of the radius of the spherical solute particle to infinity is fairly straightforward. Alternatively, one can impose planar geometry from the outset and perform appropriate Fourier transforms. The upshot is that one finds:

$$\rho(x) - \rho_b \propto A_w e^{-\kappa x} \cos(2\pi x/\lambda + \phi_w), \quad x \rightarrow \infty, \quad (2.87)$$

where κ and λ refer to the leading pole identified in Eq. (2.41), for $rh(r)$. The amplitude A_w and phase ϕ_w are not related to the corresponding quantities in Eq. (2.41). This argument is, of course, based on a linear response treatment of the asymptotics; it is close to that presented in Ref. [108].

The argument laid out above is deceptively simple. It implies that knowledge of the exact $c^{(2)}(r; \rho_b)$ is sufficient to determine the exact asymptotic decay of the one-body density profiles at a planar wall, and, indeed, of the solvation force for the liquid confined between two planar walls, provided the external potential is sufficiently short-ranged. In practice, one never has the exact $c^{(2)}(r; \rho_b)$ and it is not always clear what physics is omitted in employing an approximate $c^{(2)}(r; \rho_b)$. In one-component neutral fluids this is not a major issue, apart from state points very close to the (bulk) critical point where $c^{(2)}(r; \rho_b)$ develops power-law decay.

The situation is very different in ionic liquids where approximate IET's might omit crucial physics. For example, the MSA IET for the RPM decouples completely charge and number density correlations. The resulting $c_N^{(2)}(r; \rho_b)$, the pair direct correlation function for number-number correlations, is equal to $c_{HS}^{(2)}(r; \rho_b)$, the HS pair direct correlation function. This is why in the MSA IET the decay length ξ_N always takes the HS value and does not approach the correct value $\kappa_D \xi_N = 0.5$, appropriate in the dilute limit. The MSA is termed a linear approximation, because it neglects the coupling. Its generalization, the GMSA, is a different beast. The corresponding $c_N^{(2)}(r; \rho_b)$ is not simply equal to $c_{HS}^{(2)}(r; \rho_b)$, as there is some feedback from the charge correlations. This is why the GMSA results for ξ_N exhibit FW crossover, as illustrated in Ref. [61] and discussed in Sec. 2.3.2. However, the GMSA does not capture the correct low concentration limiting behaviour. In contrast, the Hypernetted Chain (HNC) IET is regarded as a fully non-linear theory. Here one finds $c_N^{(2)}(r; \rho_b)$ has a term that scales as $h_Z^2(r)$ (see e.g. Ref. [60]), not present in the MSA or

GMSA, that leads to the correct behaviour: $\kappa_D \xi_N \rightarrow 0.5$, in the dilute limit. Recall the HNC IET is known to be very accurate for the (bulk) RPM, across a variety of regimes [42].

Our DFT treatment of the asymptotics, see Appendix 2.D, works at the level of one-body direct correlation functions. The three treatments we implement are explicitly non-linear and capture crucial couplings. As one sees in Eq. (2.48), the number density profile $\rho_N(x)$ includes the term $\rho_Z^2(x)$, which is analogous to the HNC closure for the bulk.

2.D ANALYSING THE EULER LAGRANGE EQUATIONS IN THE FAR FIELD

We consider again the one-body profiles for the RPM in a planar geometry, as given by the self-consistency relations

$$\rho_{\pm}(x) = \rho_b \exp \left[-\beta V_{ext}(x) + c_{\pm}^{(1)}(x) - c_{\pm,b}^{(1)} \right], \quad (2.88)$$

where subscript b denotes bulk. We assume a short-ranged external potential V_{ext} that is the same for both species. The one-body direct correlation functions $c_{\pm}^{(1)}(x)$ depend on the underlying functional. For the RPM, this will be of the form

$$c_{\pm}^{(1)}(x) = \pm c_1(x) + c_2(x), \quad (2.89)$$

where distinction has been made between terms that are proportional to the valency and those that are not. Typically, $c_1(x)$ has the form

$$c_1(x; [\rho_Z, \rho_N]) = \int dx' \rho_Z(x') c^{ES}(|x - x'|; [\rho_N]), \quad (2.90)$$

where $\rho_Z = (\rho_+ - \rho_-)/\rho_b$ and $\rho_N = (\rho_+ + \rho_-)/\rho_b - 2$ are the charge and (excess) number densities as defined in the main text, and $c^{ES}(x)$ has its origin in electrostatics. For the MFC and MSAC functionals $c^{ES}(x)$ is independent of $\rho_N(x)$. However, this is not the case for the MSAu functional due to the final term in Eq. (2.79). Nevertheless, the predominant contribution to $c_1(x)$ comes from ρ_Z . The other term $c_2(x)$ in Eq. (2.89) has its origin solely in the steric (HS) repulsions for both the MFC and MSAC. In the case of the MSAu there is an additional term from the derivative of Φ^{MSA} w.r.t density. Generally we can write

$$c_2(x; [\rho_N, \rho_Z]) = - \int dx' \sum_{\alpha} \frac{\partial \Phi(\{\tilde{n}_{\alpha}\})}{\partial \tilde{n}_{\alpha}}(x') w_{\alpha}(|x - x'|), \quad (2.91)$$

where the free energy density Φ contains both the FMT contribution [47] as well as possible others, such as the MSAu term Eq. (2.34) or that from Φ^{ES} introduced in the previous Appendix Eq. (2.75), and the sum is over all weighted densities α with corresponding weight function w_{α} .

Using Eqs. (2.88) and (2.89), the Euler Lagrange equations for ρ_Z and ρ_N read

$$\rho_Z(x) = 2 \exp[-\beta V_{ext}(x) + \Delta c_2(x; [\rho_N, \rho_Z])] \sinh(\Delta c_1(x; [\rho_Z, \rho_N])), \quad (2.92)$$

$$\rho_N(x) = 2 \exp[-\beta V_{ext}(x) + \Delta c_2(x; [\rho_N, \rho_Z])] \cosh(\Delta c_1(x; [\rho_Z, \rho_N])) - 2, \quad (2.93)$$

where $\Delta c_i(x) = c_i(x) - c_{i,b}$, $i \in \{1, 2\}$. In the far field, $x \rightarrow \infty$, the quantities $\Delta c_i(x)$ are small and βV_{ext} vanishes, which allows us to expand Eqs. (2.92) and (2.93) as

$$\rho_Z(x) \approx 2\Delta c_1(x; [\rho_Z, \rho_N]), \quad (2.94)$$

$$\begin{aligned} \rho_N(x) &\approx 2\Delta c_2(x, [\rho_N, \rho_Z]) + \Delta c_1(x; [\rho_Z, \rho_N])^2, \\ &= 2\Delta c_2(x, [\rho_N, \rho_Z]) + \frac{1}{4}\rho_Z(x)^2, \end{aligned} \quad (2.95)$$

where in the last line we substituted ρ_Z for $2\Delta c_1$. This asymptotic representation of the charge and number density profiles contains important information. First we consider the case where $c_1(x; [\rho_Z])$ depends on the charge density only, which holds for the MFC and MSAC functionals. Then, to lowest order, ρ_Z does not depend on ρ_N , consistent with the notion that charge is (essentially) decoupled from the number density in the RPM. However, the expression for $\rho_N(x)$ contains the $\rho_Z(x)^2$ term. We consider first the situation where $c_2(x; [\rho_N])$ does not depend on the charge density, as is the case for the MFC and MSAC functionals. Then from Eqs. (2.94) and (2.95) we find the leading asymptotic behavior to be

$$\rho_Z(x) = A e^{-x/\xi_Z} \quad (2.96)$$

$$\rho_N(x) = B \cos\left(\frac{2\pi}{\lambda_{FMT}} x\right) e^{-x/\xi_{FMT}} + C e^{-2x/\xi_Z}, \quad (2.97)$$

as $x \rightarrow \infty$. Here ξ_{FMT} and λ_{FMT} denote, respectively, the decay length and the wavelength for a pure hard-sphere system treated by FMT, ξ_Z is the charge decay length and A, B, C are constants. These results pertain to concentrations below any Kirkwood point, where $\rho_Z(x)$ is monotonically decreasing. In this case, the ultimate decay length ξ_N of $\rho_N(Z)$ depends on whether $\xi_Z/2$ is larger or smaller than ξ_{FMT} . Fig. 2.3.3 illustrates the variation of ξ_{FMT} and ξ_Z with concentration $d\kappa_D$. At small concentrations, $\xi_Z/2$ is the larger length scale, and in the dilute limit $\kappa_D \xi_N = 0.5$. For concentrations above the Kirkwood point, where $\rho_Z(x)$ acquires an oscillatory factor; there is intricate competition between the two length scales. At sufficiently high concentrations ξ_{FMT} will dictate the asymptotics.

In the second situation, where c_1 and c_2 depend both on the charge and number density profiles, as is the case for the MSAu functional, a stronger coupling between the charge and number density profiles emerges. The resulting MSAu decay lengths differ markedly from those from MSAC, IET and simulation results for concentrations between $0.5 < d\kappa_D < 2$ (see Fig. 2.3.3), suggesting the coupling is not treated correctly in the MSAu. In particular, $\kappa_D \xi_N$ from the MSAu increases with $d\kappa_D$ in this range, see Fig. 2.3.3(b). Note that in the limit of low concentration and of high concentration, $\kappa_D \xi_N$ from the MSAu does approach the correct behavior. As mentioned previously in the text and in Appendix 2.B, one could

consider an MSAu functional that sets $\eta(\{\tilde{n}(\mathbf{r})\}) = 0$. For this choice we recover the same asymptotic Z decay as with MSAc. With this choice $c_1(x)$ is the same for both MSAc and MSAu. In sharp contrast, we found that the N decay length changes very slightly by setting $\eta(\{\tilde{n}(\mathbf{r})\}) = 0$. This is because the ϑ_2 term in Eq. (2.79), which is proportional to η , is subordinate to ϑ_1 . Hence, omitting ϑ_2 barely influences $\Delta c_2(x)$ and therefore barely influences Eq. (2.95), thereby leaving almost no mark on the N decay length. To conclude, setting $\eta(\{\tilde{n}(\mathbf{r})\}) = 0$ in Eq. (2.34) influences only the charge density profiles, leaving the number density profiles almost unchanged. However, we decided not to follow this choice in presenting our results as the procedure cannot be applied generically: breaking any symmetry in the ionic system (changing either their size or valency) will generate a non-vanishing η in the bulk. We follow Ref. [71] and retain $\eta(\{\tilde{n}(\mathbf{r})\})$.

2.E THERMODYNAMICS OF THREE FUNCTIONALS

Let us also compare some of the thermodynamic quantities that are provided by the three functionals. To this end, we consider the adsorption and the differential capacitance. In principle we could also consider the sum rule for the pressure p of the bulk,

$$\beta p = \sum_j \rho_j (d_j^+ / 2) - 2\pi \lambda_B \sigma^2, \quad (2.98)$$

where σ denotes the number elementary charges per unit area of the planar wall. However, it turns out that all the functionals we consider satisfy this sum rule and are thus internally consistent in respect. Note that only the MSAu functional gives a finite electrostatic contribution to the bulk pressure, due to the inclusion of the cohesive energy term. Henceforth, we thus focus on the adsorption and the capacitance instead.

The adsorption Γ_j , which is the excess number of particles of species j per unit area compared to a bulk system, is given by

$$\Gamma_{\pm} = \int_{R_{\pm}}^{\infty} dx [\rho_{\pm}(x) - \rho_b], \quad (2.99)$$

assuming that large-enough systems such that the density profile converges to its bulk value. It is useful to consider the charge adsorption $\Gamma_Z = \Gamma_+ - \Gamma_- = -\sigma$ (due to global charge neutrality) and the number adsorption $2\Gamma_N = \Gamma_+ + \Gamma_-$. The latter is related to the surface tension γ by

$$\Gamma_N = - \left(\frac{\partial \gamma}{\partial \mu} \right)_{T,V} \quad (2.100)$$

with $\mu_+ + \mu_- \equiv 2\mu$, which is also related to the grand potential functional according to $\Omega[\{\rho\}] = -pV + \gamma A$ where A is the surface are of the wall. The adsorption for surface potentials of 1 mV (solid) and 100 mV (dashed-dot) is plotted in Fig. 2.E.1(a) as function of the bulk concentration c in M on the upper axis and as function of $d\kappa_D$ on the lower axis,

where the color coding and linetypes are also given in Fig. 2.E.1(b). The inset shows the depletion of ions near the surface (negative Γ_N), which can only be captured by including the self-energy of the ions in the electrolyte; only the MSAu functional displays this feature. However, this effect is always apparent when one considers a functional that includes the self-energy of the ions, even when using only the limiting law Eq. (2.13), e.g. functionals of the form in Eq. (2.78), which results are not shown here. Surprisingly, the depletion effect is present up to quite high concentrations for low surface potentials, but is non-existent when applying a larger surface potential (dashed-dot). Overall, for low surface potentials there is very little difference between the adsorption from the different functionals, except for the depletion, but at high surface potential the MFC functional differs substantially from MSA functionals. Hence, the direct correlation function plays an important role for the adsorption at high surface potentials, which is also apparent from Fig. 2.3.1.

In the same density c and $d\kappa_D$ representation, the ratio between the surface charge and the surface potential σ/ϕ_0 is plotted in Fig. 2.E.1(b). The results are compared to those of Debye-Hückel theory, which is only accurate for low concentrations and surface potentials as is readily observed. The two curves for the MFC functional are almost identical, while the curves from the MSA functionals - which are quite different from the MFC - show qualitative different behavior depending on the surface potential. The differences between the MSA functionals are small.

Another relevant thermodynamic quantity, which will be the topic of the next two chapters, is the differential capacitance

$$C_\mu = \left(e^2 \beta \frac{\partial \sigma}{\partial \phi_0} \right)_{T,\mu}. \quad (2.101)$$

It is a measure for the amount of energy that can be stored inside the EDL per unit area A , but it is also a measure for the structural change of the EDL near the charged surface when changing the surface potential, as we will see in Chapter 4. Although in Chapter 4 the differential capacitance will be analyzed in more detail, let us here simply compare this quantity for the three functionals considered throughout this chapter for concentrations $d\kappa_D = 0.3, 2.96, 4.19$, and present them in Fig. 2.E.1(c). All three functionals exhibit the so-called camel- to bell crossover, but the MFC functional distinguishes itself by having a lower maximum at larger surface potentials in comparison with the other two MSA functionals. The only real agreement between all the three functionals is found for low concentrations ($d\kappa_D = 0.30$), and low surface potentials ($\phi_0 < 2$). For intermediate and higher concentrations, the MFC and MSA functionals disagree for all surface potentials, while the MSA functionals give qualitatively the same results for all concentrations.

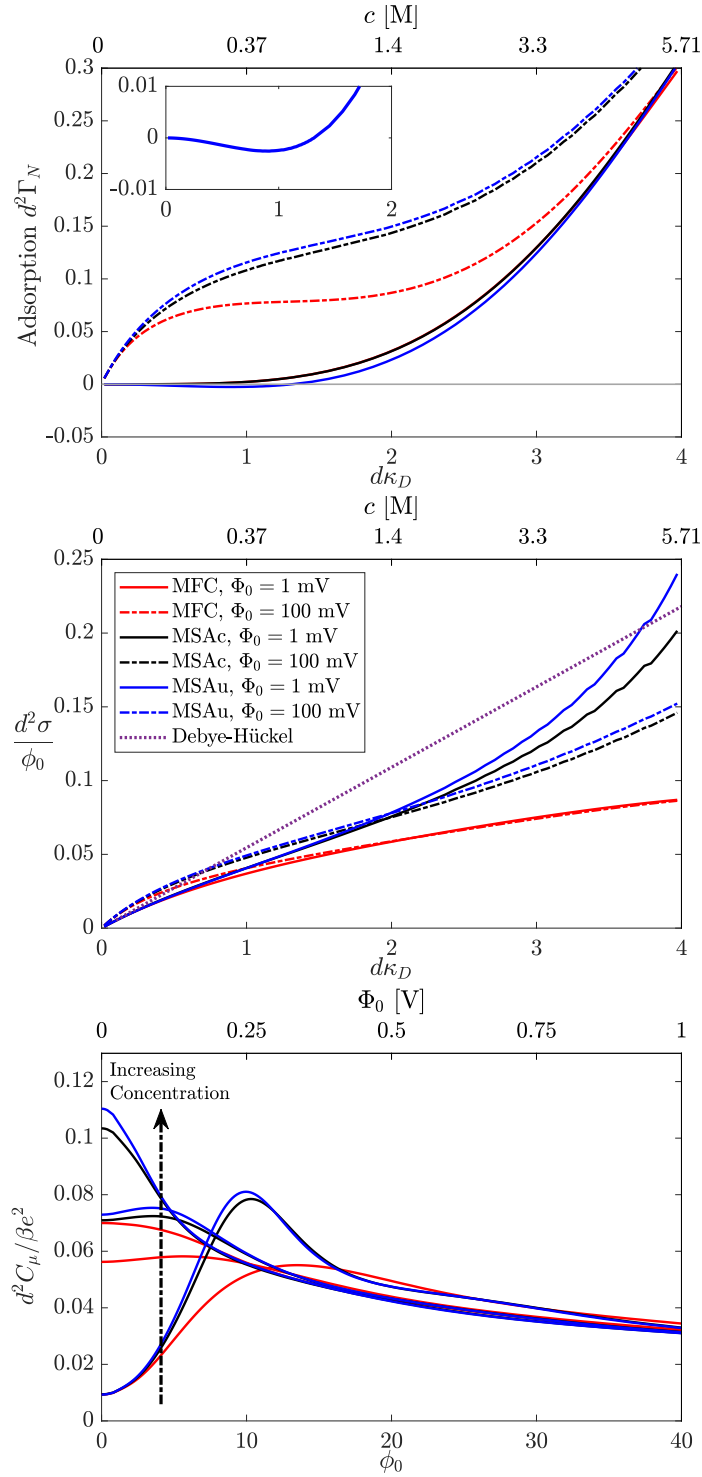


Figure 2.E.1: In (a) the dimensionless adsorption $d^2\Gamma_N$, (b) the scaled surface charge $d^2\sigma/\phi_0$ and (c) the dimensionless differential capacitance $d^2C_\mu/e^2\beta$. For the differential capacitance, the concentrations $d\kappa_D = 0.3, 2.96, \text{ and } 4.19$ were considered.

2.F ASYMPTOTIC DECAY LENGTHS

Starting from a general excess free energy functional of the form

$$\beta\mathcal{F}_{ex}[\{\rho\}] = \int d\mathbf{r}\Phi(\{n_\alpha(\mathbf{r})\}) \quad (2.102)$$

with arbitrary Helmholtz free energy density Φ^f and arbitrary number of weighted densities

$$n_\alpha(\mathbf{r}) = \sum_j \int d\mathbf{r}' \rho_j(\mathbf{r}') \omega_j^\alpha(\mathbf{r} - \mathbf{r}'), \quad (2.103)$$

such that it covers all free energy functionals, one finds a second order direct correlation function

$$c_{ij}^{(2)}(\mathbf{r}, \mathbf{r}') = - \sum_{\beta\gamma} \int d\mathbf{x} \frac{\partial^2 \Phi^f(\{n_\alpha\})}{\partial n_\beta \partial n_\gamma}(\mathbf{x}) \omega_i^\beta(\mathbf{x} - \mathbf{r}) \omega_j^\gamma(\mathbf{x} - \mathbf{r}'). \quad (2.104)$$

Far from any external potentials, we assume that $c^{(2)}$ is translational invariant, i.e. $c_{ij}^{(2)}(\mathbf{r}, \mathbf{r}') = c_{ij}^{(2)}(\mathbf{r} + \mathbf{a}, \mathbf{r}' + \mathbf{a})$ for any arbitrary displacement \mathbf{a} . This translates into

$$\begin{aligned} c_{ij}^{(2)}(\mathbf{r}, \mathbf{r}') &= - \sum_{\beta\gamma} \int d\mathbf{x} \frac{\partial^2 \Phi^f(\{n_\alpha\})}{\partial n_\beta \partial n_\gamma}(\mathbf{x} + \mathbf{r}') \omega_i^\beta(\mathbf{x} - (\mathbf{r} - \mathbf{r}')) \omega_j^\gamma(\mathbf{x}) \\ &= - \sum_{\beta\gamma} \left. \frac{\partial^2 \Phi^f(\{n_\alpha\})}{\partial n_\beta \partial n_\gamma} \right|_{\text{bulk}} \int d\mathbf{x} \omega_i^\beta(\mathbf{x} - (\mathbf{r} - \mathbf{r}')) \omega_j^\gamma(\mathbf{x}), \end{aligned} \quad (2.105)$$

by choosing $\mathbf{a} \rightarrow \infty$. The OZ for multiple species in its matrix form in Fourier space can be written as

$$\hat{H}(q) = (\mathbb{1} - \hat{C}(q)\rho)^{-1} \hat{C}(q) \quad (2.106)$$

where $\rho = \text{diag}(\rho_1^b, \dots, \rho_\nu^b)$ for a mixture of ν species. The asymptotic behavior can be extracted by looking at the poles α_k of Eq. (2.106), i.e.

$$\det(\mathbb{1} - \hat{C}(\alpha_k)\rho) = 0. \quad (2.107)$$

Fourier transforming Eq. (2.105) gives

$$\begin{aligned} \hat{c}_{ij}^{(2)}(q) &= - \sum_{\beta\gamma} \left. \frac{\partial^2 \Phi^f(\{n_\alpha\})}{\partial n_\beta \partial n_\gamma} \right|_{\text{bulk}} \int d\mathbf{r} \int d\mathbf{x} \omega_i^\beta(\mathbf{x} - \mathbf{r}) \omega_j^\gamma(\mathbf{x}) e^{-i\mathbf{k}\cdot\mathbf{r}} \\ &= - \sum_{\beta\gamma} \left. \frac{\partial^2 \Phi^f(\{n_\alpha\})}{\partial n_\beta \partial n_\gamma} \right|_{\text{bulk}} \int d\mathbf{r} \omega_i^\beta(-\mathbf{r}) e^{-i\mathbf{q}\cdot\mathbf{r}} \int d\mathbf{x} \omega_j^\gamma(\mathbf{x}) e^{-i\mathbf{k}\cdot\mathbf{x}} \\ \hat{c}_{ij}^{(2)}(k) &= - \sum_{\beta\gamma} \left. \frac{\partial^2 \Phi^f(\{n_\alpha\})}{\partial n_\beta \partial n_\gamma} \right|_{\text{bulk}} \hat{\omega}_i^\beta(-\mathbf{k}) \hat{\omega}_j^\gamma(\mathbf{k}). \end{aligned} \quad (2.108)$$

Hence, one only needs the second derivative of Φ^f w.r.t. weighted densities in the bulk and the Fourier transformation of the weight functions to determine the asymptotic decay length.

2.F.1 FMT Decay Length

The decay for the FMT functional can be found numerically by computing Eq. (2.108) and substituting it in Eq. (2.106) to find the poles, i.e.

$$1 + \rho_b \sum_{\beta, \gamma} \left[\partial_{\beta\gamma} \Phi^{FMT}(\{n_\alpha^b\}) \right] \hat{\omega}^\beta(-k) \hat{\omega}^\gamma(k) = 0, \quad (2.109)$$

where the indices β and γ run over all the weighted densities in FMT and κ denotes the inverse decay length. After some tedious algebra, one finds the condition for $y = x + i\theta = d\kappa/2 + i\pi d/\lambda$

$$1 + \eta \left[(\alpha + \Delta\alpha) g_0^2(y) + (\beta + \Delta\beta) g_0(y) g_3(y) + [\gamma(y) + \Delta\gamma(y)] g_3^2(y) \right] = 0, \quad (2.110)$$

with

$$g_0(y) = \frac{1}{y} \sinh(y), \quad (2.111)$$

$$g_3(y) = -\frac{1}{y^2} [\cosh(y) - g_0(y)], \quad (2.112)$$

$$\alpha = 3 \frac{2 + \eta}{(1 - \eta)^2}, \quad (2.113)$$

$$\Delta\alpha = \frac{6}{(1 - \eta)^2} \left((1 - \eta) \phi_1 + \frac{3}{2} \eta \phi_2 \right), \quad (2.114)$$

$$\beta = 6 \frac{(1 + 2\eta)^2}{(1 - \eta)^3}, \quad (2.115)$$

$$\Delta\beta = 18 \frac{\eta}{(1 + \eta)^3} [\Delta\beta_1 + \Delta\beta_2], \quad (2.116)$$

$$\Delta\beta_1 = 2(1 - \eta) [(1 - \eta) \partial_3 \phi_1 + \phi_1], \quad (2.117)$$

$$\Delta\beta_2 = \frac{3}{2} \eta [(1 - \eta) \partial_3 \phi_2 + 2\phi_2], \quad (2.118)$$

$$\gamma = \frac{3}{2} \frac{\eta}{1 - \eta} \beta + \alpha y^2, \quad (2.119)$$

$$\Delta\gamma = \frac{27}{2} \frac{\eta^2}{(1 - \eta)^4} [\Delta\gamma_1 + \Delta\gamma_2] + \Delta\alpha y^2, \quad (2.120)$$

$$\Delta\gamma_1 = 2(1 - \eta) \left[(1 - \eta)^2 \partial_3 \phi_1 + 2(1 - \eta) \partial_3 \phi_1 + 2\phi_1 \right], \quad (2.121)$$

$$\Delta\gamma_2 = \eta \left[(1 - \eta)^2 \partial_3 \phi_2 + 4(1 - \eta) \partial_3 \phi_2 + 6\phi_2 \right]. \quad (2.122)$$

Note that by setting all the Δ quantities to zero, one gets the condition set by the Rosenfeld functional [58], while the full equation represents the condition for the WBII functional.

This is apparent by realizing that the functions ϕ_1 and ϕ_2 are the ones appearing in the WBII free energy density,

$$\Phi^{\text{WBII}}[\{\rho\}] = \Phi^{\text{RF}}[\{\rho\}] + \phi_1(n_3) \frac{n_1 n_2 - \mathbf{n}_1 \mathbf{n}_2}{1 - n_3} + \phi_2(n_3) \frac{n_2^3 - 3n_2 \mathbf{n}_2 \cdot \mathbf{n}_2}{24\pi(1 - n_3)^2}, \quad (2.123)$$

and give the correction on top of the Rosenfeld free energy density Φ^{RF} . The expression for those functions ϕ_1 and ϕ_2 are given in Appendix 1.A. The numerical solution for Eq. (2.110) is shown in Fig. 2.3.3(b).

2.F.2 MSAC Decay Length

The asymptotic decay in the charge density profiles for the MSAC functional is found similarly as for FMT, giving the condition (see also Ref. [109])

$$-\left(\bar{b} \frac{y^2}{d\kappa_D}\right)^2 + y^2(\bar{b} - 1)^2 \cosh(y) + 2y(\bar{b} - 1) \sinh(y) + 2[\cosh(y) - 1] = 0, \quad (2.124)$$

where $\bar{b} = D/d$. The numerical solution to this equation is shown in Fig. 2.3.3(a).

CAPACITANCE AND STRUCTURE OF ELECTRIC DOUBLE LAYERS: COMPARING BROWNIAN DYNAMICS AND CLASSICAL DENSITY FUNCTIONAL THEORY

We present a study of the structure and differential capacitance of electric double layers of aqueous electrolytes. We consider electric double layer capacitors (EDLC) composed of spherical cations and anions in a dielectric continuum confined between a planar cathode and anode. The model system includes steric as well as Coulombic ion-ion and ion-electrode interactions. We compare results of computationally expensive, but “exact”, Brownian Dynamics (BD) simulations with approximate, but cheap, calculations based on classical Density Functional Theory (DFT). Excellent overall agreement is found for a large set of system parameters, including variations in concentration, ionic size- and valency-asymmetries, applied voltages and electrode separation, provided the differences between the canonical ensemble of the BD simulations and the grand-canonical ensemble of DFT are properly taken into account. In particular, a careful distinction is made between the differential capacitance C_N at fixed number of ions and C_μ at fixed ionic chemical potential. Furthermore, we derive and exploit their thermodynamic relations. In the future these relations will also be useful for comparing and contrasting experimental data with theories for supercapacitors and other systems. The quantitative agreement between simulation and theory indicates that the presented DFT is capable of accounting accurately for coupled Coulombic and packing effects. Hence it is a promising candidate to cheaply study room temperature ionic liquids at much lower dielectric constants than that of water.

Electric double layer capacitors (EDLCs) are promising energy storage devices, in which electric energy is stored in the net ionic charge that is present in the vicinity of an electrode-electrolyte interface. In EDLCs the cathode attracts cations and repels anions and vice versa for the anode; more so the higher the applied voltage between the cathode and the anode [110]. This energy storage mechanism leads to much higher *power* densities than those of batteries; the discharge of the so-called Electric Double Layer (EDL) of an EDLC can be much faster than the redox reactions in batteries [111, 112]. However, the *energy* densities of EDLCs are much lower than those of batteries [111].

One of the factors that contributes to the low energy density in EDLCs is the limited potential window in which conventional electrolytes are stable with respect to detrimental chemical reactions. Conventional electrolytes in EDLCs consist of a salt (e.g. tetraethylammonium tetrafluoroborate) dissolved in a solvent (e.g. propylene carbonate or acetonitrile) [113]. In order to maximise the energy density of EDLCs, one could use alternative electrolytes with a larger potential window [114]. Room temperature Ionic liquids (ILs) are potential alternatives to conventional electrolytes in EDLCs, since they can have a potential window of up to 6 V [115]; conventional electrolytes in EDLCs have a potential window of only 2.5 to 2.8 V [114]. Other advantages of ILs over conventional electrolytes are their stability at high temperatures and a low vapour pressure (low volatility and non-flammability), which makes IL-based EDLCs much safer [114, 116]. Modeling and theoretically understanding concentrated ILs is difficult, because of the steric repulsions at short ionic separations and the Coulombic interactions at longer ranges are simultaneously at play. While in experiments dispersion forces, polarization, and orientation degrees of freedom often also play a role, we restrict attention to the combined effects of packing and electrostatics. In order to prepare for the challenges posed by ILs, we here focus on the parameter regime of aqueous systems.

Several methods have been applied to investigate the electric double layer of EDLCs. On the one hand there are continuum methods, such as the mean field Gouy-Chapman-Stern (GCS) theory for point ions and classical Density Functional Theory (DFT) that can include steric effects. On the other hand there are methods in which each ionic constituent is treated explicitly, such as in Molecular Dynamics (MD) and Brownian Dynamics (BD) simulations. All have their advantages and disadvantages. GCS theory can be solved analytically, but is rather inaccurate for larger ionic concentrations and surface charges, DFT is computationally fast but is an approximate theory for a given model. MD simulations might be considered as 'exact' and provide dynamics at the molecular scale but are computationally expensive. DFT calculations [117, 118, 119, 120, 121, 122, 123] and MD simulations are extensively used to study double layers in ILs and aqueous electrolytes [124, 125, 126, 127, 128, 129, 130, 131, 132, 133, 134, 135, 136, 137, 138, 139, 140, 141, 142]. As an alternative to the MD simulation method, BD is less accurate but computationally cheaper. In BD the explicit solvent of MD is eliminated by including solvent effects – like friction, Brownian noise and the dielectric constant of the medium – in an approximate way in the equations of motion of the ions [143].

The main aim of the chapter is to explore whether DFT can be used to efficiently model electrolytes; therefore we are interested in the ability of DFT to quantitatively match BD simulations of a primitive model electrolyte. To this end, we study the EDLs of an aqueous electrolyte confined between a planar anode and cathode using BD simulations, performed by Ranisha Sitlapersad, Wouter den Otter, and Anthony Thornton at Twente University of Technology, and classical DFT. A given potential difference is applied between the two electrodes, which are modeled as graphene-like electrodes in the BD simulations and as impenetrable planar walls in the DFT calculations. We compare both the ion concentration profiles between the electrodes (see also Refs.[144, 145]) and the differential capacitance C . The differential capacitance characterizes the (additional) charge per (additional) applied voltage, a quantity that is experimentally measurable and often used as a characteristic of the energy storage qualities of a capacitor.

Also it is shown that a careful distinction is required between the capacitance C_N at constant number of ions and C_μ at constant ion chemical potential, where the former follows naturally from the canonical BD simulations and the latter from the grand-canonical DFT calculations. However, they are related and we show the connecting expressions. We start by a detailed study of our **reference system**: a 1 M 1:1 electrolyte of equal-sized ions of diameter $d = 0.5$ nm in the 4 nm gap between two electrodes at a potential difference of 0.2 V. Then we vary the salt concentration, the ion valencies, the diameter ratio, the electrode-electrode distance, and the applied voltage. Throughout, the whole explored 5-dimensional parameter space / design of experiments we find excellent agreement between our BD and DFT results.

3.1 MODEL

We consider an aqueous electrolyte confined by two planar electrodes at fixed surface potential Φ_L and Φ_R , separated by a distance H . The electrolyte contains spherical cations (+) and anions (-) with a diameter d_\pm and valency z_\pm dissolved in a structureless medium with dielectric constant $\epsilon_r = 78$ at room temperature $T = 298$ K (see Fig. 3.1.1). The medium is fully characterized by its Bjerrum length $\lambda_B = \beta e^2 / 4\pi\epsilon_r\epsilon_0 = 0.72$ nm, where $\beta = 1/k_B T$ and ϵ_0 the dielectric permittivity of free space. The pair potential $u_{ij}(r)$ between a pair of ions of species i and j separated by a distance r is composed of a steric repulsions, characterized by the diameter d , and the Coulombic interaction, i.e.

$$\beta u_{ij}(r) = \beta u_{ij}^{rep}(r) + z_i z_j \frac{\lambda_B}{r}. \quad (3.1)$$

In the DFT calculations we describe the steric repulsions with a hard-sphere potential

$$\beta u_{ij}^{HS}(r) = \begin{cases} \infty & \text{for } r < d_{ij}; \\ 0 & \text{for } r > d_{ij}, \end{cases} \quad (3.2)$$

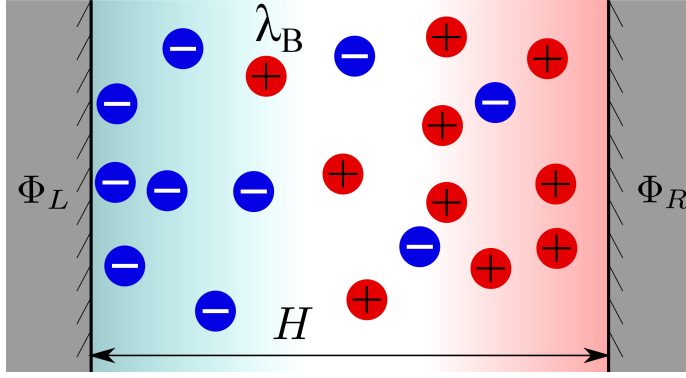


Figure 3.1.1: Illustration of the electrolyte with cations (+) and anions (-) dissolved in a dielectric medium characterized by the Bjerrum length $\lambda_B = \beta e^2 / 4\pi\epsilon_r\epsilon_0$ confined between two planar electrodes separated by a distance H at which a potential Φ_L and Φ_R is applied on the left and right electrode, respectively. The gradient background color indicates the charge density.

whereas in the BD simulations we employ the Weeks-Chandler-Andersen (WCA) pair potential

$$u_{ij}^{WCA}(r) = \begin{cases} 4\epsilon \left[\left(\frac{d_{ij}}{r} \right)^{12} - \left(\frac{d_{ij}}{r} \right)^6 \right] + \epsilon & \text{for } r < 2^{1/6}d_{ij}; \\ 0 & \text{for } r > 2^{1/6}d_{ij}. \end{cases} \quad (3.3)$$

Here ϵ is the interaction parameter that we set to $\epsilon = k_B T$, and $d_{ij} = (d_i + d_j)/2$. Note that the WCA potential, which is just the repulsive part of the Lennard-Jones potential, is only slightly softer for $r < d$ than the hard-sphere potential used in the DFT calculations. However, we will show remarkable agreement between the DFT and BD results in the parameter regime of study, indicating the limited sensitivity of the functional form of the repulsive interaction.

By confining the system, we also introduce an external potential, i.e. the interaction of the ions with the fixed particles in the electrode. This ion-electrode interaction is described by the WCA potential and Coulombic interactions, in both DFT and BD. In the DFT description we integrate out the in-plane dimensions, finding for the WCA part of the external potential

$$\beta V_{ext}^j(x < d_{wj}) = 2\pi\rho_w\epsilon_w d_{wj}^2 \left[\frac{2^{4/3}}{5} + \frac{2}{5} \left(\frac{d_{wj}}{x} \right)^{10} - \left(\frac{d_{wj}}{x} \right)^4 - \frac{1}{2} \left(2^{1/3} - \left(\frac{x}{d_{wj}} \right)^2 \right) \right] \quad (3.4)$$

where ρ_w is the surface density of wall particles in number of particles per unit area; ϵ_w the interaction strength between the wall particles and ions, for which we take $\epsilon_w = \epsilon = k_B T$; the contact distance is $d_{wj} = (d_w + d_j)/2$ with d_w and d_j the diameter of the wall particles and ions of species j , respectively. For $x > d_{wj}$ the external potential vanishes. Note that the second electrode is described by the same interaction potential with x replaced by $H - x$. Our primitive model captures the key features of an electrolyte, within the practical conditions posed by DFT and BD respectively, thereby enabling a quantitative comparison

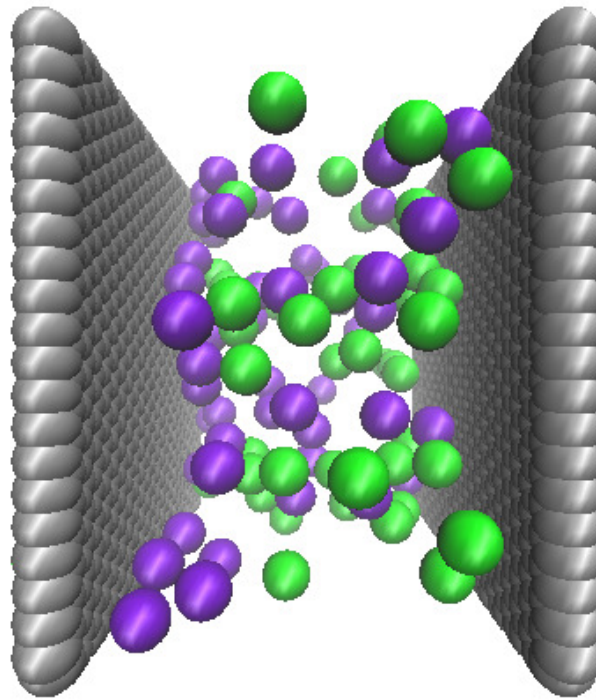


Figure 3.2.1: Simulation snapshot of a system containing 51 ion pairs, corresponding to a reservoir salt concentration of 1 M, between two graphene-like electrodes with a separation of $H = 4$ nm. The potential difference between the electrodes is 0.2 V, with the electrode on the right at a higher potential than the electrode on the left. The valencies of the cations (purple) and anions (green) are $z_+ = 1$ and $z_- = -1$, respectively, and both have the same diameter $d = 0.5$ nm.

between both methods. For simplicity, we use the same diameter for all ions and electrode particles in the reference system, namely $d = 0.5$ nm.

3.2 METHOD

3.2.1 *Brownian Dynamics*

We focus here on the description of the reference system used in the BD simulations, as illustrated in Fig. 3.2.1; detailed information on the variations to this system are provided in Section 3.4. The simulations were performed by our collaborators, who used LAMMPS [146]. For details regarding the simulation we refer to the Ref. [2]. A simulation typically covered 200 ns, requiring about 2-3 days on 32 cores in parallel, with the first 10% serving as equilibration phase and the remainder as production run.

The two parallel electrodes each consist of one graphene-like layer of 960 particles, covering an area of $A = 100.6 d^2$, see Fig. 3.2.1. The inter-particle bond lengths in these hexagonal layers are taken as the usual carbon-carbon distance, 0.142 nm $= 0.284d$. The distance between the electrodes, as measured between the centers of the constituent particles,

is $H = 8d = 4\text{ nm}$. All wall particles are frozen, i.e. are excluded from the equation of motion, because the elimination of their rapid vibrations permits the use of a larger time step. Their charges are calculated using the Constant Potential Method (CPM) by imposing a constant voltage difference of $\Psi = 0.2\text{ V}$ between the two walls [135, 147]. In brief, the CPM determines the charges of all wall particles at every simulation step by solving the linear set of equations that determines the potential at every wall particle, given the positions of all wall particles and ions. A brief comparison with the fixed charge method, in which all charges are permanently fixed, is provided in Appendix 3.D for the system at zero voltage. The system is periodically repeated in space, with the box lengths in the two directions parallel to the walls dictated by the geometry of the lattice and the height perpendicular to the walls taken as three times the width of the slit. Adding additional layers to the electrodes, creating thin slabs of graphite, does not significantly affect the ion density profiles nor the average total charge of the electrodes; the differences are within the accuracy of the calculation.

3.2.2 Density Functional Theory

The DFT that is used for this analysis is the MSAc functional explained in Section 2.1.2.2. Note that the direct correlation function c^{MSA} from MSA (see Eq.(2.29)) depends on the reservoir concentration ρ_r through the parameter D , presented in Eq. (2.18), and therefore it also depends on the chemical potential μ . Due to the approximation for the Helmholtz free energy functional $\mathcal{F}_{ex}^{ES}[\{\rho\}]$, it now also depends on μ , which it formally should not depend on. As a result, the Maxwell relation introduced in the next section does not hold exactly and we have two ‘routes’ to calculate the adsorption Γ (see Appendix 3.C). This inconsistency is known for functionals that are based on bulk-density expansions. When we need to calculate the adsorption Γ we use the route of Eq.(3.8) given in the next section for the remainder of the chapter.

As a final note we mention that our DFT calculations assume planar symmetry in which the in-plane coordinates can again be integrated out, leaving the normal coordinate x perpendicular to the electrodes as the only spatial variable in the numerical calculations.

3.3 THERMODYNAMICS

We will treat the above-mentioned model theoretically via DFT, and by BD simulations. However, firstly we discuss the thermodynamics of both methods.

Let us start by considering the ensemble of the BD simulations, which is a closed system with a fixed number of N_+ cations and N_- anions in a volume V at temperature T confined between two planar electrodes of equal area A separated by a distance H and held at a surface potential difference Ψ (see Fig. 3.3.1). The system, i.e. electrolyte and the electrodes, together with the charge reservoirs is charge neutral $\sum_{j=\pm} ez_j N_j + Q_L + Q_R = 0$. Applying a potential difference Ψ creates an electric field across the system. Since the ions in the system are mobile they will respond to this electric field, and because the electrolyte

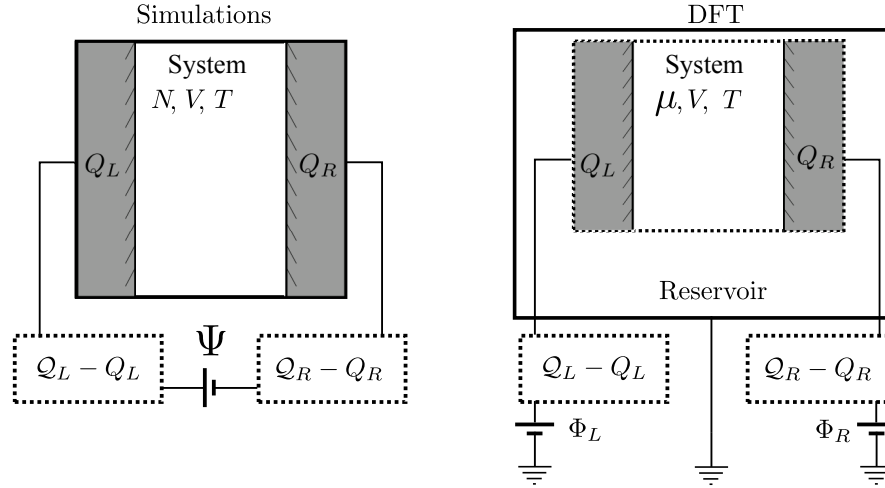


Figure 3.3.1: Illustration of the thermodynamic ensembles applicable to the BD simulations (left) and DFT (right). The simulations are performed with a fixed number of particles N in a fixed volume V at a fixed temperature T , while the DFT calculations employ a fixed chemical potential μ or reservoir concentration ρ_r . In the simulations the potential difference between the electrodes is fixed at Ψ , while in the DFT calculations the potentials of both electrodes relative to the reservoir are fixed at $\Phi_{L/R}$ for the left and right electrode, respectively. In both cases, the electrodes can implicitly exchange charge with charge reservoirs to maintain the imposed potential difference(s).

is confined they will create a charge density near both electrodes. These electrodes are connected to charge reservoirs with which they can exchange charges, such that the charge on the electrode is balanced with the charge density in the electrolyte. In other words, the charge in the electrolyte together with the average charge on the electrodes must vanish, i.e. $\sum_{j=\pm} ez_j N_j + Q_L + Q_R = 0$, where $Q_{L/R}$ denotes the average charge. The corresponding thermodynamic potential for this system is the free energy $F(N_+, N_-, V, T, \Psi, A, H)$, for which the differential form reads

$$dF = -SdT - pdV + \sum_{j=\pm} \mu_j dN_j - (Q_R - Q_L)d\Psi + \gamma dA - fdH, \quad (3.5)$$

with S the entropy, p the pressure, μ_{\pm} the chemical potential of the cations and anions, respectively, A the surface area, and γ is the total surface tension (which has contributions from the electrode-electrolyte and in the case of EDL-overlap also from electrode-electrode interactions). We also introduced the force f between the two planar electrodes, where f/A is also referred to as the disjointing pressure. We will call F the Helmholtz free energy, even though it is only a Helmholtz free energy for the ionic species while it is actually a grand-canonical potential for the charge carriers in the electrodes.

The DFT calculations, on the other hand, are performed at constant chemical potential μ_{\pm} instead of constant number of ions N_{\pm} . This system has been extensively discussed in the introduction 1.1. Here, we denote the surface potential Φ_L and Φ_R on the left and right electrode, respectively, which generate an independent electric field, not only between the electrodes but also between the electrodes and the reservoir. The ions both within the system and in the reservoir respond to this electric field. The role of the charge reservoirs is the same in both ensembles. Global charge neutrality of the system plus reservoirs

only holds on average within this ensemble, i.e. $\sum_{j=\pm} ez_j \langle N_j \rangle + \langle Q_L \rangle + \langle Q_R \rangle = 0$. The corresponding thermodynamic potential is the grand potential $\Omega(\mu_{\pm}, V, T, \Phi_L, \Phi_R, A, H)$ with differential

$$d\Omega = -SdT - pdV - \sum_j N_j d\mu_j - Q_L d\Phi_L - Q_R d\Phi_R + \gamma dA - fdH. \quad (3.6)$$

The distinction between $F(N_{\pm}, V, T, \Psi, A, H)$ and $\Omega(\mu_{\pm}, V, T, \Phi_L, \Phi_R, A, H)$ is crucial when comparing results from DFT (constant chemical potential) with BD simulations (constant number of ions).

For macroscopically large systems we can use volumetric and areal extensivity arguments to write $\Omega = -p(\mu_+, \mu_-)V + \gamma(\mu_+, \mu_-, \Psi_L, \Psi_R, H)A$, where we drop the T dependence for convenience as we keep the temperature fixed throughout. Combining the resulting differential $d\Omega = -pdV - Vdp + \gamma dA + Ad\gamma$ with Eq.(3.6) gives the Gibbs-Duhem equation for the volumetric terms and, for $dH = 0$, the Lippmann equation

$$d\gamma = -\sigma_L d\Phi_L - \sigma_R d\Phi_R - \sum_j \Gamma_j d\mu_j, \quad (3.7)$$

where $\sigma_{L/R} = Q_{L/R}/A$ denotes the average surface charge density and Γ_j the adsorption of ions of species j onto both electrodes defined by

$$\Gamma_j = \int_0^H dx (\rho_j(x) - \rho_{j,r}). \quad (3.8)$$

Here, x denotes the coordinate describing the distance perpendicular to the parallel electrodes, $\rho_j(x)$ the local number density of species j at position x , and $\rho_{j,r}$ the reservoir concentration of species j which is dictated by the chemical potentials μ_{\pm} . See Appendix 3.A for a more detailed derivation.

The main observable that we focus on in this chapter is the differential capacitance (per unit area), which can either be obtained at constant number of particles C_N or at constant chemical potential C_{μ} , i.e.

$$C_N = \left(\frac{\partial \sigma}{\partial \Psi} \right)_N = -\frac{1}{A} \left(\frac{\partial^2 F}{\partial \Psi^2} \right)_N, \quad C_{\mu} = \left(\frac{\partial \sigma}{\partial \Psi} \right)_{\mu} = -\frac{1}{A} \left(\frac{\partial^2 \Omega}{\partial \Psi^2} \right)_{\mu}, \quad (3.9)$$

where, for simplicity, we consider the RPM where $N_+ = N_- \equiv N$ and $d\mu_+ = d\mu_- \equiv d\mu/2$, which allows us to write $\Gamma = \Gamma_+ \equiv \Gamma_2$. On top of that, we also apply the same (but opposite) potential on both electrodes within the Ω ensemble, i.e. $\Phi_R = -\Phi_L \equiv \Psi/2$, which leads to the same (but opposite) surface charge $\sigma_L = -\sigma_R \equiv \sigma$ on both electrodes.

Interestingly, C_{μ} and C_N are related via expressions that are very similar to those between the constant-volume and constant-pressure heat capacities, namely (see Appendix 3.A)

$$C_{\mu} - C_N = \frac{\alpha^2}{\chi_{\Psi}} \geq 0 \quad \text{and} \quad \frac{C_{\mu}}{C_N} = \frac{\chi_{\Psi}}{\chi_{\sigma}} \geq 1, \quad (3.10)$$

where α can be taken equal either to α_μ or α_Ψ defined by

$$\alpha_\mu \equiv \left(\frac{\partial \Gamma}{\partial \Psi} \right)_\mu = \left(\frac{\partial \sigma}{\partial \mu} \right)_\Psi \equiv \alpha_\Psi. \quad (3.11)$$

In an exact theory the Maxwell relation $\alpha_\mu = \alpha_\Psi$ is satisfied identically, however our excess free-energy functional is approximate and does not identically satisfy the Maxwell relation. As a consequence our conversion between C_N and C_μ depends on the choice for α , and thus leads to an inconsistency. However, the numerical differences are limited, as we will see in section 3.4.7. We also defined

$$\chi_\sigma = \left(\frac{\partial N/A}{\partial \mu} \right)_\sigma \quad \text{and} \quad \chi_\Psi = \left(\frac{\partial N/A}{\partial \mu} \right)_\Psi, \quad (3.12)$$

which resemble (osmotic) compressibilities of the ions at constant σ and Ψ , respectively. The relations in this section allow us to compare and convert the capacitances at constant N (natural to BD simulation) and at constant μ (natural to DFT).

In the BD simulations, the differential capacitances were determined by three routes. Running a set of equilibrium simulations at a range of potential differences Ψ between the electrodes yielded the mean total charge difference between the electrodes, $\langle Q \rangle_{N,\Psi} = (1/2)\langle Q_R - Q_L \rangle_{N,\Psi}$. The angular brackets denote the canonical ensemble average at the indicated potential difference, which is evaluated in simulations as a time-average [143, 148]. The differential capacitance at constant numbers of ions, see Eq. 3.9, is obtained by numerically differentiating the surface charge with respect to the potential difference,

$$C_N^\Delta(N, \Psi) = \frac{\langle Q \rangle_{N,\Psi+\Delta\Psi} - \langle Q \rangle_{N,\Psi-\Delta\Psi}}{2A\Delta\Psi} \quad (3.13)$$

using the central difference formula. Alternatively, the same differential capacitance is extracted from the thermal fluctuations of the wall charge around the average, $\delta Q = Q - \langle Q \rangle_{N,\Psi}$, over a single equilibrium simulation [23, 40],

$$C_N^\delta(N, \Psi) = \frac{\langle (\delta Q)^2 \rangle_{N,\Psi}}{k_B T A} + C_0, \quad (3.14)$$

The intrinsic capacitance C_0 , which is a constant independent of Ψ and N , accounts for the thermal fluctuations of the atomic charges around the idealized constant-potential charges calculated using the CPM. The numerical value of C_0 is obtained by the fitting procedure discussed in Appendix 3.B.

The differential capacitance at constant chemical potential, see Eq. 3.9, is obtained from the BD simulations as

$$C_\mu^\Delta(N, \Psi) = \frac{\langle Q \rangle_{N(\mu,\Psi+\Delta\Psi),\Psi+\Delta\Psi} - \langle Q \rangle_{N(\mu,\Psi-\Delta\Psi),\Psi-\Delta\Psi}}{2A\Delta\Psi}, \quad (3.15)$$

where each simulation was preceded by a DFT calculation to establish the required numbers of ions $N(\mu, \Psi)$ under the prevailing conditions. The same finite difference relations

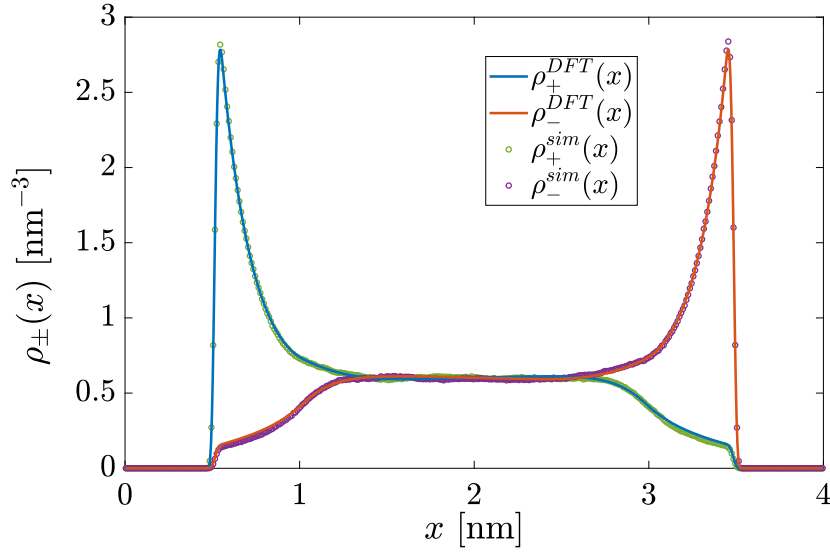


Figure 3.4.1: The reference system, where the electrodes are separated by $H = 4$ nm and are held at a potential $\Phi_L = -0.1$ V and $\Phi_R = 0.1$ V ($\Psi = 0.2$ V), for the left and right electrode respectively. The electrolyte consists of monovalent ions with radius $d = 0.5$ nm at a reservoir concentration $\rho_r = 1$ M in the reservoir, resulting in 51 ion pairs in the BD simulation.

were used to calculate the capacitance by DFT. The calculations of C_N via Eq.(3.11) will be referred to as $C_N^{\alpha_\mu}$ and $C_N^{\alpha_\Psi}$, when using α_μ and α_Ψ , respectively.

3.4 RESULTS

In this section, the density profiles and the differential capacitances obtained with BD and DFT are presented and compared. The reference system will be considered first, followed by an exploration of the impacts of its various parameters by varying them one by one. Various authors have previously used DFT and MD to study systems similar to the systems discussed below [71, 72, 117, 140, 141, 142, 149, 150]. Although those systems are not identical to the systems we consider, they do show very similar density profiles.

3.4.1 Reference system

In the reference system, the electrodes are separated by $H = 4$ nm while the applied electrode potentials are $\Phi_L = -0.1$ V and $\Phi_R = +0.1$ V in DFT and $\Psi = 0.2$ V in the BD simulations. The reservoir salt concentration is $\rho_r = 1$ M, *i.e.* cations and anions have identical concentrations of 1 M, which corresponds to 51 ion pairs in the BD system with electrode surface areas of $A = 25.1$ nm². The cations and anions have the same size $d_+ = d_- = 0.5$ nm, and are monovalent $z_+ = -z_- = 1$, see Fig. 3.2.1. The results from DFT and the simulations for this reference system are presented in Fig. 3.4.1. Applying a negative (positive) surface potential on the left (right) electrodes causes a negative (positive) surface charge, attracting positively (negatively) charged ions and repelling negative (positively)

charged ions. Away from the walls, the concentrations of both ions level off to a flat density profile. The agreement between DFT and BD is excellent.

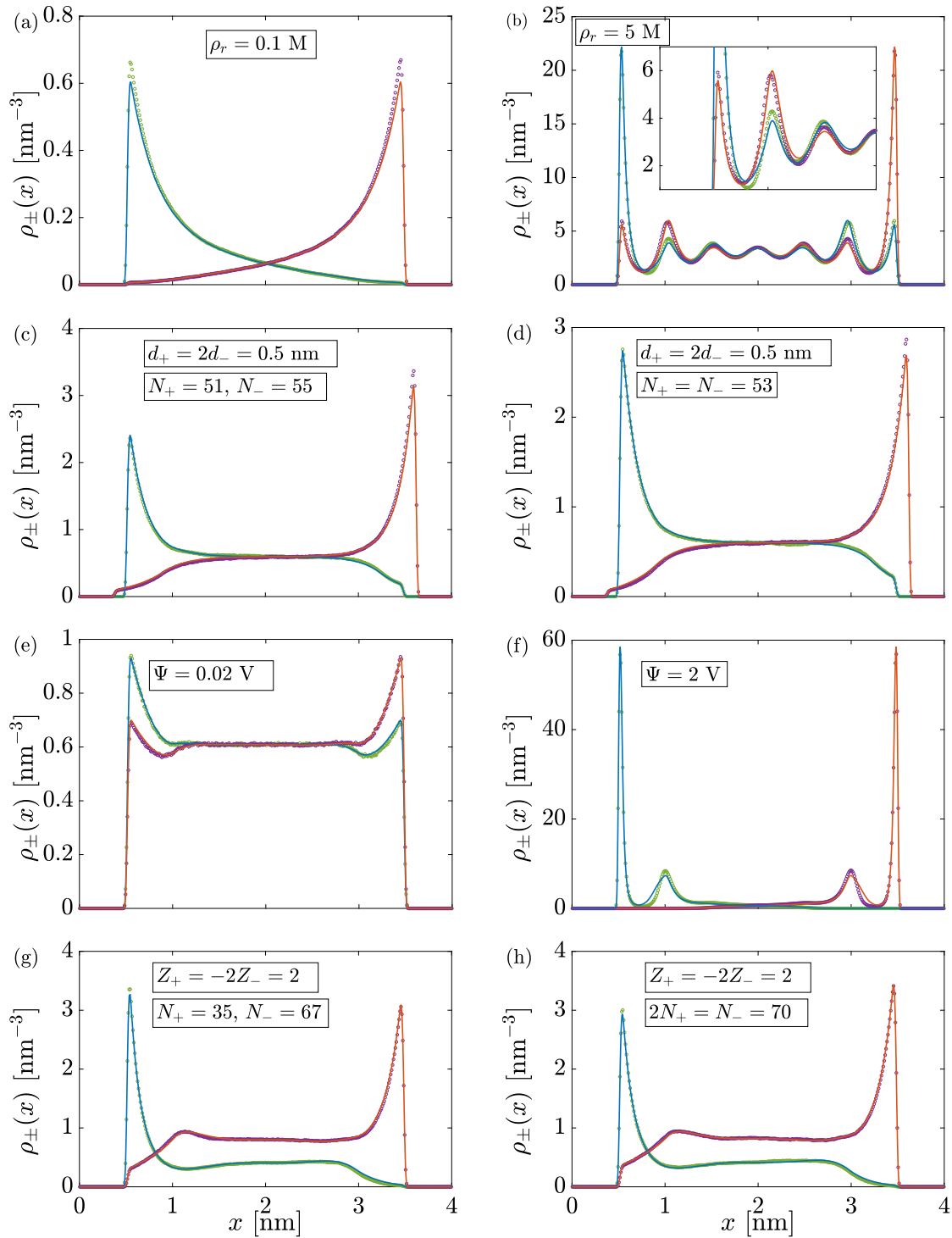


Figure 3.4.2: (continued on the next page)

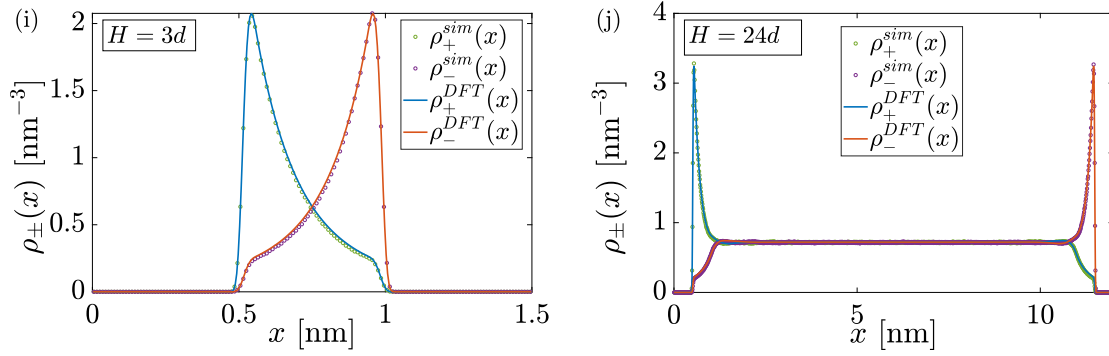


Figure 3.4.2: Density profiles of the sets specified in the main text. The solid lines represent the DFT calculations and the symbols the BD simulations. The left electrode placed at $x = 0$ has a negative surface potential attracting cations (blue line for DFT and green circles for BD simulations) and repelling the anions (solid orange line for DFT and purple circles for BD simulations) and the right electrode placed at $x = H$ has a positive potential. In (a) and (b) we change the concentrations w.r.t. reference case, in (c) and (d) the size of the cations, in (e) and (f) the potential, in (g) and (h) the valency of the cation, and in (i) and (j) the electrode separation. The x -labels are the same for (a)-(h) and are given in (g) and (h).

3.4.2 Varying ion concentrations

The first parameter to be varied is the concentration of the electrolyte in the reservoir, from $\rho_r = 0.1 \text{ M}$ to $\rho_r = 5 \text{ M}$, corresponding to 9 and 252 ion pairs in the BD simulation, respectively. The latter concentration is similar to that of the ion concentration in ILs, while the dielectric constant and the shapes of the ions are markedly different in ILs. The results, see Fig. 3.4.2(a) and Fig. 3.4.2(b), reveal a slight difference at the peaks for both cases. The lower density shows only one peak, so we can consider this to be in the diluted limit. The higher density shows strong oscillations, due to the layering commonly found at high packing fractions, like the current $\eta = 0.394$. The wavelength and amplitude of the oscillations are well captured with DFT, as indicated by the good agreement between the two methods. Nevertheless, there are small discrepancies in the heights of the peaks and valleys. These are mainly due to the treatment of the hard-core potential by the FMT part of the functional [49] and the difference in the representation of the repulsive interactions as WCA in BD and as hard spheres in DFT.

3.4.3 Differently-sized ions

Figure 3.4.2(c) and (d) show results for differently-sized ions, with cations twice the diameter of anions, $d_+ = 2d_- = 0.5 \text{ nm}$. The difference between the two plots is in the ensemble being used to control the ion number densities in the slit. Because the anions are smaller than the cations, they both come closer to the electrode – thereby lowering their electrostatic energy – and pack at a higher density. Consequently, as illustrated in Fig. 3.4.2(c), when using DFT to impose reservoir concentration of $\rho_r = 1 \text{ M}$ for both ions, the heights of the density peaks adjacent to both electrodes become unequal at the ref-

erence potentials of $\Phi_L = -0.1\text{ V}$ and $\Phi_R = 0.1\text{ V}$, hence $\Psi = 0.2\text{ V}$. From these density profiles, the numbers of ions were calculated as $N_+ = 51$ and $N_- = 55$, to the nearest integer, and these numbers were used in the BD simulations shown in the same plot. Figure 3.4.2(d) presents results for equal numbers of cations and anions in the slit, taken as the average of the two previous values: $N_{\pm} = 53$. To obtain the desired numbers of ions of each type in DFT, the potential of one electrode was fitted, at constant potential difference Ψ to arrive at $\Phi_L = -0.1116\text{ V}$ and $\Phi_R = 0.0884\text{ V}$. The density peaks at both electrodes now resemble each other. Note the asymmetry in both plots in the density of the cations at the positive electrode versus that of the anions at the negative electrode, both in their distance from the wall relative to the other ion at the same wall and the distance to the electrode before reaching the constant density plateau in the center of the slit. For both equal and unequal numbers of ions, BD and DFT show good agreement in the density profiles.

3.4.4 Changing the Surface Potential

Figure 3.4.2 (e) and (f) present the comparison for smaller $\Psi = 0.02\text{ V}$ and larger $\Psi = 2\text{ V}$ potential differences with respect to the reference system. Because convergence of the density profile at the lower potential required a very long BD production run, the simulation was performed instead using Newtonian mechanics in combination with a Nosé-Hoover thermostat [143, 148]. The thermostat works by rescaling the velocities of all ions at every time step, in such a way as to recover the correct mean kinetic energy and kinetic energy fluctuations at the desired temperature, and therefore samples the Boltzmann equilibrium distribution also obtained by the BD simulation. The thermostatted method samples configuration space more efficiently by ignoring the slow Brownian motion, which affects the dynamical properties of the system but not the thermodynamic properties studied in this work.

Applying a small potential on the electrodes causes a smaller charge density, i.e. the density profiles of the cations and anions are more similar. At high potentials, a large portion of the ions are adsorbed onto the electrodes, causing strong layering. The agreement between the simulations and DFT is excellent for the smaller potentials, while small deviations are observed for the larger potential near the second peak. The latter are a result of strong packing, where, as mentioned before, the WCA potential differs from the FMT approximation to the hard sphere potential in DFT.

3.4.5 Different Valencies

In Fig. 3.4.2(g) and (h), the valency of the cation is doubled to twice that of the anion, $z_+ = -2z_- = 2$. Charge neutrality of the reservoir, $\sum_j z_j \rho_{r,j} = 0$, implies that the anion concentration in the reservoir must be double the cation concentration. Here we choose the cation reservoir concentration to be the same as in the reference system, i.e. $2\rho_{r,+} = \rho_{r,-} = 2M$. Because the symmetry between cations and anions is broken, ions exchange with

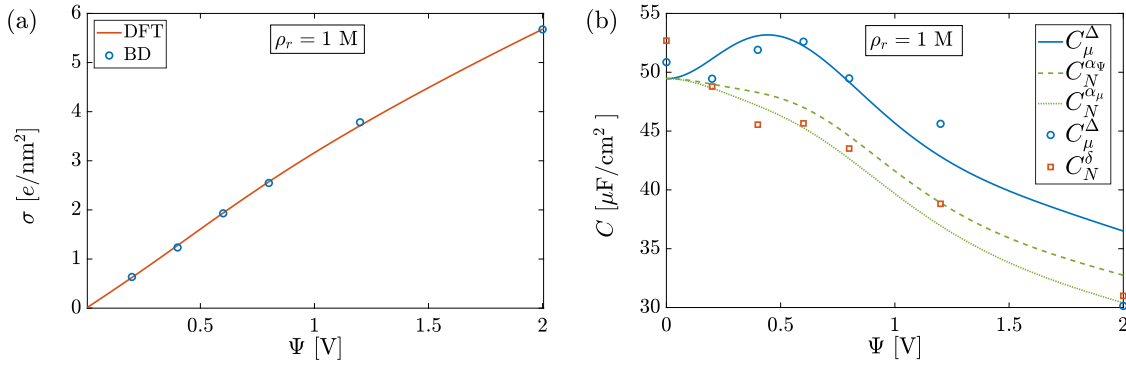


Figure 3.4.3: (a) The average surface charge on the electrodes $(\sigma_L - \sigma_R)/2$ and (b) the corresponding differential capacitance, as function of the potential difference between the electrodes, for a system in thermal equilibrium with a reservoir at a salt concentration of 1 M, by DFT and BD calculations. The number of ion pairs in the BD simulations was determined by DFT, and varies with the potential.

the reservoir resulted in distinct number of ions in the DFT calculations of Fig. 3.4.2(g). The corresponding BD simulations were based on $N_+ = 35$ and $N_- = 67$, following the procedure outlined in Sec. 3.4.3. The simulations in Fig. 3.4.2(h) impose charge neutrality in the slit, $2N_+ = N_- = 70$. The situation is realized in DFT at the electrode potentials $\Phi_L = -0.091 \text{ V}$ and $\Phi_R = 0.109 \text{ V}$ at the left and right electrode, respectively.

The most interesting difference between the reference system and this case is the little hump in the anion density profiles around $x = 1 \text{ nm}$. This effect is referred to as over-screening [151], where one finds a negatively charged layer of anions next to the positively charged first layer of cations adjacent to the cathode. Again, excellent agreement is observed between DFT and BD.

3.4.6 Slit width

Lastly, the distance between the electrodes H was varied from $H = 1.5 \text{ nm}$ in Fig. 3.4.2(i) to $H = 12 \text{ nm}$ in Fig. 3.4.2(h). Because a very long production run was required in the BD simulations, these were performed using the Nosé-Hoover thermostat rather than by Langevin Dynamics, as explained in subsection 3.4.4. At the lower slit width the EDLs overlap substantially, while for the large width the electrolyte acquires the flat distribution of a bulk fluid in the middle of the system. The DFT and BD results are again in excellent agreement.

3.4.7 Capacitance

The capacitance was calculated as a function of the surface potential difference Ψ , at both a constant reservoir concentration and at constant number of ion pairs in the slit. In the former case, which comes naturally to DFT, the DFT calculations at a concentration in the reservoir of $\rho_r = 1 \text{ M}$ were used to determine the numbers of ions in the BD simulations. In the latter case, which comes naturally to BD, the number of ion pairs was fixed at $N = 156$

and the concentration in the reservoir was varied to reach the desired number of ions in DFT. The charge on the electrode surface in the former case is shown in Fig. 3.4.3(a), where the line represents the DFT calculations and the markers the BD simulations. Note that each simulation, although performed at constant numbers of ions, belongs to the same chemical potential. As expected, the charge on the wall and the number of ions in the slit increase with the potential difference between the electrodes. The two methods are in good agreement. The corresponding capacitance is presented in Fig. 3.4.3(b), where several calculation methods have been used. The blue solid line and the blue circles represent C_μ^Δ of Eq. (3.15) using the data in Fig. 3.4.3(a). Because the number of time-consuming BD simulations is necessarily low, the numerical derivative is limited in its accuracy, especially for the last data point at $\Psi = 2$ V. Nevertheless, the agreement is satisfactory and both methods yield similar camel-shaped curves [152]. Also shown in Fig. 3.4.3(b) are calculations of C_N , where it should be emphasized that N is not constant across the plot but varies with Ψ . The capacitance C_N^δ (orange squares) is based on the charge fluctuations in the BD simulations, given in Eq. (3.14) where also C_0 appears. The value for C_0 , which depends neither on the number of particles nor on the potential difference, is found to be $C_0 = 17.6 \mu\text{F cm}^{-2}$ (see Appendix 3.B). The DFT calculations of $C_N^{\alpha\mu}$ (green dotted line) and $C_N^{\alpha\Psi}$ (green dashed line) are based on the relations in Eq. (3.10). The approximation made in Sec. 3.2.2, namely the assumed dependence of the direct correlation function c^{MSA} in Eq. (2.29) on the chemical potential, resurfaces at this point. The adsorption Γ can be obtained either from Eq. (3.8) or from the derivative of Eq. (3.19) with respect to the chemical potential, as derived in Appendix 3.C. In the latter case, the derivative of $\mathcal{F}_{ex}^{ES}[\{\rho\}]$ does not vanish, though in principle it should have. The capacitance C_N can therefore be calculated from C_μ using either α_Ψ or α_μ , where the expression for Γ in Eq. (3.8) was used to calculate α_μ . Note, however, that the calculation of the surface charge density σ is consistent by construction, since charge neutrality is imposed.

As expected from Eq. (3.9), in both cases C_N is smaller than C_μ . Both DFT calculations are in reasonable agreement with the BD results; notably, all three show a bell-shaped curve. The plot shows a substantial difference between C_N and C_μ , and although the various calculations do not exactly match quantitatively, they agree reasonably well and support the qualitative difference. The reason for the rather large difference between C_μ and C_N is due to the small electrode-electrode separation, where the region of the EDLs contribute substantially to the total number of ions in the system. In the limit where the separation between the electrodes is infinite, the difference between C_μ and C_N disappears.

Lastly, we consider the system with a fixed number of ion pairs, $N = 156$, and vary the surface potential difference Ψ . Shown in Fig. 3.4.4 are the capacitances using the same color and line coding as in Fig. 3.4.3, with the addition of an orange curve for C_N^Δ using DFT. For $\Psi = 0$ V to $\Psi = 0.3$ V, the simulations were run for 800 ns, treating the first 200 ns as equilibration phase, since for lower potential differences the simulations required a long production run for the capacitances to converge. Both differential capacitances are bell-shaped. The agreement between simulations and DFT is remarkably good, and compared to the results in Fig. 3.4.3(b), there is little to no qualitative difference between C_N and C_μ .

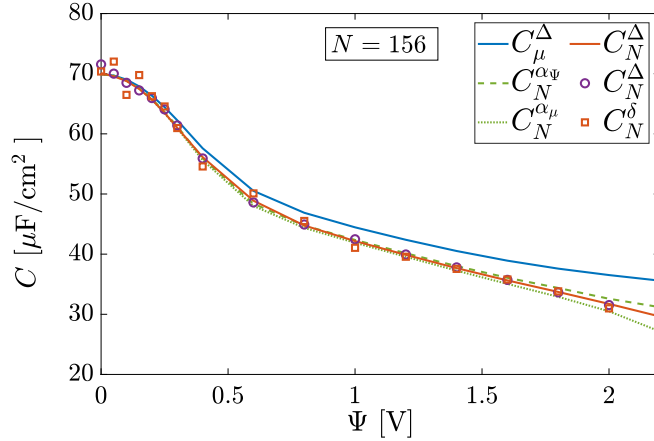


Figure 3.4.4: The differential capacitance as a function of potential difference between the electrodes, using BD and DFT, for a system containing 156 ion pairs. Because the number of ion pairs is fixed, their chemical potential varies with the electrostatic potential difference.

The small qualitative difference, especially at small potential differences, is mainly due to the relatively large number of ions in the system and therefore a correspondingly large reservoir concentration. For comparison, the number of ions at $\Psi = 0.2$ V in Fig. 3.4.3 is 51, while only at $\Psi = 2$ V it is 156. The camel shaped curve in C_μ is only existent for small reservoir concentrations $\rho_r < 1.5$ M and bell shaped otherwise. Hence, no camel-shaped capacitance curve is observed within these parameters.

3.5 DISCUSSIONS, CONCLUSIONS AND OUTLOOK

We presented ionic density profiles for a broad range of parameters applicable to aqueous electrolytes confined between a planar cathode and anode, and found very good agreement between results from DFT calculations and BD simulations. Both methods were also used to calculate differential capacitances, either C_μ at constant ionic chemical potential μ or C_N at constant number N of ions, via several routes. For a fixed chemical potential of mono-valent ions, at which the ionic reservoir concentration equals $\rho_r = 1$ M, the capacitance curves obtained from DFT and BD are overall in good agreement. The DFT prediction for the capacitance at fixed N , however, gave two somewhat different results due to the approximation for the electrostatic part of the employed functional. Nevertheless, the DFT predictions bracket those of the BD simulations, except at potential differences between cathode and anode below 0.3 V where the simulations were extremely slow. Interestingly, the qualitative difference between C_μ and C_N is substantial, where C_μ is camel shaped and C_N is bell shaped. This has to do with the nonlinear relation between μ and N . Furthermore, C_μ is found from a linear cut through the landscape in the three-dimensional space spanned by $\{\sigma, \Psi, \mu\}$, whereas C_N is the result of a non-trivial path through this landscape. We also considered capacitance curves at constant numbers of ions, $N = 156$, and found excellent agreement between DFT and BD simulations. In this case there is no qualitative difference between C_μ and C_N . Let us stress the time it takes to obtain the results from DFT

and BD simulations. A typical BD simulation of a state point took 2 to 3 days on 32 cores, whereas the DFT calculations took not even 2 seconds on a regular laptop, which amounts to a difference of about 7 orders of magnitude. The accuracy that is lost by applying DFT on these systems is very small, as we have shown throughout this chapter.

We conclude that with DFT one can obtain the same accuracy in *structural and thermodynamic* quantities as in BD simulations, at least for aqueous systems. This allows one to explore parameter space much more effectively and to study the properties of these systems thoroughly. A drawback of DFT is that it gives only an equilibrium description of the system, whereas BD simulations also provide the dynamics. We furthermore conclude that one needs to be careful and specify the differential capacitance that is being studied, e.g. C_μ or C_N , because they can differ both qualitatively and quantitatively. Also the natural choice changes depending on the method employed i.e. C_μ for DFT and C_N for BD, meaning the direct comparison of results from different methods is not straightforward.

A natural next step will be to divert from aqueous systems, to study systems with a lower dielectric constant. An interesting direction will be to study room temperature ionic liquid (ILs). Although the concentration of $\rho_r = 5$ M in Fig. 3.4.2(b) is comparable to that of ionic liquids, the dielectric constant here is considerably higher due to the solvent. It is not sufficient to simply reduce the dielectric constant and redo the calculations, since the electrostatic correlations become much stronger at the low dielectric constants of ILs: a cation-anion pair of sub-nm diameter will bind at contact by Coulombic attractions of several tens of $k_B T$. It is therefore not evident whether DFT or BD simulation will work in this regime. Moreover, the ionic shape in ILs is often non-spherical and needs to be accounted for in DFT. Interestingly, there have been developments in DFT to account for chain-like ions and molecules [153], and these have been applied to some extent to study ILs [118, 119, 120, 121, 122, 123]. Besides chain-like ions, another approach to implement shape and polarizability is via molecular DFT [154, 155, 156, 157]. Although molecular DFT has been mostly applied to model water, it might prove worthwhile to use this approach for ionic liquids in the future. Not only DFT is challenging at lower dielectric constant, but also simulations become much more challenging due to clustering that occurs at low dielectric constants as a result of the stronger electrostatic interactions. This leads to longer simulation times, which were already non-negligible in the aqueous systems. Hence, a proper functional can provide the means to study ILs and electrolytes at low dielectric media effectively.

A different line of investigation would be the study of the differences of the differential capacitance C_N and C_μ . Until now the distinction has not often been made explicitly and further studies are needed to map out the properties and relations between both.

APPENDIX

3.A THERMODYNAMICS DERIVATION

For details see Ref.[158]. The differential for surface grand potential γ (or also called the surface tension) can be derived from taking the differential of $\Omega = -pV + \gamma A$ and equating it with Eq. (3.6), i.e.

$$d\Omega = -pdV - Vdp + \gamma dA + Ad\gamma \quad (3.16)$$

$$= -SdT - pdV - \sum_j N_j d\mu_j - A\sigma_L d\Phi_L - A\sigma_R d\Phi_R + \gamma dA - fdH. \quad (3.17)$$

One now needs to separate the volumetric bulk terms from the surface terms. For convenience, let us define $N_j = V\rho_{r,j} + A\Gamma_j$ and $S = Vs_r + As_s$, where $\rho_{r,j}$ and s_r denote the particle density and the entropy density in the reservoir, respectively, while Γ_j denotes the adsorption of species j and s_s the areal excess entropy. This separation into volumetric and surface terms allows us to properly gather the volume terms on the left and the surface terms on the right of the equation, i.e.

$$-V\left(dp - s_r dT - \sum_j \rho_{r,j} d\mu_j\right) = A\left(-d\gamma - s_s dT - \sum_j \Gamma_j d\mu_j - \sigma_L d\Phi_L - \sigma_R d\Phi_R - fdH\right). \quad (3.18)$$

Given that the surface has no influence on the volume term, both sides vanish and we obtain both the Gibbs-Duhem as well as the full Lippmann equation

$$dp = s_r dT + \sum_j \rho_{r,j} d\mu_j, \quad (3.19)$$

$$d\gamma = -s_s dT - \sum_j \Gamma_j d\mu_j - \sigma_L d\Phi_L - \sigma_R d\Phi_R - fdH. \quad (3.20)$$

The systems that we considered when calculating the capacitances were at constant temperature T and constant electrode separation H . Moreover, in those calculations we considered the RPM such that $\Gamma_+ = \Gamma_- \equiv \Gamma$ and $d\mu_+ = d\mu_- \equiv d\mu/2$ and we symmetrized the surface potentials so that $d\Phi_R = -d\Phi_L \equiv d\Psi/2$ and $\sigma_L = -\sigma_R \equiv \sigma$. The Lippmann equation in this situation simplifies to

$$d\gamma = -\Gamma d\mu - \sigma d\Psi. \quad (3.21)$$

Within the Ω ensemble $\sigma(\mu, \Psi)$ is a function of μ and Ψ , hence

$$d\sigma = \left(\frac{\partial\sigma}{\partial\Psi}\right)_\mu d\Psi + \left(\frac{\partial\sigma}{\partial\mu}\right)_\Psi d\mu.$$

Because $N(\mu)$ is a function of μ , we therefore find that

$$\left(\frac{\partial\sigma}{\partial\Psi}\right)_N = \left(\frac{\partial\sigma}{\partial\Psi}\right)_\mu + \left(\frac{\partial\sigma}{\partial\mu}\right)_\Psi \left(\frac{\partial\mu}{\partial\Psi}\right)_N, \quad (3.22)$$

which can be rewritten using the Maxwell relation $\left(\frac{\partial\sigma}{\partial\mu}\right)_\Psi = \left(\frac{\partial\Gamma}{\partial\Psi}\right)_\mu$, that can be obtained from Eq. (3.21), and the identity $\left(\frac{\partial\mu}{\partial\Psi}\right)_N = -\left(\frac{\partial\mu}{\partial N}\right)_\Psi \left(\frac{\partial N}{\partial\Psi}\right)_\mu$. Using the differential capacitances from Eq. (3.9) and introducing the compressibilities

$$\chi_\sigma = \left(\frac{\partial N/A}{\partial\mu}\right)_\sigma, \quad \chi_\Psi = \left(\frac{\partial N/A}{\partial\mu}\right)_\Psi, \quad (3.23)$$

and the Maxwell relation

$$\alpha_\mu := \left(\frac{\partial\Gamma}{\partial\Psi}\right)_\mu = \left(\frac{\partial\sigma}{\partial\mu}\right)_\Psi =: \alpha_\Psi, \quad (3.24)$$

one can rewrite Eq. (3.22) as

$$C_\mu - C_N = \frac{\alpha_\Psi^2}{\chi_\Psi} \geq 0. \quad (3.25)$$

Using the same relations, one can show that

$$\frac{C_\mu}{C_N} = \frac{\left(\frac{\partial\sigma}{\partial\Psi}\right)_\mu}{\left(\frac{\partial\sigma}{\partial\Psi}\right)_N} = \frac{-\left(\frac{\partial\sigma}{\partial\mu}\right)_\Psi \left(\frac{\partial\mu}{\partial\Psi}\right)_\sigma}{-\left(\frac{\partial\sigma}{\partial N}\right)_\Psi \left(\frac{\partial N}{\partial\Psi}\right)_\sigma} = \frac{\left(\frac{\partial\sigma}{\partial\mu}\right)_\Psi \left(\frac{\partial N}{\partial\sigma}\right)_\Psi}{\left(\frac{\partial\Psi}{\partial\mu}\right)_\sigma \left(\frac{\partial N}{\partial\Psi}\right)_\sigma} = \frac{\left(\frac{\partial N}{\partial\mu}\right)_\Psi}{\left(\frac{\partial N}{\partial\mu}\right)_\sigma} \quad (3.26)$$

$$= \frac{\chi_\Psi}{\chi_\sigma} \geq 1. \quad (3.27)$$

These relations allows us to relate the differential capacitance obtained from simulations C_N to the differential capacitance from DFT C_μ . Within DFT one can calculate C_μ , χ_Ψ and α_Ψ , which through Eq. (3.10) gives access to C_N . Notice the similarity with the relations between the heat capacity at constant pressure c_p and the heat capacity at constant volume c_V (see e.g. the thermodynamics book [159]). Although this derivation was done for the symmetric RPM, one can generalize these equations for any system. This is necessary when considering unequal ion sizes/valencies, but also when the potential on both electrodes differ. Hence, in general one needs to consider both electrodes separately.

3.B CALCULATION OF THE CAPACITANCE

The calculation of a differential capacitance C_N in BD using the fluctuation expression of Eq. (3.14) requires the evaluation of the constant C_0 accounting for the neglected thermal

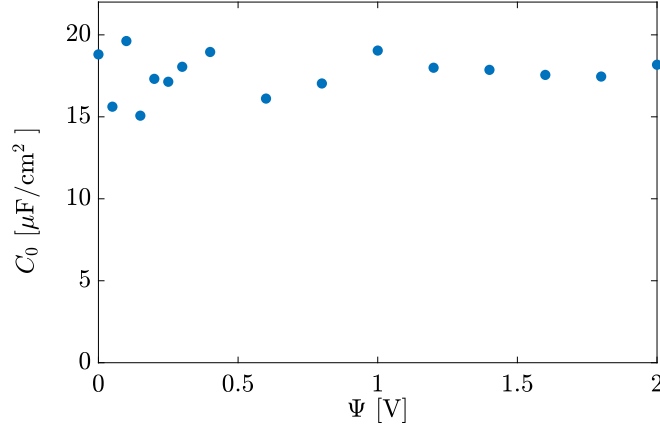


Figure 3.B.1: The difference in BD between the capacitance C_N as obtained by numerical differentiation of the surface charge with potential, see Eq. (3.9), and as obtained from the thermal charge fluctuations only, see Eq. (3.14), confirms that the constant C_0 in the latter expression is indeed independent of the potential difference.

charge fluctuations around the idealized charges calculated by CPM. Because C_0 is a property of the electrodes that depends neither on the number of ions nor on surface potential, its value was determined as the difference between the C_N obtained from the conventional charge-potential relation, see Eq. 3.9, and that obtained from the fluctuating contribution in Eq. (3.14) for $C_0 = 0$. This difference, plotted in Fig. 3.B.1 for a range of potentials, appears indeed to be a constant, with a value of $C_0 = 17.6 \mu\text{F cm}^{-2}$. The noise in the data is higher at low potentials, because the simulations converge more slowly at low potentials as well as due to the increased signal-to-noise ratio at the smaller step sizes in numerical differentiation.

3.C ADSORPTION INCONSISTENCY

The adsorption can be calculated via the two routes

$$\Gamma = - \left(\frac{\partial \gamma}{\partial \mu} \right)_{T, \Psi, H}, \quad \text{and} \quad \Gamma = \frac{1}{2} \sum_{j=\pm} \int_0^H dx (\rho_j(x) - \rho_{j,b}), \quad (3.28)$$

which are both plotted in Fig. 3.C.1 at a reservoir concentration of $\rho_r = 1 \text{ M}$. As a short note, any intrinsic Helmholtz free energy functional that is based upon a bulk expansion like the one we use for the electrostatics suffers from this inconsistency.

3.D CONSTANT POTENTIAL VERSUS FIXED CHARGE

The constant potential method (CPM) and fixed charge method (FCM) were compared by running simulations at zero voltage and zero charge, respectively. Based on DFT calculations, the equilibrium with a 1 M reservoir results in 47 ion pairs in the simulated slit. In the BD simulations the total charges on the left and right electrodes fluctuate around averages of $\pm 7 \text{ nC} \cdot \text{cm}^{-2}$, which is less than 1% of their standard deviations of $0.8 \mu\text{C} \cdot \text{cm}^{-2}$.

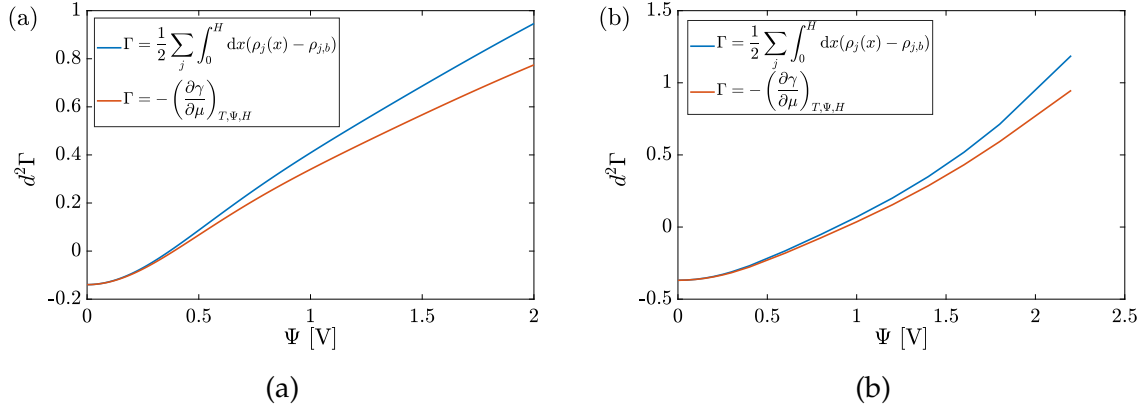


Figure 3.C.1: The inconsistency in the adsorption at (a) a fixed reservoir concentration of $\rho_r = 1$ M and at (b) a fixed number of ion pairs $N = 156$ (b).

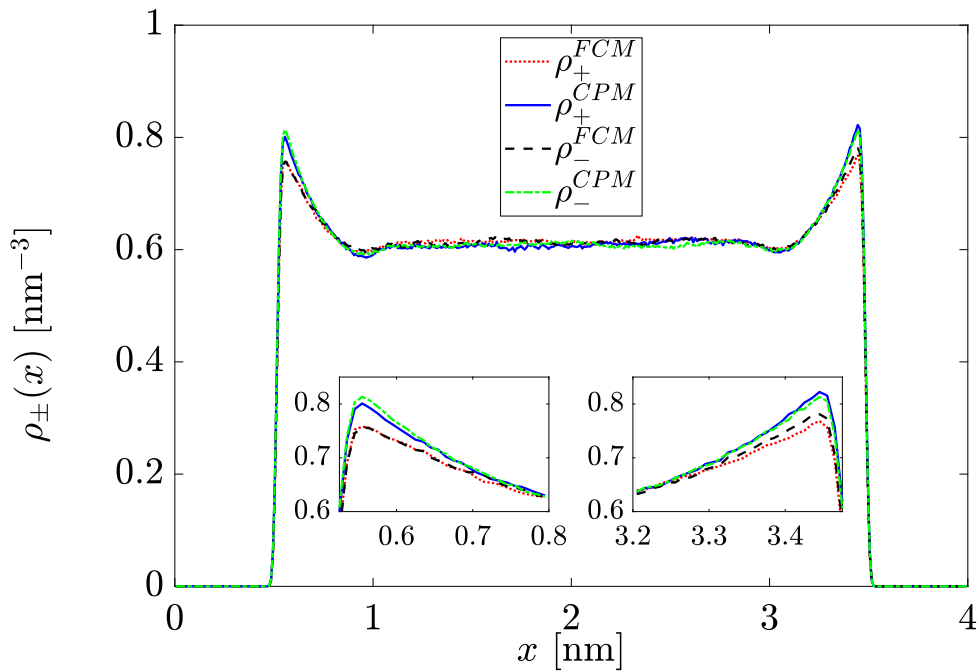


Figure 3.D.1: Number densities of cations, ρ_+ , and anions, ρ_- , for the fixed charged method (FCM) at vanishing surface charge on the electrodes and the constant potential method (CPM) at vanishing potential difference between the electrodes, for capacitors in equilibrium with a 1 M salt concentration. The insets show enlargements of the density peaks adjacent to the electrode surface.

Hence, the mean total charge on the electrodes is essentially zero. The ionic number densities in both CPM and FCM simulations are similar, see Fig. 3.D.1. The slightly higher density peaks near the electrodes for CPM are probably caused by the ions inducing a mirror charge in the electrode and being attracted by that mirror charge; this effect evidently does not occur at fixed wall charges.

4

THE DIFFERENTIAL CAPACITANCE AS A PROBE FOR THE ELECTRIC DOUBLE LAYER STRUCTURE AND THE ELECTROLYTE BULK COMPOSITION

In this chapter, we theoretically study the differential capacitance of an aqueous electrolyte in contact with a planar electrode, using classical density functional theory, and show how this measurable quantity can be used as a probe to better understand the structure and composition of the electric double layer at play. Specifically, we show how small trace amounts of divalent ions can influence the differential capacitance greatly and also how small ions dominate its behavior for high electrode potentials. In this study, we consider primitive model electrolytes and not only use the standard definition of the differential capacitance but also derive a new expression from mechanical equilibrium in a planar geometry. This expression reveals explicitly that the first layer of ions near the charged surface is key to its understanding. Our insights might be used as a guide in experiments to better understand the electrolyte–electrode interface as well as the (composition of the) bulk electrolyte.

Within a density functional theory that captures Coulomb and hard-sphere interactions accurately [2] for aqueous electrolytes, we calculate the differential capacitance for several electrolytes, changing the size and valency of the ions similar to work done in Refs. [152, 160, 161, 162, 163, 164, 165, 166, 167, 168, 169]. We also derive a new relation for the differential capacitance, which explicitly shows that the response of the first layer of ions near the electrode to the applied potential on the electrode is key to its understanding. We utilize this insight to understand two- and three-component electrolytes (the latter of which was also the subject of Ref. [169]) and explain how impurities can have a large effect on the differential capacitance.

4.1 DIFFERENTIAL CAPACITANCE

4.1.1 *The System*

As mentioned in the introduction, we wish to focus on EDL capacitors, of which there is a variety of different types, each having a different electrode-electrolyte combination [170]. For now, we consider two porous (carbon) electrodes held at a potential difference Ψ immersed in an aqueous electrolyte at room temperature T and dielectric constant ϵ . We will focus on a single pore inside one electrode, and model it as two planar surfaces with the same static surface potential Φ_0 , separated by a distance H [171, 172], as depicted in Fig. 4.1.1. We stress that the surface potential Φ_0 on the surfaces of the pore is w.r.t. a potential in a macroscopic electrolyte reservoir (the space between the two electrodes), while Ψ is the potential difference between the two electrodes in the EDL capacitor.

We will employ the primitive model (PM) in which the solvent is treated as a continuous dielectric medium. The properties of the solvent can then be completely captured by a single parameter: the Bjerrum length $\lambda_B = e^2\beta/4\pi\epsilon_r\epsilon_0$, where e is the proton charge and $\beta = 1/k_B T$ the inverse temperature. The Bjerrum length of water at room temperature is $\lambda_B = 0.73$ nm, which will be kept constant throughout this work. The ions of species j are modeled as hard spheres with diameter d_j and a centro-symmetric charge ez_j with z_j denoting the valency; the pair potential $u_{ij}(r)$ between ions of species i and j separated by a distance r is described by

$$\beta u_{ij}(r) = \begin{cases} \infty, & \text{for } r < d_{ij}; \\ z_i z_j \frac{\lambda_B}{r}, & \text{for } r \geq d_{ij}, \end{cases} \quad (4.1)$$

where $d_{ij} = (d_i + d_j)/2$. Note that the PM neglects dispersion and polarizability. We denote the bulk concentration of ion species j in the macroscopic electrolyte reservoir between the two electrodes by $\rho_{b,j}$, and define the total ionic packing fraction in the bulk as

$$\eta_b = \frac{\pi}{6} \sum_j d_j^3 \rho_{b,j}. \quad (4.2)$$

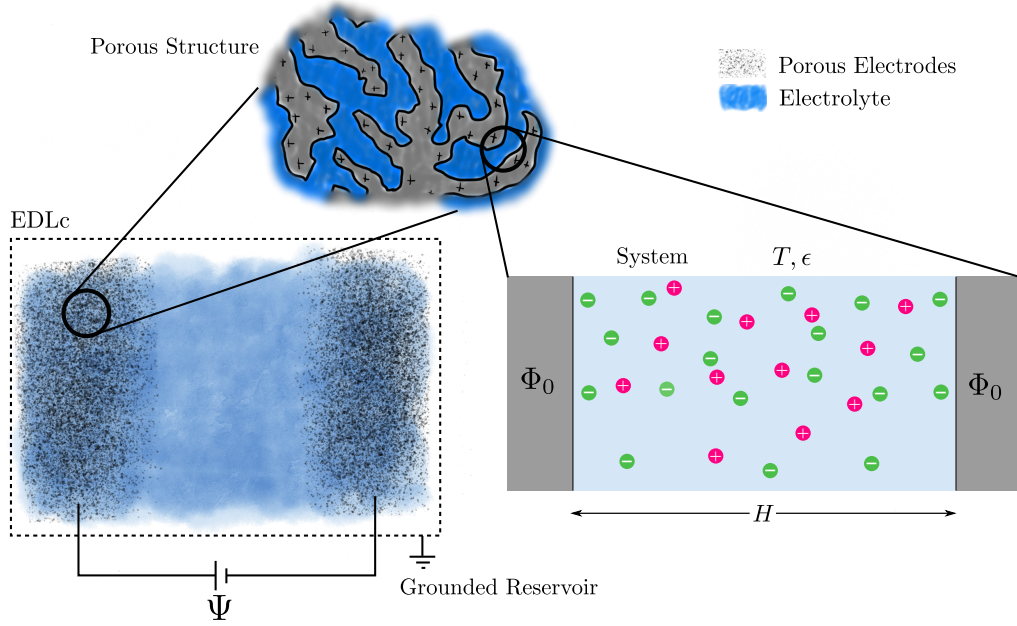


Figure 4.1.1: An illustration of an EDL capacitor and its structure. The EDL capacitor within the dashed box contains two porous electrodes (black dots), held at a potential difference Ψ , through which the electrolyte (blue) can flow. Zooming in on a porous electrode reveals a lot of structure which is depicted on top. Throughout this chapter the focus lies on one tiny part of the electrode (the pore of interest), which we consider our system, and model it as two parallel charged surfaces separated by a distance H being part of the same electrode. Hence, the potential on the two surfaces, denoted by Φ_0 , is the same and measured w.r.t. the potential in the reservoir, which we assume to be grounded. Invoking the primitive model reduces the solvent to a continuous dielectric medium at temperature T and with uniform dielectric constant ϵ .

When all particles have the same diameter and valency, the model is referred to as the Restrictive Primitive Model (RPM). The bulk RPM is completely characterized by the ionic bulk concentration and the dimensionless temperature $T^* = d/\lambda_B$. We stress that the medium and the diameters are chosen such that $T^* \gg T_c^* = 0.05$ the critical temperature [173], e.g. in this chapter $\lambda_B = 0.73$ nm is fixed and the ion diameters range from $d_j = 0.2$ nm to $d_j = 1$ nm, for which T^* ranges from $T^* = 0.27$ to $T^* = 1.37$, respectively.

The (non-electrostatic part of the) external potential that determines the pore size reads

$$V_{ext}^j(x) = \begin{cases} \infty & \text{for } x \leq \frac{d_j}{2}; \\ 0 & \text{for } \frac{d_j}{2} < x < H - \frac{d_j}{2}; \\ \infty & \text{for } x \geq H - \frac{d_j}{2}, \end{cases} \quad (4.3)$$

which describes two planar hard walls positioned at $x = 0$ and $x = H$. Throughout this chapter, the surface separation is fixed at $H = 5$ nm. Note that the electrostatic part of the external potential, due to the surface charge on the electrodes, will be taken into account through the Poisson equation, as discussed in Appendix 2.A.

Within this simplification, we can controllably study the differential capacitance as a function of the surface potential Φ_0 , for several choices of the ion diameter d_j , valency z_j , and ionic bulk concentrations in the reservoir $\rho_{b,j}$.

4.1.2 Thermodynamics in the Pore

Let us now focus on a single pore as depicted in Fig. 4.1.1. The remainder of the electrode and the space between the electrodes we consider to be the ion and heat reservoir for the pore of interest. Assuming that the space between the electrodes is large enough, we can treat the pore of interest grand canonically. This justifies the introduction of a bulk ionic concentration $\rho_{b,j}$ (corresponding to a fixed ionic chemical potential μ_j) in the reservoir that is independent of the electric potential difference Ψ between the electrodes. Exchange of ions between the system and reservoir takes place and we assume equilibrium. The surface potential Φ_0 on the surfaces in the pore is fixed, which allows exchange of electronic charge between the electrode and a charge reservoir; however, no charge exchange takes place between electrode and the electrolyte, i.e. no electrochemistry is considered. The pore also has a fixed volume $V = AH/2$ (rigid electrode) with total surface area A , and temperature T . To summarize, the system is described by a $\{\mu\}, V, T, \Phi_0, A, H$ ensemble, characterized by the grand potential $\Omega(\{\mu\}, V, T, \Phi_0, A, H)$ [2], where the brackets $\{\mu\}$ denote the set of chemical potentials of each of the ion species. The differential of Ω for this system reads

$$d\Omega = -pdV - SdT - \sum_j N_j d\mu_j - Qd\Phi_0 + \gamma dA - f dH, \quad (4.4)$$

where N_j is the average number of ions of species j in the pore, p the pressure, Q the electronic charge on both surfaces of the pore, γ the electrode-electrolyte surface tension, and f the force between the surfaces that are separated by a distance H . It is convenient to separate the volumetric and areal contributions in Eq. (4.4), and write $\Omega = -p(T, \{\mu\})V + \gamma(T, \{\mu\}, \Phi_0, H)A$ as two separate differentials [2]

$$dp = s_b dT + \sum_j \rho_{b,j} d\mu_j, \quad (4.5)$$

$$d\gamma = -s_s dT - \sum_j \Gamma_j d\mu_j - \sigma d\Phi_0 - \frac{f}{A} dH, \quad (4.6)$$

where S and N_j have been separated into a volumetric and areal part according to $S = Vs_b + As_s$, and $N_j = V\rho_{b,j} + A\Gamma_j$ with $\rho_{b,j}$ the bulk concentration and Γ_j the adsorption of species j . The average electronic surface charge density is denoted by $\sigma = Q/A$ and obeys the charge neutrality condition

$$\sigma = - \sum_j ez_j \Gamma_j. \quad (4.7)$$

Eq. (4.5) is the Gibbs-Duhem equation and Eq. (4.6) the Lippmann equation.

Now the question arises: what does this have to do with capacitances? The short answer to this question is that the (areal) differential capacitance is defined by

$$C_{\mu,T,H} = \left(\frac{\partial \sigma}{\partial \Phi_0} \right)_{\mu,T,H} \quad (4.8)$$

$$= - \left(\frac{\partial^2 \gamma}{\partial \Phi_0^2} \right)_{\mu,T,H}, \quad (4.9)$$

which opens the door for the longer answer. First of all, it turns out that there is not *one* differential capacitance C , but a whole set of differential capacitances, one for each ensemble. This is similar to constant-volume and constant-pressure heat capacities, and isothermal and isentropic compressibilities, for instance. Throughout this chapter we will study the differential capacitance at fixed temperature T and surface separation H , and simplify the notation: the ensemble in Eq. (4.4) gives rise to C_{μ} , while an $\{N\}, V, T, \Psi, H$ ensemble would give rise to C_N . Those two are, in fact, not unrelated and follow similar thermodynamic identities as those of the heat capacities at constant volume or pressure [2, 158]. We will focus on $C_{\mu}(\Phi_0, \{\mu\})$.

Before we continue, let us briefly consider the electric free energy that can be stored inside a pore at fixed $\{\mu\}, V, T, H$. This follows from Eqs. (4.4) and (4.8) as

$$\Omega(\Phi_2) - \Omega(\Phi_1) = -A \int_{\Phi_1}^{\Phi_2} d\Phi_0 \sigma(\Phi_0) = -A \int_{\Phi_1}^{\Phi_2} d\Phi \int_{\Phi_{PZC}}^{\Phi_0} d\Phi'_0 C_{\mu}(\Phi'_0), \quad (4.10)$$

where Φ_{PZC} is the potential of zero charge (PZC), i.e. the potential for which the surface charge density σ vanishes. To grasp the underlying physics, let us consider the case that $\Phi_{PZC} = 0$, and choose $\Phi_1 = 0$ and $\Phi_2 = \Phi_0 > 0$, for which we can write (see Appendix 4.A)

$$E_{\text{cap}} = \Omega(0) - \Omega(\Phi_0) = 2A \int_0^{\Phi_0} d\Phi' (\Phi_0 - \Phi') C_{\mu}(\Phi'), \quad (4.11)$$

where we note that $\Omega(0) > \Omega(\Phi_0)$. For a potential-independent capacitance, e.g. a conventional two-plate capacitor, one finds the known results $E_{\text{cap}} = \frac{1}{2} \mathcal{C} \Phi_0^2$, with $\mathcal{C} = AC_{\mu}$ the total capacity. The reason why it is very convenient to study the differential capacitance, is because that quantity can be measured in voltammetric experiments, while measuring the surface charge is extremely difficult. By using Eq. (4.11) one is therefore also able to measure the energy by measuring the differential capacitance as a function of the applied potential.

4.1.3 Differential Capacitance Revisited

Before tackling the primitive-model electrolyte confined between two hard walls by Density Functional Theory (DFT), let us first discuss the mechanical equilibrium in a planar

geometry. The xx (normal) component of the pressure tensor within the pore follows from the force balance [174, 175]

$$p_{xx}(H) = \sum_j \int_0^H dx \rho_j(x) F_x^j(x), \quad (4.12)$$

where $\rho_j(x)$ is the local density of species j , $F_x^j(x) = -\partial V_j(x)/\partial x$ the normal force on the surface due to the full interaction potential $V_j(x)$ (including the electrostatic interactions due to the surface charge). If the integral in Eq. (4.12) does not depend on H , which is the case when the range of F_x^j is much smaller than H , then $p_{xx}(H) = p$ is the actual bulk pressure of the electrolyte and Eq. (4.12) reduces to [174, 175]

$$\beta p = \sum_j \rho_j \left(\frac{d_j}{2} \right) - \frac{\beta \sigma^2}{2\epsilon_r \epsilon_0}, \quad (4.13)$$

where it is understood that $\rho_j(d_j/2)$ is the limit $\lim_{x \downarrow d_j/2} \rho_j(x)$. This sum rule relates the bulk pressure p of the ion reservoir to the local contact densities $\rho_j(d_j/2)$ and the surface charge density σ . In the case of two charged hard parallel surfaces separated by a finite distance, the integral in Eq. (4.12) does depend on H , especially at low ionic bulk concentrations. However, with the parameters chosen throughout this chapter, this only plays a minor role and can be neglected for all practical purposes. Let us note that for soft particle-wall interactions the integral in Eq. (4.12) does not reduce to a contact value and needs to be fully evaluated. Nonetheless, the gradient of the particle-wall interaction is by construction largest at values close to the contact distance $d_j/2$ at which it gives the largest contribution to the integral.

One interesting feature of Eq. (4.13) is that the global bulk pressure is independent of the surface potential Φ_0 , while the local quantities are not. Therefore, taking the derivative of Eq. (4.13) w.r.t. Φ_0 leads to

$$0 = \sum_j \left(\frac{\partial \rho_j(d_j/2)}{\partial \Phi_0} \right)_\mu - \frac{\beta \sigma}{\epsilon_r \epsilon_0} \left(\frac{\partial \sigma}{\partial \Phi_0} \right)_\mu, \quad (4.14)$$

where we recognize the differential capacitance given in Eq. (4.8) in the second term. Hence, Eq.(4.14) can be rewritten as

$$C_\mu = \frac{\epsilon_r \epsilon_0}{\beta \sigma} \sum_j \left(\frac{\partial \rho_j(d_j/2)}{\partial \Phi_0} \right)_\mu, \quad (4.15)$$

where in the summand one can recognize a fluctuation profile as discussed in Ref. [176]. Within the RPM, Eq. (4.15) simplifies to

$$C_\mu = \frac{\epsilon_r \epsilon_0}{\beta \sigma} \left(\frac{\partial \rho_N(d/2)}{\partial \Phi_0} \right)_\mu, \quad (4.16)$$

where we introduce the total ion density

$$\rho_N(x) = \sum_j \rho_j(x). \quad (4.17)$$

Hence, the differential capacitance is to a large extent dictated by the response of the number density $\rho_N(d/2)$ at contact (first layer of ions) to the potential Φ_0 . As stated previously, this key-concept will stand even for soft particle-wall interactions; the contact value will be replaced by an integral, whose integrand is peaked near $x = d_j/2$.

Interestingly, another observation leads to yet another expression for the differential capacitance. Due to the ions having a hard core interaction with the wall and a central charge, the charge density for $x < d/2$ (also for $x > H - d/2$) vanishes, leading to a linear drop of the electrostatic potential profile $\Phi(x)$ in that region. Hence, the potential at $x = d/2$ is given by

$$\Phi(d/2) = \Phi_0 + \left. \frac{\partial\Phi(x)}{\partial x} \right|_{x=0} \frac{d}{2} = \Phi_0 - \frac{d}{2\varepsilon_r\varepsilon_0} \sigma, \quad (4.18)$$

where we used Gauss' law. Taking again the derivative w.r.t. the surface potential Φ_0 and reordering results in

$$C_\mu = \frac{2\varepsilon_r\varepsilon_0}{d} \left[1 - \left(\frac{\partial\Phi(d/2)}{\partial\Phi_0} \right)_\mu \right], \quad (4.19)$$

which was also derived in a slightly different form in Ref. [177]. The region between $x = 0$ and $x = d/2$ is sometimes referred to as the Stern layer [178], with the corresponding Stern-layer capacitance [152, 179, 180, 181] $C_s = 2\varepsilon_r\varepsilon_0/d$, although that will not be used in this work ¹.

The relations in Eqs. (4.15) and (4.19) will allow for a new and independent investigation into the differential capacitance, which helps in understanding the underlying physics.

4.1.4 Density Functional Theory

We will use the MSAC functional described in Section 2.1.2.2 and validated for a wide variety of parameters in Chapter 3. Because the grand potential at its minimum is the

¹ The Stern layer separates the diffuse layer from the electrode, each layer having their own capacitance, which in a serial circuit gives the total capacitance C_{EDL} of the EDL, given by

$$\frac{1}{C_{EDL}} = \frac{1}{C_s} + \frac{1}{C_{DL}}.$$

With little effort, one can show that, by introducing the Stern-layer capacitance C_s , the capacitance of the diffuse layer reads

$$C_{DL} = C_s \left[\left(\frac{\partial\Phi_0}{\partial\Phi(d/2)} \right)_\mu - 1 \right],$$

which can take negative values in case of overscreening. Hence, splitting the EDL into a diffuse layer and the Stern layer seems not to be desirable for a generic system, and we will not further distinguish between Stern layers and other layers, but instead only discuss the total capacitance C_μ .

actual grand potential of the system, i.e. $\Omega[\{\rho_0\}] = \Omega(\{\mu\}, V, T, \Phi_0, H)$, DFT is a powerful theoretical framework to combine thermodynamics and structure as it gives access to the thermodynamics of the system via the density profiles. Furthermore, it gives directly both the ionic charge density profile $q(x) = \sum_j z_j \rho_j(x)$ and via the Poisson equation also the potential profile $\Phi(x)$ from which the surface charge follows, where we note that in a planar geometry the profiles only depend on the out-of-plane coordinate x . In principle, we have thus access to C_μ via any of the routes in Eqs. (4.8), (4.9), (4.15), and (4.19) laid out in the previous sections; however, the results that will be presented are calculated from Eq. (4.8), while the other definitions are used as a tool to interpret the data. Nevertheless, we have validated each of the Eqs. (4.8), (4.9), (4.15), and (4.19) for the sake of consistency.

4.1.5 Simulations

Although DFT is a very powerful framework, the intrinsic functionals \mathcal{F}_{ex}^{HS} and \mathcal{F}_{ex}^{ES} are approximate and need to be tested against simulations or experiments. Although we do not go into detail here on any specific type of simulation, we wish to present a novel sumrule that connects quantities that can be measured in simulation but not with DFT. The quantity of interest throughout this chapter is the differential capacitance. From elementary statistical physics one can derive the relation [23, 41, 158, 182]

$$C(\Phi_0) = \frac{\beta}{A} (\langle Q^2 \rangle - \langle Q \rangle^2), \quad (4.20)$$

where the brackets $\langle \dots \rangle$ indicate either a time or an ensemble average. The ensemble average can either include a fixed number of ions N_\pm , or a fixed chemical potential μ_\pm .

Inspired by Ref. [176], we also found a new expression to calculate the differential capacitance within our ensemble, namely

$$C = \frac{\varepsilon_r \varepsilon_0}{\sigma} \sum_j [\langle \hat{\rho}_j(d_j/2)Q \rangle - \langle \hat{\rho}_j(d_j/2) \rangle \langle Q \rangle], \quad (4.21)$$

where $\hat{\rho}_j(\mathbf{r}) = \sum_{i=1}^{N_j} \delta(\mathbf{r} - \mathbf{r}_i)$ denotes the density operator. Note that we use the notation $\sigma = \langle \sigma \rangle$ throughout the chapter, but it is important to keep in mind that the surface charge $\sigma = Q/A$ fluctuates as a consequence of fixing the surface potential Φ_0 .

Employing DFT causes the loss of direct information on the fluctuations, because DFT only returns equilibrium density profiles. Hence, within our DFT approach one does not have direct access to the quantities such as $\langle Q^2 \rangle$ and $\langle \hat{\rho}_j(d_j/2)Q \rangle$. However, they can in principle be measured within simulations.

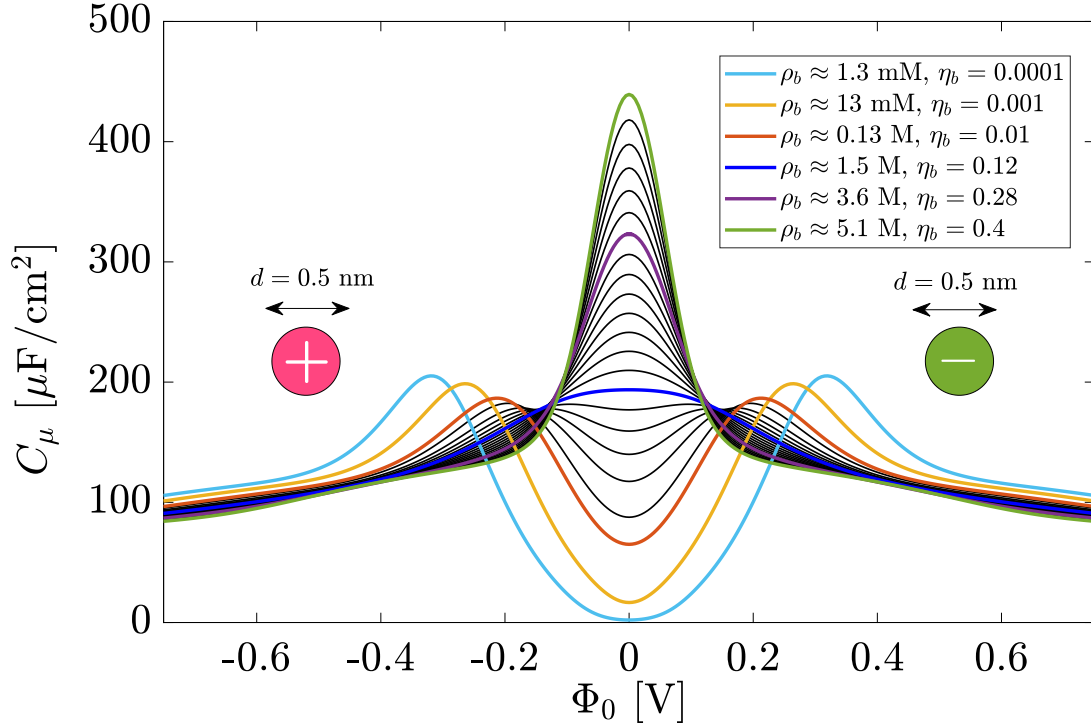


Figure 4.2.1: The differential capacitance C_μ for the RPM with monovalent ions with diameter $d = 0.5$ nm and for a surface separation $H = 5$ nm and Bjerrum length $\lambda_B = 0.73$ nm. The curves are shown for concentrations ranging from $\rho_b = 1.3$ mM (light-blue) to $\rho_b = 5.1$ M (green) with several concentrations in between. The concentrations for the other colored lines are given in the legend; the concentration for the black lines are equally spaced to illustrate the trend. The legend also shows the corresponding bulk packing fractions η_b .

4.2 CAPACITANCE CURVES

4.2.1 First Glance: Symmetric Electrolyte

The system that we investigate first is an RPM electrolyte consisting of two monovalent species of ions (i.e. $z_+ = -z_- = 1$), such that $\rho_{b,+} = \rho_{b,-} \equiv \rho_b$. In Fig. 4.2.1 we show the differential capacitance, calculated via Eq. (4.8), as a function of the applied voltage Φ_0 for ions with $d = 0.5$ nm at several ionic bulk packing fractions ranging from $\eta_b = 0.0001$ to $\eta_b = 0.4$, corresponding to bulk ionic concentrations ranging from $\rho_b \approx 1$ mM to $\rho_b \approx 5$ M. As stated previously, the surface separation is fixed at $H = 5$ nm and the solvent is characterized by $\lambda_B = 0.73$ nm. The foremost noticeable feature of Fig. 4.2.1 is the crossover around a bulk packing fraction $\eta_c \approx 0.12$ (blue line) from the so-called camel-shaped ($\eta_b < \eta_c$) to the bell-shaped curves ($\eta_b > \eta_c$). This crossover has been a subject in many theoretical and experimental studies [119, 121, 152, 165, 183, 184, 185, 186, 187, 188, 189, 190, 191], and is ascribed to excluded-volume effects. Let us, for convenience, introduce Φ^* as the surface potential at which the capacitance $C_\mu(\Phi_0)$ takes its maximum value at a given ρ_b or η_b , i.e. $C_\mu(\Phi^*) \geq C_\mu(\Phi_0)$. Then the camel-shaped capacitance curves correspond to a finite Φ^* , while the bell-shaped capacitance curves are characterized by $\Phi^* = 0$ V.

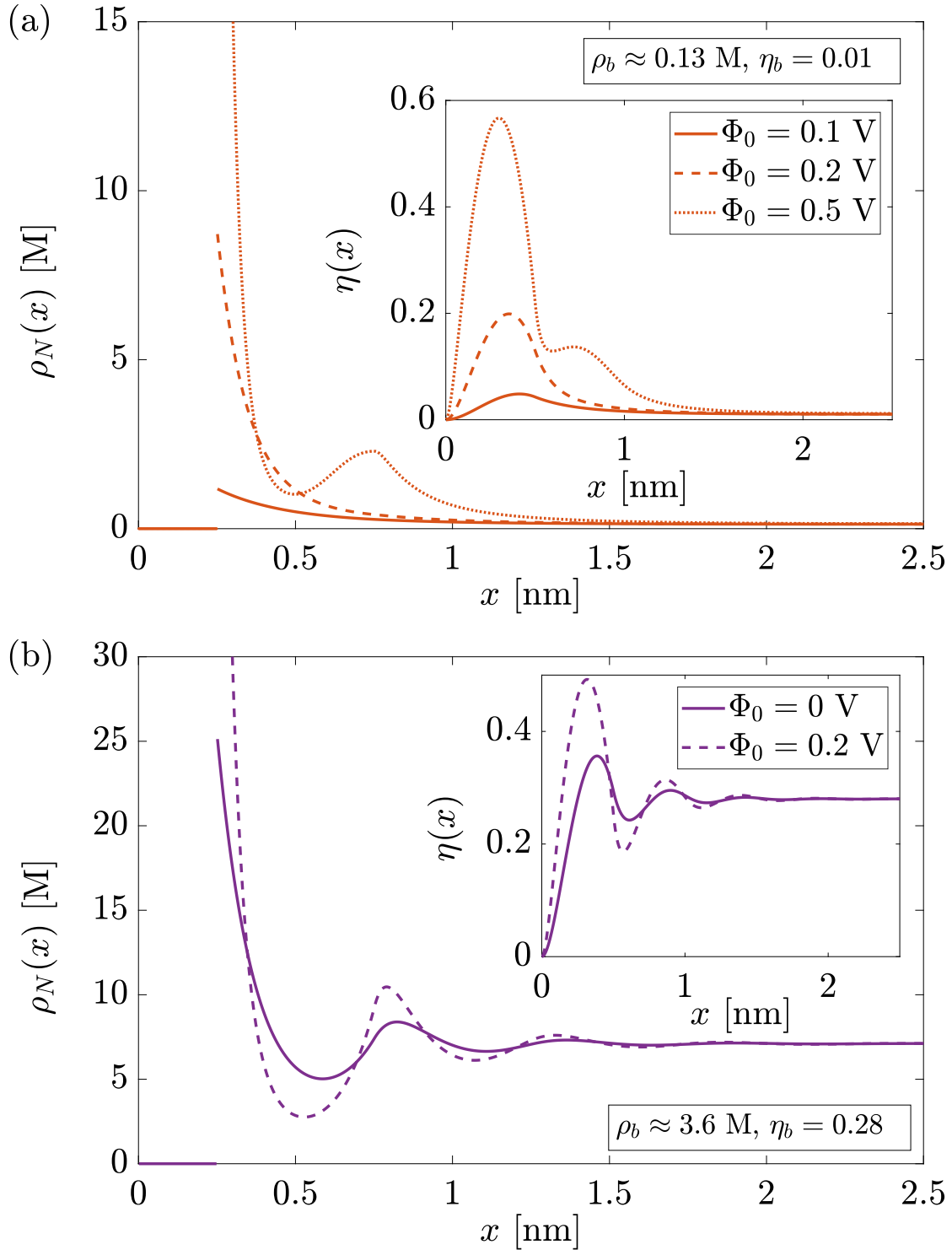


Figure 4.2.2: (a) The number density profiles $\rho_N(x)$ for the surface potentials $\Phi_0 = 0.1$ V (solid), $\Phi_0 = 0.2$ V (dashed), and $\Phi_0 = 0.5$ V (dotted) at a bulk concentration of $\rho_b \approx 0.13$ M (i.e. $\eta_b = 0.01$). The inset shows the local packing fraction $\eta(x)$ as defined in Eq. (4.22). The potential at which the capacitance has its maximum is $\Phi^* \approx 0.2$ V. For $\Phi_0 < \Phi^*$ the profiles only have one peak at $x = d/2 = 0.25$ nm, while for $\Phi_0 > \Phi^*$ the profiles have two peaks; the second located at $x = 3d/2 = 0.75$ nm. Around the maximum at $\Phi_0 \approx \Phi^*$ the second layer starts forming. (b) The number density profiles $\rho_N(x)$ for the surface potentials $\Phi_0 = 0$ V (solid) and $\Phi_0 = 0.2$ V (dashed) at a bulk concentration of $\rho_b \approx 3.6$ M (i.e. $\eta_b = 0.28$). The inset shows the local packing fraction $\eta(x)$ as defined in Eq. (4.22). This bulk concentration $\rho_b \approx 3.6$ M corresponds to the same-colored (purple) bell-shaped capacitance curve in Fig. 4.2.1.

To understand this crossover, one has to understand what causes the maximum in $C_\mu(\Phi_0)$. Consider the orange camel-shaped capacitance curve in Fig. 4.2.1 belonging to $\rho_b \approx 0.13\text{ M}$ (i.e. $\eta_b = 0.01 < \eta_c$) with $\Phi^* \approx 0.2\text{ V}$. For the same ρ_b (and in the same color) we present in Fig. 4.2.2(a) the number density profiles $\rho_N(x)$ for $\Phi_0 = 0.1\text{ V}$ (solid), $\Phi_0 = 0.2\text{ V}$ (dashed), and $\Phi_0 = 0.5\text{ V}$ (dotted). The inset shows, for the same state points, the profile of the weighted packing fraction, defined by ²

$$\eta(x) = \pi \sum_j \int_{x-d_j/2}^{x+d_j/2} dx' \rho_j(x') \left[\left(\frac{d_j}{2} \right)^2 - (x-x')^2 \right], \quad (4.22)$$

which reduces to Eq. (4.2) in the homogeneous bulk. Interestingly, while the density profile for $\Phi_0 < \Phi^*$ (solid) only has one (contact) peak at $x = d/2 = 0.25\text{ nm}$, the one for $\Phi_0 > \Phi^*$ (dotted) has a second peak at $x = 3d/2 = 0.75\text{ nm}$. Hence, the maximum in C_μ indicates a structural change, analogous to peaks in the heat capacity indicating (smooth) changes of the thermal occupancy of microstates. When we consider the purple bell-shaped capacitance curve in Fig. 4.2.1, belonging to $\rho_b \approx 3.6\text{ M}$ (i.e. $\eta_b = 0.28 > \eta_c$), and investigate the corresponding $\rho_N(x)$ and $\eta(x)$ in Fig. 4.2.2(b) for $\Phi_0 = 0\text{ V}$ (solid) and $\Phi_0 = 0.2\text{ V}$ (dashed), we find the presence of the second peak in $\rho_N(x)$ for both (and in fact for all) surface potentials. Hence, the maximum in $C_\mu(\Phi_0)$ is clearly related to the onset of layering of counter-ions near the surface, as is in fact also consistent with Eq. (4.15). Moreover, considering the profile of the weighted packing fraction (see insets in Figs. 4.2.2(a) and (b)) at $x = d/2 = 0.25\text{ nm}$, one finds that its value is close to or even larger than the packing fraction at which hard-sphere freezing takes place in the bulk (i.e. around $\eta_b \approx 0.5$). This suggests that the first layer of ions might in fact even be frozen [192], and invites a study into the in-plane structure of ions at the charged surface. However, that is beyond the scope of this chapter.

To characterize and interpret the crossover from camel- to bell-shaped curves further, let us consider the crossover potential $\Phi^*(\eta_b)$ as function of the bulk packing fraction η_b plotted in Fig. 4.2.3, for three ion diameters. The dashed line at $\eta_c \approx 0.12$ represents for $d = 0.5\text{ nm}$ the capacitance curve crossing over from two maxima at $\Phi_0 = \Phi^* > 0$ (camel) to one maximum at $\Phi_0 = \Phi^* = 0$ (bell). From Fig. 4.2.3, it is evident that the crossover is rather gradual and therefore we refer to a crossover rather than a transition. This is in line with the maximum in the capacitance curves being finite rather than infinite, the latter case would imply a thermodynamic phase transition. This graduality is found in the density profiles as well: where profiles for $\Phi_0 \ll \Phi^*$ and $\Phi_0 \gg \Phi^*$ can be easily discerned by the absence and presence of a second peak at $x = 1.5d = 0.75\text{ nm}$ (see Fig. 4.2.2(a)), those for potentials close to Φ^* cannot. The same holds for density profiles at $\Phi_0 = 0$; for low bulk concentrations layering is almost absent, while at high bulk concentrations layering is clearly present (see Fig. 4.2.2(b)), but one cannot qualitatively discern the two cases close to $\eta_b \approx \eta_c$.

² $\eta(x)$ is identical to the weighted density $n_3(x)$ from Fundamental Measure Theory [47].

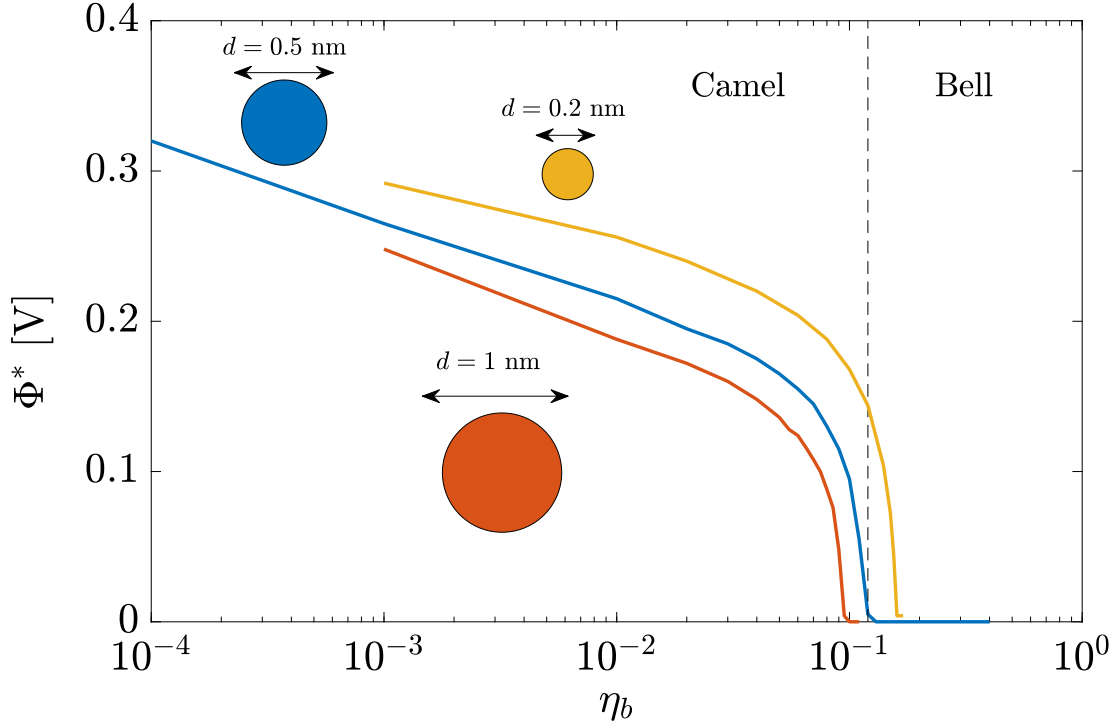


Figure 4.2.3: The surface potential Φ^* at which $C_\mu(\Phi_0)$ has its maximum as function of the bulk concentration expressed as the bulk packing fraction η_b , for the RPM with ion diameter $d = 0.2$ nm (yellow), $d = 0.5$ nm (blue), and $d = 1$ nm (orange). The vertical dashed line is located at $\eta_b = 0.12$ and represents the crossover for ions with $d = 0.5$ nm from camel-shaped capacitance curves to bell-shaped capacitance curves.

The results so far were all for ions with a common diameter $d = 0.5$ nm and $\lambda_B = 0.73$ nm. Let us now investigate the effect of ion size, keeping λ_B fixed at $\lambda_B = 0.73$ nm. To this end, we next consider ions of a common diameter $d = 0.2$ nm and $d = 1$ nm, for which $C_\mu(\Phi_0)$ is presented in Fig. 4.2.4 for a variety of ionic bulk concentrations. There is little qualitative difference in $C_\mu(\Phi_0)$ for the different ion sizes. However, quantitatively, one finds that the smaller the ions, the larger $C_\mu(\Phi_0)$ at a given bulk packing fraction η_b . It is important to note that ionic bulk concentration ρ_b and packing fraction η_b , although linearly related, are not the same quantity; small ions have a higher molarity at the same packing fraction and the balance between packing and electrostatics is quite different. Experimentally, one often characterizes bulk concentrations in molarity rather than packing fractions, which renders the ion diameter an important fit parameter. Fig. 4.2.4 shows that the ion size can determine the shape of $C_\mu(\Phi_0)$ at a given molarity ρ_b . We note, for instance, that the camel-bell crossover packing fraction η_c only changes slightly from $\eta_c \approx 0.1$ for $d = 1$ nm to $\eta_c \approx 0.15$ for $d = 0.2$ nm, while the crossover bulk concentration changes by two orders of magnitude from $\rho_c \approx 32$ M for $d = 0.2$ nm to $\rho_c = 0.16$ M for $d = 1$ nm. Fig. 4.2.4 also shows a bell-shaped capacitance curve for sufficiently concentrated electrolytes, and a camel-to-bell crossover for dilute electrolytes at a sufficiently high electrode potential, with a higher Φ^* for lower η_b and smaller d . The generally lower capacitance for larger ions can be understood qualitatively in terms of the close proximity of smaller ions to the electrode. This is explicit in Eq. (4.19),

in which C_μ is inversely proportional to the ion diameter d . Hence, a larger ion diameter results in an overall smaller $C_\mu(\Phi_0)$.

The results presented in this section evidently show that ion size is a key parameter that largely determines the magnitude of the differential capacitance at a given ionic bulk concentration.

4.2.2 Second Glance: Asymmetric Electrolytes

Let us now consider an asymmetric electrolyte consisting of cations with diameter $d_+ = 0.4$ nm and anions with diameter $d_- = 0.6$ nm. The voltage-dependent differential capacitance for this system is presented in Fig. 4.2.5(a), again for bulk packing fractions ranging from $\eta_b = 0.0001$ ($\rho_b \approx 1.1$ nm) to $\eta_b = 0.4$ ($\rho_b \approx 4.5$ M). The asymmetry in the electrolyte is reflected by the asymmetry of Fig. 4.2.5(a) w.r.t. $\Phi_0 \rightarrow -\Phi_0$; the smaller cations can approach the surface to closer distances than the anions, causing a larger capacitance for negative potentials compared to positive potentials. The capacitance $C_\mu(\Phi_0)$ at its maximum for the camel-shaped curves at $\Phi_0 < 0$ is therefore larger than that at $\Phi_0 > 0$, which motivates the introduction of the notation Φ_+^* and Φ_-^* for the maxima located at positive and negative potentials, respectively. For high bulk concentrations with only one maximum (bell-shaped curves), we keep using the notation Φ^* , which is not necessarily close to zero now that the symmetry is broken. In Fig. 4.2.5 we see that Φ^* does indeed not vanish in the asymmetric electrolyte, rather it is located at negative potentials, and seems for the present choice of parameters to converge to $\Phi^* \approx -0.03$ V at high bulk concentrations. This also implies that the potential of zero charge takes non-vanishing values.

In Fig. 4.2.5(b) the differential capacitance of the asymmetric electrolyte of Fig. 4.2.5(a) is compared to those of the symmetric RPM. We replot the six colored differential capacitance curves of the asymmetric electrolyte of Fig. 4.2.5(a) in black now, while in blue ($\Phi_0 > 0$) and red ($\Phi_0 < 0$) we plot those for the RPM with $d = 0.6$ nm and $d = 0.4$ nm, respectively, at the same bulk concentration ρ_b . For the three lowest bulk concentrations $\rho_b = 1.1$ nm, $\rho_b = 11$ nm, and $\rho_b = 0.11$ M, we see that the differential capacitance of the asymmetric electrolyte with $d_+ = 0.4$ nm and $d_- = 0.6$ nm (black) is indistinguishable from those of the RPM with $d = 0.4$ nm (red) at negative potentials and $d = 0.6$ nm (blue) at positive potentials. Hence, C_μ at negative potentials is fully dictated by the cations, while at positive potentials it is fully dictated by the anions. However, at higher bulk concentrations, close to the camel-bell transition, one finds differences between the RPM-approximation and the actual asymmetric electrolytes, although primarily only for $|\Phi_0| < 100$ mV. This can be explained by considering Eq. (4.15), where packing of asymmetric-sized ions in the first layer $\sum_j \rho(d_j/2)$ is evidently different from the RPM. Nevertheless, at higher surface potentials the differential capacitance of the asymmetric electrolyte follows again that of the RPM, because the counterions are fully repelled resulting in a similar packing as in the RPM.

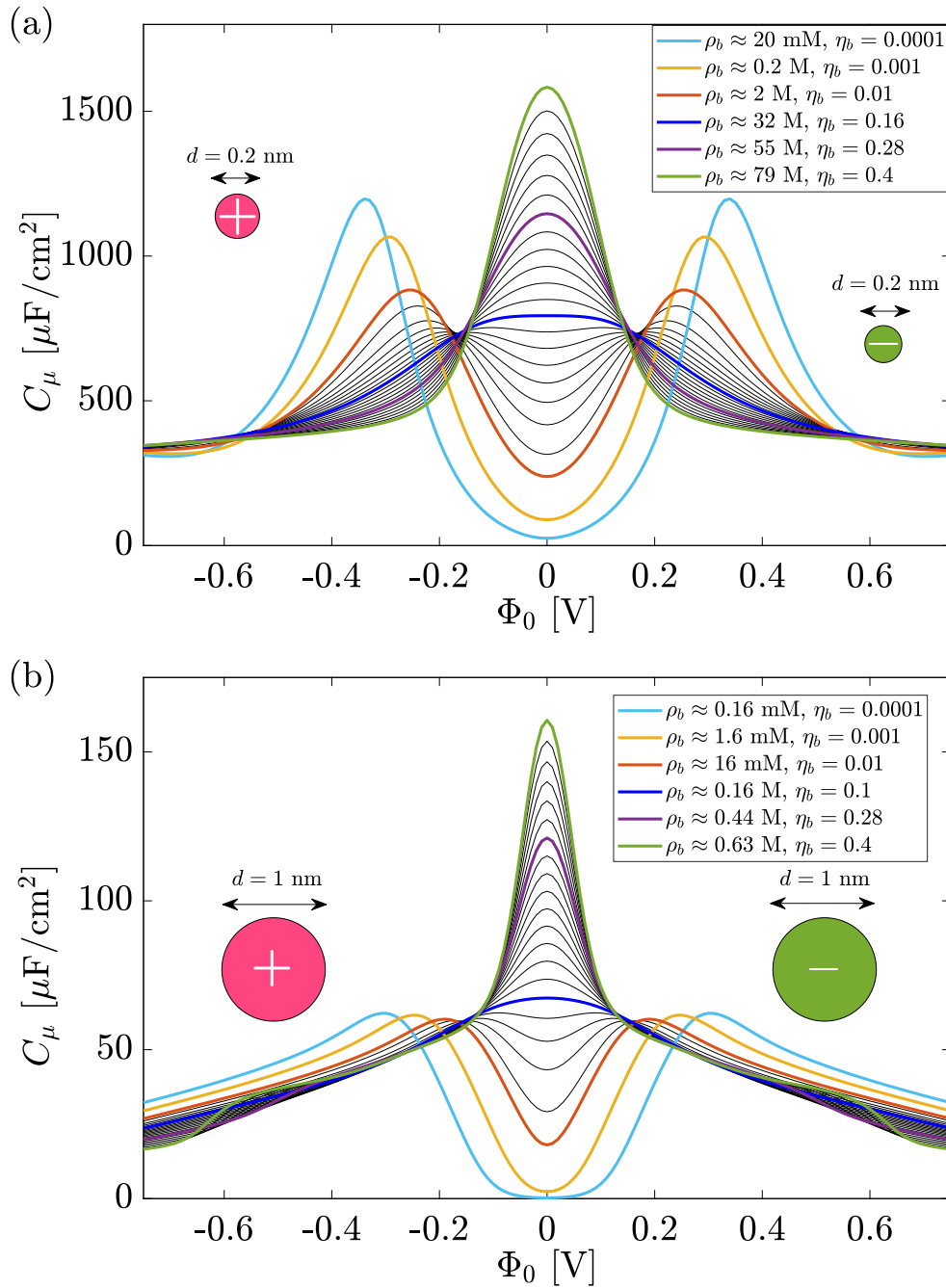


Figure 4.2.4: The differential capacitance for ions with diameter (a) $d = 0.2$ nm and (b) $d = 1$ nm for a surface separation $H = 5$ nm and Bjerrum length $\lambda_B = 0.73$ nm. The bulk concentration/packing fraction at which the camel-bell crossover occurs is depicted in dark blue, i.e. $\eta_c \approx 0.1$ ($\rho_c \approx 32$ M) for $d = 0.2$ nm and $\eta_c \approx 0.16$ ($\rho_c \approx 0.16$ M) for $d = 1$ nm.

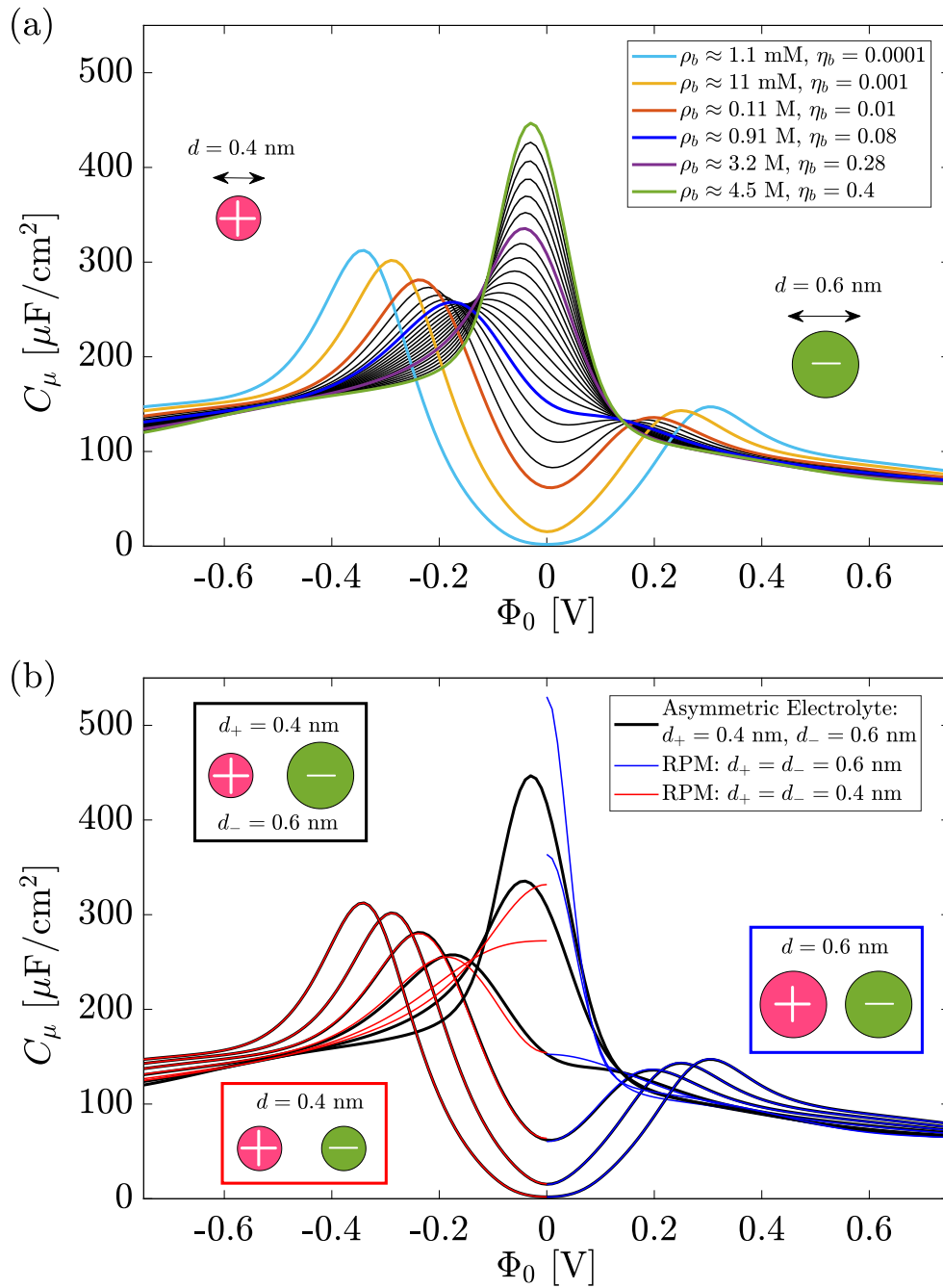


Figure 4.2.5: (a) The differential capacitance for an asymmetric electrolyte with $d_+ = 0.4$ nm and $d_- = 0.6$ nm for a surface separation $H = 5$ nm and Bjerrum length $\lambda_B = 0.73$ nm. The thick black curves in (b) correspond to the colored ones in (a) and are compared with the differential capacitance of the RPM with $d_+ = d_- = 0.4$ nm (red) and $d_+ = d_- = 0.6$ nm (blue) at the same bulk concentration ρ_b .

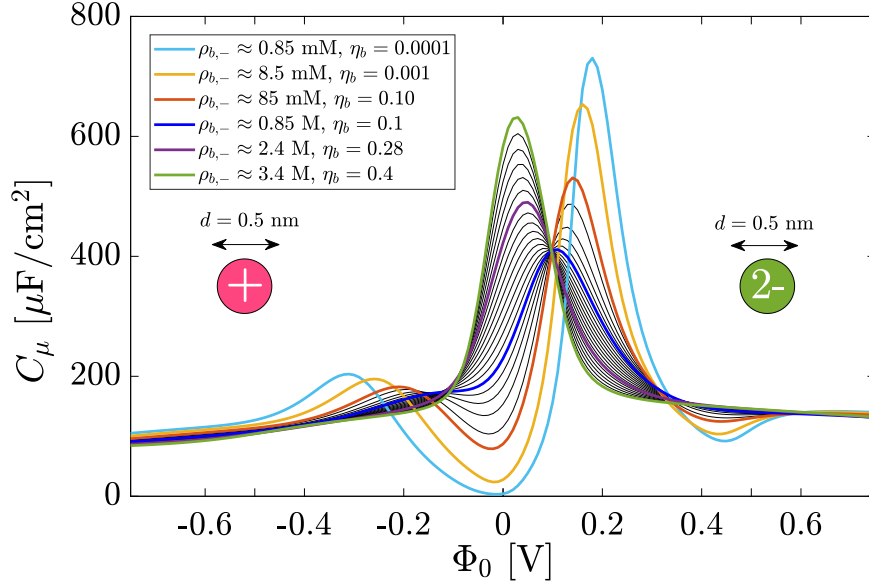


Figure 4.2.6: The differential capacitance for an asymmetric 1:2 electrolyte with $d_+ = d_- = 0.5$ nm. The bulk concentrations for the colored lines are given in the legend and range from $\rho_{b,-} = \rho_{b,+}/2 = 0.85$ mM to $\rho_{b,-} = \rho_{b,+}/2 = 3.4$ M.

Another type of asymmetric electrolyte that we consider is a 1:2 electrolyte in which $z_+ = 1$ and $z_- = -2$, for convenience with equal diameter $d_+ = d_- = 0.5$ nm. The capacitance curves for this system are given in Fig. 4.2.6, again for $H = 5$ nm and $\lambda_B = 0.73$ nm. First let us note that the maximum at positive potentials for bulk concentrations below $\rho_{b,-} = 0.85$ M is larger than that of the monovalent RPM at the same packing fraction (see Fig. 4.2.1 or consider the negative potentials). This is a consequence of the higher valency of the anions; fewer ions are needed to screen the charge on the surface and therefore layering/packing requires higher surface potentials, allowing more charge to be stored within the first layer. One peculiar feature that was not present in all previous monovalent cases is the minimum capacitance around $\Phi_0 \approx 0.4$ V (and therefore also a second maximum at $\Phi_0 = \Phi_{++}^* \approx 0.6$), which is caused by overscreening [152]. At such relative high surface potentials, the positively charged surface attracts the divalent anions to such an extent that it creates a layer of anions with negative charge that exceeds the magnitude of the charge on the surface. Therefore the ions further away from the electrode perceive the surface as being negatively charged, rather than positive, which causes a net attraction of positive ions. This is shown in Fig. 4.2.7(b) and (c), which presents the anion and cation density profiles, respectively, at the surface potentials indicated by the vertical lines in the capacitance curve of Fig. 4.2.7(a), for the bulk concentration of $\rho_{b,-} = \rho_{b,+}/2 \approx 85$ mM ($\eta_b = 0.1$). The inset in Fig. 4.2.7(b) shows the local packing fraction as defined by Eq. (4.22). For low surface potentials $\Phi_0 < \Phi_+^* \approx 0.14$ V (dashed-dotted lines) the behavior is similar to the RPM, but upon increasing the surface potential to $\Phi_+^* < \Phi_0 = 0.3$ V $< \Phi_{++}^*$ (dotted line) a clear peak in the cation density profile is formed, as if the surface is negatively charged. Note that in this case, there is still only one dense layer of anions near the surface. Increasing the surface potential to $\Phi_0 = 0.5$ V (dashed lines) causes a dense second layer of anions, while the cations are repelled. Overscreening

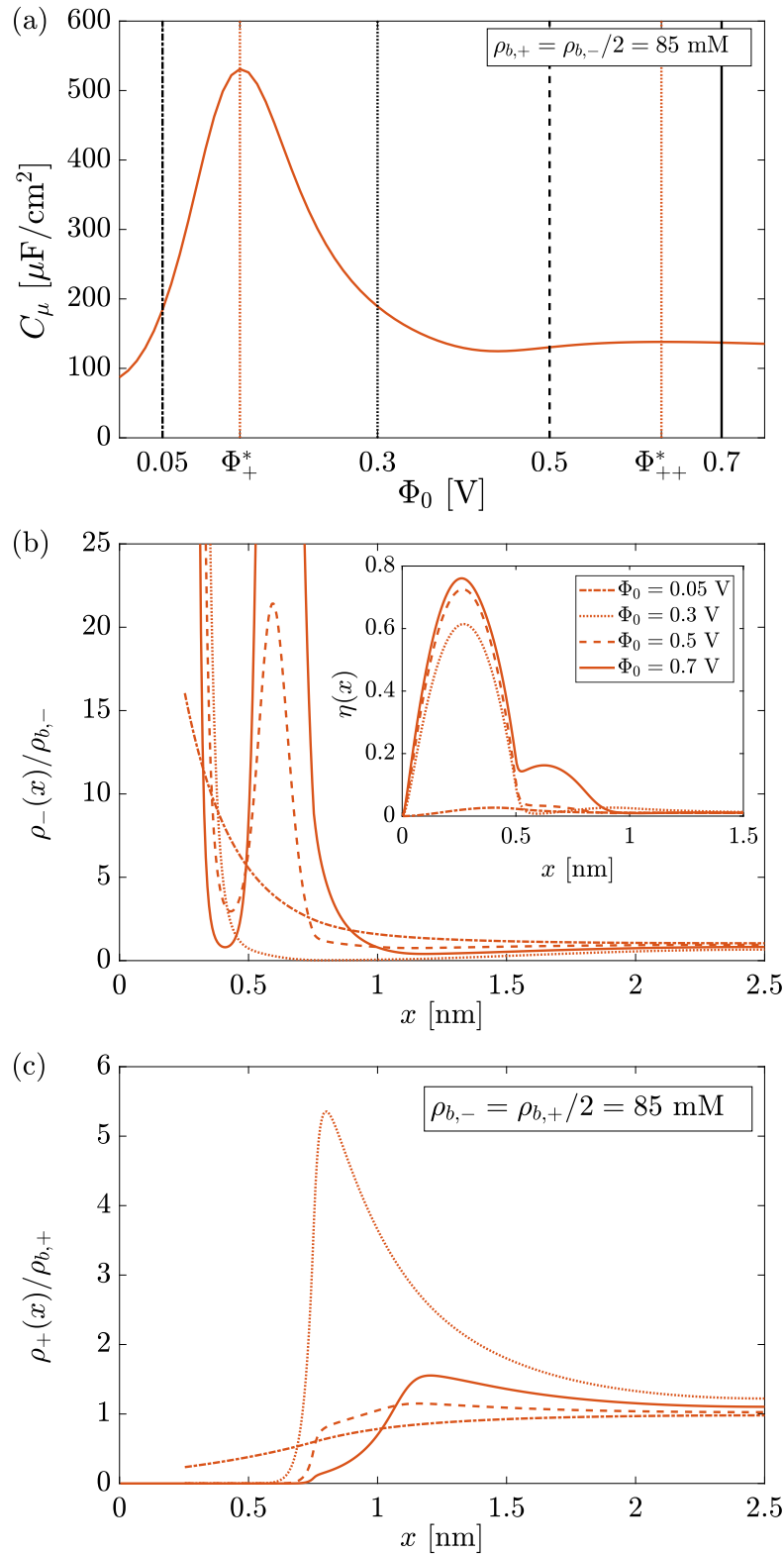


Figure 4.2.7: In (a) the C_μ curve of the asymmetric 1:2 electrolyte for which the anion and cations density profiles are portrayed in (b) and (c), respectively, at the surface potentials $\Phi_0 = 0.05$ V (dashed-dotted), $\Phi_0 = 0.3$ V (dotted), $\Phi_0 = 0.5$ V (dashed), and $\Phi_0 = 0.7$ V (solid), as indicated by the vertical lines in (a). The bulk concentration corresponding to these results is $\rho_{b,+} = \rho_{b,-}/2 = 85 \text{ mM}$ ($\eta_b = 0.01$). The inset in (b) shows the local packing fraction. The vertical lines at Φ_+^* and Φ_{++}^* are the surface potentials at which C_μ has a local maximum.

is found again at $\Phi_0 = 0.7\text{V} > \Phi_{++}^*$ (solid lines). Hence, the structural changes of the EDL are manifested in the differential capacitance; from a diffuse EDL to overscreening with one layer of cations and anions (up to the first maximum in C_μ), to two layers of anions and a diffuse cation layer (between the first maximum and the first minimum in C_μ), to overscreening with two layers of anions (beyond the second maximum in C_μ). This is also visible in the local packing fraction (see inset in Fig. 4.2.7(b)), which shows that a densely-packed first layer is formed for $\Phi_0 > \Phi_+^*$ and a second dense layer for $\Phi_0 > \Phi_{++}^*$.

4.2.3 Impurities

It is extremely difficult to experimentally study an aqueous electrolyte in which only one type of salt is dissolved. Generally, there are always "impurities", with a much lower bulk concentration than that of the dominant species. Common cations in water are Calcium (Ca^{2+}), Magnesium (Mg^{2+}), Sodium (Na^+), and Potassium (K^+), while the most common anions are Carbonate (CO_3^{2-}), Chloride (Cl^-), and Sulfate (SO_4^{2-}). Although there are techniques to obtain purified (deionized, demineralized) water, extracting all ion types is challenging [193, 194, 195]. One particular example would be the presence of divalent ions such as Calcium (Ca^{2+}) and Carbonate (CO_3^{2-}), which typically have concentrations ranging from below 0.01 mM (purified water) to 0.5 mM (recommended amount of Calcium in tap water) to 2 mM (very hard water) [196, 197].

Let us therefore now consider three-component electrolytes (see also Ref.[169]) consisting of one cation species and two anion species, with an asymmetry between the anions. First, we consider a 1:1:2 electrolyte of equisized ions with diameter $d = 0.5\text{nm}$ and $\rho_{b,+} = \rho_{b,-} + 2\rho_{b,2-}$ where the anion composition is characterized by $\nu = \rho_{b,2-} / \rho_{b,-}$. The differential capacitance for this system with a bulk packing fraction $\eta_b = 0.1$ is presented in Fig. 4.2.8, where ν takes the values $\infty, 10^{-1}, 10^{-2}, 10^{-3}, 10^{-4}, 10^{-5}$, and 0, where $\nu = 0$ corresponds to a 1:1 electrolyte and $\nu = \infty$ to a 1:2 electrolyte. Interestingly, even for $\nu = 10^{-6}$ (corresponding to $\rho_{b,2-} \approx 1.3 \cdot 10^{-6}\text{M}$) we find the divalent anion species to be predominant for surface potentials $\Phi_0 > 0.3\text{V}$. Again, this can be explained by using Eq. (4.15), which for a 1:2 electrolyte can be written in terms of the effective composition $\tilde{\nu} \equiv \nu e^{\beta\Phi(d/2)}$ that indicates whether or not the divalent ions dominate the surface composition, i.e. for $\tilde{\nu} \ll 1$ the monovalent anions dominate while for $\tilde{\nu} \gg 1$ the divalent anions dominate. Because $(e\beta)^{-1} \approx 25\text{mV}$, one finds for $\Phi_0 = 0.3\text{V} \approx 12/e\beta$ that Boltzmann factor $\exp(e\beta\Phi(d/2))$ is large, such that $\mathcal{O}(\tilde{\nu}) \approx 1$, even if $\nu = 10^{-6}$. That is, the two anion species compete with each other on who may fill the first layer near the surface, and since a divalent ion has a much stronger interaction with the surface charge it wins over the monovalent ion for large surface charges, even if their bulk concentration is much lower (see also Appendix 4.B). To conclude, even a trace amount of divalent ions, like Ca^{2+} or CO_3^{2-} , in a predominant monovalent electrolyte, such as NaCl, can play a dominant role in the differential capacitance at high surface potentials.

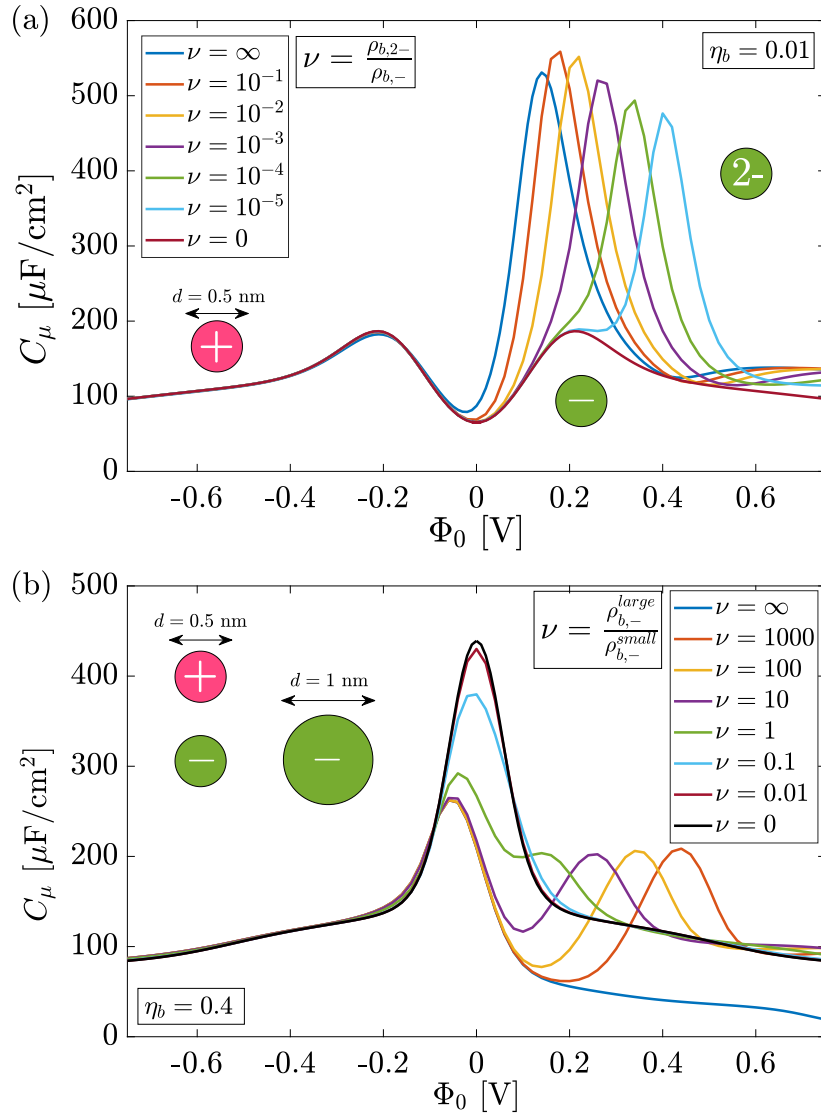


Figure 4.2.8: (a) The differential capacitance of a three-component electrolyte of one monovalent cation species and two anion species, of which one is monovalent and the other divalent. The parameter ν gives the ratio between the bulk density of those two anion species and ranges from ∞ (one divalent anion species) to 0 (on monovalent anion species), while the bulk packing fraction for all curves is fixed at $\eta_b = 0.01$. (b) Similar as in (a), but there are two monovalent anions with different size; one being $d_- = d_+ = 0.5$ nm, and the other $d_-^{large} = 2d = 1$ nm. The parameter ν is the ratio between the bulk density of the large anion w.r.t. small anion, i.e. $\nu = 0$ represents the RPM, while $\nu = \infty$ represents the system with one large anion species, while the bulk packing fraction for all curves is fixed at $\eta_b = 0.4$.

For two species of anions which differ in size rather than valency, the story is quite different. Let us again consider a three-component system with monovalent ion species with different ion diameters specified by $d \equiv d_+ = 0.5$ nm, $d_-^{small} = d$, and $d_-^{large} = 2d$. Fig. 4.2.8 shows the differential capacitance for this system for different anion composition ratios $\nu = \rho_{b,-}^{large} / \rho_{b,-}^{small}$ ranging from $\nu = 0$ (one anion species with $d_- = d$) to $\nu = \infty$ (one anion species with $d_- = 2d$) at a bulk packing fraction of $\eta_b = 0.4$. Similar to the previous three-component case with different valencies there is a competition between the two anion species; smaller anions can approach the surface to closer distances than

the larger anions, obviously, and therefore the two anion species again compete on who may fill the first layer. For $\nu < 1$, the smaller anions dominate at all surface potentials, and Fig. 4.2.8(b) only shows one discernible peak in the capacitance profile. When ν is increased to $\nu > 1$ (the bulk concentration of the larger anions exceeds that of the smaller anions) the larger anions fill the first layer up to a certain surface potential beyond which the smaller anions take over (see also Appendix 4.B). This point is indicated by a peak in the differential capacitance, after which the smaller anions, although having a much lower bulk concentration, are the dominating factor for the differential capacitance. Again, this can be explained from Eq. (4.15), where it becomes apparent that the competition is between $\rho_-^{\text{small}}(d/2)$ and $\rho_-^{\text{large}}(d)$. For $\nu > 1$ and for surface potentials at which the larger anions make up the first layer, the quantity $\rho_-^{\text{large}}(d)$ is similar to the case of which there is only one large cation species. However, when the surface potential is increased such that the smaller ions make up the first layer, then $\rho_-^{\text{large}}(d)$ basically vanishes, due to the presence of the smaller anions that repel the larger ones. Hence, the differential capacitance of the impurity system then follows the curve of the differential capacitance of the system for which there is only one anion species with $d_- = d$. Looking at Fig. 4.2.8, it becomes apparent that a camel-shaped curve can occur at very high packing fractions, although its minimum does not coincide with the potential of zero charge.

4.3 CONCLUSION

We have carefully investigated the differential capacitance for primitive model electrolytes within classical DFT. A new equation (4.15) to interpret the differential capacitance was introduced, which greatly helped to understand its behavior, because it explicitly showed the importance of the first layer of ions near the surface. Specifically, it helped to further rationalize the camel-bell crossover, that has been a topic of interest across many studies, as a (smooth) structural change in the density profiles near the electrode. Analogous to peaks in the heat capacity indicating (smooth) changes of the thermal occupancy of microstates, peaks in the differential capacitance indicate structural change. This can either be the forming of dense-packed layers of counterions near the surface, but can also be the reorganization of layers of cations and anions as we showed for the 1:2 electrolyte with divalent anions, in which overscreening causes a rich structural behavior that seeped through in the capacitance curves. When the impurities in three-component electrolytes were studied, we again found that the competition for the first layer of ions near the surface determined the behavior of the capacitance curves. This three-component electrolyte that was studied, with one species of cations and two species of anions in which the relative concentration of the anions was changed, gave much richer physics than perhaps anticipated. Both an asymmetry in the anion valency as well as in the anion diameter was considered. Surprisingly at first, even when the composition of the bulk mixture is very asymmetric, both anion species still have their regime in which they fill up the first layer. For anion asymmetry in the valency, where the relative concentration of the divalent anions is very small, we found that the divalent anions can still fill up the first layer when the surface potential is

large enough, due to the much stronger interaction with the charged surface. For diameter asymmetry of the anions, with a low relative concentration of the small anions, we found that they can still fill up the first layer at large surface potential because they can screen the charge on the surface more efficiently. For both cases it is the competition between the two anion species that shapes the differential capacitance. Hence, impurities, as we call them, have a rather strong effect on the differential capacitance. The differential capacitance can thus be used as a probe for the electrolyte composition. Knowing that the differential capacitance is largely determined by the first layer of adsorbed ions, and that peaks in the differential capacitance indicate structural changes, can therefore help to distinguish the components in the electrolyte.

Although Eq. (4.15) for the differential capacitance that we derived strictly only holds for the primitive model electrolytes in contact with charged hard walls, the physics that the first layer of ions near the surface dominate its behavior still holds when the conditions are loosened up. Important is that the ion-ion and ion-surface interaction are strongly repulsive at short separations; our results will be modified if dispersion forces are relevant.

The next step would be to confront the knowledge gained from this analysis to experimental data, allowing interpretation of the measured differential capacitance in terms of EDL structure and bulk electrolyte composition. This could, in turn, lead to a better understanding of the differential capacitance, and consequently to an improved performance of real EDL capacitors. An ultimate goal is to provide knowledge to create sustainable alternatives for Lithium-ion batteries [12, 14], which would contribute directly to the transition towards renewable energy.

APPENDIX

4.A CAPACITIVE ENERGY

Changing the order of the integration in Eq. (4.10) leads to

$$\begin{aligned}
 \Omega(\Phi_2) - \Omega(\Phi_1) &= -A \int_{\Phi_1}^{\Phi_2} d\Phi \int_{\Phi_{PZC}}^{\Phi} d\Phi' C_\mu(\Phi') \quad (4.23) \\
 &= -A \left\{ \left[(\Phi_2 - \Phi_1) \int_{\Phi_{PZC}}^{\Phi_1} d\Phi' C_\mu(\Phi') + \int_{\Phi_1}^{\Phi_2} d\Phi' (\Phi_2 - \Phi') C_\mu(\Phi') \right] \Theta(\Phi_1 - \Phi_{PZC}) + \right. \\
 &\quad \left[\int_{\Phi_1}^{\Phi_{PZC}} d\Phi' (\Phi' - \Phi_1) C_\mu(\Phi') + \int_{\Phi_{PZC}}^{\Phi_2} d\Phi' (\Phi_2 - \Phi') C_\mu(\Phi') \right] \Theta(\Phi_{PZC} - \Phi_1) \Theta(\Phi_2 - \Phi_{PZC}) + \\
 &\quad \left. \left[\int_{\Phi_1}^{\Phi_2} d\Phi' (\Phi' - \Phi_1) C_\mu(\Phi') + (\Phi_2 - \Phi_1) \int_{\Phi_2}^{\Phi_{PZC}} d\Phi' C_\mu(\Phi') \right] \Theta(\Phi_{PZC} - \Phi_2) \right\}, \quad (4.24)
 \end{aligned}$$

where $\Theta(x)$ denotes the Heaviside function. Then considering the case that $\Phi_{PZC} = 0$, $\Phi_1 = 0$ and $\Phi_2 = \Phi_0 > 0$, leads to Eq. (4.11).

4.B DENSITY PROFILES: IMPURITIES

The density profiles for the three-component system with one monovalent anion species (blue) and one divalent anion species (red) for the relative bulk concentration $\nu = \rho_{b,2-} / \rho_{b,-} = 10^{-3}$ and surface potentials $\Phi_0 = 0.1$ V (dashed), $\Phi_0 = 0.2$ V (dotted), $\Phi_0 = 0.5$ V (dash-dotted), and $\Phi_0 = 0.7$ V (solid) are presented in Fig. 4.B.1(a). At low surface potentials the divalent anion density profile (dashed red) is has low values at any x . Upon increasing the surface potential, the divalent anion species take in the place of the monovalent anion species, up to the point where the first layer only contains the divalent anion species (dashed-dot and solid), and the monovalent anion species are moved into the second layer (dashed-dot). Increasing the surface potential even more, causes a second layer of divalent ions (solid).

The density profiles for the three-component system with one small anion species (blue) and one large anion species (red) for the relative bulk concentration $\nu = \rho_{b,-}^{large} / \rho_{b,-}^{small} = 100$ and surface potentials $\Phi_0 = 0.1$ V (dotted), $\Phi_0 = 0.3$ V (dash-dotted), and $\Phi_0 = 0.5$ V (solid) are presented in Fig. 4.B.1(b). For low surface potentials, the concentration of the small anion species is negligible (dotted line). Upon increasing the surface potential, the concentration of the smaller anion species near the charged surface increases dramatically, pushing away the larger anion species. This results in the appearance of a (red) peak at $x = 1$ nm instead of one at $x = 0.5$ nm, shifting the phase of oscillations in the density profile (compare solid line with the dashed-dotted line).

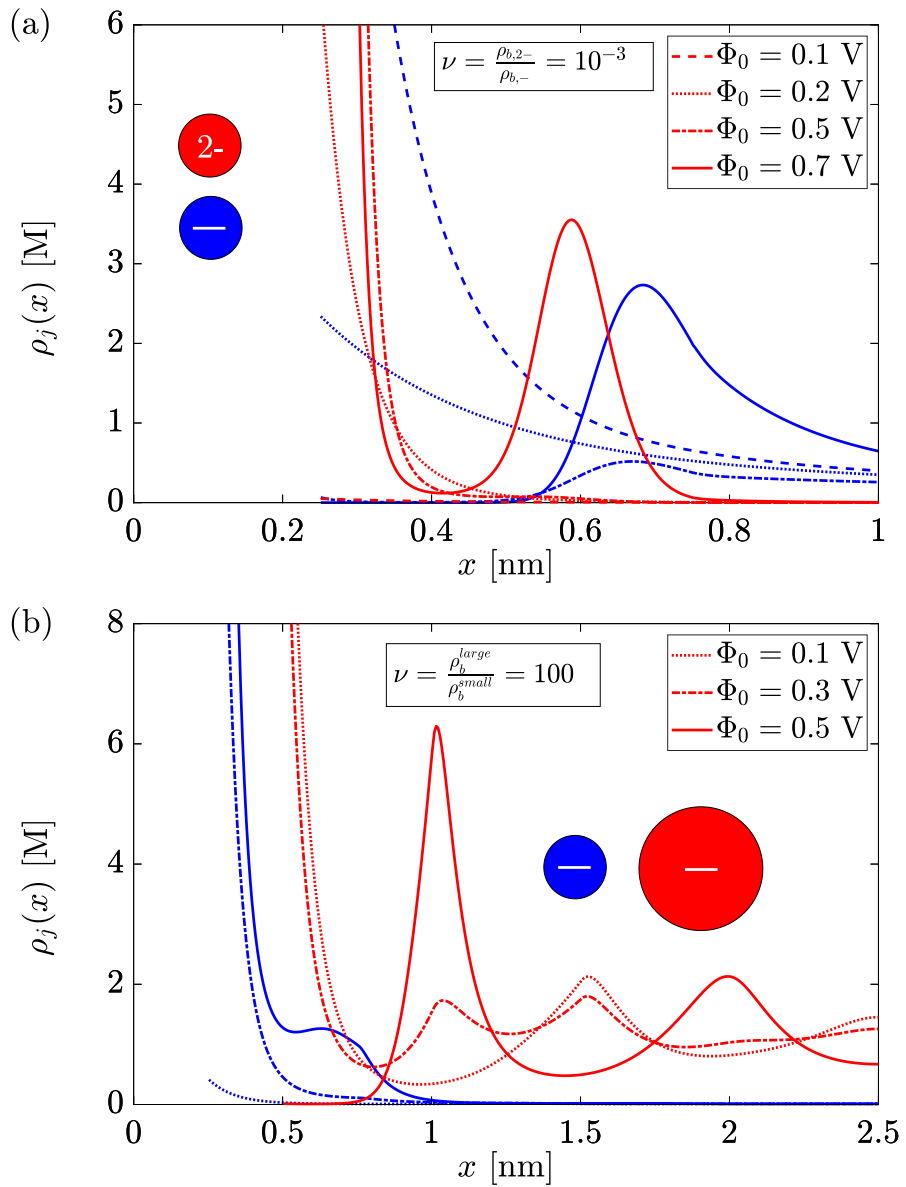


Figure 4.B.1: (a) The density profiles for the monovalent (blue) and divalent (red) anion species for the relative concentration $\nu = 10^{-3}$ and surface potentials $\Phi_0 = 0.1$ V (dashed), $\Phi_0 = 0.2$ V (dotted), $\Phi_0 = 0.5$ V (dash-dotted), and $\Phi_0 = 0.7$ V (solid). (b) The density profiles for the small (blue) and large (red) anion species for the relative concentration $\nu = 100$ and surface potentials $\Phi_0 = 0.1$ V (dotted), $\Phi_0 = 0.3$ V (dash-dotted), and $\Phi_0 = 0.5$ V (solid).

MACHINE-LEARNING FREE-ENERGY FUNCTIONALS USING DENSITY PROFILES FROM SIMULATIONS

The formally exact framework of equilibrium Density Functional Theory (DFT) is capable of simultaneously and consistently describing thermodynamic and structural properties of interacting many-body systems in arbitrary external potentials. In practice, however, DFT hinges on approximate (free-)energy functionals from which density profiles (and hence the thermodynamic potential) follow via an Euler–Lagrange equation. Here, we explore a relatively simple Machine-Learning (ML) approach to improve the standard mean-field approximation of the excess Helmholtz free-energy functional of a 3D Lennard-Jones system at a supercritical temperature. The learning set consists of density profiles from grand-canonical Monte Carlo simulations of this system at varying chemical potentials and external potentials in a planar geometry only. Using the DFT formalism, we nevertheless can extract not only very accurate 3D bulk equations of state but also radial distribution functions using the Percus test-particle method. Unfortunately, our ML approach did not provide very reliable Ornstein–Zernike direct correlation functions for small distances.

Given the massive present-day availability of computer power and data, the grown general interest in machine learning (ML) should not come as a big surprise. This interest also extends to physics, whose community excels at gathering, organizing, and analyzing data in order to predict and model the behavior of systems with many degrees of freedom, which is also one of the strengths of ML. An important distinction between the field of physics and ML is that physicists tend to understand, model, and predict the systems of their interest via a stepwise chain of reasoning from cause to effect, whereas ML algorithms tend to “only” directly relate cause to effect without necessarily understanding (in the traditional “human” sense) the steps in between. In other words, ML can often be regarded as a black box that is as incomprehensible as the initial raw data itself.

Here we will also suffer, at least to some extent, from this black-box character of ML applied to a problem in classical Density Functional Theory (DFT) [42, 46]. However, only in a limited way because we can build on the foundations of physics to exploit, in this case, a few ingredients of the DFT formalism. As we will explain in full detail below, DFT is an exact framework to describe thermodynamic and structural properties of interacting many-body systems. This involves the solution of Euler-Lagrange equations for the equilibrium density profile for a particle system in an external potential. Now, DFT hinges for given particle-particle interactions on approximate free-energy density functionals. By comparison with Monte Carlo simulations, performed by MSc student Sander Kuipers, of density profiles in a learning set of external potentials, a free-energy functional can be constructed during an ML process. The additional physics that can be extracted beyond the learning set not only includes density profiles for external potentials outside the learning set but also (i) thermodynamic bulk quantities (because the minimal value of the functional corresponds to the thermodynamic potential at equilibrium from which for instance the bulk pressure follows) and (ii) the two-body direct correlation function (because it is related to the second functional derivative of the functional) from which the radial distribution function follows. Moreover, thermodynamic surface properties such as the adsorption and the interfacial tension can be extracted from the functional. Our work is strongly inspired by recent ML work to construct a classical DFT for the Lennard-Jones (LJ) fluid in one spatial dimension [198, 199], which we here extend to the three-dimensional LJ fluid. Similar to Refs. [198, 199] we use grand-canonical Monte Carlo (MC) simulations at a learning set of chemical potentials and external potentials, however in a planar geometry. We stress that the planar geometry yields an effective 1D problem embedded in 3D, not to be confused with an actual 1D problem. We will show the ability to “learn” a free-energy functional that predicts density profiles of this system at chemical and external potentials **outside** the training set, but also to extract several system properties that were **not at all** present in the data of the training set, or at least not explicitly. In particular, we will show that from a learning set in a *planar* geometry a machine-learned functional can be constructed that is capable of predicting the 3D mechanical bulk equation of state of the *homogeneous* fluid (the pressure-density-chemical potential relations), the 3D *radially symmetric* direct correlation function and the radial distribution function at any density, and (in principle) the prediction of Lennard-Jones density profiles in an arbitrary external potential in 3D.

The agreement of these predictions against simulations varies from very good (equation of state, radial distributions from the Percus test particle method, density profiles outside learning set) to, admittedly, rather poor (direct correlation function). The poor prediction for the latter is probably due to the rather simple form (and in retrospect perhaps an overly-simple form compared to Ref. [199]) for the free-energy functional, and due to the treatment of the repulsive part of the LJ interaction. The main thrust of our findings at this point, therefore, is not the construction of the Lennard-Jones free-energy functional that compares “best” with MC simulations, but rather the notion that free-energy functionals for 3D systems can be constructed from relatively simple geometries (here planar) in the learning set. Extensions to other systems, for instance electrolytes and ionic liquids forming an electric double layer in contact with planar electrodes, could be a next step with actual applications in modeling the osmotic equation of state, the differential capacitance, and the adsorption in porous geometries.

This chapter is organized as follows. We start in section II with an extensive introduction into classical DFT -that can easily be skipped by readers familiar with this framework. In section III and IV we discuss the system and the (simulation and machine-learning) methods that we use, and in section V we discuss the resulting kernels, density profiles, equations of state, and pair correlation functions. We end in section VI with a discussion and outlook.

5.1 CLASSICAL DENSITY FUNCTIONAL THEORY

5.1.1 Formalism

We consider a classical one-component system of N spherical particles with linear momenta \mathbf{p}_i and center-of-mass positions \mathbf{r}_i with $i = 1, \dots, N$ the particle label. The particles interact with each other via an isotropic pair potential $u(r_{ij})$, where $r_{ij} = |\mathbf{r}_i - \mathbf{r}_j|$ is the distance between particle i and j . All particles are subject to a static external potential $V_{ext}(\mathbf{r}_i)$, such that the Hamiltonian of the system reads

$$H_N = \sum_{i=1}^N \frac{\mathbf{p}_i^2}{2m} + \sum_{i<j}^N u(r_{ij}) + \sum_{i=1}^N V_{ext}(\mathbf{r}_i), \quad (5.1)$$

where m denotes the mass of the particles. Here we note that Eq. (5.1) can also describe macroscopic bulk systems by considering the external potential to be zero in a box of volume V at a homogeneous density $\rho = N/V$ and temperature T . For these homogeneous systems, typical thermodynamic equilibrium quantities of interest include the caloric and mechanical equations of state $u(\rho, T)$ and $p(\rho, T)$ for the internal energy and pressure, respectively. Also structural quantities such as the radial distribution function $g(r)$ (at particle-particle separation r) and the structure factor $S(q)$ (at wavenumber q) are of interest for homogeneous systems [42]. Equilibrium statistical mechanics offers a variety of techniques to calculate (approximations to) these quantities, for instance systematic low- ρ or high- T expansions, integral equations based on the Ornstein-Zernike equation, or com-

puter simulations. However, the situation is more complicated in the case of a nontrivial external potential due to, for instance, the Earth's gravity, an attractive or repulsive substrate, or a porous matrix that may confine the particles of interest. In this case, the system described by Eq. (5.1) becomes heterogeneous in thermodynamic equilibrium, such that the local density $\rho(\mathbf{r})$ varies in space. Consequently, the energy density u and the pressure p become ill-defined (except, of course, within a local density approximation), and the broken translation invariance causes the radial distribution function to be of the form $g(\mathbf{r}, \mathbf{r}')$ rather than $g(|\mathbf{r} - \mathbf{r}'|)$. Nevertheless, the formalism of Density Functional Theory (DFT) can provide a consistent picture of the thermodynamic and structural properties of inhomogeneous fluids in an external potential. Although DFT finds its roots in the quantum-many body description of electrons, it has also found many applications in the (essentially) classical context of soft-matter systems to describe molecular liquids, electrolytes, colloidal dispersions, etc. [46, 47, 48, 58, 149, 200, 201, 202, 203].

DFT is essentially a grand-canonical framework in which the temperature T and the chemical potential μ of the particles are fixed to characterise the heat bath and the particle bath with which the system is in thermal and diffusive equilibrium. The corresponding thermodynamic potential is the grand potential Ω_0 defined by $\beta\Omega_0 = -\ln \sum_{N=0}^{\infty} \int d\mathbf{p}^N d\mathbf{r}^N \exp[-\beta(H_N - \mu N)] / N! h^{3N}$, where $\beta^{-1} = k_B T$, k_B the Boltzmann constant, and h an arbitrary constant with the same dimension as the Planck constant. From Ω_0 essentially all thermodynamic properties would follow, for instance the pressure of the homogeneous system equals $-\Omega_0/V$ and the internal energy is $\partial\beta\Omega_0/\partial\beta$. Of course, this involves the immense problem of evaluating the $6N$ -dimensional phase-space integral in the definition of Ω_0 . The key of classical DFT is that it circumvents this high-dimensional phase-space integral by a proof [46] of the existence of a grand-potential *functional* $\Omega[\rho]$ of the variational one-body density profile $\rho(\mathbf{r})$, with the properties that (i) the equilibrium density profile $\rho_0(\mathbf{r})$ minimizes the functional $\Omega[\rho]$, and (ii) this minimum equals the equilibrium grand potential Ω_0 . This implies that

$$\left. \frac{\delta\Omega[\rho]}{\delta\rho(\mathbf{r})} \right|_{\rho_0(\mathbf{r})} = 0; \quad \Omega[\rho_0] = \Omega_0. \quad (5.2)$$

The problem is thus reduced to finding the functional $\Omega[\rho]$, and after that to solve the 3D Euler-Lagrange equation (5.2), which amounts to a huge reduction of the problem compared to the high-dimensional phase-space integral.

One can also prove rigorously [42, 45, 46] that the grand potential functional $\Omega[\rho]$ can always be written as

$$\Omega[\rho] = \mathcal{F}[\rho] - \int d\mathbf{r} \rho(\mathbf{r}) (\mu - V_{ext}(\mathbf{r})), \quad (5.3)$$

where $\mathcal{F}[\rho]$ is the *intrinsic* Helmholtz free-energy functional that, and this is crucial for our machine-learning approach, *only and uniquely* depends on the particle-particle interactions (here the pair potential $u(r)$) and on the temperature, and *not* on μ and $V_{ext}(\mathbf{r})$. In other words, the same and unique functional $\mathcal{F}[\rho]$ for a given $u(r)$ applies at any chemical and ex-

ternal potential. That $\mathcal{F}[\rho]$ is a *Helmholtz* free-energy functional follows straightforwardly from the thermodynamic relation $\Omega_0 = F_0 - \mu N_0$ with $N_0 = \int d\mathbf{r} \rho_0(\mathbf{r})$ the equilibrium number of particles and F_0 the equilibrium Helmholtz free energy, which can be decomposed into the sum of the potential energy $\int d\mathbf{r} \rho_0(\mathbf{r}) V_{ext}(\mathbf{r})$ due to the external field and the remaining intrinsic free energy $\mathcal{F}[\rho_0]$.

Unfortunately, $\mathcal{F}[\rho]$ is not explicitly known in most cases. An exception is the ideal-gas case of $u(r) \equiv 0$, where it is possible to construct the intrinsic free-energy functional as $\mathcal{F}^{id}[\rho] = k_B T \int d\mathbf{r} \rho(\mathbf{r}) (\ln \rho(\mathbf{r}) \Lambda^3 - 1)$, with $\Lambda = h / \sqrt{2\pi m k_B T}$ the thermal wavelength. The common practice in DFT is now to split the intrinsic free energy into the ideal and the excess-over-ideal part, $\mathcal{F}[\rho] = \mathcal{F}^{id}[\rho] + \mathcal{F}^{exc}[\rho]$, and to find an explicit (usually approximate) expression for $\mathcal{F}^{exc}[\rho]$. Once such an explicit expression has been found, we can cast the minimum condition for $\rho_0(\mathbf{r})$ of Eq. (5.2) in the explicit form

$$\rho_0(\mathbf{r}) = \frac{\exp(\beta\mu)}{\Lambda^3} \exp \left[\left(-\beta \frac{\delta \mathcal{F}^{exc}[\rho]}{\delta \rho(\mathbf{r})} \Big|_{\rho=\rho_0} - \beta V_{ext}(\mathbf{r}) \right) \right]. \quad (5.4)$$

Note that Eq. (5.4) is a self-consistency relation for interacting systems, that usually takes the form of a nonlinear integro-differential equation that needs to be solved numerically for a given μ and $V_{ext}(\mathbf{r})$ for a system of interest with pair potential $u(r)$ at temperature T — and hence with a given excess functional $\mathcal{F}^{exc}[\rho]$. In relatively simple geometries, for instance with planar or radial symmetry, a numerical solution of Eq. (5.4) can be found at relatively low computational cost by means of e.g. a Picard iteration scheme.

Thus, the remaining problem of DFT lies in constructing an explicit form for $\mathcal{F}^{exc}[\rho]$, for which no universal recipe is available — not unlike the case of partition functions of interacting systems. There is, however, one more exact relation that can be and has been exploited, and involves the second functional derivative $-\beta \delta^2 \mathcal{F}^{exc}[\rho] / \delta \rho(\mathbf{r}) \delta \rho(\mathbf{r}')$, which equals by definition the Ornstein-Zernike direct correlation function $c(\mathbf{r}, \mathbf{r}')$ and is hence directly related to the two-body structure of the system. In particular, in a homogeneous bulk system the direct correlation function is of the form $c_b(|\mathbf{r} - \mathbf{r}'|)$ and its Fourier transform $\hat{c}_b(q)$ yields the structure factor $S(q) = (1 - \rho \hat{c}_b(q))^{-1}$, from which the radial distribution function $g(r)$ follows by an inverse Fourier transformation.

In this chapter we will focus on a Lennard-Jones fluid. In the DFT treatment, we split the pair potential $u(r) = u_0(r) + u_1(r)$ into a steep repulsion $u_0(r)$ at short distances and an attractive tail $u_1(r)$ of well depth $-\epsilon < 0$ in accordance with Barker-Henderson theory, as further detailed in section 5.2. On the basis of the vast body of knowledge on the thermodynamics and the two-body structure of the hard-sphere system, extremely accurate approximations have been constructed for its intrinsic excess Helmholtz free-energy functional $\mathcal{F}_{HS}^{exc}[\rho]$, for which we will use the White-Bear mark II[48] version of the fundamental measure theory[47, 58] throughout this chapter. It is common practice in liquid-state theory to treat the attractions as a perturbation on the hard-sphere system, and a popular version results in the Van der Waals-like mean-field (MF) approximation

$$\mathcal{F}_{MF}^{exc}[\rho] \approx \mathcal{F}_{HS}^{exc}[\rho] + \frac{1}{2} \int d\mathbf{r} d\mathbf{r}' \rho(\mathbf{r}) \rho(\mathbf{r}') u_1(|\mathbf{r} - \mathbf{r}'|). \quad (5.5)$$

The high-temperature limit of Eq. (5.5) returns the hard-sphere limit, but the MF approximation fails to give accurate results for lower temperatures where the attractions play a more prominent role [42, 198, 204]. We therefore seek improved excess free-energy functionals in terms of corrections to the mean-field functional of Eq. (5.5) of the quadratic and cubic form

$$\beta\mathcal{F}_{ML2}^{exc}[\rho] = \beta\mathcal{F}_{MF}^{exc}[\rho] + \frac{1}{2} \int d\mathbf{r}d\mathbf{r}' \rho(\mathbf{r})\rho(\mathbf{r}')\Omega_2(|\mathbf{r} - \mathbf{r}'|), \quad (5.6)$$

$$\beta\mathcal{F}_{ML3}^{exc}[\rho] = \beta\mathcal{F}_{ML2}^{exc}[\rho] + \frac{1}{3} \int d\mathbf{r}d\mathbf{r}' \rho^2(\mathbf{r})\rho(\mathbf{r}')\Omega_3(|\mathbf{r} - \mathbf{r}'|), \quad (5.7)$$

where the labels ML2 and ML3 refer to the fact that we will use machine learning (ML) to find the optimal form of the kernels $\Omega_2(r)$ and $\Omega_3(r)$. We note that ML2 reduces to the mean-field form for $\Omega_2(r) \equiv 0$ and that ML3 reduces to ML2 for $\Omega_3(r) \equiv 0$. We also emphasize that the ML3 form of the functional is *not* compatible with the third-order virial-type expansion which would have entailed an additional spatial integration (say over \mathbf{r}'') and a kernel of the triple product form $f(|\mathbf{r} - \mathbf{r}'|)f(|\mathbf{r}' - \mathbf{r}''|)f(|\mathbf{r}'' - \mathbf{r}|)$; finding the optimal kernel $f(r)$ proved to be computationally too demanding and inconvenient at the exploration phase of this project and hence we settled for the simpler form of the cubic term ML3.

The building of ML functionals upon the MF functional is important. For long-ranged potentials the mean-field functional retrieves the correct asymptotic decay of the direct correlation function, such that the range of the ML corrections can conveniently be limited. For short-ranged potentials, the direct correlations are short-ranged anyway, and the inclusion of the mean-field term puts no constraint on the resulting ML functional.

5.1.2 Planar geometry

Interestingly, we can exploit the fact that the optimal kernels $\Omega_2(r)$ and $\Omega_3(r)$ that we seek *must* be independent of μ and $V_{ext}(\mathbf{r})$ to determine them in systems with a planar geometry, i.e. systems that have translation invariance in the y - and z -direction with external potentials $V_{ext}(x)$ and density profiles $\rho(x)$ that only depend on the normal coordinate x . One easily checks that the non-HS part of the MF functional of Eq. (5.5) then reduces to

$$\mathcal{F}_{MF}^{exc}[\rho] = \frac{A}{2} \int dx dx' \rho(x)\rho(x')u_{1,x}(|x - x'|), \quad (5.8)$$

where $A = \int dy dz$ is the (macroscopically large) area of the planar surface and $u_{1,x}(|x - x'|) = \int dy dz u_1(\sqrt{(x - x')^2 + y^2 + z^2})$ is the laterally-integrated pair potential $u_1(r)$. Likewise the non-HS contributions to the functionals of Eq. (5.6) can be cast in the form

$$\beta\mathcal{F}_{ML2}^{exc}[\rho] = \beta\mathcal{F}_{MF}^{exc}[\rho] + \frac{A}{2} \int dx dx' \rho(x)\rho(x')\omega_2(|x - x'|), \quad (5.9)$$

$$\beta\mathcal{F}_{ML3}^{exc}[\rho] = \beta\mathcal{F}_{ML2}^{exc}[\rho] + \frac{A}{3} \int dx dx' \rho^2(x)\rho(x')\omega_3(|x - x'|), \quad (5.10)$$

where the laterally-integrated kernels ω_2 and ω_3 can be written as

$$\omega_i(x) = 2\pi \int_{|x|}^{\infty} dr r \Omega_i(r); \quad i = 2, 3. \quad (5.11)$$

Interestingly, Eq. (5.11) can be inverted, such that we find

$$\Omega_i(|\mathbf{r}|) = -\frac{1}{2\pi} \left(\frac{1}{x} \frac{d\omega_i(x)}{dx} \right) \Big|_{x=|\mathbf{r}|}. \quad (5.12)$$

In other words, once we find $\omega_2(x)$ and $\omega_3(x)$ from calculations in planar geometry, we can determine $\Omega_2(r)$ and $\Omega_3(r)$ from Eq. (5.12) such that the direct correlation function follows by taking second functional derivatives of Eqs. (5.6) and (5.7). Hence, we have access to thermodynamic as well as structural properties in bulk, in any geometric confinement, in any external potential, at any chemical potential, solely on the basis of input in a planar geometry.

5.2 SYSTEM

In this chapter, we consider a 3D fluid in which the particles interact with a truncated and shifted Lennard-Jones (LJ) interaction given by

$$u^{LJ}(r) = \begin{cases} 4\epsilon \left(\left(\frac{\sigma}{r}\right)^{12} - \left(\frac{\sigma}{r}\right)^6 \right) + \epsilon_{cut}, & \text{for } r \leq r_{cut}; \\ 0, & \text{for } r > r_{cut}, \end{cases} \quad (5.13)$$

where $\epsilon > 0$ denotes the well depth and σ is the LJ particle diameter. The full LJ potential is truncated at $r_{cut} = 4\sigma$ and shifted upwards by $\epsilon_{cut} = 0.98 \cdot 10^{-3} \epsilon$ such that $u^{LJ}(r_{cut}) = 0$. The splitting of $u^{LJ}(r)$ into a hard-sphere reference and an attractive tail in the DFT treatment is performed on the basis of the well-known Barker-Henderson theory [205, 206] that leads to an effective and temperature-dependent hard-core diameter $0 < d \leq \sigma$ that does not depend on the bulk density as explained in Refs. [205, 207]. At the temperature $k_B T / \epsilon = 2$ of our main interest the effective diameter is given by $d = 0.9568\sigma$. The resulting expression for $u_1(r)$ then reads

$$u_1(r) = \begin{cases} 0, & \text{for } r \leq \sigma; \\ u^{LJ}(r), & \text{for } r > \sigma. \end{cases} \quad (5.14)$$

We stress that the value inside the core, i.e. $u_1(r < d)$, is not uniquely defined [208, 209] and its value can be used as a fit parameter for better agreement between simulations and DFT. However, we choose here to set it to zero in line with previous studies on the LJ system [210, 211, 212].

The external potentials $V_{ext}(x)$ that we consider in this chapter all mimic a planar slit geometry. The slit is translationally invariant in the lateral y - z plane and is mirror-symmetric

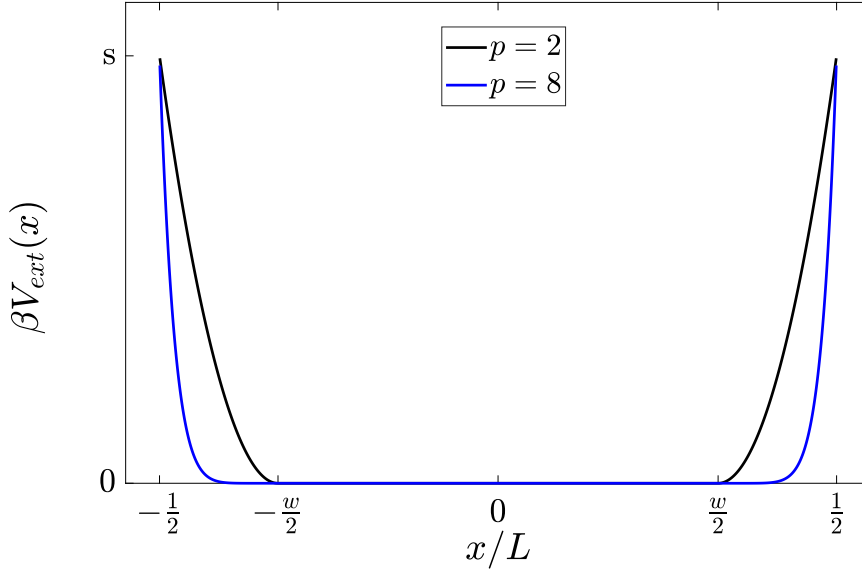


Figure 5.2.1: A general visualization of the external potential described in Eq. (5.15). This external potential is applied in the training data and is given by the parameters w , s , p and L . In this figure two values of p are considered, namely $p = 2$ (black) and $p = 8$ (blue).

in the midplane $x = 0$ such that $V_{ext}(x) = V_{ext}(-x)$. We employ a family of external wall-particle potentials that is repulsive and parameterised by

$$\beta V_{ext}(x) = \begin{cases} 0, & \text{for } |x| \leq w\frac{L}{2}; \\ s \left(\frac{|x| - w\frac{L}{2}}{(1-w)\frac{L}{2}} \right)^p, & \text{for } |x| > w\frac{L}{2}, \end{cases} \quad (5.15)$$

where the dimensionless strength $s = \beta V_{ext}(L/2) \geq 40$ characterizes the potential at $|x| = L/2$, $w \in [0, 1]$ denotes the width of the central part of the slit where $\beta V_{ext}(x) = 0$, and $p > 0$ the power that characterizes the steepness of the potential. Fig. 5.2.1 illustrates the external potential for general s , w , and L and for steepness parameters $p = 2$ (black) and $p = 8$ (blue).

5.3 METHODS

5.3.1 Simulations

To generate the training and validation data sets to “learn” the density functional, MSc student Sander Kuipers performed grand-canonical Monte Carlo (MC) simulations of the 3D truncated and shifted Lennard-Jones (LJ) fluid confined between two planar soft-repulsive walls described by the external potential $V_{ext}(x)$ of Eq. (5.15). Here, we only consider highly repulsive walls with $s \geq 40$ to ensure that the density reduces to essentially zero at $|x| = L/2$. We measure the equilibrium density profile $\rho^{MC}(x)$ in a cubic simulation box of volume $V = L^3$ with $L = 10\sigma$. Further details regarding the simulations can be found in Ref. [4].

In order to avoid (interesting but at this stage undesired) complications due to possible phase transitions (condensation, pre-wetting, capillary evaporation, etc.), we consider only a supercritical temperature $k_B T/\epsilon = 2$. Eight different chemical potentials μ are imposed in the grand-canonical MC simulations of the LJ system, given by $\beta\mu \in \{-3.0, -2.5, \dots, 0.0, 0.5\}$. Here, the arbitrary offset of μ is chosen such that the thermal wavelength equals the particle diameter, $\Lambda = \sigma$; it implies that $\beta\mu \rightarrow \log \rho_b \sigma^3$ in the dilute (ideal-gas) limit $\rho_b \sigma^3 \ll 1$. A total of 24 different external potentials are considered as training sets, all with total slit length $L = 10\sigma$ and strengths $s \in \{40, 60\}$, widths $w \in \{0.4, 0.65, 0.9\}$, and steepness parameters $p \in \{2, 4, 8, 10\}$.

As an illustration, we show in Fig. 5.3.1 the simulated density profiles $\rho^{MC}(x)$ of a LJ fluid at $k_B T/\epsilon = 2$ and chemical potentials $\beta\mu = \{-3.0, -2.5, -2, -1.5, -1.0, -0.5, 0, 0.5\}$ (symbols) corresponding to (separately simulated) bulk densities $\rho_b \sigma^3 \approx \{0.056, 0.10, 0.19, 0.33, 0.47, 0.56, 0.62, 0.67\}$ in the external potential $V_{ext}(x)$ characterized by $s = 60$, $w = 0.4$, and $p = 4$ as denoted by the red solid line. We observe monotonous density profiles at the lowest μ 's, the development of density oscillations at higher μ 's, and a fairly well-defined "bulk" density in the vicinity of $x = 0$ (except at the highest μ 's, where the profiles of the two walls show some overlap due to the limited system size).

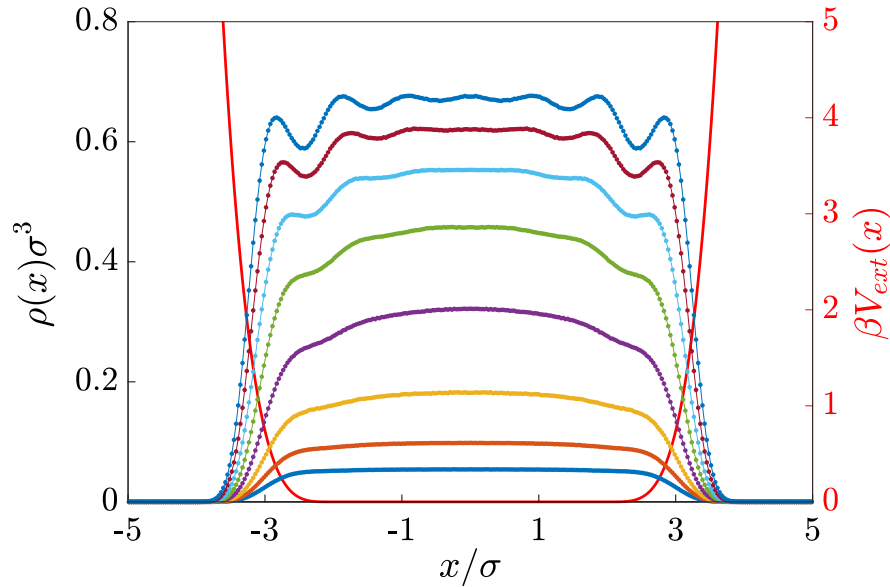


Figure 5.3.1: Equilibrium density profiles $\rho(x)$ (symbols) of a LJ fluid at temperature $k_B T/\epsilon = 2$ and chemical potentials $\beta\mu = -3.0, -2.5, -2, -1.5, -1.0, -0.5, 0, 0.5$ from bottom to top, as obtained from Monte Carlo simulations, in an external potential $V_{ext}(x)$ (red solid line, right vertical axis) characterized by a strength $s = 60$, a width $w = 0.4$, and steepness parameter $p = 4$.

5.3.2 Machine Learning Methods

With an optimization process that uses several techniques from the field of ML, we will construct intrinsic free-energy functionals of the form of Eqs. (5.9) and (5.10) such that the density profiles $\rho^{ML}(x)$ that follow from this machine-learned functional are an “optimal” approximation to the corresponding MC densities $\rho^{MC}(x)$. We recall that $\rho^{ML}(x)$ is to be determined as a solution of the Euler-Lagrange equation (5.4), not only for $\Lambda = \sigma$ at a given temperature, chemical potential, and external potential, but also for a given excess functional $\mathcal{F}^{exc}[\rho]$. In other words, we are interested in optimal kernels $\omega_2(x)$ and $\omega_3(x)$ (where $\omega_3(x) \equiv 0$ for ML2).

In order to quantify “optimal” we define a so-called loss function \mathcal{L} that characterises the difference between ML and MC profiles, and that we will minimize with respect to $\omega_2(x)$ and $\omega_3(x)$. Here we define $\mathcal{L} = \mathcal{L}_1 + \mathcal{L}_2$ to consist of a dominant contribution \mathcal{L}_1 and a regularization term \mathcal{L}_2 . The dominant loss term is defined by the mean-square error [213] between the MC and ML profiles,

$$\mathcal{L}_1 = \frac{1}{n} \sum_{j=1}^n \frac{1}{L} \int_{-L/2}^{L/2} dx \left(\frac{\rho_j^{MC}(x) - \rho_j^{ML}(x)}{\rho_b^{MC}(\mu_j)} \right)^2, \quad (5.16)$$

where $j = 1, \dots, n$ labels the $n = 24 \times 8 = 192$ combinations of 24 external potentials and the 8 chemical potentials of the training set as identified above. We normalize the difference between the MC and ML profiles by the MC bulk density at the chemical potential μ_j of training set j , for which we performed separate bulk simulations. This scaling promotes equal weights to high- and low-density states during the learning process. The regularization term \mathcal{L}_2 is independent of the MC and ML profiles and defined by

$$\mathcal{L}_2 = \frac{\lambda}{L} \int_{-L/2}^{L/2} dx \frac{1}{2} \left(\left(\frac{\omega_2(x)}{\sigma^2} \right)^2 + \left(\frac{\omega_3(x)}{\sigma^5} \right)^2 \right) f(x), \quad (5.17)$$

where $f(x)$ is given by

$$f(x) = \begin{cases} 1 & \text{for } |x| < \sigma; \\ e^{x/\sigma-1} & \text{for } |x| \geq \sigma. \end{cases} \quad (5.18)$$

It accounts for the constraint that $\omega_2(x)$ and $\omega_3(x)$ must decay smoothly to zero for $x \gg \sigma$, where our statistics is poor. Moreover, \mathcal{L}_2 also suppresses undue high-wavenumber undulations that tend to develop at $|x| < \sigma$. We tune the (positive) regularization parameter λ by trial and error such that it contributes less to the minimization procedure than \mathcal{L}_1 , while not being too small to be irrelevant. Note that \mathcal{L}_2 effectively reduces the range of $\omega_i(x)$ by suppressing it exponentially for $|x| > \sigma$.

The minimization of the total loss function \mathcal{L} is performed with the stochastic and iterative optimization method Adam as proposed by Kingma and Ba in Ref. [214]. We use their suggested default step size $\alpha = 0.001$ and exponential decay rates $\beta_1 = 0.9$, $\beta_2 = 0.999$,

and refer the reader to their work for a full description of the method and its parameters. During each iteration of the minimization process the gradient of the loss function w.r.t. the kernels $\omega_i(x)$ is required, which are straightforwardly derived for \mathcal{L}_2 to be the functional derivatives

$$\frac{\delta \mathcal{L}_2}{\delta \omega_i(x)} = \frac{\lambda \omega_i(x)}{L \sigma^{6i-8}} f(x). \quad (5.19)$$

The functional derivatives of \mathcal{L}_1 with respect to $\omega_i(x)$ for $i = 2, 3$ is more involved and stems from the dependence of \mathcal{L}_1 on the ML density profiles $\rho_j^{ML}(x)$ for $j = 1, \dots, n$, such that the functional chain-rule yields

$$\frac{\delta \mathcal{L}_1}{\delta \omega_i(x)} = \frac{-2}{n} \sum_{j=1}^n \frac{1}{L} \int_{-L/2}^{L/2} dx' \frac{\rho_j^{MC}(x') - \rho_j^{ML}(x')}{(\rho_b^{MC}(\mu_j))^2} \frac{\delta \rho_j^{ML}(x')}{\delta \omega_i(x)}, \quad (5.20)$$

where we replaced the dummy integration variable x of Eq. (5.16) by x' . From the Euler-Lagrange equation (5.4) for the DFT equilibrium profiles ρ_0 – which are represented by ρ_j^{ML} in Eq. (5.20) – one checks that $\delta \rho_0(x') / \delta \omega_i(x) = -\rho_0(x') \times \delta^2 \beta \mathcal{F}^{exc} / \delta \rho(x') \delta \omega_i(x)$. Upon considering ω_i and ρ independent variables in Eqs. (5.9) and (5.10) for the ML2 and ML3 excess functional, respectively, the second (cross) derivative for $i = 2$ equals $\rho_0(x + x')$, and for ML3 and $i = 3$ it equals $\frac{1}{3}[\rho_0^2(x + x') + 2\rho_0(x')\rho_0(x + x')]$. Hence, within this approximation a numerical integration of x' suffices to evaluate Eq. (5.20), and in combination with Eqs. (5.19) we can numerically calculate $\delta \mathcal{L} / \delta \omega_i(x)$ for the grid points x of our system. Thus, we have all ingredients to minimize \mathcal{L} by means of Adam [214].

5.3.3 The Training Process

The training process starts with an initial guess for the two kernels, for which we take the MF approximation $\omega_2^0(x) = \omega_3^0(x) \equiv 0$, where the superscript 0 denotes the 0-th iteration in the training process. Next, we use these kernels to calculate the n density profiles $\rho_{j,k}^{ML}(x)$ for learning sample $j = 1, \dots, n$ and iteration label $k = 0$ by solving the Euler-Lagrange equation Eq. (5.4) using a Picard iteration scheme with the MC profile $\rho_j^{MC}(x)$ as the initial guess.

On the basis of Eqs. (5.16)-(5.20) we can then evaluate \mathcal{L} and $\delta \mathcal{L} / \delta \omega_i(x)$ for $i = 1, 2$, from which improved kernels $\omega_i^k(x)$ are constructed for $k = 1$ by employing Adam[214], which will give rise to improved density profiles $\rho_{j,1}^{ML}(x)$, etc. For $k \geq 2$ we take $\rho_{j,k-1}^{ML}(x)$ as initial guess in the Picard-iteration of ρ_j^{ML} . The iteration process is repeated until the loss function has converged.

Although Adam is already an efficient algorithm for the learning process, its computational cost can be significantly reduced by making use of stochastic optimization. Rather than using all n elements of the training set in every iteration, which involves the addition of all n terms in Eq. (5.20) at every iteration level k , we consider mini batches with only 20 randomly selected elements of the training set during each Picard iteration k . The gradient of the loss function \mathcal{L}_1 is computed by only taking into account this mini batch,

thus the summation over the n density profiles of Eq. (5.20) changes to a summation over 20 randomly-selected density profiles and the normalization factor $1/n$ becomes $1/20$. A new mini batch is randomly selected during every iteration in the ML process.

5.4 RESULTS FOR THE LENNARD-JONES SYSTEM

We perform MC simulations of the LJ system to generate MC density profiles with 24 different external potentials, described in section 5.2, and 8 equi-distant different chemical potentials, $\beta\mu \in \{-3.0, -2.5, \dots, 0.0, 0.5\}$, for the temperature $k_B T/\epsilon = 2$. We describe the kernels, the resulting density profiles, the mechanical equations of state of the bulk fluid, and the radial distribution functions that follow from the functionals ML2 and ML3 using two different routes.

5.4.1 The Kernels

For several choices of the regularization parameter λ in Eq. (5.17) we determined the kernel $\omega_2(x)$ for ML2 and $\omega_2(x)$ and $\omega_3(x)$ for ML3. Without a significant \mathcal{L}_2 contribution, $\lambda \leq 10^{-3}$, we found spurious peaks in both $\omega_2(x)$ and $\omega_3(x)$ for $|x| > 8\sigma$, i.e. at the largest separations (with the poorest statistics) we considered in the learning set; these spurious peaks disappeared and $\omega_2(x)$ smoothly decayed to zero for $\lambda \geq 10^{-2}$, and throughout we settle for $\lambda = 10^{-2}$ as a reasonable compromise between error-correction and minimization of the actual loss function of interest \mathcal{L}_1 .

In Fig. 5.4.1 we present the evolution of the loss functions \mathcal{L}_1 (blue) and \mathcal{L}_2 (red) during the training process with iteration label k , in (a) for ML2 and in (b) for ML3; the grey curves in (a) and (b) represent a moving average of \mathcal{L}_1 over 15 iterations. We observe good convergence after, say $k = 5000$ iterations. We note that the minimized loss function \mathcal{L}_1 of ML2 is as small as 5×10^{-4} , and for ML3 it is even about four times smaller. We also note that $\mathcal{L}_2 < \mathcal{L}_1$ for ML2, as desired for a regularization term that is (naively) supposed to be a small correction to the total loss function. However, for ML3 we find \mathcal{L}_1 to be so small that it has dropped below the regularization term \mathcal{L}_2 , which in retrospect should be seen as a consequence of the good accuracy of the ML3 functional rather than as a problem for the relative magnitude of the two contributions to the loss function.

In Fig. 5.4.2(a) we show the MF (scaled) kernel $\beta u_{1,x}(x)$ (dashed blue line) and its ML2 correction $\beta u_{1,x}(x) + \omega_2(x)$ (black solid line), as obtained after 5000 iterations. For all x the ML2 kernel is more negative than the MF kernel, as if there is actually more cohesive energy in the system than predicted by MF. We see that $\omega_2(x)$ develops a peculiar and unexpected small “bump” close to $x = 0$. For ML3 a similar feature occurs close to $x = 0$ in both $\omega_2(x)$ and $\omega_3(x)$, as can be seen in Fig. 5.4.2(b) where we plot $\omega_2(x)$ (green solid line) and $\omega_3(x)$ (green dotted line) for the ML3 case as obtained after 5000 iterations, together with the ML2 kernel $\omega_2(x)$ (black solid line) for comparison. We see that ω_2 from ML3 is again essentially negative (except for a tiny positive feature at $x = 0$ and $|x| \simeq 2\sigma$), and contains a “bump” similar to the ML2 case. We also see that $\omega_3(x)$ has a structure that

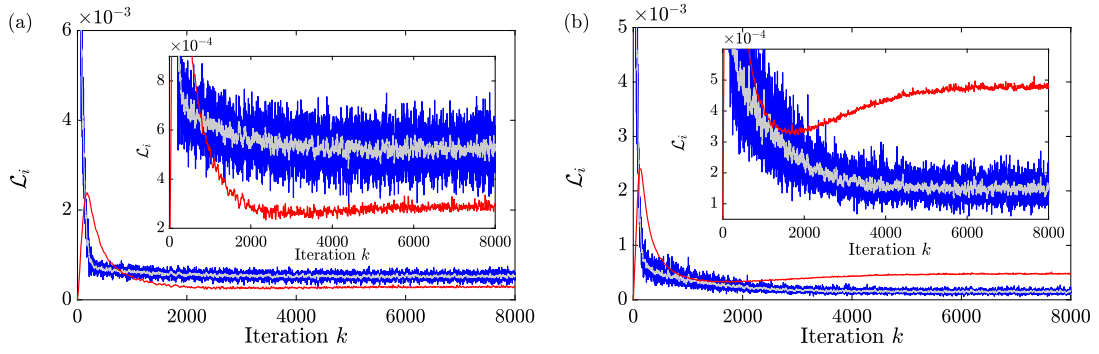


Figure 5.4.1: The loss function contributions \mathcal{L}_1 (blue) and \mathcal{L}_2 (red) as function of the iteration label k , in (a) for ML2 and in (b) for ML3. The grey traces in (a) and (b) represent moving average of \mathcal{L}_1 , and the insets only zoom in.

is quite similar to $\omega_2(x)$, however more pronounced with a higher peaks and lower valleys. Below we will investigate the thermodynamic and structural properties that follow from DFT based on these kernels.

5.4.2 The Density Profiles

The first test of the quality of the ML functionals is a comparison of their resulting density profiles with the simulated ones from the training set. In Fig. 5.4.3 this comparison is illustrated for the external potential parameterised by $w = 0.65$, $p = 2.0$, and $s = 40$ (shown in red) and the four chemical potentials $\beta\mu \in \{-2.5, -1.5, -0.5, 0.5\}$; for symmetry reasons we only plot the regime $0 < x < L/2$, and for comparison we also show the MF profiles. Clearly, the MF predictions are substantially worse than ML2 and ML3, except at the lowest μ , and ML3 constitutes a small improvement over ML2, especially at the peaks of the profiles at intermediate to high μ . In fact we can also conclude from Fig. 5.4.3 that the main improvement of ML2 and ML3 over MF compared to the simulations concerns the bulk density ρ_b that is approached in the center of the slit at $x = 0$, as will be made more explicit below.

In Fig. 5.4.4 we consider a comparison of MC simulations with MF, ML2, and ML3 density profiles in a particular external potential outside the training set, at $\beta\mu = -1$. The external potential consists of hard walls at $x = 0$ and $x = 20\sigma$, and for $x \in [0, 20\sigma]$ the potential varies irregularly with wells and barriers between $\pm k_B T$ as shown by the solid red curve in Fig. 5.4.4. We see again that both ML2 and ML3 are largely of comparable quality and substantially more accurate than MF.

5.4.3 Mechanical equation of state of the bulk

The (isothermal) mechanical bulk equation of state provides relations between the bulk density ρ_b , the pressure p , and the chemical potential μ , satisfying the constraint of the Gibbs-Duhem equation $dp = \rho_b d\mu$ such that we can equivalently consider $\rho_b(\mu)$, $p(\mu)$, or $p(\rho_b)$. Within DFT the bulk density $\rho_b(\mu)$ that follows from a particular free-energy excess

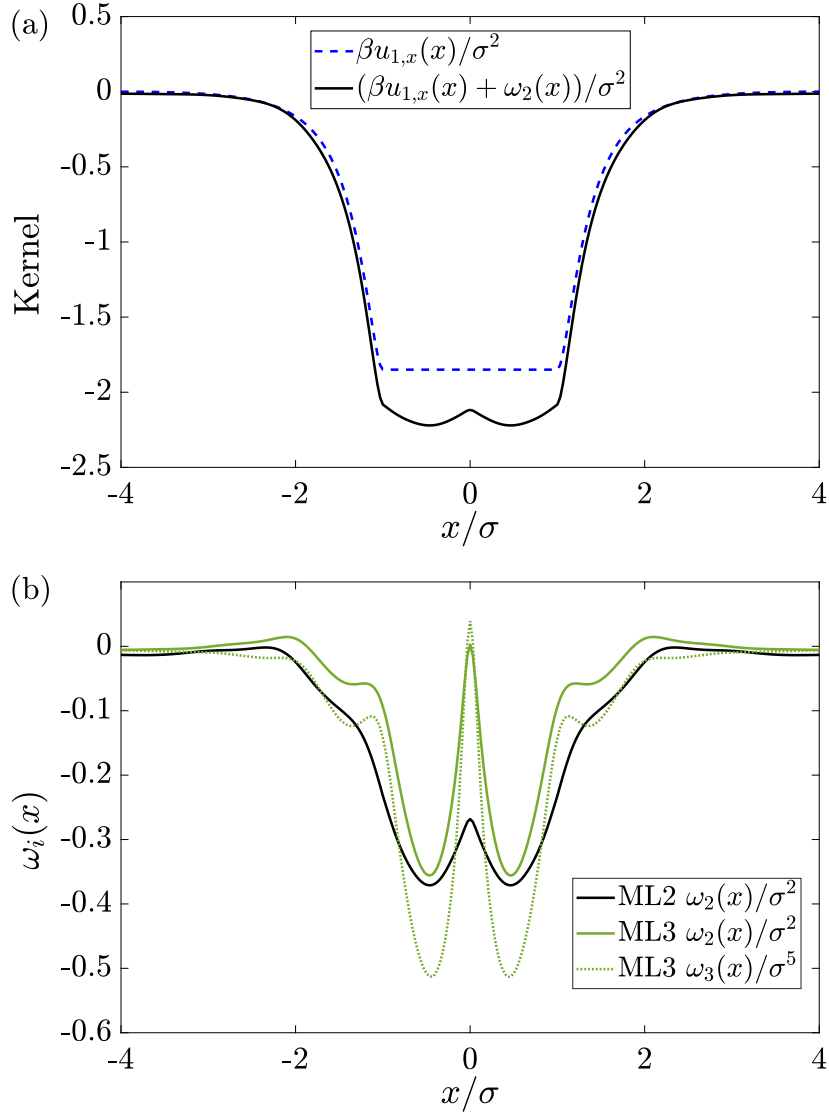


Figure 5.4.2: (a) The mean-field (MF) kernel $\beta u_{1,x}(x)/\sigma^2$ (dashed blue line) and its quadratic Machine Learning (ML2) improvement $(\beta u_{1,x}(x) + \omega_2(x))/\sigma^2$ (black solid line), as obtained for the LJ system at temperature $k_B T/\epsilon = 2$. (b) The cubic Machine Learning (ML3) kernels $\omega_2(x)/\sigma^2$ (green solid line) and $\omega_3(x)/\sigma^5$ (green dotted line), also at $k_B T/\epsilon = 2$, for comparison together with the ML2 kernel $\omega_2(x)/\sigma^2$ (black solid line).

functional follows from the solution of the Euler-Lagrange equation (5.4) for the homogeneous bulk case $V_{ext} \equiv 0$, which reduces for ML2 and ML3 to a nonlinear algebraic equation with coefficients that depend on $\int dx \omega_i(x)$. Hence $\rho_b(\mu)$ is straightforwardly solved numerically for the three functionals ML2, ML3, and MF of our interest here. The bulk pressure follows as $p(\mu) = -\Omega[\rho_b]/V$, from which $p(\rho_b)$ follows upon inversion of $\rho_b(\mu)$. For the temperature of interest, $k_B T/\epsilon = 2$, these three representations of the equation of state are shown in Fig. 5.4.5(a)-(c) for the three functionals MF (blue dashed line), ML2 (black solid line), and ML3 (green solid line) together with the MC data (purple symbols). The regime of the training set is hatched grey. In the μ -dependent curves of (a) $\rho_b(\mu)$ and (b) $p(\mu)$, we find agreement in the low-density limit $\beta\mu < -3$, as expected, since all functionals include the ideal-gas limit properly. In the regime of the training set we also

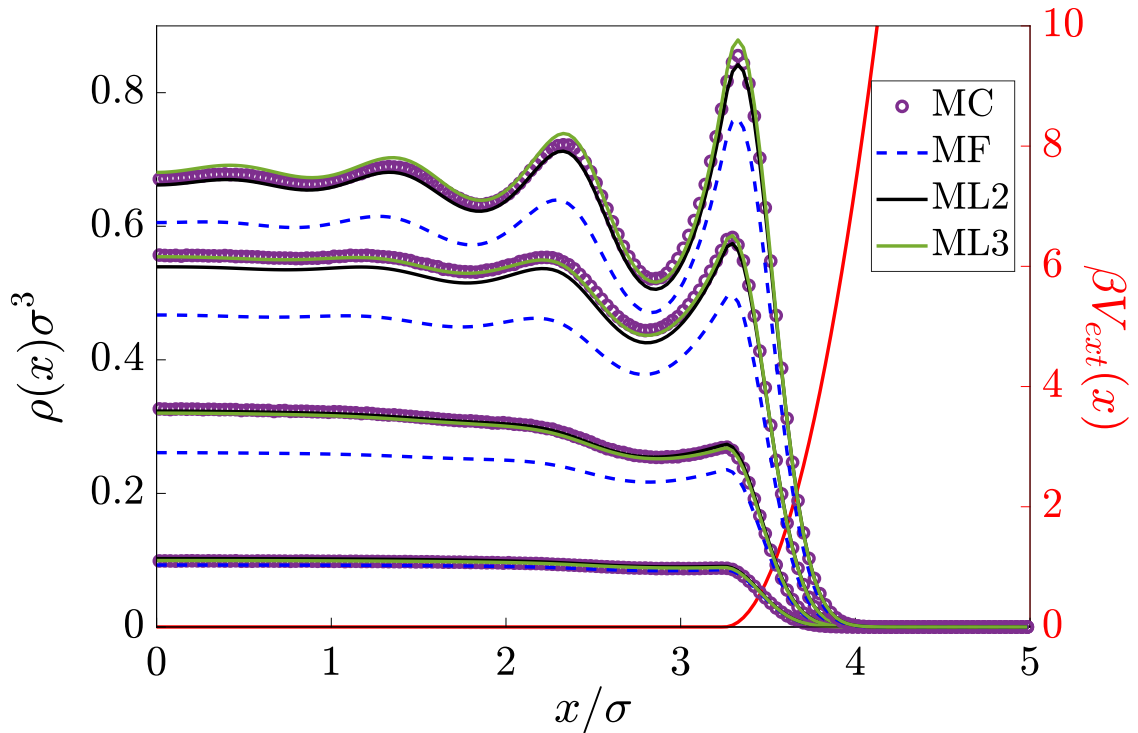


Figure 5.4.3: Density profiles of a (truncated) Lennard-Jones fluid confined in a planar slit characterized by a repulsive external potential given by Eq. (5.15) with parameters $w = 0.65$, $p = 2.0$, $s = 40$ at temperature $k_B T/\epsilon = 2$ and at four chemical potentials $\beta\mu \in \{-2.5, -1.5, -0.5, 0.5\}$ from bottom to top. Symbols stem from the grand-canonical MC simulations, and curves from the MF (blue dashed), ML2 (black solid), and ML3 (green solid) functionals; all four state points are part of the training set.

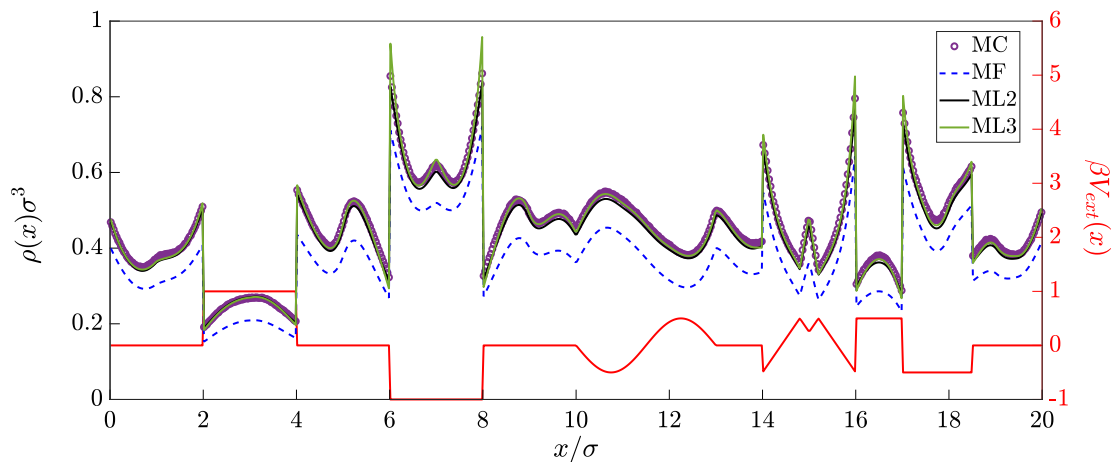


Figure 5.4.4: The equilibrium density profile for a LJ fluid at chemical potential $\beta\mu = -1$ and temperature $k_B T/\epsilon = 2$ in the external potential $V_{ext}(x)$ (red solid line) outside the ML training set. Symbols stem from grand-canonical Monte Carlo (MC) simulations, and lines are DFT predictions based on the mean-field (MF) approximation (blue dashed) and on the quadratic (ML2, black solid) and cubic (ML3, green solid) corrections with machine-learned kernels.

see ML2 and ML3 outperforming MF by a large margin in (a) and (b), with a small but hardly noticeable improvement of ML3 compared to ML2, as we could have expected on the basis of the density profiles of Fig. 5.4.4 and the loss functions of Fig. 5.4.1. At the high- μ side outside the training set, Fig. 5.4.5(a) shows an increasingly deteriorating quality of the ML2 and especially the ML3 prediction, which are systematically higher than the MC data, although they are still much more accurate than the predictions based on the MF functional. Interestingly, however, the picture that emerges from the $p(\rho_b)$ representation shown in 5.4.5(c) is much more forgiving for the MF functional, which is now of comparable good agreement in the complete regime of the training set and deviates as much as ML2 (and even less than ML3) from the MC data. Clearly, this relatively good MF and ML2 performance is due to a fortunate cancellation of errors occurring in the process of eliminating the dependence on the chemical potential.

It is perhaps remarkable that rather accurate *bulk* equations of state in a complete density interval can be obtained from MC simulations at only a few chemical potentials in only a few external potentials. Here it is crucial to appreciate the DFT formalism, which includes the statement that the intrinsic excess free-energy functional $\mathcal{F}^{exc}[\rho]$ that we construct by the ML Ansätze of Eqs. (5.9) and (5.10) is independent of the external and chemical potential, and hence can also be applied at any μ in the homogeneous bulk where $V_{ext} \equiv 0$.

5.4.4 The structure of the bulk fluid

A key feature of DFT is that it provides not only thermodynamic but also structural information, where we have seen that the first functional derivative $\delta\mathcal{F}^{exc}[\rho]/\delta\rho(\mathbf{r})$ plays a key role in the Euler-Lagrange equation (5.4) for the equilibrium one-body distribution function. We have also seen already that the second functional derivative $-\beta\delta^2\mathcal{F}^{exc}[\rho]/\delta\rho(\mathbf{r})\delta\rho(\mathbf{r}') \equiv c(\mathbf{r}, \mathbf{r}')$ equals the direct correlation function and governs the two-body distribution function[42, 46]. In a homogeneous and isotropic bulk fluid symmetry dictates that the direct correlation takes the bulk form $c_b(|\mathbf{r} - \mathbf{r}'|)$, and the radial distribution function $g(r)$ follows from the Ornstein-Zernike equation $g(r) - 1 = c_b(r) + \rho_b \int d\mathbf{r}' (g(r') - 1)c_b(|\mathbf{r} - \mathbf{r}'|)$. Since the ML2 and ML3 functionals have been fully determined in terms of $\omega_i(x)$ in planar geometry and its conversion to $\Omega_i(r)$ according to Eq. (5.12), we can write from Eqs. (5.9) and (5.10)

$$c_b(r) = c_{HS}(r) - \beta u_1(r) - \Omega_2(r) - 2\rho_b\Omega_3(r), \quad (5.21)$$

where for $c_{HS}(r)$ we used the White-Bear mark I direct correlation function reported in Ref. [50] (and where $\Omega_3 \equiv 0$ for ML2). Consequently, our ML2 and ML3 functionals (and likewise also the MF functional) give direct access to the two-body structure encoded in $c_b(r)$ and $g(r)$.

In Fig. 5.4.6 we plot the resulting $c_b(r)$ for bulk density $\rho_b\sigma^3 = 0.39$, and find fairly good agreement between MF, ML2, and ML3, except close to $r = 0$ where the $c_b(r)$ from ML2 and especially ML3 become deeply negative. This can be traced back directly to Fig. 5.4.2, which reveals that (i) there is close structural similarity between the functionals outside

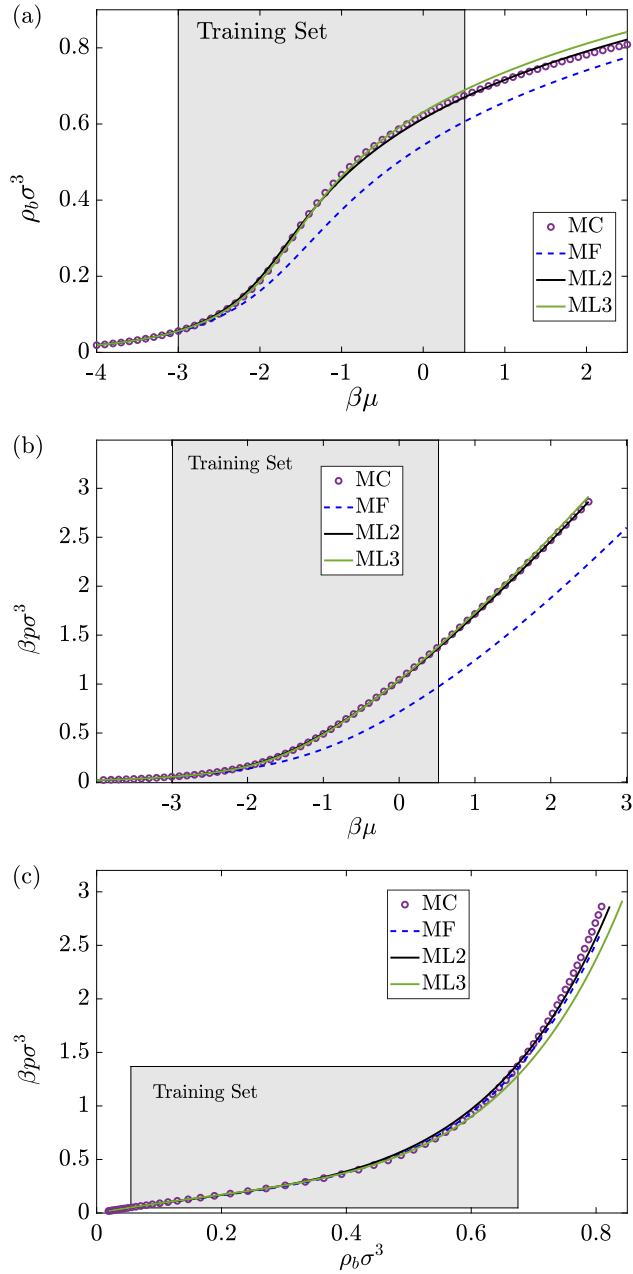


Figure 5.4.5: The relations between (a) the bulk density ρ_b and (b) the bulk pressure p as a function of the chemical potential μ for the (truncated) Lennard-Jones fluid at temperature $k_B T / \epsilon = 2$ as obtained from grand-canonical Monte Carlo simulations (MC, symbols), the machine learning functionals ML2 (black) and ML3 (green), and the mean-field function (MF, blue dashed). In (c) the corresponding pressure-density relation $p(\rho_b)$ are shown, obtained by elimination of μ from $\rho_b(\mu)$ of (a) and $p(\mu)$ of (b).

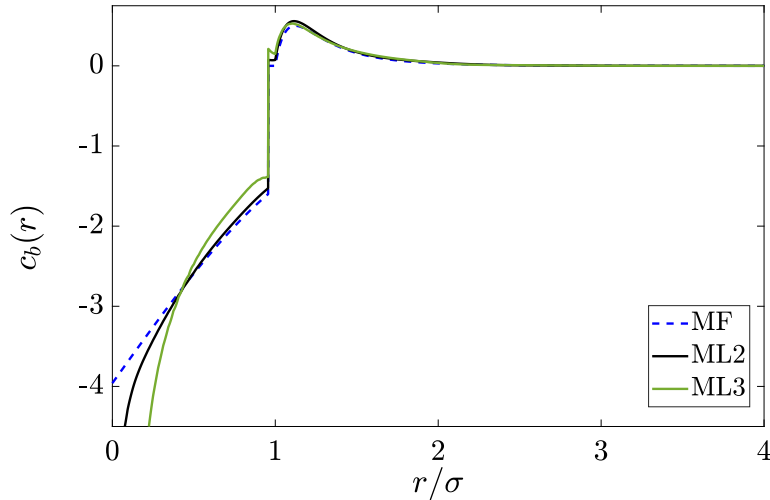


Figure 5.4.6: The Ornstein-Zernike direct correlation function $c_b(r)$ of the bulk Lennard-Jones system at temperature $k_B T/\epsilon = 2$ and bulk density $\rho_b \sigma^3 = 0.39$, as predicted by the second functional derivative of the excess free-energy functional within the mean-field (MF) approximation and its quadratic (ML2) and cubic (ML3) Machine Learning corrections.

the hard core, and (ii) that the “bumps” of $\omega_2(x)$ and $\omega_3(x)$ close to $x = 0$ give rise to a substantial slope $d\omega_3(x)/dx$ for $x/\sigma \in [0, 0.05]$ that translates via Eq. (5.12) in a relatively large effect in $c_b(r)$ in the vicinity of $r = 0$. Note also that $c_b(r)$ vanishes for $d < r \leq \sigma$ due to the Barker-Henderson splitting, and that all three versions of $c_b(r)$ agree pretty accurately outside the hard core, at least on the scale of the plot.

Upon insertion of $c_b(r)$ into the (Fourier transform of the) Ornstein-Zernike equation, we find (after an inverse Fourier transform) the radial distribution functions $g(r)$ that we compare with canonical MC simulations at a given density ρ_b (at the fixed temperature of interest $k_B T/\epsilon = 2$). The three lines in Fig. 5.4.7 show these radial distribution functions for MF, ML2 and ML3 at bulk density (a) $\rho_b \sigma^3 = 0.39$ and (b) $\rho_b \sigma^3 = 0.837$, together with the MC simulation results (symbols). For both the lower density in (a) and the higher one in (b) we find reasonably good overall agreement outside the hard core ($r > d$), with MF and ML2 actually outperforming ML3 close to contact. Inside the hard core our prediction for the $g(r)$ is poor in all cases, which is not surprising given that the underlying $c_{HS}(r)$ is constructed such as to cause a vanishing $g(r)$ inside the hard core; any tampering of the direct correlation (such as adding terms as we do in Eq. (5.21)) will give rise to spurious nonzero contributions to $g(r)$ for $r < d$ [54].

Interestingly, DFT provides another procedure to calculate the radial distribution function of a bulk fluid. This so-called “Percus test-particle method” [215] is based on the identification of $\rho_b g(r)$ with the equilibrium density profile $\rho_0(r)$ that surrounds a given (test) particle that is fixed in the origin of an otherwise homogeneous fluid at bulk density $\rho_b \equiv \rho_0(\infty)$. In other words, $g(r) = \rho_0(r)/\rho_0(\infty)$ with $\rho_0(r)$ the spherically symmetric density profile of the fluid in an external potential that equals the pair potential, $V_{ext}(\mathbf{r}) = u(r)$, scaled such that $g(\infty) = 1$. For a given chemical potential μ and a given functional $\mathcal{F}^{exc}[\rho]$ one thus obtains $g(r)$ through the solution $\rho_0(r)$ of the Euler-Lagrange

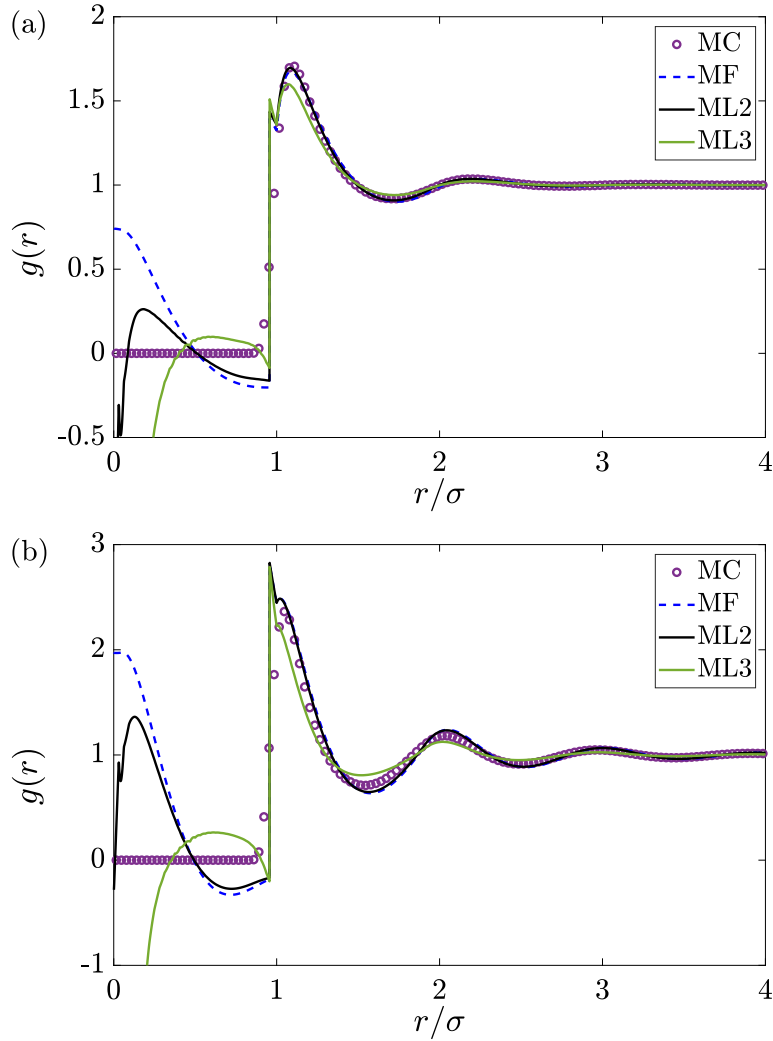


Figure 5.4.7: The radial distribution function $g(r)$ of a truncated Lennard-Jones fluid at bulk density (a) $\rho_b \sigma^3 = 0.39$ and (b) $\rho_b \sigma^3 = 0.837$, as obtained from the Ornstein-Zernike equation with a direct correlation function $c_b(r)$ that follows from the free-energy functionals ML2 (black), ML3 (green), and MF (blue dashed). The symbols denote $g(r)$ as obtained from canonical Monte Carlo simulations at the same bulk density and temperature.

equation (5.4). For the same two state points as used in Fig. 5.4.7 we present the resulting radial distributions in Fig. 5.4.8(a) and (b). For both densities the agreement between simulation and all three DFTs is substantially better than obtained from the Ornstein-Zernike route shown in Fig. 5.4.7, not only for $r < \sigma$ where the Boltzmann factor of the external potential in Eq. (5.4) ensures a vanishingly small contribution to $g(r)$ but also at larger distances where the oscillations in the MC data are rather accurately captured by all three DFTs. Interestingly, however, the peaks of the oscillations in (b) are actually better accounted for by MF and ML2 than by ML3, which underestimates them especially at close contact. The relatively good performance of MF in predicting $g(r)$ via the Percus test-particle method compared to its relatively poor prediction of the equation of state $\rho_b(\mu)$ is due to the scaling-out of ρ_b in the density profile $\rho_0(r)$ such that $g(\infty) = 1$ by construction. Clearly, an overall comparison of Fig. 5.4.7 and Fig. 5.4.8 shows that $g(r)$

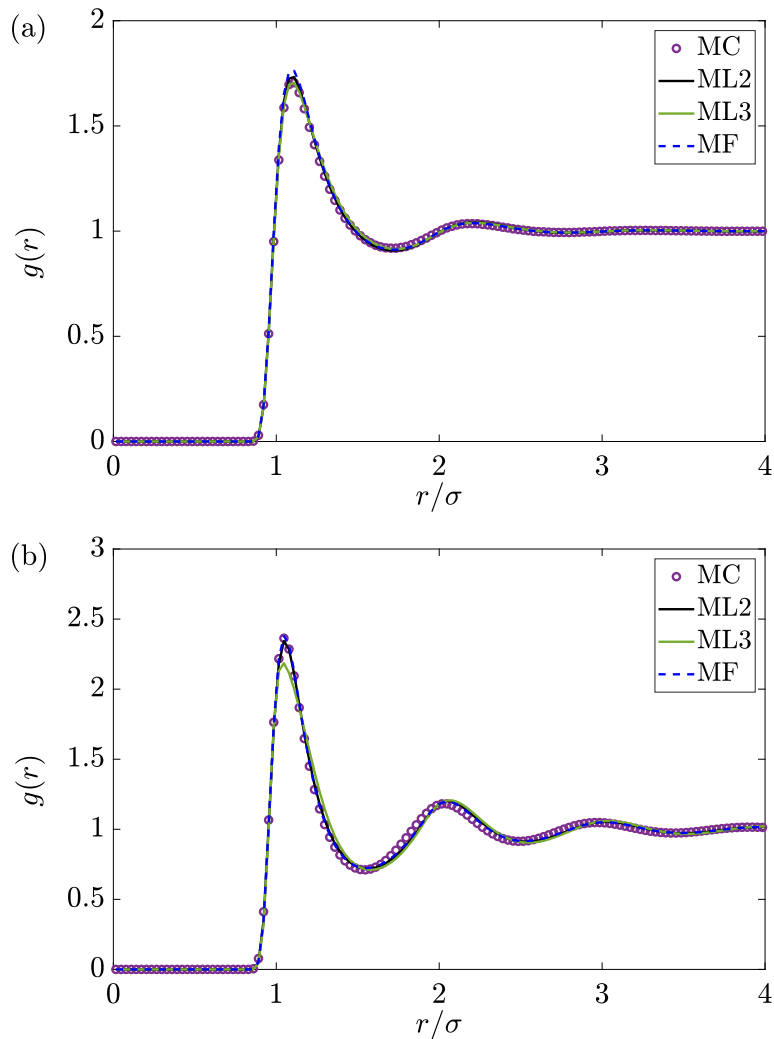


Figure 5.4.8: The radial distribution function $g(r)$ for the Lennard-Jones system as obtained from the Percus test-particle method for a bulk density (a) $\rho_b \sigma^3 = 0.39$ and (b) $\rho_b \sigma^3 = 0.837$. System, legends, and the MC data are identical to those in Fig. 5.4.7.

based on the test-particle method is much more accurate compared to the MC simulations than those based on the Ornstein-Zernike equation. This is not surprising given that we constructed the direct correlation function in Eq. (5.21) based on a modification of that of a reference hard-sphere system, which yields a non-vanishing radial distributions inside the hard core if the OZ route is used. A more careful discussion on the different radial distribution functions from the two routes can be found in Ref. [54].

5.5 SUMMARY, DISCUSSION, AND OUTLOOK

In this chapter we combine the formalism of classical density functional theory (DFT) with machine learning (ML) density profiles from Monte Carlo (MC) simulations to construct approximations to the excess intrinsic Helmholtz free-energy functional $\mathcal{F}^{exc}[\rho]$ of a (truncated and shifted) Lennard-Jones fluid at the supercritical temperature $k_B T / \epsilon = 2$. This functional consists of a well-known and accurate hard-sphere contribution, a standard Van

der Waals type mean-field account of the attractions, and new machine-learned corrections that are, for simplicity, either of a quadratic (ML2) or an additional cubic (ML3) form in the density. The kernels of ML2 and ML3 are radially symmetric and translation-invariant two-point functions of the form $\Omega_i(|\mathbf{r} - \mathbf{r}'|)$ for $i = 2$ and 3 , see Eqs. (5.9) and (5.10). By comparing DFT predictions of the equilibrium density profiles $\rho_0(x)$ with grand-canonical MC simulations at a **learning set** of chemical potentials μ and external potentials $V_{ext}(x)$ in a 3D **planar** geometry, we can construct the optimal planar kernels $\omega_i(|x - x'|)$ using Adam to minimize a suitable loss function, from which we can reconstruct the full **radially** symmetric kernels $\Omega_i(|\mathbf{r} - \mathbf{r}'|)$. Given that $\mathcal{F}^{exc}[\rho]$ is independent from the external potential and the chemical potential, the functional and its Euler-Lagrange equation (5.4) for $\rho_0(\mathbf{r})$ can be applied to any μ and any $V_{ext}(\mathbf{r})$. By comparisons with density profiles obtained from grand-canonical MC simulations, for conditions within and outside of the learning set, we find that the ML2 and ML3 functionals generally outperform MF by far because the latter predicts densities that are systematically too low; ML3 improves ML2 somewhat on some of the details at higher μ , at least within the training set. A similar picture emerges from the resulting representations of the mechanical equations of state, *viz.* the bulk density $\rho_b(\mu)$ and the pressure $p(\mu)$, where MF is too low by a large margin and ML3 performs only slightly better than ML2 within the training set, while showing a slightly poorer performance outside. The functional $\mathcal{F}^{exc}[\rho]$ can also be used to calculate the direct pair correlation function, from which the radial distribution $g(r)$ of a bulk fluid follows via the Ornstein-Zernike equation. At the relatively low bulk density $\rho_b\sigma^3 = 0.39$ this yields, outside the hard core, an (almost) equally satisfying result for MF, ML2, and ML3, see Fig. 5.4.7. Inside the hard core, and also close to contact, say $\sigma < r < 1.3\sigma$, the prediction for $g(r)$ is poor in all cases. However, all three functionals give a rather good account of the simulated $g(r)$ at these two state points if the Percus test-particle method is employed, although here ML3 overestimates the peaks at the higher density slightly. The reason for the relatively good MF performance for $g(r)$ compared to the equation of state $\rho_b(\mu)$ and density profiles stems from the imposed asymptotic normalization $g(r \rightarrow \infty) = 1$.

A disadvantage of the ML approach is its black-box character, and the associated difficulty to interpret the outcome. In particular the “hump” in the ML2 and ML3 kernels $\omega_i(x)$ close to $x = 0$ shown in Fig. 5.4.2 and the associated deeply negative direct correlation $c_b(r)$ close to $r = 0$ for ML3 in Fig. 5.4.6 are actually rather suspicious. In retrospect, we expect these features to be the result of some degree of overfitting the data in the learning process. This is also borne out by closer inspection of the bulk equations of state $\rho_b(\mu)$ and $p(\mu)$ in Fig. 5.4.5(a) and (b), respectively, where ML3 hardly improves upon ML2 in the (hatched) regime of the learning set while performing even poorer outside, and likewise for the $g(r)$ of Figs. 5.4.7(a) and 5.4.8(a) at the density $\rho_b\sigma^3 = 0.39$ that lies comfortably in the middle of the training set. Of course, ML3 does outperform ML2 somewhat for the density profiles of Fig. 5.4.3. Nevertheless, some more caution could or should have been exercised in the diversity of the training set of external potentials, perhaps with attractive components and discontinuities. We leave studies along these lines for future work.

Although there is room for improvement and extensions, we have shown here anyway that it is in principle possible to construct a free-energy functional for an atomic fluid by an ML process that takes data from grand-canonical MC simulations at a variety of chemical and external potentials, from which further predictions **outside** the training set can be made. Interestingly, even data taken in a planar geometry can suffice to construct the full functional, at least for the (relatively simple) functional forms that we considered here which are linear in the kernels $\Omega_i(|\mathbf{r} - \mathbf{r}'|)$; nonlinear forms probably require a different treatment. It is important to realize that we fixed the temperature, and although $\mathcal{F}^{exc}[\rho]$ is independent of μ and $V_{ext}(\mathbf{r})$ it is dependent on T , so strictly speaking a new functional is to be constructed at every temperature of interest. We leave the T -dependence of the functional to future work. Another rather straightforward extension is to use the newly constructed functional to calculate the Gibbs adsorption and the tensions of wall-fluid interfaces, for which we expect good accuracy on the basis of the good agreement of the density profiles. We also expect that it is possible to extend studies of this type to other systems with spherically symmetric particles, also to mixtures such as electrolytes. Systems of particles with orientation degrees of freedom are probably challenging in practice because of their larger number of variables, although one could imagine first attempts based on truncated expansions in spherical harmonics or an initial focus on homogeneous bulk states (nematics). We hope that this chapter will stimulate further explorations of the combination of DFT, ML, and MC simulation.

SUMMARY, CONCLUSION AND OUTLOOK

SUMMARY AND CONCLUSION

chapter 2

We have investigated in detail primitive model (PM) electrolytes in contact with planar electrodes, both in the near field as well as in the far field. The tool that was used to tackle this system is classical density functional theory (DFT). There are several functionals that deal with the electrostatic (ES) interactions between the ions. The simplest of such functionals is the mean-field Coulomb (MFC) functional, which was used as the basis for two other functionals that were considered and those can therefore be regarded as corrections on top of the MFC. The corrections come from the mean-spherical approximation (MSA), a closure to solve exactly the Ornstein-Zernike equation; an equation relating the total correlation function to the direct correlation function, the latter is directly related to the functionals. The energy and compressibility route allow one to go from the total correlation function to thermodynamic quantities, such as the free energy and pressure. Hence, this opens up two possibilities for improvements of the MFC functional, namely using the direct correlation function from MSA and the MSA expression for the (free) energy. The former we abbreviate with MSAC (c standing for correlation function) and the latter with MSAu (u standing for (free) energy). Carefully examining the MFC, MSAC, and MSAu functional let us to conclude that the MFC functional falls short on many instances; the comparison of the density profiles and thermodynamic quantities between MFC and simulations shows large deviations for high surface potentials and high bulk concentrations as expected. The remaining competitors are the MSAC and MSAu functional. Both perform well in the near field, where especially at high concentrations and surface potential their performance is almost identical to the eye. At low concentrations and surface potentials, the MSAu is the only functional that predicts depletion near the surface, which comes from taking into account the functionalized bulk free energy. It has become clear that, in order to find depletion, one needs an electrostatic free energy term that is negative and scales as $\rho^{3/2}$, a power that is lower than the scaling in the hard-sphere free energy that goes as ρ^2 and therefore dominates in the dilute limit. In the far field, however, the MSAu functional displays a different asymptotic decay than the MSAC functional, due to unnatural coupling between the charge and number densities that originates from the MSA-energy term. The far-field behavior of the MSAC functional, on the other hand, compares very well to simulations and Integral Equation Theory (IET), and is considered to have the best

overall performance and therefore was used in the subsequent studies on the electrode-electrolyte interface. Returning shortly to the far-field results in general, we showed that the asymptotic charge decay of the MSAC functional is unsurprisingly exactly the same as the predicted asymptotic charge decay from IET using the MSA. The restricted (R) PM has the nice property that the charge and number densities/correlation function decouple, allowing us to investigate the asymptotic decay of the charge and number densities/correlation functions separately. We showed that the number decay length follows half the charge decay length up to the Fisher-Widom (FW) point, after which the number decay length is exactly the same as the one for the uncharged system. Hence, for concentrations beyond the FW point, the steric repulsion determine the asymptotic number decay. The measurable decay length in the system is always the highest of the charge and number decay lengths, and by using DFT one has access to the solvation force, which is the quantity that is comparable to the quantity measured in atomic force microscopy (AFM) and surface force apparatus (SFA) experiments. We showed that the asymptotic decay in the solvation force is indeed always the largest of the charge and number decay length. However, although we did find an increase in the decay length at high concentrations, the increase is much slower than those measured in the SFA experiments. This discrepancy between theory and simulations on the one hand, and the experiments on the other is still an open question that needs further investigation.

chapter 3

Once settled on the MSAC functional we continue our journey in electrolyte world and arrive at the differential capacitance. However, we first need to establish a proper basis on which we base our trust in the MSAC functional. Therefore we carefully compared results from DFT with those from Brownian Dynamics (BD) simulations across a wide range of parameters, while keeping the temperature and dielectric constant fixed at room temperature in water. However, the model that was used in DFT and BD was slightly different. In DFT, the ions have a hard-core steric repulsion, while the ions in the BD simulations have a softer WCA steric repulsion, with the reason that hard-core repulsion are difficult to model in BD and with DFT there is a good approach to deal with hard-core repulsion in the form of Fundamental Measure Theory (FMT). As a reference, we considered a system of two planar electrodes separated by a distance of $H = 4$ nm, held at a surface potential difference of $\Psi = 0.2$ V with an RPM electrolyte with ion diameters $d = 0.5$ nm and connected to an ion reservoir at a concentration of $\rho_r = 1$ M. Excellent agreement between DFT and MD was found. From this reference system, we first changed the reservoir concentration to $\rho_r = 0.1$ M and $\rho_r = 5$ M. The only discrepancy at lower concentrations was found at contact, where the simulations predict a higher local density than the DFT calculations, which we attributed to the difference in the treatment of the steric repulsions in DFT and BD. At high concentrations the agreement between DFT and BD is very good, with small deviations that occur due to known deficiencies of FMT. The next system that was considered is the asymmetric electrolyte in which the anions are twice

as small as the cations, i.e. $d_+ = 2d_- = 0.5$ nm. Again, almost perfect agreement between DFT and BD was found. Similarly when changing the surface potential to low ($\Psi = 0.02$ V) and high ($\Psi = 2$ V) values. Even when considering asymmetric electrolytes in which the valency of the cation is $z_+ = +2$, while the anions are kept monovalent, do we find excellent agreement. Finally, we changed the surface separation, and also here excellent agreement was found. Overall, we conclude that the MSAC DFT performs remarkably well for aqueous electrolytes with the parameters considered here. This allows us to make the next step and investigate the differential capacitance. We note at this point that the differential capacitance differs fundamentally between the BD simulations, which were performed canonical and the DFT calculations, which are grand canonical. However, one can relate the differential capacitance in the canonical ensemble C_N (constant number of particles) to the one in the grand-canonical ensemble C_μ (constant chemical potential), using relations that are similar to the ones that relate the heat capacities at constant volume and pressure. That said, properly comparing the two shows again excellent agreement between BD and DFT. Moreover, we found interesting differences between C_N and C_μ for a reservoir concentration of $\rho_r = 1$ M, where C_μ has a camel shape and C_N a bell shape. This is mainly attributed to the soft-natured WCA particle-wall interaction that induces a flexibility in the adsorption of ions near the surface, and hence a larger difference between C_N and C_μ . For the first time, we explicitly showed the difference between C_N and C_μ and emphasize the importance of properly relating the system under study and the corresponding ensemble.

chapter 4

We continued our journey further into the mountains of the differential capacitance and explored its hills and valleys in more detail. Given the previous experience, we use the MSAC functional and study C_μ as a function of the applied potential for several different electrolytes. Revisiting the model made us realize that the differential capacitance is directly related to the response of the first layer of ions to the applied electric potential. This observation has not been made before, and gives new insight into the behavior of the differential capacitance and how to interpret its hills and valleys. Again, we first consider the symmetric RPM which undergoes the famous camel to bell crossover upon increasing the concentration. Understanding this crossover, requires an understanding of the features that lead to the maximum in the differential capacitance; the crossover can be understood as the two maxima merging (at surface potential of 0 V for the RPM). It turns out that this maximum is a result of structural change due to ionic packing effects. For the RPM at low concentrations (camel-shaped capacitance curves), increasing the surface potential attracts the counterions, which fill the first layer near the electrode, up to the point at which it becomes energetically favorable to build a second layer of ions, after which C_μ starts to decrease. Hence, a peak in C_μ is related to a change in the structure of the electrolyte near the charged surface: from one layer of ions to two layer of ions near the electrode. At high concentrations, one always gets layering due to packing, regardless the applied potential,

and therefore changing the surface potential does not change the structure, except near the potential of zero charge (0 V for the RPM) at which the cations and anions replace each other, causing a maximum in C_μ at 0 V and hence a bell-shaped curve. Changing the ion size of the symmetric electrolyte does not change this story, neither for the asymmetric electrolyte in which the cations and anions have a different diameter. However, the latter case is interesting in a different manner, because using our newly discovered equation for C_μ shows explicitly that the cations determine C_μ at negative potentials, while the anions determine C_μ at positive potentials, which was indeed explicitly shown. More interesting is the electrolyte with a valency asymmetry. Divalent ions behave differently from monovalent ions, which becomes manifest in the curves of C_μ . At low bulk concentrations C_μ can have two maxima occurring at positive potential in the case of divalent anions. Both these maxima indicate a structural change. The first maximum indicates overscreening in the first layer of divalent anions, the minimum thereafter indicates that the system gets rid of overscreening, while the second maximum again shows overscreening due to the second layer of divalent anions. Hence, this rich behavior is captured in the differential capacitance. Gathering this gained knowledge let us to investigate three-component systems in which there is one species of monovalent cations and two species of anions, which either differ in valency or size. In the former case in which there is one monovalent and one divalent anion species, it turns out that even a tiny concentration of divalent anions w.r.t. monovalent anions (down to $\rho_{b,2-}/\rho_{b,-} = 10^{-5}$) can have a large signature in C_μ . This is due to the competition between divalency and monovalency close to the electrode, which the former wins in case of large enough surface potentials even though their bulk concentration is much lower. This manifests in the Boltzmann factor of the product of the valency and the electric potential, i.e. $\rho_{b,-}e^{e\beta\Phi}$ versus $\rho_{b,2-}e^{2e\beta\Phi}$, which the latter wins for large enough $e\beta\Phi$. Another three-component system that we considered contained two anion species of which one has a large anion diameter and the other a small anion diameter. Even when the bulk concentration of the large anion species is 1000 times larger than that of the small anion species do we find that the small anion species determines C_μ at large surface potentials. This can again be understood from realizing that the first layer of anions determines C_μ to a large extent: smaller anions can approach the surface to smaller distances than the large anions. At high surface potentials the smaller ions will compose the first layer, and by doing so they will push the large anions into the second layer. Hence, at large surface potentials, C_μ will be determined by the small anions, even though their bulk concentration can be much smaller. Both these cases of three-component electrolytes are important for both theoreticians and experiments, because impurities turn out to be important as we just showed and it is extremely difficult to perform experiments with ultra clean water. An example of an impurity that is present in water, even when "purified" is SO_4^{2-} , which has a molar concentration in the range of μM . Hence ions like these will play a role in measurements of the differential capacitance.

chapter 5

Finally, we zoom out and focus on the basics of DFT in a system of neutral particles, and construct the approximate Helmholtz free energy functional for a Lennard-Jones (LJ) system in which the particles interact via the cut-and-shifted LJ pair potential. Although this model system is rather simple, it is a challenging system for which to predict the density profiles beyond mean-field theory, for instance. To tackle this problem, machine learning (ML) algorithms are used and applied to improve the mean-field functional by exploiting the fact that the Helmholtz free energy functional is independent of the external and chemical potential. To this end, we consider two types of corrections on top of a mean-field functional that contains a function (or kernel) that connects local densities at two different positions within a planar geometry. Using Monte-Carlo (MC) simulations, density profiles are determined “exactly” for a variety of different chemical and external potentials, with in mind that the Helmholtz free energy functional is independent of both. The two learned functionals both improved the accuracy of the functional a lot compared to the mean-field functional, even for parameters outside the training set. Interestingly, even though the functional was learned within a planar geometry, it also performed well in a spherical geometry after a proper transformation of the kernel. Hence, the learned kernel contains essential information about the system in general, independent of the geometry.

OUTLOOK

Having studied all of these systems, lets us revisit the model and the assumptions that were made.

The first approximation that was made towards the PM is that the interactions between the ions and solvent particles in the system can be described by pair potentials. This is not at all obvious, especially when considering high concentrations and surface potentials, where three-body and higher-body potentials might become relevant. However, anything beyond two-body potentials is difficult to treat, and is often neglected for convenience; strictly speaking this is only justified in the dilute limit.

The second approximation that was made was integrating out the solvent, leaving behind a continuous dielectric medium with a certain dielectric constant (relative dielectric permittivity), which is the response function of the solvent to electric fields, and which we kept bulk-concentration independent and homogeneous for convenience. However, the environment of the solvent changes with other ions present, and therefore there is a coupling between the dielectric permittivity and the ion concentration, both in the bulk and local. This coupling actually leads to a dielectric permittivity that is non-local and anisotropic, which makes it very difficult to include in the calculations. This the reason that the dielectric permittivity is taken to be constant throughout this work. Inspired by Ref. [216], we have implemented a local-concentration-dependent dielectric permittivity, but have not used it throughout our work, due to lack of simulation results to validate this approach. This implementation uses the mean-field and loop-corrected expression for the dielectric

permittivity from Ref. [216], but with the bulk concentrations replaced with weighted densities. Unfortunately, this approach has not been tested further, but it might be a step in the right direction for a better treatment of the dielectric permittivity, and therefore a better treatment of the solvent without the need to explicitly include it. Nevertheless, one might argue that explicitly taking the solvent particles into account is important when considering very small surface separations. For water molecules, this is very difficult due to the complex nature of the interaction and the anisotropic character of water.

The next simplification towards the PM was to ignore the dispersion interactions, like the LJ interactions. This does become important when considering the asymptotic decay of the density profiles and correlation functions. We have work in progress that shows that including LJ interactions changes the asymptotic decay in the system, changing from exponential decay due to the electrostatic interactions to algebraic decay due to the LJ interactions. In particular, we can show that there is a crossover distance from the electrode at which the exponential decay length due to the electrostatic interactions is taken over by the algebraic decay of the LJ interactions. This is preliminary work and therefore not included in this thesis.

One assumption that was not touched upon, is the assumption that all the salt molecules are fully dissolved. This is also a condition that may be flexed upon when considering high concentrations and surface potentials. One method of taking this into account would be using statistical associating fluid theory [217, 218, 219]. Interestingly, taking the limit of full association can be used as a basis for constructing a functional to describe chain-like particles (polymers) of spherical monomers Ref. [153]. Subsequently, one can assign charge to individual monomers inside the chainlike particle, which allows for inclusion of non-spherical ions, relevant for ionic liquids for instance. We have implemented this into our code, and have tested the resulting functional against BD simulations from our collaborators in Twente (Sitlapersad, Den Otter, and Thornton from the University of Technology in Twente). However, we have not continued investigating electrolytes with these chain-like ions, due to our focus on other projects. Nevertheless, other groups have used similar approaches to describe ionic liquids [220, 221].

The electrodes that are considered in this work are flat structureless electrodes, while in reality they are solid conductors that are made up of molecules and atoms and therefore do have structure. In chapter 3, we did compare the density profiles in contact with a flat electrode using DFT and a structured electrode using BD and did not find large deviations between the two. This suggests that the actual structure of the electrode on average does not play a large role. However, this might not be the case when stretching the parameters into the regime in which there might be crystallization occurring at the electrode, i.e. when in-planar structure becomes important [222]. Besides, perfect conductors do not exist in reality, and therefore, instead of a surface charge that wholly resides on the surface of the electrodes, one might consider less trivial electrode charge densities, for which one needs to employ other theories like quantum DFT [44, 223]. The latter can also provide information on specific ion-electrode interactions. Current work in progress shows that specific ion-surface interactions do have a significant effect on the differential

capacitance, for instance, and investigating these interactions will be part of a future work. Also, the electrodes themselves have a differential capacitance, which in case of perfect conductors diverges to infinity and therefore does not play a role in the total capacitance. This so-called quantum capacitance plays a role when the conductivity of the electrode gets smaller, which is the case for single-atom-layered electrode materials, or semiconductors. In that case, information about the differential capacitance in the EDL is not enough to model the capacitance of realistic EDL capacitors. Future efforts should be directed towards combining state-of-the-art classical and quantum DFT.

Overall, the simple PM is a very convenient to work with. Especially, when employing DFT to tackle the model, in which it is relatively straightforward to include hard-sphere interactions and Coulombic interactions. That said, the model might not be the most accurate model to describe the EDL due to several assumptions that are made in its construction. Definitely, one could improve the model by including dispersion interactions, incorporating non-global dielectric permittivity, explicit solvent particles, and more. However, each addition increases the complexity of the model. Unfortunately, measuring the density profiles is very challenging and almost impossible, which lets us to lean on macroscopic thermodynamic observables, which are often integrated quantities are less sensitive to structural information. Hopefully, more experimental data will be available in the future that can help us learn more about the important ingredients of the model for the electrolyte and electrode, such that one can use theories like DFT to develop better batteries, blue energy devices, etc. Nevertheless, there is still room for more discoveries using the PM. One feature, that is also very important to further investigate, is optimizing the energy stored within the EDL/or pores in the electrode. Thus far, we mapped out the differential capacitance for many parameters and have gained a proper understanding of its features. The next step would be to scale up this pore system and calculate the actual energy that can be stored in macroscopic battery-sized systems. However, energy-storage devices are not solely characterized by its energy density, but also by its power density. Thus far, we have focused on the former, but the latter is determined by the charging and discharging dynamics, which is a different story altogether. One of the most straightforward methods to investigating the dynamics is by employing dynamical DFT (DDFT) (see e.g. Refs. [224, 225]). This DDFT assumes the system to be in quasi equilibrium, which might or might not be a good approximation for these systems. The more general framework, only recently developed, to describe dynamical systems goes by the name Power Functional Theory (see e.g. Refs. [226, 227, 228, 229]). A future direction would be to understand the dynamics of the electrode-electrolyte interface, which could contribute to real-life developments of the EDL capacitors, blue energy devices, and more.

Overall, ions matter, and there is still a lot of uncharted territory that needs to be explored.

SAMENVATTING

Het elektrode-elektrolyt grensvlak, ook wel de elektrische dubbellaag (EDL) genoemd, is het voornaamste onderwerp dat nader wordt onderzocht in dit proefschrift. Deze EDL bestaat uit de lading op de elektrode (eerste "laag") welke wordt afgeschermd door de lading in het elektrolyt (tweede "laag"), vandaar de naam dubbellaag. Deze wisselwerking tussen de lading op de elektrode en in het elektrolyt, als gevolg van herschikking van de ionen daarin, is niet zo vanzelfsprekend als men in eerste instantie zou denken. Aan de ene kant heb je de interne energie die idealiter zo klein mogelijk is en aan de andere kant heb je de entropie van de ionen die naar een maximum streeft. De eerste term wil de ionen met tegengestelde lading t.o.v. die op de elektrode zo dicht mogelijk bij de elektrode hebben, dusdanig dat de lading in de elektrode wordt gebalanceerd met die van de ionen tegen de elektrode aan. Het tweede neigt naar een zo homogeen mogelijk elektrolyt. De competitie van de interne energie aan de ene hand en de entropie aan de andere zorgt voor een complexe structuur van ionen nabij een geladen oppervlak. Dusdanig complex dat men na meer dan honderd jaar na de "ontdekking" hiervan nog steeds geen compleet beeld heeft van wat er nou daadwerkelijk gaande is. Een opvallend voorbeeld hiervan zijn recente experimenten bij hoge zoutconcentraties, welke laten zien dat de verdeling van ionen nabij geladen oppervlaktes veel langer van dracht is dan wat was verwacht op basis van bestaande theorieën. In dit proefschrift hebben we dit nader onderzocht, gebruik makend van Dichtheids Functionaal Theorie (DFT), welke als uitgangspunt heeft een functionaal voor de grootkanonieke potentiaal. Deze is geminimaliseerd voor de evenwichtsdichtheidsprofielen, en op het minimum is deze ook daadwerkelijk de thermodynamische grootkanonieke potentiaal. DFT is daardoor een uitermate geschikte en krachtige theorie om de EDL te bestuderen, omdat het zowel toegang geeft tot de structurele (dichtheidsprofielen van de ionen) alsook thermodynamische grootheden (druk, aantal ionen in systeem, differentiële capaciteit, etc.). In eerste instantie focussen we op de structurele dichtheidsprofielen, en in het bijzonder het asymptotische verval hiervan. Hiervoor beschouwde we drie verschillende functionalen voor de beschrijving van de elektrostatische interacties; een mean-field (MF) benadering, en twee correcties daarop gebaseerd op de mean-spherical-approximation (MSA). Dat laatste is een sluitingsrelatie om de Ornstein-Zernike (OZ) vergelijking op te kunnen lossen, welke een relatie is tussen de totale correlatie functie en de directe correlatie functie. De oplossing van de OZ vergelijking geeft de directe correlatie functie (c), alsook, via de energie-route, de interne energie (u). Eén functionaal gebruikt de MSA directe correlatie functie en noemen we MSAC, en de tweede functionaal gebruikt daarbovenop ook de interne energie en noemen we MSACu.

De drie functionalen MF, MSAC, en MSAu passen we toe om het verval te bestuderen van de ionenstructuur (dichtheidsprofielen), welke we vergelijken met simulaties en experimenten. Binnen het primitieve model - waarbij de oplossing (bijvoorbeeld water) niet expliciet wordt meegenomen, maar wordt beschouwd als een continu medium met een bepaald diëlektrische constante - blijkt dat de theoretische voorspellingen uit DFT, alsook voorspellingen literatuur gebruik makend van andere theorieën, niet de experimenten kunnen verklaren. Dat betekent dat ofwel, het primitieve model is te primitief, ofwel dat de experimenten elementen bevatten die niet worden meegenomen. De eerste optie lijkt op het eerste gezicht het meest logisch, maar zelfs simulaties die alle atomen meenemen, inclusief die van het oplosmiddel, voorspellen niet de langedrachtsafval die gezien wordt in de experimenten. Dit blijft op moment dus nog een open vraag. Het antwoord op de vraag welke van de drie functionalen het meest accuraat is, blijkt de MSAC functionaal te zijn als gekeken wordt naar het totaalplaatje. Echter, in de lage-concentratie limiet waar ook de elektrische potentiaal op de elektrode laag is, is de MSAu de enige functionaal die depletie meeneemt als gevolg van de inclusie van de energie-term. Dit blijkt echter bij hogere concentraties en potentialen geen grote rol meer te spelen.

We hebben gezien dat de MSAC functionaal in het algemeen het beste presteert, en zeker in het verre veld. Nu gaan we deze functionaal gebruiken en vergelijken met resultaten uit Brownse Dynamica (BD) simulaties voor een groot scala aan parameters. Het systeem dat we beschouwen betreft twee evenwijdige platen waarop een potentiaal/potentiaal verschil wordt gezet. Tussen de twee platen in bevindt zich het elektrolyt met ionen die een bepaalde concentratie, grootte en valentie hebben. We beschouwen weer het PM waarbij het oplosmiddel niet expliciet wordt meegenomen. Het referentiesysteem waarvan we uitwijken door telkens een andere parameter aan te passen, heeft een plaatafstand van 4 nm, reservoir concentratie van 1 M, potentiaalverschil van 0.2 V, ion diameters van 0.5 nm, en valenties ± 1 . We vinden voortreffelijke overeenkomst tussen DFT en BD resultaten. Vervolgens variëren we in elk afzonderlijk geval de reservoir concentratie, beschouwen we grote kationen en klein anionen, passen we de elektrode potentiaal aan, beschouwen we ongelijke ionen valenties, en als laatst variëren we de plaatafstand. In elk van de gevallen zien we voortreffelijke overeenkomst tussen DFT en BD. Dit geeft ons vertrouwen in de theorie, en stelt ons in staat om de thermodynamisch grootheid de differentiële capaciteit nader te onderzoeken. In het bijzonder laten we zien dat er in kleine systemen daadwerkelijk een verschil is in de differentiële capaciteit die wordt berekend bij een constant aantal deeltjes C_N (canoniek ensemble in BD) en constante chemisch potentiaal C_μ (grootkanoniek ensemble in DFT). Echter, deze twee zijn gerelateerd op soortgelijke manier als dat de warmtecapaciteit bij constant volume en druk is gerelateerd. Daardoor kunnen we ze goed vergelijken en laten zien dat C_N en C_μ kwantitatieve verschillen, maar ook kwalitatieve verschillen kunnen vertonen. Dit laat dus expliciet zien dat het onderliggende ensemble goed in ogenschouw moet worden genomen voor analyses op de differentiële capaciteit.

We vervolgen het avontuur in de heuvels en dalen van de differentiële capaciteit door C_μ nader te onderzoeken. Zorgvuldig wordt het C_μ landschap stap voor stap afgetast.

Beginnend met het meest eenvoudige restrictieve PM (RPM), waarbij alle ionen dezelfde grootte hebben, lopen we door het C_μ landschap heen om te zien waar de heuvels en dalen vandaan komen. Dit doen we onder meer met behulp van een nieuw afgeleide uitdrukking voor C_μ , die laat zien dat voornamelijk de respons van de eerste laag van ionen tegen de elektrode op de aangelegde elektrodepotentiaal zeer van belang is. Bij lage concentraties heeft C_μ kameel-vormige curves, oftewel het heeft een maximum op eindige waarden. De oorsprong hiervan ligt in het feit dat we eindig-grootte ionen beschouwen, wat ervoor zorgt dat de ionen een maximum pakking hebben en er dus gelaagde structuren kunnen gaan vormen tegen de elektrode aan. In essentie, het maximum in de differentiële capaciteit is een gevolg van de vorming van een laag ionen tegen de elektrode, waardoor er een tweede laag van tegenionen gevormd moet worden om de lading op de elektrode af te schermen. Dus, over het maxima heen, is er een hoog-gepakte laag van tegenionen tegen de elektrode aan, waardoor er nog maar nauwelijks plek is voor meer ionen in de eerste laag. Bij hoge bulk concentraties vind men, in plaats van een kameel-vormige curve, een bel-vormige curve, en deze crossover wordt dan ook wel de kameel-bel crossover genoemd. Een bel-curve gaat gepaard met slechts één maximum bij een potentiaal van nul, en men ziet dan ook dat er in dat geval al lagen ionen zijn, zelfs als er geen lading op de elektrode zit. Verhogen of verlagen van de potentiaal, zal dan niet voor een structuurverandering zorgen. We concluderen dan ook dat maxima in de differentiële capaciteit gepaard gaat met verandering in de structuur van de ionen. Hetzelfde geldt ook voor asymmetrische elektrolyten met asymmetrie in de iongroottes. Bijzonder aan dit geval is dat we m.b.v. de nieuwe vergelijking voor C_μ kunnen laten zien dat, zeker bij lage concentraties, de differentiële capaciteit wordt gedomineerd bij negatieve potentialen door de kationen en bij positieve potentialen door de anionen. Verder gaande met asymmetrische elektrolyten met een asymmetrie in de valentie, vinden we het effect van overscreening terug in de curves voor C_μ . Dit allemaal gecombineerd, liet ons ertoe om drie-componenten elektrolyten te beschouwen met twee verschillende soorten anionen. In het eerste geval beschouwden we twee anion soorten waarbij een soort monovalent was en de andere divalent. Hierbij varieerde we de verhouding tussen de bulk concentratie van de monovalente en divalente anion van alleen monovalente ionen tot alleen divalente ionen. Wat blijkt is dat er zelfs voor een zeer kleine hoeveelheid divalente ionen (1 divalent anion op 100000 monovalente anionen), een sterke signatuur van de divalente anionen te vinden is in C_μ . Dit is als gevolg van de competitie tussen de monovalente ionen die exponentieel schalen met de potentiaal en de divalente ionen die exponentieel schalen met twee keer de potentiaal. Dus, er is een competitie tussen de bulk concentratie en de opgelegde potentiaal, wat de divalente anionen zullen winnen bij een voldoende hoge potentiaal vanwege de exponentiele schaling. Bij een drie-component systeem met twee anion soorten die verschillen in grootte, zien we ook een competitie. Namelijk, kleine anionen kunnen dichter tegen de elektrode aan zitten dan de grote anionen, wat energetisch voordeliger is. We zien daarom ook dat zelfs bij een kleine hoeveelheid kleine ionen t.o.v. grote ionen (1:1000) de differentiële capaciteit wordt bepaald door de kleine ionen bij voldoende hoge potentialen. De reden is dat de kleine ionen de grote ionen wegduwen als de potentiaal op de elektrode maar hoog genoeg is, en

gebruik makend van de nieuwe vergelijking voor C_μ wordt het duidelijk dat daarom C_μ wordt bepaald door de eerste laag van kleine ionen tegen de elektrode. Wij concluderen dat onzuiverheden in een elektrolyt niet vergeten mogen worden in de analyse van de differentiële capaciteit. Aangezien het vrijwel onmogelijk is om alle onzuiverheden uit water te filteren (sulfaat SO_4^{2-} is bijvoorbeeld in zeer gezuiverd water aanwezig in concentraties van μM), is dit dus een belangrijk element om mee te nemen.

Als laatst zoomen we uit en beschouwen we fundamentele eigenschappen van DFT nader. In het bijzonder beschouwen we een Lennard-Jones (LJ) systeem zonder ladingen; er is dus maar één soort deeltje in het systeem. Een van de eigenschappen van de Helmholtz vrije energie functionaal \mathcal{F} , is dat deze onafhankelijk is van de opgelegde externe en chemische potentiaal. Door middel van machine-learning (ML) technieken wordt de mean-field functionaal voor het LJ systeem verbeterd. Hiervoor worden Monte-Carlo simulaties gedaan bij verschillende externe en chemische potentialen, met in het achterhoofd dat \mathcal{F} onafhankelijk is hiervan. We beschouwen zowel correcties op de mean-field functionaal die gaan als de dichtheid in het kwadraat alsook daarbovenop correcties die gaan als de dichtheid tot de derde macht. Door middel van een ML algoritme, kunnen we de correcties bovenop mean field fitten. De resulterende ML functionalen vertonen inderdaad beter resultaten dan de mean-field functionaal, zowel de toestandsvergelijking alsook de dichtheidsprofielen zelf zijn in grote mate verbeterd. Er is relatief weinig verschil tussen de twee ML functionalen. In het bijzonder hebben we ook gekeken naar hoe de ML functionalen zich gedragen in een sferische geometrie d.m.v. een transformatie van planaire geometrie naar sferische geometrie; de ML functionalen zijn ontwikkeld in een planaire geometrie, maar ook in een sferische geometrie doen de ML functionalen het goed, waarbij de eenvoudigste ML functionaal zelfs nog het beste presteert.

REFERENCES

- [1] P. Cats, R. Evans, A. Härtel and R. van Roij, Primitive model electrolytes in the near and far field: Decay lengths from dft and simulations, *J. Chem. Phys.* **154**, 124504 (2021)
- [2] P. Cats, R. Sitlapersad, W. den Otter, A. Thornton and R. van Roij, Capacitance and structure of electric double layers: Comparing brownian dynamics and classical density functional theory, *J. Solution Chem.* (2021), iLMAT-V Special Issue, doi:10.1007/s10953-021-01090-7
- [3] P. Cats and R. van Roij, The differential capacitance as a probe for the electric double layer structure and the electrolyte bulk composition, *J. Chem. Phys.* **155**, 104702 (2021)
- [4] P. Cats, S. Kuipers, S. de Wind, R. van Damme, G. M. Coli et al., Machine-learning free-energy functionals using density profiles from simulations, *APL Materials* **9**, 031109 (2021)
- [5] Online etymology dictionary: Origin, history and meaning of english words, <https://www.etymonline.com/search?q=ion>, accessed at 2021-10-25
- [6] D. Gielen, F. Boshell, D. Saygin, M. D. Bazilian, N. Wagner et al., The role of renewable energy in the global energy transformation, *Energy Strategy Reviews* **24**, 38 (2019)
- [7] I. Graabak and M. Korpås, Variability characteristics of european wind and solar power resources - a review, *Energies* **9**, 449 (2016)
- [8] M. Huber, D. Dimkova and T. Hamacher, Integration of wind and solar power in europe: Assessment of flexibility requirements, *Energy* **69**, 236 (2014)
- [9] E. Bullich-Massagué, F.-J. Cifuentes-García, I. Glenny-Crende, M. Cheah-Mañé, M. Aragüés-Peñalba et al., A review of energy storage technologies for large scale photovoltaic power plants, *Applied Energy* **274**, 115213 (2020)
- [10] C. R. Matos, J. F. Carneiro and P. P. Silva, Overview of large-scale underground energy storage technologies for integration of renewable energies and criteria for reservoir identification, *Journal of Energy Storage* **21**, 241 (2019)
- [11] T. C. Wanger, The lithium future-resources, recycling, and the environment, *Conservation Letters* **4**, 202 (2011)
- [12] R. B. Kaunda, Potential environmental impacts of lithium mining, *Journal of Energy & Natural Resources Law* **38**, 237 (2020)
- [13] D. B. Agusdinata, W. Liu, H. Eakin and H. Romero, Socio-environmental impacts of lithium mineral extraction: towards a research agenda, *Environmental Research Letters* **13**, 123001 (2018)
- [14] A. Izquierdo, R. Grau, J. Carilla and E. Casagrande, Side effects of green technologies: the potential environmental costs of lithium mining on high elevation andean wetlands in the context of climate change, *Newsletter of the Global Land Project* **12**, 53 (2015)
- [15] W. Liu and D. B. Agusdinata, Interdependencies of lithium mining and communities sustainability in salar de atacama, chile, *Journal of Cleaner Production* **260**, 120838 (2020)
- [16] Lithium: Tibet's green energy treasure, <https://freetibet.org/lithium-tibet>, accessed: 2021-06-03

- [17] D. Denniston, Plunder behind the bamboo curtain. [environmental effects of mining and deforestation in tibet], *World Watch* **24** (1993)
- [18] J. Górka, A. Zawislak, J. Choma and M. Jaroniec, Adsorption and structural properties of soft-templated mesoporous carbons obtained by carbonization at different temperatures and koh activation, *Applied Surface Science* **256**, 5187 (2010)
- [19] K. Urita, C. Urita, K. Fujita, K. Horio, M. Yoshida et al., The ideal porous structure of edlc carbon electrodes with extremely high capacitance, *Nanoscale* **9**, 15643 (2017)
- [20] T. M. Gür, Review of electrical energy storage technologies, materials and systems: challenges and prospects for large-scale grid storage, *Energy Environ. Sci.* **11**, 2696 (2018)
- [21] P. Simon and G. Y., Materials for electrochemical capacitors, *Nat. Mater.* **7**, 845 (2008)
- [22] M. C., R. B., M. P.A., T. PL., S. P. et al., On the molecular origin of supercapitance in nanoporous carbon electrodes, *Nat. Mater.* **11**, 306 (2012)
- [23] D. T. Limmer, C. Merlet, M. Salanne, D. Chandler, P. A. Madden et al., Charge fluctuations in nanoscale capacitors, *Phys. Rev. Lett.* **111**, 106102 (2013)
- [24] A. Härtel, M. Janssen, D. Weingarth, V. Presser and R. van Roij, Heat-to-current conversion of low-grade heat from a thermocapacitive cycle by supercapacitors, *Energy Environ. Sci.* **8**, 2396 (2015)
- [25] D. Brogioli, Extracting renewable energy from a salinity difference using a capacitor, *Phys. Rev. Lett.* **103**, 058501 (2009)
- [26] M. Janssen and R. van Roij, Reversible heating in electric double layer capacitors, *Phys. Rev. Lett.* **118**, 096001 (2017)
- [27] S. Porada, R. Zhao, A. van der Wal, V. Presser and P. Biesheuvel, Review on the science and technology of water desalination by capacitive deionization, *Progress in Materials Science* **58**, 1388 (2013)
- [28] H. Helmholtz, Ueber einige gesetze der vertheilung elektrischer ströme in körperlichen leitern mit anwendung auf die thierisch-elektrischen versuche, *Annalen der Physik* **165**, 211 (1853)
- [29] Gouy, M., Sur la constitution de la charge électrique à la surface d'un électrolyte, *J. Phys. Theor. Appl.* **9**, 457 (1910)
- [30] D. L. Chapman, Li. a contribution to the theory of electrocapillarity, *The London, Edinburgh, and Dublin Philosophical Magazine and Journal of Science* **25**, 475 (1913)
- [31] P. Debye and E. Hückel, Zur theorie der elektrolyte. i. gefrierpunktserniedrigung und verwandte erscheinungen, *Physikalische Zeitschrift* **24**, 305 (1923)
- [32] J. Zeman, S. Kondrat and C. Holm, Bulk ionic screening lengths from extremely large-scale molecular dynamics simulations, *Chem. Commun.* **56**, 15635 (2020)
- [33] S. W. Coles, C. Park, R. Nikam, M. Kanduč, J. Dzubiella et al., Correlation length in concentrated electrolytes: Insights from all-atom molecular dynamics simulations, *J. Phys. Chem. B* **124**, 1778 (2020)
- [34] M. A. Gebbie, H. A. Dobbs, M. Valtiner and J. N. Israelachvili, Long-range electrostatic screening in ionic liquids, *Proc. Natl. Acad. Sci. U. S. A.* **112**, 7432 (2015)
- [35] H.-W. Cheng, P. Stock, B. Moeremans, T. Baimpos, X. Banquy et al., Characterizing the influence of water on charging and layering at electrified ionic-liquid/solid interfaces, *Advanced Materials Interfaces* **2**, 1500159 (2015)

- [36] R. M. Espinos-Marzal, A. Arcifa, A. Rossi and N. D. Spencer, Microslips to “avalanches” in confined, molecular layers of ionic liquids, *J. Phys. Chem. Lett.* **5**, 179 (2014)
- [37] A. M. Smith, A. A. Lee and S. Perkin, The electrostatic screening length in concentrated electrolytes increases with concentration, *J. Phys. Chem. Lett.* **7**, 2157 (2016)
- [38] M. A. Gebbie, A. M. Smith, H. A. Dobbs, A. A. Lee, G. G. Warr et al., Long range electrostatic forces in ionic liquids, *Chem. Commun.* **53**, 1214 (2017)
- [39] C. Merlet, D. T. Limmer, M. Salanne, R. van Roij, P. A. Madden et al., The electric double layer has a life of its own, *J. Phys. Chem. C* **118**, 18291 (2014)
- [40] L. Scalfi, D. T. Limmer, A. Coretti, S. Bonella, P. A. Madden et al., Charge fluctuations from molecular simulations in the constant-potential ensemble, *Phys. Chem. Chem. Phys.* pp. – (2020)
- [41] L. Scalfi, D. T. Limmer, A. Coretti, S. Bonella, P. A. Madden et al., Charge fluctuations from molecular simulations in the constant-potential ensemble, *Phys. Chem. Chem. Phys.* **22**, 10480 (2020)
- [42] J.-P. Hansen and I. McDonald, *Theory of simple liquids; 4th ed.*, Academic Press, New York, NY (2013)
- [43] B. Grosjean, M. Bocquet and R. Vuilleumier, Versatile electrification of two-dimensional nanomaterials in water, *Nature Communications* **10**, 1656 (2019)
- [44] B. A. Ali and N. K. Allam, A first-principles roadmap and limits to design efficient supercapacitor electrode materials, *Phys. Chem. Chem. Phys.* **21**, 17494 (2019)
- [45] N. D. Mermin, Thermal properties of the inhomogeneous electron gas, *Phys. Rev.* **137**, A1441 (1965)
- [46] R. Evans, The nature of the liquid-vapour interface and other topics in the statistical mechanics of non-uniform, classical fluids, *Advances in Physics* **28**, 143 (1979)
- [47] R. Roth, Fundamental measure theory for hard-sphere mixtures: a review, *J. Phys.: Condens. Matter* **22**, 063102 (2010)
- [48] H. Hansen-Goos and R. Roth, Density functional theory for hard-sphere mixtures: the white bear version mark II, *J. Phys.: Condens. Matter* **18**, 8413 (2006)
- [49] R. Davidchack, B. Laird and R. Roth, Hard spheres at a planar hard wall: Simulations and density functional theory, *Condensed Matter Physics* **19**, 23001 (2016)
- [50] R. Roth, R. Evans, A. Lang and G. Kahl, Fundamental measure theory for hard-sphere mixtures revisited: the white bear version, *J. Phys.: Condens. Matter* **14**, 12063 (2002)
- [51] Y. Rosenfeld, Free-energy model for the inhomogeneous hard-sphere fluid mixture and density-functional theory of freezing, *Phys. Rev. Lett.* **63**, 980 (1989)
- [52] S. M. Tschopp, H. D. Vuijk, A. Sharma and J. M. Brader, Mean-field theory of inhomogeneous fluids, *Phys. Rev. E* **102**, 042140 (2020)
- [53] S. M. Tschopp and J. M. Brader, Fundamental measure theory of inhomogeneous two-body correlation functions, *Phys. Rev. E* **103**, 042103 (2021)
- [54] A. J. Archer, B. Chacko and R. Evans, The standard mean-field treatment of inter-particle attraction in classical dft is better than one might expect, *J. Chem. Phys.* **147**, 034501 (2017)
- [55] L. Ornstein and F. Zernike, Accidental deviations of density and opalescence at the critical point of a single substance, *KNAW* **17**, 793 (1914)
- [56] Classical dft code, <http://www.classicalDFT.com>, currently being developed

- [57] I. Borukhov, D. Andelman and H. Orland, Steric effects in electrolytes: A modified poisson-boltzmann equation, *Phys. Rev. Lett.* **79**, 435 (1997)
- [58] Y. Rosenfeld, Free-energy model for the inhomogeneous hard-sphere fluid mixture and density-functional theory of freezing, *Phys. Rev. Lett.* **63**, 980 (1989)
- [59] P. Attard, Asymptotic analysis of primitive model electrolytes and the electrical double layer, *Phys. Rev. E* **48**, 3604 (1993)
- [60] J. Ennis, R. Kjellander and D. J. Mitchell, Dressed ion theory for bulk symmetric electrolytes in the restricted primitive model, *J. Chem. Phys.* **102**, 975 (1995)
- [61] R. L. de Carvalho and R. Evans, The decay of correlations in ionic fluids, *Molecular Physics* **83**, 619 (1994)
- [62] R. Evans, M. Oettel, R. Roth and G. Kahl, New developments in classical density functional theory, *J. Phys.: Condens. Matter* **28**, 240401 (2016)
- [63] A. Härtel, Structure of electric double layers in capacitive systems and to what extent (classical) density functional theory describes it, *J. Phys.: Condens. Matter* **29**, 423002 (2017)
- [64] L. Blum, Solution of a model for the solvent-electrolyte interactions in the mean spherical approximation, *J. Chem. Phys.* **61**, 2129 (1974)
- [65] L. Blum, Mean spherical model for asymmetric electrolytes, *Molecular Physics* **30**, 1529 (1975)
- [66] L. Blum and J. S. Hoeye, Mean spherical model for asymmetric electrolytes. 2. thermodynamic properties and the pair correlation function, *The Journal of Physical Chemistry* **81**, 1311 (1977)
- [67] K. Hiroike, Supplement to blum's theory for asymmetric electrolytes, *Molecular Physics* **33**, 1195 (1977)
- [68] E. Waisman and J. L. Lebowitz, Exact solution of an integral equation for the structure of a primitive model of electrolytes, *J. Chem. Phys.* **52**, 4307 (1970)
- [69] E. Waisman and J. L. Lebowitz, Mean spherical model integral equation for charged hard spheres. i. method of solution, *J. Chem. Phys.* **56**, 3086 (1972)
- [70] E. Waisman and J. L. Lebowitz, Mean spherical model integral equation for charged hard spheres. ii. results, *J. Chem. Phys.* **56**, 3093 (1972)
- [71] R. Roth and D. Gillespie, Shells of charge: a density functional theory for charged hard spheres, *J. Phys.: Condens. Matter* **28**, 244006 (2016)
- [72] L. Mier-y Teran, S. Suh, H. White and H. Davis, A nonlocal free-energy density-functional approximation for the electric double layer, *J. Chem. Phys.* **92**, 5087 (1990)
- [73] A. Voukadinova, M. Valiskó and D. Gillespie, Assessing the accuracy of three classical density functional theories of the electrical double layer, *Phys. Rev. E* **98**, 012116 (2018)
- [74] L. Blum and Y. Rosenfeld, Relation between the free energy and the direct correlation function in the mean spherical approximation, *J. Stat. Phys.* **63**, 1177 (1991)
- [75] G. Orkoulas and A. Z. Panagiotopoulos, Free energy and phase equilibria for the restricted primitive model of ionic fluids from monte carlo simulations, *J. Chem. Phys.* **101**, 1452 (1994)
- [76] F. Weik, R. Weeber, Szuttor, K. Breitsprecher, J. de Graaf et al., Particle methods in natural science and engineering, *Eur. Phys. J. Special Topics* **227**, 1493 (2019)
- [77] H. C. Andersen, J. D. Weeks and D. Chandler, Relationship between the hard-sphere fluid and fluids with realistic repulsive forces, *Phys. Rev. A* **4**, 1597 (1971)

- [78] J. D. Weeks, D. Chandler and H. C. Andersen, Role of repulsive forces in determining the equilibrium structure of simple liquids, *J. Chem. Phys.* **54**, 5237 (1971)
- [79] J. Ulander and R. Kjellander, The decay of pair correlation functions in ionic fluids: A dressed ion theory analysis of monte carlo simulations, *J. Chem. Phys.* **114**, 4893 (2001)
- [80] P. González-Mozuelos, G. I. Guerrero-García and M. Olvera de la Cruz, An exact method to obtain effective electrostatic interactions from computer simulations: The case of effective charge amplification, *J. Chem. Phys.* **139**, 064709 (2013)
- [81] R. Evans, J. Henderson, D. Hoyle, A. Parry and Z. Sabeur, Asymptotic decay of liquid structure: Oscillatory liquid-vapour density profiles and the fisher-widom line, *Molecular Physics* **80**, 755 (1993)
- [82] P. Attard, D. R. Bérard, C. P. Ursenbach and G. N. Patey, Interaction free energy between planar walls in dense fluids: An ornstein-zernike approach with results for hard-sphere, lennard-jones, and dipolar systems, *Phys. Rev. A* **44**, 8224 (1991)
- [83] P. Attard, C. P. Ursenbach and G. N. Patey, Long-range attractions between solutes in near-critical fluids, *Phys. Rev. A* **45**, 7621 (1992)
- [84] R. Evans, R. J. F. Leote de Carvalho, J. R. Henderson and D. C. Hoyle, Asymptotic decay of correlations in liquids and their mixtures, *J. Chem. Phys.* **100**, 591 (1994)
- [85] R. Kjellander and D. Mitchell, An exact but linear and poisson-boltzmann-like theory for electrolytes and colloid dispersions in the primitive model, *Chemical Physics Letters* **200**, 76 (1992)
- [86] M. E. Fisher and B. Widom, Decay of correlations in linear systems, *J. Chem. Phys.* **50**, 3756 (1969)
- [87] M. Dijkstra and R. Evans, A simulation study of the decay of the pair correlation function in simple fluids, *J. Chem. Phys.* **112**, 1449 (2000)
- [88] J. G. Kirkwood, Statistical mechanics of liquid solutions., *Chemical Reviews* **19**, 275 (1936)
- [89] R. Kjellander and D. J. Mitchell, Dressed-ion theory for electrolyte solutions: A debye-hückel-like reformulation of the exact theory for the primitive model, *J. Chem. Phys.* **101**, 603 (1994)
- [90] C. Outhwaite and V. Hutson, The mean spherical model for charged hard spheres, *Molecular Physics* **29**, 1521 (1975)
- [91] C. W. Outhwaite and L. Bhuiyan, Comments on the linear modified poisson-boltzmann equation in electrolyte solution theory, *Condensed Matter Physics* **22**, 23801 (2019)
- [92] R. Evans and U. Marini Bettolo Marconi, Phase equilibria and solvation forces for fluids confined between parallel walls, *J. Chem. Phys.* **86**, 7138 (1987)
- [93] A. A. Lee, C. S. Perez-Martinez, A. M. Smith and S. Perkin, Scaling analysis of the screening length in concentrated electrolytes, *Phys. Rev. Lett.* **119**, 026002 (2017)
- [94] A. A. Lee, C. S. Perez-Martinez, A. M. Smith and S. Perkin, Underscreening in concentrated electrolytes, *Faraday Discuss.* **199**, 239 (2017)
- [95] F. Coupette, A. A. Lee and A. Härtel, Screening lengths in ionic fluids, *Phys. Rev. Lett.* **121**, 075501 (2018)
- [96] B. Rotenberg, O. Bernard and J.-P. Hansen, Underscreening in ionic liquids: a first principles analysis, *J Phys Condens Matter* **30**, 054005 (2018)
- [97] G. Feng, M. Chen, S. Bi, Z. A. H. Goodwin, E. B. Postnikov et al., Free and bound states of ions in ionic liquids, conductivity, and underscreening paradox, *Phys. Rev. X* **9**, 021024 (2019)

- [98] R. Kjellander, A multiple decay-length extension of the debye-hückel theory: to achieve high accuracy also for concentrated solutions and explain underscreening in dilute symmetric electrolytes, *Phys. Chem. Chem. Phys.* **22**, 23952 (2020)
- [99] A. M. Smith, A. A. Lee and S. Perkin, Switching the structural force in ionic liquid-solvent mixtures by varying composition, *Phys. Rev. Lett.* **118**, 096002 (2017)
- [100] A. Zeidler, *Ordering in Amorphous Binary Systems*, Ph.D. thesis, University of Bath (2009), chapter 3: The Structure of Molten Sodium Chloride
- [101] P. Koblinski, J. Eggebrecht, D. Wolf and S. R. Phillpot, Molecular dynamics study of screening in ionic fluids, *J. Chem. Phys.* **113**, 282 (2000)
- [102] R. Kjellander, The intimate relationship between the dielectric response and the decay of intermolecular correlations and surface forces in electrolytes, *Soft Matter* **15**, 5866 (2019)
- [103] R. Kjellander, Nonlocal electrostatics in ionic liquids: The key to an understanding of the screening decay length and screened interactions, *J. Chem. Phys.* **145**, 124503 (2016)
- [104] A. Maciołek, A. Drzewiński and P. Bryk, Solvation force for long-ranged wall-fluid potentials, *J. Chem. Phys.* **120**, 1921 (2004)
- [105] J. K. Percus, Approximation methods in classical statistical mechanics, *Phys. Rev. Lett.* **8**, 462 (1962)
- [106] M. C. Walters, P. Subramanian, A. J. Archer and R. Evans, Structural crossover in a model fluid exhibiting two length scales: Repercussions for quasicrystal formation, *Phys. Rev. E* **98**, 012606 (2018)
- [107] D. Stopper, H. Hansen-Goos, R. Roth and R. Evans, On the decay of the pair correlation function and the line of vanishing excess isothermal compressibility in simple fluids, *J. Chem. Phys.* **151**, 014501 (2019)
- [108] R. Evans and R. J. F. L. de Carvalho, *Decay of Correlations in Bulk Fluids and at Interfaces: A Density-Functional Perspective*, American Chemical Society, chapter 12, pp. 166–184 (1996)
- [109] R. J. F. L. D. CARVALHO and R. EVANS, The screened coulomb (yukawa) charged hard sphere binary fluid, *Molecular Physics* **92**, 211 (1997)
- [110] S. T. Revankar, Chapter six - chemical energy storage, in H. Bindra and S. Revankar, eds., *Storage and Hybridization of Nuclear Energy*, Academic Press, pp. 177 – 227 (2019)
- [111] Y. Wang, Y. Song and Y. Xia, Electrochemical capacitors: mechanism, materials, systems, characterization and applications, *Chem. Soc. Rev.* **45**, 5925 (2016)
- [112] M. Winter and R. J. Brodd, What are batteries, fuel cells, and supercapacitors?, *Chemical Reviews* **104**, 4245 (2004)
- [113] F. Béguin, V. Presser, A. Balducci and E. Frackowiak, Carbons and electrolytes for advanced supercapacitors, *Advanced Materials* **26**, 2219 (2014)
- [114] H. Liu and H. Yu, Ionic liquids for electrochemical energy storage devices applications, *Journal of Materials Science & Technology* **35**, 674 (2019)
- [115] M. Galiński, A. Lewandowski and I. Stępnia, Ionic liquids as electrolytes, *Electrochimica Acta* **51**, 5567 (2006)
- [116] M. Salanne, *Ionic Liquids for Supercapacitor Applications*, Springer International Publishing, Cham, pp. 29–53 (2018)
- [117] A. Härtel, Structure of electric double layers in capacitive systems and to what extent (classical) density functional theory describes it, *J. Phys.: Condens. Matter* **29**, 423002 (2017)

- [118] J. Forsman, C. E. Woodward and M. Trulsson, A classical density functional theory of ionic liquids, *J. Phys. Chem. B* **115**, 4606–4612 (2011)
- [119] M. V. Fedorov and A. A. Kornyshev, Ionic liquids at electrified interfaces, *Chemical Reviews* **114**, 2978 (2014)
- [120] D. Henderson, S. Lamperski, Z. Jin and J. Wu, Density functional study of the electric double layer formed by a high density electrolyte, *J. Phys. Chem. B* **115**, 12911 (2011)
- [121] D. Jiang, D. Meng and J. Wu, Density functional theory for differential capacitance of planar electric double layers in ionic liquids, *Chemical Physics Letters* **504**, 153 (2011)
- [122] J. Yang, C. Lian and H. Liu, Chain length matters: Structural transition and capacitance of room temperature ionic liquids in nanoporous electrodes, *Chemical Engineering Science* **227**, 115927 (2020)
- [123] G. Shen, Y. Sun, Y. Wang, X. Lu and X. Ji, Interfacial structure and differential capacitance of ionic liquid/graphite interface: A perturbed-chain soft density functional theory study, *Journal of Molecular Liquids* **310**, 113199 (2020)
- [124] O. J. Lanning and P. A. Madden, Screening at a charged surface by a molten salt, *J. Phys. Chem. B* **108**, 11069 (2004)
- [125] M. V. Fedorov and A. A. Kornyshev, Ionic liquid near a charged wall: Structure and capacitance of electrical double layer, *J. Phys. Chem. B* **112**, 11868 (2008)
- [126] G. Feng, J. S. Zhang and R. Qiao, Microstructure and capacitance of the electrical double layers at the interface of ionic liquids and planar electrodes, *J. Phys. Chem. C* **113**, 4549 (2009)
- [127] S. A. Kislenko, I. S. Samoylov and R. H. Amirov, Molecular dynamics simulation of the electrochemical interface between a graphite surface and the ionic liquid [bmim][pf6], *Phys. Chem. Chem. Phys.* **11**, 5584 (2009)
- [128] E. Paek, A. J. Pak and G. S. Hwang, A computational study of the interfacial structure and capacitance of graphene in [BMIM][PF6] ionic liquid, *Journal of The Electrochemical Society* **160**, A1 (2012)
- [129] X. Si, S. Li, Y. Wang, S. Ye and T. Yan, Effects of specific adsorption on the differential capacitance of imidazolium-based ionic liquid electrolytes, *ChemPhysChem* **13**, 1671 (2012)
- [130] J. Vatamanu, O. Borodin and G. D. Smith, Molecular insights into the potential and temperature dependences of the differential capacitance of a room-temperature ionic liquid at graphite electrodes, *Journal of the American Chemical Society* **132**, 14825 (2010)
- [131] C. Merlet, M. Salanne, B. Rotenberg and P. A. Madden, Imidazolium ionic liquid interfaces with vapor and graphite: Interfacial tension and capacitance from coarse-grained molecular simulations, *J. Phys. Chem. C* **115**, 16613 (2011)
- [132] C. Merlet, C. Péan, B. Rotenberg, P. A. Madden, P. Simon et al., Simulating supercapacitors: Can we model electrodes as constant charge surfaces?, *J. Phys. Chem. Lett.* **4**, 264 (2013)
- [133] Z. Wang, Y. Yang, D. L. Olmsted, M. Asta and B. B. Laird, Evaluation of the constant potential method in simulating electric double-layer capacitors, *J. Chem. Phys.* **141**, 184102 (2014)
- [134] J. Vatamanu, L. Cao, O. Borodin, D. Bedrov and G. D. Smith, On the influence of surface topography on the electric double layer structure and differential capacitance of graphite/ionic liquid interfaces, *J. Phys. Chem. Lett.* **2**, 2267 (2011)
- [135] S. K. Reed, O. J. Lanning and P. A. Madden, Electrochemical interface between an ionic liquid and a model metallic electrode, *J. Chem. Phys.* **126**, 084704 (2007)

- [136] M. Pounds, S. Tazi, M. Salanne and P. A. Madden, Ion adsorption at a metallic electrode: an ab initio based simulation study, *J. Phys.: Condens. Matter* **21**, 424109 (2009)
- [137] J. Vatamanu, O. Borodin and G. D. Smith, Molecular simulations of the electric double layer structure, differential capacitance, and charging kinetics for n-methyl-n-propylpyrrolidinium bis(fluorosulfonyl)imide at graphite electrodes, *J. Phys. Chem. B* **115**, 3073 (2011)
- [138] Z. Bo, H. Yang, S. Zhang, J. Yang, J. Yan et al., Molecular Insights into Aqueous NaCl Electrolytes Confined within Vertically-oriented Graphenes, *Scientific Reports* **5**, 14652 (2015)
- [139] G. Jiang, C. Cheng, D. Li and J. Z. Liu, Molecular dynamics simulations of the electric double layer capacitance of graphene electrodes in mono-valent aqueous electrolytes, *Nano Research* **9**, 174 (2016)
- [140] P. S. Crozier, R. L. Rowley and D. Henderson, Molecular dynamics calculations of the electrochemical properties of electrolyte systems between charged electrodes, *J. Chem. Phys.* **113**, 9202 (2000)
- [141] P. S. Crozier, R. L. Rowley and D. Henderson, Molecular-dynamics simulations of ion size effects on the fluid structure of aqueous electrolyte systems between charged model electrodes, *J. Chem. Phys.* **114**, 7513 (2001)
- [142] E. Spohr, Molecular dynamics simulations of water and ion dynamics in the electrochemical double layer, *Solid State Ionics* **150**, 1 (2002)
- [143] M. P. Allen and D. J. Tildesley, *Computer Simulation of Liquids*, Clarendon Press, New York, NY, U.S.A. (1989)
- [144] A. Voukadinova, M. Valiskó and D. Gillespie, Assessing the accuracy of three classical density functional theories of the electrical double layer, *Phys. Rev. E* **98**, 012116 (2018)
- [145] M. Valiskó, T. Kristóf, D. Gillespie and D. Boda, A systematic monte carlo simulation study of the primitive model planar electrical double layer over an extended range of concentrations, electrode charges, cation diameters and valences, *AIP Advances* **8**, 025320 (2018)
- [146] S. Plimpton, Fast parallel algorithms for short-range molecular dynamics, *J. Comput. Phys.* **117**, 1 (1995)
- [147] J. I. Siepmann and M. Sprik, Influence of surface topology and electrostatic potential on water/electrode systems, *J. Chem. Phys.* **102**, 511 (1995)
- [148] D. Frenkel and B. Smit, *Understanding molecular simulations. From algorithms to applications*, Academic press, San Diego, CA, 2 edition (2002)
- [149] A. Härtel, M. Janssen, S. Samin and R. van Roij, Fundamental measure theory for the electric double layer: implications for blue-energy harvesting and water desalination, *J. Phys.: Condens. Matter* **27**, 194129 (2015)
- [150] D. Gillespie, W. Nonner and R. S. Eisenberg, Density functional theory of charged, hard-sphere fluids, *Phys. Rev. E* **68**, 031503 (2003)
- [151] M. Z. Bazant, B. D. Storey and A. A. Kornyshev, Double layer in ionic liquids: Overscreening versus crowding, *Phys. Rev. Lett.* **106**, 046102 (2011)
- [152] A. A. Kornyshev, Double-layer in ionic liquids: Paradigm change?, *J. Phys. Chem. B* **111**, 5545 (2007)
- [153] Y.-X. Yu and J. Wu, Density functional theory for inhomogeneous mixtures of polymeric fluids, *J. Chem. Phys.* **117**, 2368 (2002)
- [154] M. Levesque, R. Vuilleumier and D. Borgis, Scalar fundamental measure theory for hard spheres in three dimensions: Application to hydrophobic solvation, *J. Chem. Phys.* **137**, 034115 (2012)

- [155] G. Jeanmairet, M. Levesque and D. Borgis, Molecular density functional theory of water describing hydrophobicity at short and long length scales, *J. Chem. Phys.* **139**, 154101 (2013)
- [156] L. Ding, M. Levesque, D. Borgis and L. Belloni, Efficient molecular density functional theory using generalized spherical harmonics expansions, *J. Chem. Phys.* **147**, 094107 (2017)
- [157] G. Jeanmairet, B. Rotenberg, D. Borgis and M. Salanne, Study of a water-graphene capacitor with molecular density functional theory, *J. Chem. Phys.* **151**, 124111 (2019)
- [158] R. van Roij, Statistical thermodynamics of supercapacitors and blue engines, in D. S. Dean, J. Dobnikar, A. Naji and R. Podgornik, eds., *Electrostatics of Soft and Disordered Matter*, Jenny Stanford Publishing (2014)
- [159] S. Blundell and K. Blundell, *Concepts in Thermal Physics*, OUP Oxford (2010)
- [160] G. V. Bossa, D. L. Caetano, S. J. de Carvalho and S. May, Differential capacitance of an electrical double layer with asymmetric ion sizes in the presence of hydration interactions, *Electrochimica Acta* **321**, 134655 (2019)
- [161] M. Kaja, S. Lamperski, W. Silvestre-Alcantara, L. Bhuiyan and D. Henderson, Influence of anisotropic ion shape, asymmetric valency, and electrolyte concentration on structural and thermodynamic properties of an electric double layer, *Condensed Matter Physics* **19**, 13804 (2016)
- [162] D. Henderson, W. Silvestre-Alcantara, M. Kaja, S. Lamperski, J. Wu et al., Structure and capacitance of an electric double layer of an asymmetric valency dimer electrolyte: A comparison of the density functional theory with monte carlo simulations, *Journal of Molecular Liquids* **228**, 236 (2017)
- [163] P. Biesheuvel and M. van Soestbergen, Counterion volume effects in mixed electrical double layers, *Journal of Colloid and Interface Science* **316**, 490 (2007)
- [164] D. L. Z. Caetano, G. V. Bossa, V. M. de Oliveira, M. A. Brown, S. J. de Carvalho et al., Role of ion hydration for the differential capacitance of an electric double layer, *Phys. Chem. Chem. Phys.* **18**, 27796 (2016)
- [165] Y. Nakayama and D. Andelman, Differential capacitance of the electric double layer: The interplay between ion finite size and dielectric decrement, *J. Chem. Phys.* **142**, 044706 (2015)
- [166] A. L. Frischknecht, D. O. Halligan and M. L. Parks, Electrical double layers and differential capacitance in molten salts from density functional theory, *J. Chem. Phys.* **141**, 054708 (2014)
- [167] K. Ma, C. E. Woodward and J. Forsman, Classical density functional study on interfacial structure and differential capacitance of ionic liquids near charged surfaces, *J. Phys. Chem. C* **118**, 15825 (2014)
- [168] P. Vo, J. Forsman and C. E. Woodward, A semi-gcmc simulation study of electrolytic capacitors with adsorbed titrating peptides, *J. Chem. Phys.* **153**, 174703 (2020)
- [169] M. Valiskó, D. Boda and D. Gillespie, Selective adsorption of ions with different diameter and valence at highly charged interfaces, *J. Phys. Chem. C* **111**, 15575 (2007)
- [170] X. Chen, R. Paul and L. Dai, Carbon-based supercapacitors for efficient energy storage, *National Science Review* **4**, 453 (2017)
- [171] Y. Zhai, Y. Dou, D. Zhao, P. F. Fulvio, R. T. Mayes et al., Carbon materials for chemical capacitive energy storage, *Advanced Materials* **23**, 4828 (2011)
- [172] M. Winter and R. J. Brodd, What are batteries, fuel cells, and supercapacitors?, *Chemical Reviews* **104**, 4245 (2004)

- [173] G. Orkoulas and A. Z. Panagiotopoulos, Free energy and phase equilibria for the restricted primitive model of ionic fluids from monte carlo simulations, *J. Chem. Phys.* **101**, 1452 (1994)
- [174] D. Henderson and L. Blum, Some exact results and the application of the mean spherical approximation to charged hard spheres near a charged hard wall, *J. Chem. Phys.* **69**, 5441 (1978)
- [175] D. Henderson, L. Blum and J. L. Lebowitz, An exact formula for the contact value of the density profile of a system of charged hard spheres near a charged wall, *Journal of Electroanalytical Chemistry and Interfacial Electrochemistry* **102**, 315 (1979)
- [176] T. Eckert, N. C. X. Stuhlmüller, F. Sammüller and M. Schmidt, Fluctuation profiles in inhomogeneous fluids, *Phys. Rev. Lett.* **125**, 268004 (2020)
- [177] D. Henderson, Some analytic expressions for the capacitance and profiles of the electric double layer formed by ions near an electrode, *Hungarian Journal of Industry and Chemistry* **43**, 55 (2015)
- [178] O. Stern, The theory of the electrolytic double layer, *Z. Elektrochem. Angew. Phys. Chem.* **30**, 508 (1924)
- [179] R. van Hal, J. Eijkel and P. Bergveld, A general model to describe the electrostatic potential at electrolyte oxide interfaces, *Advances in Colloid and Interface Science* **69**, 31 (1996)
- [180] V. Lockett, M. Horne, R. Sedev, T. Rodopoulos and J. Ralston, Differential capacitance of the double layer at the electrode/ionic liquids interface, *Phys. Chem. Chem. Phys.* **12**, 12499 (2010)
- [181] S. May, Differential capacitance of the electric double layer: mean-field modeling approaches, *Current Opinion in Electrochemistry* **13**, 125 (2019)
- [182] J. Stafiej, On statistical thermodynamics of the ideal polarizable interface, *Journal of Electroanalytical Chemistry* **351**, 1 (1993)
- [183] M. Fedorov, N. Georgi and A. Kornyshev, Double layer in ionic liquids: The nature of the camel shape of capacitance, *Electrochemistry Communications* **12**, 296 (2010)
- [184] Y. Uematsu, R. R. Netz and D. J. Bonthuis, The effects of ion adsorption on the potential of zero charge and the differential capacitance of charged aqueous interfaces, *J. Phys.: Condens. Matter* **30**, 064002 (2018)
- [185] M. Giroto, R. M. Malossi, A. P. dos Santos and Y. Levin, Lattice model of ionic liquid confined by metal electrodes, *J. Chem. Phys.* **148**, 193829 (2018)
- [186] R. Downing, G. V. Bossa and S. May, The role of ion-ion correlations for the differential capacitance of ionic liquids, *J. Phys. Chem. C* **122**, 28537 (2018)
- [187] M. M. Islam, M. T. Alam and T. Ohsaka, Electrical double-layer structure in ionic liquids: A corroboration of the theoretical model by experimental results, *J. Phys. Chem. C* **112**, 16568 (2008)
- [188] M. Jitvisate and J. R. T. Seddon, Direct measurement of the differential capacitance of solvent-free and dilute ionic liquids, *J. Phys. Chem. Lett.* **9**, 126 (2018)
- [189] S. Lamperski, C. W. Outhwaite and L. B. Bhuiyan, The electric double-layer differential capacitance at and near zero surface charge for a restricted primitive model electrolyte, *J. Phys. Chem. B* **113**, 8925 (2009)
- [190] S. Lamperski and D. Henderson, Simulation study of capacitance of the electrical double layer of an electrolyte near a highly charged electrode, *Molecular Simulation* **37**, 264 (2011)
- [191] S. Lamperski, M. Pluciennik and C. W. Outhwaite, The planar electric double layer capacitance for the solvent primitive model electrolyte, *Phys. Chem. Chem. Phys.* **17**, 928 (2015)
- [192] M. Dijkstra, Capillary freezing or complete wetting of hard spheres in a planar hard slit?, *Phys. Rev. Lett.* **93**, 108303 (2004)

- [193] M. Bassyouni, M. Abdel-Aziz, M. S. Zoromba, S. Abdel-Hamid and E. Drioli, A review of polymeric nanocomposite membranes for water purification, *Journal of Industrial and Engineering Chemistry* **73**, 19 (2019)
- [194] J. G. Gamaethiralalage, K. Singh, S. Sahin, J. Yoon, M. Elimelech et al., Recent advances in ion selectivity with capacitive deionization, *Energy Environ. Sci.* **14**, 1095 (2021)
- [195] F. Yang, Y. He, L. Rosentsvit, M. E. Suss, X. Zhang et al., Flow-electrode capacitive deionization: A review and new perspectives, *Water Research* **200**, 117222 (2021)
- [196] W. team, *Calcium and magnesium in drinking-water*, World Health Organisation (2009)
- [197] F. Kozisek, Regulations for calcium, magnesium or hardness in drinking water in the european union member states, *Regulatory Toxicology and Pharmacology* **112**, 104589 (2020)
- [198] S.-C. Lin and M. Oettel, A classical density functional from machine learning and a convolutional neural network, *SciPost Phys.* **6**, 25 (2019)
- [199] S.-C. Lin, G. Martius and M. Oettel, Analytical classical density functionals from an equation learning network, *J. Chem. Phys.* **152**, 021102 (2020)
- [200] R. Evans, *Fundamentals of inhomogeneous fluids*, CRC Press (1992)
- [201] A. Härtel, M. Oettel, R. E. Rozas, S. U. Egelhaaf, J. Horbach et al., Tension and stiffness of the hard sphere crystal-fluid interface, *Phys. Rev. Lett.* **108**, 226101 (2012)
- [202] M. Marechal and H. Löwen, Density functional theory for hard polyhedra, *Phys. Rev. Lett.* **110**, 137801 (2013)
- [203] M. Schmidt, H. Löwen, J. M. Brader and R. Evans, Density functional for a model colloid-polymer mixture, *Phys. Rev. Lett.* **85**, 1934 (2000)
- [204] S. de Wind, *Constructing the excess Helmholtz free-energy functional of a supercritical Lennard-Jones fluid with Machine Learning*, Master's thesis, University Utrecht (2019)
- [205] J. A. Barker and D. Henderson, Perturbation theory and equation of state for fluids. ii. a successful theory of liquids, *J. Chem. Phys.* **47**, 4714 (1967)
- [206] Y.-X. Yu, A novel weighted density functional theory for adsorption, fluid-solid interfacial tension, and disjoining properties of simple liquid films on planar solid surfaces, *J. Chem. Phys.* **131**, 024704 (2009)
- [207] R. Cotterman, B. Schwarz and J. Prausnitz, Molecular thermodynamics for fluids at low and high densities. part i: Pure fluids containing small or large molecules, *AIChE Journal* **32**, 1787 (1986)
- [208] A. J. Archer, D. Pini, R. Evans and L. Reatto, Model colloidal fluid with competing interactions: Bulk and interfacial properties, *J. Chem. Phys.* **126**, 014104 (2007)
- [209] P. I. Ravikovitch, A. Vishnyakov and A. V. Neimark, Density functional theories and molecular simulations of adsorption and phase transitions in nanopores, *Phys. Rev. E* **64**, 011602 (2001)
- [210] Y. Tang, Z. Tong and B. C.-Y. Lu, Analytical equation of state based on the ornstein-zernike equation, *Fluid Phase Equilibria* **134**, 21 (1997)
- [211] Y. Tang, Role of the barker-henderson diameter in thermodynamics, *J. Chem. Phys.* **116**, 6694 (2002)
- [212] Y. Tang and J. Wu, A density-functional theory for bulk and inhomogeneous lennard-jones fluids from the energy route, *J. Chem. Phys.* **119**, 7388 (2003)
- [213] F. Ruehle, Data science applications to string theory, *Physics Reports* **839**, 1 (2020)

- [214] D. P. Kingma and J. Ba, Adam: A method for stochastic optimization, *arXiv:1412.6980* (2014)
- [215] J. Percus, Approximation methods in classical statistical mechanics, *Phys. Rev. Lett.* **8**, 462 (1962)
- [216] A. Levy, D. Andelman and H. Orland, Dipolar poisson-boltzmann approach to ionic solutions: A mean field and loop expansion analysis, *J. Chem. Phys.* **139**, 164909 (2013)
- [217] W. Chapman, Saft: Equation-of-state solution model for associating fluids, *Fluid Phase Equilibria* **52**, 31 (1989)
- [218] J. Gross and G. Sadowski, Perturbed-chain saft: An equation of state based on a perturbation theory for chain molecules, *Industrial & Engineering Chemistry Research* **40**, 1244 (2001)
- [219] Y.-X. Yu and J. Wu, A fundamental-measure theory for inhomogeneous associating fluids, *J. Chem. Phys.* **116**, 7094 (2002)
- [220] J. Wu, T. Jiang, D.-e. Jiang, Z. Jin and D. Henderson, A classical density functional theory for interfacial layering of ionic liquids, *Soft Matter* **7**, 11222 (2011)
- [221] H. Lu, S. Nordholm, C. E. Woodward and J. Forsman, A classical density functional theory for the asymmetric restricted primitive model of ionic liquids, *J. Chem. Phys.* **148**, 193814 (2018)
- [222] A. Härtel, S. Samin and R. van Roij, Dense ionic fluids confined in planar capacitors: in- and out-of-plane structure from classical density functional theory, *J. Phys.: Condens. Matter* **28**, 244007 (2016)
- [223] C. Song, J. Wang, Z. Meng, F. Hu and X. Jian, Density functional theory calculations of the quantum capacitance of graphene oxide as a supercapacitor electrode, *ChemPhysChem* **19**, 1579 (2018)
- [224] U. M. B. Marconi and P. Tarazona, Dynamic density functional theory of fluids, *J. Chem. Phys.* **110**, 8032 (1999)
- [225] A. J. Archer and R. Evans, Dynamical density functional theory and its application to spinodal decomposition, *J. Chem. Phys.* **121**, 4246 (2004)
- [226] M. Schmidt and J. M. Brader, Power functional theory for brownian dynamics, *J. Chem. Phys.* **138**, 214101 (2013)
- [227] M. Schmidt, Power functional theory for newtonian many-body dynamics, *J. Chem. Phys.* **148**, 044502 (2018)
- [228] S. Hermann and M. Schmidt, Noether's theorem in statistical mechanics, *Commun Phys* **4**, 176 (2021)
- [229] J. F. Lutsko and M. Oettel, Reconsidering power functional theory, *J. Chem. Phys.* **155**, 094901 (2021)

ABOUT THE AUTHOR

Born on 1 November 1991, Peter grew up in a small village called Hank together with his twin sister and older sister. After finishing high school, and working for a year at several companies in order to prepare for a music academy in electrical guitar, he realized that music was for him more of a hobby than anything else. His dad showed him that doing his bachelor in engineering physics at Fontys Hogescholen in Eindhoven might be an interesting choice instead. After visiting one of the open days with his mom he enrolled in this bachelor. However, due to his lack of interest in school during his high school period and therefore having forgotten most about mathematics, he joined a summer school for a short course on basic math at which he met Mike Sas. Together they were excellent students at Fontys and even managed, with a few other students, to bring in an experimental setup to measure quantum entanglement, for which they were granted the KIVI NIRIA award. After doing his first internship at Microflown, a company specialized in acoustics, he went on to do his minor at Utrecht University. Enjoying especially the statistical physics course, he did his bachelor thesis under supervision of René van Roij on blue energy devices, in particular focusing on the charging and discharging dynamics. After successfully finishing his engineering physics education, he continued doing a master in theoretical physics at Utrecht University and graduated cum laude on one-dimensional topological superconductors under supervision of Cristiane Morais Smith. Afterwards he embraced the opportunity to do a PhD on Ionic Liquids under supervision of René van Roij, leading to this thesis.

ACKNOWLEDGMENTS

The first person I need to acknowledge is my supervisor René van Roij. The first time I met him was in 2013 during my minor, at which I followed courses at Utrecht University (UU) of which Statistical Physics was one of them. He immediately inspired me by his enthusiastic way of teaching, and by introducing me to blue energy. The latter caused me to do my Bachelor thesis with him on this topic. René motivated me to do the Theoretical Physics master in the first place, which is the reason I can present this thesis. After finishing my master, I was fortunate that he had a PhD position available on the topic of Ionic Liquids, which opportunity I grabbed with both hands. Fortunately, I got the position, and I am very glad I made that choice. Overall, he was an excellent supervisor that taught me to be very precise in every aspect, from my way of thinking to writing down my thoughts, which helped me a lot and I thank him for it. Moreover, he did not push me in any specific direction, gave me room to let me investigate my own interests, but helped me to focus and prevented me from drifting in all directions. I hope we can continue on collaborating in the future.

Then there is Mike Sas, a long-time friend, with whom I lunched almost daily together while visiting the botanical gardens or walking around the campus. I met him in 2010 during a basic mathematics summer course, preceding the bachelor Engineering Physics at Fontys Hogescholen in Eindhoven. During the time at Fontys, we always challenged each other for the best, which motivated me and helped me reach a higher level. He is also the person that led me to do the minor at the UU by preceding me and motivating me to follow courses there. After our bachelor, we both continued in Utrecht, although I went the theoretical path and he choose the experimental path. Nevertheless, it is safe to state that without him, I would not present this thesis.

I thank my collaborators Bob Evans and Andreas Härtel for our lengthy collaboration on the decay lengths in electrolytes. Bob revealed to me his knowledge and the literature regarding this topic, which helped me to gain a deeper understanding on the matter. But let me not forgot to mention the drinks together in Tübingen and Freiburg at the preCorona-time DFT meetings, which I also enjoyed greatly. I met Andreas Härtel in 2014, whom was one of my supervisors during my bachelor thesis with René, and I enjoyed working together. He was one of the first who gave me access to simulation data against which I could test my DFT code. This helped me a lot in building confidence in my code.

The next collaborators I want to thank are Ranisha Sitlapersad, Wouter den Otter, and Anthony Thornton from Technical University in Twente (TUT). It was a great pleasure to work with them. Together we obtained a better understanding of the system under consideration, and the many comparisons between the DFT calculations and BD simulations, gave us a lot of confidence in both our implementations. Together we also went to Bengaluru in India, where we had a great time. We visited our collaborators Balasub-

ramanian Sundaram and Nikhil Avula, whom I thank a lot for the well-organized accommodation, and, of course, also for organizing very nice sightseeing trips. Unfortunately, due to Covid-19, there was no opportunity to invite them over to the Netherlands and work together on a project.

Next, I thank my colleagues for engaging discussions. Special thanks goes to Willem Boon, who always managed to raise ideas I had not thought of. He pointed me in useful directions, and helped me to think on matters from a more chemical perspective. I always enjoyed our useful and useless conversations. Another colleague and office roommate I want to thank is Alexander Barnavelli. We had quite some interesting, but not always relevant, conversations. He also made the beautiful photo of salt shown in the introduction.

Of course, special thanks goes to my beloved wife, Lunamae Cats, for supporting me all this time. She was, and still is, the one that keeps me grounded and I owe her a lot.

The last persons I want to thank are my parents, who have always supported me all my life. Thanks to them, I could enjoy my education and arrive at where I am now.

Finally, I thank NWO for paying me during my PhD.

COLOPHON

This document was authored using TeXmaker¹ and typeset based on the La Trobe PhD Thesis Template² (customization of the classicthesis³ L^AT_EX template). Other notable software tools used during the production of this document: Matlab⁴ used for writing the DFT code; Inkscape⁵ for working with graphics. This thesis was printed by PrintQuest⁶.

1 <https://www.xmlmath.net/texmaker/>

2 <https://github.com/bashimao/ltu-thesis>

3 <https://bitbucket.org/amiede/classicthesis>

4 https://nl.mathworks.com/?s_tid=gn_logo

5 <https://inkscape.org>

6 <https://www.printquest.nl>